Charge and spin correlations in transition metal oxides

Wilkins, Stuart Brian

Charge and Spin Correlations In Transition Metal Oxides

Stuart Brian Wilkins

A thesis submitted in partial fulfillment of the requirements for the degree of Doctor of Philosophy

Department of Physics
University of Durham
2002

This thesis is dedicated to my parents, Brian and Hazel who have been a constant source of inspiration.

This document was prepared using LaTeX 2_ε with the MiKTeX distribution.

Abstract

Strongly correlated electron systems such as the transition metal oxides have provided important results in condensed matter physics over the past few years. They display intriguing phenomena such as superconductivity, colossal magnetoresistance and stripe ordering due to charge and spin correlations at low temperatures. This thesis presents the study of hole doped nickelate and manganite materials using X-ray scattering over an extended energy range. The development of X-ray scattering at energies ranging from 600 eV up to 130 keV is reported.

High energy scattering results, are presented on the $La_{2-x}Sr_xNiO_{4+\delta}$ system with $x = 0.33$. The sensitivity of X-ray scattering to the charge distribution combined with the use of high energy X-rays has allowed the bulk of the sample to be probed, and have resulted in the discovery of a 'charge stripe glass' within the bulk of the material. We compare these results to previous measurements in the near surface region using ~ 12 keV X-rays.

Jahn - Teller, charge and orbital ordering has been studied in the $Bi_{1-x}Ca_xMnO_3$ system with $x = 0.74$ and the bilayer manganite $La_{2-2x}Sr_{1+2x}Mn_2O_7$ with $x = 0.475$ using resonant X-ray scattering techniques at the manganese K edge and high energy X-ray scattering. These results have confirmed the wavevector of ordering along with their associated correlations.

The design, and commissioning of a novel diffractometer using focused X-rays from graded d-spacing parabolic mirrors is presented. Results show an increase of 10 fold in intensity, together with a simultaneous increase in resolution of 7.5 over previous systems employing graphite monochromating crystals.

The first single-crystal X-ray diffraction results are presented which display huge resonances at the L edges of manganese. The resonant enhancement is sufficiently large to allow the observation of magnetic scattering from a correlated antiferromagnetic alignment of spins. Resonant soft X-ray scattering will become a important technique for the study of $3d$ magnetic materials in the future such as the superconducting, striped cuprate systems.

Contents

List of Figures

List of Tables

The work described in this thesis is that of the author (unless otherwise stated) and has not been submitted, in whole or in part, to this or any other university for any other degree.

Stuart Brian Wilkins 2002

Acknowledgements

Throughout the course of this thesis there are many people who have given me help and encouragement. Here I would like to express my thanks and my apologies to anyone I have missed out.

Firstly may I thank Prof. M. R. Pennington for the assistance and excellent facilities of the department.

I would like to thank my supervisors Dr. Peter Hatton and Prof. Brian Tanner. Peter, who was convinced that he would appear in *Appendix J : "Those who have hindered my research"* for reasons which include venting the soft X-ray beamline after taking over the experiment 2 hours after I had been awake for 36 hours. With this point aside I would like to express my thanks for both the constant encouragement and freedom which he has allowed me to have to explore the results presented in this thesis. I am also grateful for his excellent supervision which has always made me feel like a team player rather than a research student. My thanks also go to Brian for his encouragement and allowing me, under guidance, to follow my own course of research in addition to his habit of 'throwing projects at me'.

I would like to also thank the members of the X-ray scattering and magnetism research group. My thanks go to Tom Hase, the other and founder member of *beamline venting club*, Phil Spencer for offering to cover the night

shift, Mohammad Ghazi, James Buchanan, Ian Terry, Sean Giblin and Dan Read. For the wider department I would like to thank the audio-visual department of Mike Lee, Vicki Greener and Pauline Russell, the support staff of Penny Carse, Joanne Pallister, Rebecca Dunn, Clare Davies, Angela Healer and others. I am also grateful to Wayne Dobby and Ian Manfren for the loan of equipment from the teaching laboratories and making demonstrating bearable. My thanks also go to the managing director of *Dobson Direct Ltd.*, Mr. John Dobson for the excellent technical support which he has provided. The computing support of Dave Srockdale, Lydia Heck and Andrew Hunter is also acknowledged along with there replies to my 'short questions'.

This project was additionally funded under the CASE award scheme and I would like to thank my CASE supervisor Dr. D. K. Bowen and members of Bede Scientific Instruments Ltd. among which I would like to thank Tamzin Lafford, Mark Taylor, Neil Loxley, John Spence and the service technicians who managed to remove the "added extra features", from the D^3. Thanks also goes to Kevin Matney of Bede Scientific Incorporated for his help with interfacing with the MINICAM.

The measurements in this thesis would not have been possible without many collaborations. My thanks go to Dr. Andrew Boothroyd and Dr. D. Prabhakaran of the Clarendon Laboratory, Department of Physics at the University of Oxford who have not only provided excellent single crystal samples but have always been keen to discuss the results which I have obtained. Also I must thank Prof. S-W. Cheong of Rutgers University, USA for samples of the $Bi_{1-x}Ca_xMnO_3$ and $La_{2-x}Sr_xNiO_{4+\delta}$. Finally, my thanks go to Prof. G. H. Lander for the safe acquisition of a crystal of UAs.

With the majority of the experimental data of this thesis being collected at international synchrotron facilities, I am thankful for the help of the following members of staff; Mark Roper of Daresbury Laboratory for his excellent modifications to the soft X-ray diffractometer, help during the experiments and for foregoing the opportunity to cut his grass, to pump down the beamline after it was vented by Peter to NO, NO_2 etc. Secondly to the staff of the *XMaS* beamline at the ESRF of Simon Brown, Danny Mannix, Paul Thompson, David Paul, Sandra Beufoy, Prof. M. Cooper and Prof. W. G. Stirling, who have always ensured that the instrument was working effectively. I would like also to thank Dr. Martin von Zimmermann of HASYLAB for his help and support during our beamtime in Hamburg.

My thanks also go to all the friends who over the last years have put up with all my idiosyncracies. In no particular order I would like to thank Amber and Phil Webster, Helen Bridges, Simon and Julia Coopey, Ady Weetman, Phil Hands and Julie Bell, John and Denise M^{c}Lean and others. They have made the last three years very enjoyable.

Finally I would like to thank my parents Brian and Hazel, throughout my life they have offered nothing but encouragement and have always supported me in any decision or project that I undertake. They have been a source of constant inspiration and encouragement to me. This thesis therefore is dedicated to them.

Publication List

Ghazi, M. E., Wilkins, S. B., Spencer, P. D., Hatton, P. D., Mannix, D., Prabhakaran, D. and Boothroyd, A. T. (2002). *Charge stripe melting in* $La_{2-x}Sr_xNiO_4$ *with* $x = 0.33$, *0.30 and 0.275*, Physical Review B . In Preparation.

Hase, T. P. A., Fulthorpe, B. D., Wilkins, S. B., Tanner, B. K., Marrows, C. H. and Hickey, B. J. (2001*a*). *Soft X-ray magnetic scattering study of rotational magnetisation processes in cobalt/copper multilayers*, Journal of Magnetism and Magnetic Materials **226**, 1717–1719.

Hase, T. P. A., Fulthorpe, B. D., Wilkins, S. B., Tanner, B. K., Marrows, C. H. and Hickey, B. J. (2001*b*). *Weak magnetic moment on IrMn exchange bias pinning layers*, Applied Physics Letters **79**, 985–987.

Hatton, P. D., Ghazi, M. E., Wilkins, S. B., Spencer, P. D., Mannix, D., D'Almeida, T., Prabhakaran, P. and Boothroyd, A. (2002). *X-ray scattering studies of charge stripes in* $La_{2-x}Sr_xNiO_4$ *(*$x = 0.20 - 0.33$*)*, International Journal of Modern Physics B **16**, 1633–1640.

Hatton, P. D., Ghazi, M. E., Wilkins, S. B., Spencer, P. D., Mannix, D., d'Almeida, T., Prabhakaran, P., Boothroyd, A. and Cheong, S.-W. (2002). *X-ray scattering studies of charge stripes in* $La_{2-x}Sr_xNiO_4$ *(*$x = 0.20 - 0.33$*)*, Physica B **318**(4), 289–294.

Hatton, P. D., Wilkins, S. B., Spencer, P. D., Mannix, D., Brown, S. D., D'Almeida, T. and Cheong, S. W. (2002). *Charge and orbital order in the electron doped magnanite* $(Bi,Ca)MnO_3$, International Journal of Modern Physics B **16**, 1661–1666.

Wilkins, S. B., Hase, T. P. A., Tanner, B. K., Hatton, P. D. and Lander, G. H. (2002). *Soft X-Ray magnetic diffraction from* $UAs_{1-x}Se_x$ *(*$x = 0.12$*) at the* N_V *and* N_{IV} *edges*, Physical Review B . In Preparation.

Wilkins, S. B., Hatton, P. D., d'Almedia, T., Liss, K.-D. and Cheong, S.-W. (2002). *High Resolution, High Energy diffraction from $La_{2-x}Sr_xNiO_4$ with $x = 0.33$*, Journal of Physics- Condensed Matter . In Preparation.

Wilkins, S. B., Hatton, P. D., Liß, K. D., Ohler, M., Katsufuji, T. and Cheong, S. W. (2000*a*). *High-resolution high energy X-ray diffraction studies of charge ordering in CMR manganites and nickelates*, International Journal of Modern Physics B **14**, 3753–3758.

Wilkins, S. B., Hatton, P. D., Liss, K. D., Ohler, M., Katsufuji, T. and Cheong, S. W. (2000*b*). *High-resolution high energy X-ray diffraction studies of charge ordering in CMR manganites and nickelates*, ESRF Highlights pp. 56–57.

Wilkins, S. B., Hatton, P. D., Roper, M. D., Prabhakaran, D. and Boothroyd, A. T. (2002). *Soft X-Ray Resonant Magnetic Diffraction*, Physical Review Letters . Submitted.

Wilkins, S. B., Spencer, P. D., Beale, T. A. W., Hatton, P. D., v. Zimmermann, M., Prabhakaran, D. and Boothroyd, A. T. (2002). *X-Ray diffraction study of Charge and Jahn - Teller order in $La_{2-2x}Sr_{1-2x}Mn_2O_7$ ($x = 0.475$ and 0.5)*, Physical Review B . Submitted.

Wilkins, S. B., Spencer, P. D., Hatton, P. D., Brown, S. D., Mannix, D. and Cheong, S.-W. (2002). *Charge and Orbital ordering in the electron doped manganite $Bi_{0.24}Ca_{0.76}MnO_3$*, Physical Review Letters . In Preparation.

Wilkins, S. B., Spencer, P. D., Hatton, P. D., Mannix, D., Brown, S. D., d'Almeida, T. and Cheong, S.-W. (2002). *Charge and orbital order in the electron doped magnanite $(Bi,Ca)MnO_3$*, Physica B **318**(4), 295–299.

Wilkins, S. B., Spencer, P. D., Hatton, P. D., Tanner, B. K., Lafford, T. A., Spence, J. and Loxley, N. (2002). *Novel Diffractometer Utilising crossed Parabolic Mirrors for the Study of Weak Superlattice Reflections*, Review of Scientific Instruments **73**(7), 2666–2671.

Chapter 1

Introduction

Since the discovery of superconductivity in ceramic samples which display much higher transition temperatures than has been previously discovered in metals, research into transition metal oxides has enjoyed a rejuvenation. These materials and their related compounds are often termed *strongly correlated electron* systems and are known to display such exciting phenomena as superconductivity, colossal magnetoresistance, charge and spin stripes and orbital ordering. In such, the interactions between the degrees of freedom in the material, for example the electron - phonon coupling, is very strong in contrast to such Fermi liquid systems where the interactions are considered to be weak. The breakdown in the weak interaction approximation makes theoretical calculations on such materials very difficult. Indeed, such effects as charge ordering and metal insulator transitions can be realised by only changing the temperature by a few Kelvin which can cause dramatic changes in the material properties.

Interest started in the perovskite compounds with the discovery superconductivity in the single layered perovskite compounds. It was found that the doping of holes into the parent compound La_2CuO_4 through the partial

substitution of Ba for La caused superconductivity. The doping region was found to be $0.05 \leq x \leq 0.2$ where x is the barium concentration. Such results were reported by Bednorz and Muller (1986). Later superconductivity was found in the Sr doped system by Cava *et al.* (1987) for similar doping levels. This caused an explosion in the study of copper containing perovskite and related compounds. Notably transition temperatures of $\sim$ 90 K have been found in $YBa_2Cu_3O_{6.8}$ by Wu *et al.* (1987) and above 120 K in $Tl_2Ba_2Ca_2Cu_3O_{10}$ by Hazen *et al.* (1988). While the technological applications for high T_C superconductors are numerous, all these systems are intriguing to physicists as they provide for a virtual playground where all the different ordering processes interplay with each other.

Returning to the case of the perovskite superconductors, the phase diagrams of which are shown in Figures 1.1 and 1.2, some surprising effects were found when the hole concentration was varied. The transition temperature was found to be suppressed around a 'magic number', at a doping level of $x = 0.12$. This effect visible in both Sr doped and Bi doped samples has been labelled the 'one eighth' problem. The origin of the suppression around this level has been of some debate (Wilson, 1998) as to its origin, the question is what is special about $\frac{1}{8}$?

The value of $\frac{1}{8}$ corresponds to a commensurate value with the crystal lattice. In these superconducting materials the superconductivity is found in a certain region upon doping holes into the system. Upon cooling where do these holes go? Is it possible that the holes order with the most stable ordering at commensurate values? The proposal of charge and spin ordering has therefore become a very topical debate.

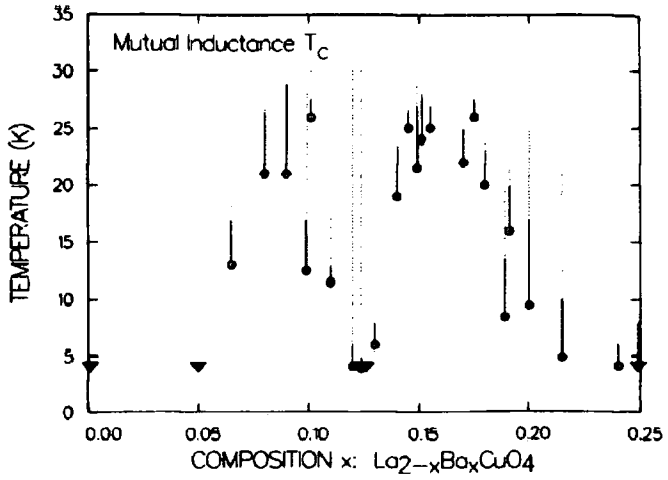

Figure 1.1: Mutual inductance T_C vs composition for $La_{2-x}Ba_xCuO_4$. Solid circles represent T_C. Triangles represent samples whose T_C's are not above 4.2 K. Solid lines are drawn between T_C and the 'bulk onset;' dotted lines are drawn between bulk onset and highest onset.

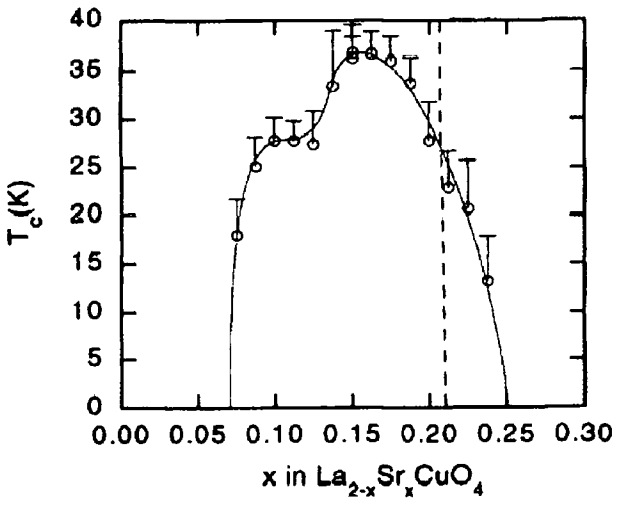

Figure 1.2: Onset (top of error bars) and midpoint (open circles) critical temperatures verses x, from a.c. susceptibility measurements. The solid line is a guide to the eye. The dotted line indicates the position of the orthorhombic to tetragonal phase line determined from neutron powder diffraction.

In the hole doped cuprate system $La_{2-x}Sr_xCuO_4$ Cheong *et al.* (1991) found incommensurate magnetic fluctuations by inelastic neutron scattering. Their results, on samples with $x = 0.075$ and 0.14, within the superconducting region of $La_{2-x}Sr_xCuO_4$, show wavevectors which suggest a 'stripe' like magnetic structure. Further studies by Suzuki *et al.* (1998) on a sample of $La_{2-x}Sr_xCuO_4$ with $x = 0.12$ showed that as the sample is cooled through the superconducting transition temperature T_C the antiferromagnetic diffraction peak splits from the $(\frac{1}{2}, \frac{1}{2}, 0)$ reciprocal lattice point to form satellite reflections located at positions $(\frac{1}{2} \pm \varepsilon, \frac{1}{2}, 0)$ and $(\frac{1}{2}, \frac{1}{2} \pm \varepsilon, 0)$ with a value of $\varepsilon = 0.126$ as shown in Figure 1.3. These peaks were found to be extremely weak but indicative of long range magnetic ordering. Kimura *et al.* (2000), performing similar experiments on a crystal with the same doping again found similar incommensurate peaks. These were found to have a correlation length of $\xi = 200$ Å, again indicating long range magnetic order. These incommensurate magnetic peaks were found to occur at the same points in reciprocal space as the dynamic correlations seen with inelastic neutron scattering.

Surprisingly, incommensurate magnetic peaks have been found in the non-superconducting doping range for samples with $x = 0.05$ by Wakimoto *et al.* (2000) suggesting that the spin stripes are only weakly connected with superconductivity, however in this work and later in a more systematic study over the doping range $0.03 \leq x \leq 0.12$ (Wakimoto *et al.*, 2001) they found that the stripes which exist in the insulating phase are rotated by 45° from the stripes which exist in the superconducting phase. Figure 1.4 shows the incommensurability of the spin stripes in $La_{2-x}Sr_xCuO_4$ as a function of the hole concentration x. In addition only two pairs of satellite reflections were

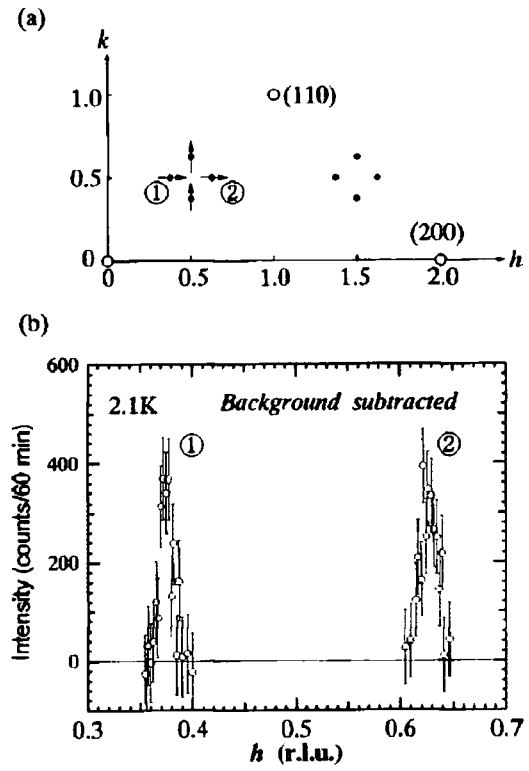

Figure 1.3: (a) A diagram of (h, k, 0) reciprocal plane for $La_{2-x}Sr_xCuO_4$ $x = 0.12$ at 2.1 K. The scan direction on the neutron diffraction is $\langle 1/2 + h,\ 1/2,\ 0 \rangle$ as indicated by the arrow. Closed circles represent the reflection points of magnetic superlattice peaks. Open circles correspond to Bragg peaks. (b) Scan through magnetic superlattice peaks along the direction indicated in (a) at 2.1 K.(taken from Suzuki *et al.*, 1998)

found in the insulating samples compared to the four satellites found in the superconducting region.

Tranquada *et al.* (1996) studying the $La_{2-x-y}Nd_ySr_xCuO_4$ system with $x = 0.12$ and $y = 0.4$ found superlattice reflections corresponding to both charge and spin correlations at wavevectors $\left(\frac{1}{2} \pm \varepsilon,\ \frac{1}{2},\ 0\right)$ and $(2 - 2\varepsilon,\ 0,\ 0)$ respectively. The magnetic peaks were found to have a correlation length of $\sim$ 170 Å within the copper oxygen planes but only a very weak correlation

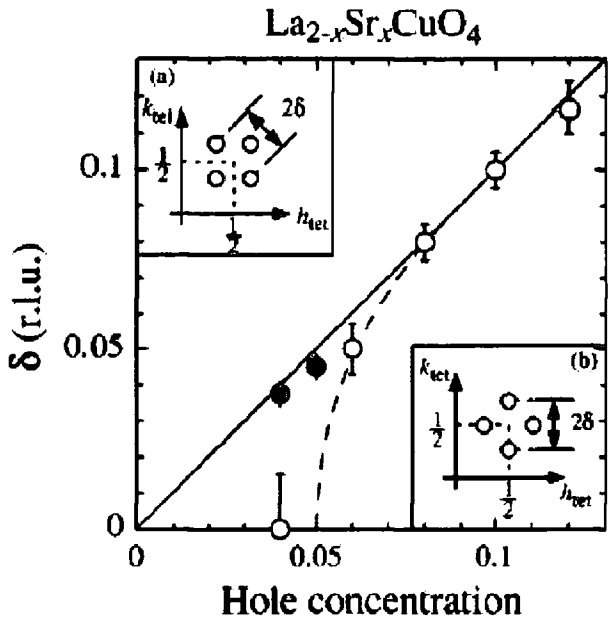

Figure 1.4: Hole concentration dependance of the incommensurate amplitude δ. δ is defined as the distance between the incommensurate peaks and the (π, π) position. (taken from Wakimoto *et al.*, 2000)

out of the plane, indicating a two dimensional nature of the magnetic ordering. The intensity of such modulation was found to be much stronger in the neodymium doped system than the undoped $La_{2-x}Sr_xCuO_4$ system. Their stripe like modulations are shown diagrammatically in Figure 1.5 with the corresponding elastic neutron scattering results being shown in Figure 1.6. X-ray diffraction, being sensitive to the charge distribution, presents itself as an ideal technique for the study of such charge modulations. von Zimmermann *et al.* (1998) used high energy X-ray scattering to study such charge correlations. Their measurements confirmed the origin and position of the charge based modulations.

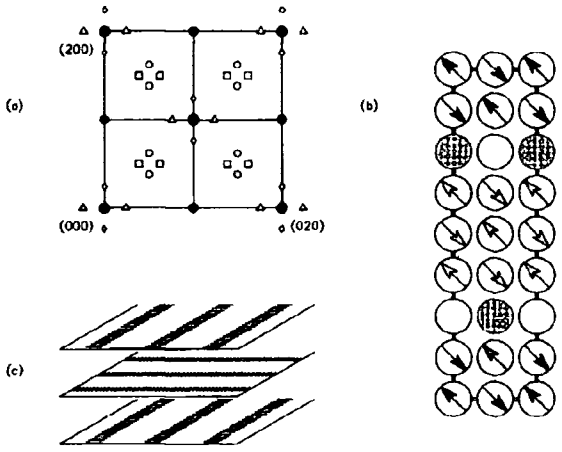

Figure 1.5: (a) Diagram of the (h, k, 0) zone in reciprocal space of $La_{2-x-y}Nd_ySr_xCuO_4$. (b) Proposed stripe like ordering pattern of charge and spin. (c) Stacking of planes of stripes along the c axis.(taken from Tranquada *et al.*, 1996)

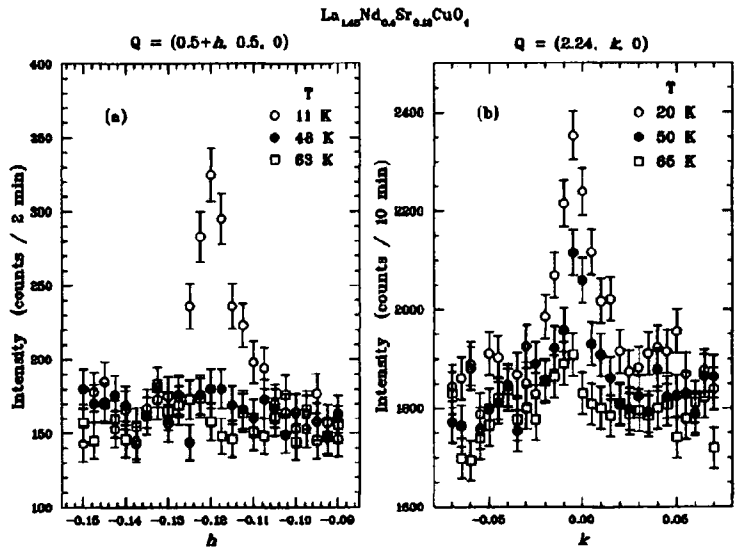

Figure 1.6: (a) Scans through the ($1/2 + 2\varepsilon$, 1/2, 0) magnetic peak at temperatures of 11, 48, and 63 K. (b) Transverse scans through the ($2 + 2\varepsilon$, 0, 0) charge-order peak at temperatures of 20, 50, and 65 K.(taken from Tranquada *et al.*, 1996)

The detection of both spin correlations in $La_{2-x}Sr_xCuO_4$ and $La_{2-x-y}Nd_ySr_xCuO_4$ and charge correlations in $La_{2-x-y}Nd_ySr_xCuO_4$ has lead to many arguments concerning the interplay between such ordering and superconductivity. The model proposed for such ordering is one in which the mobile holes segregate to form 'stripes' within the copper oxygen planes, with each hole rich stripe acting as a π domain wall for local antiferromagnetic order. It has been suggested that the addition of Nd into the $La_{2-x}Sr_xCuO_4$ system causes, due to the smaller ionic radius, a change of the low temperature tilt pattern of the copper octahedra seen by Crawford *et al.* (1991) by X-ray and neutron diffraction. Such a change acts to pin the 'stripes', which turn them from dynamic, or very weakly static form in $La_{2-x}Sr_xCuO_4$ to the pinned, static form in $La_{2-x-y}Nd_ySr_xCuO_4$.

Despite numerous studies to date the relationship between stripes and superconductivity is not clear. Do stripes suppress superconductivity? The 'one eighth' problem seems to suggest so, but no conclusive proof has been found to date. Stripes are not exclusively found in superconducting systems with even insulating $La_{2-x}Sr_xCuO_4$ showing stipe formation and recently stripes have been found in CuO (Zheng *et al.*, 2000).

With such intriguing phenomena occurring in these systems which result in forms of charge and spin ordering an accurate, high resolution probe is required to solve many of the problems. Recently through the availability of the new range of third generation synchrotron sources extremely high brilliancies have become available which allow experimentalists to study such weak charge modulations, which often have less than one electron difference, that would have been previously unobservable. The development of labora-

tory based instrumentation however, have not been so great. In this thesis, Chapter 4 reports the developments of a laboratory based diffractometer using the next generation of X-ray optics, d-spacing graded parabolic mirrors, which have been optimised for the study of such weak charge modulations. Results have confirmed that the performance is far greater than previous laboratory based instruments, and indeed approaches the intensity available at an unfocussed second generation synchrotron source.

Charge and spin stripes have been found not to be exclusive to copper containing compounds. The iso-structural $La_{2-x}Sr_xNiO_{4+\delta}$ compounds have been found to display charge and spin stripes. Previous studies have used neutron diffraction, which while being an obvious choice for the study of spin correlations, is not an obvious choice for the study of charge based correlations, as neutrons scatter from the atomic nucleus not the charge density distribution. X-ray scattering is an ideal choice for the study of charge modulations but, at traditional X-ray wavelengths, suffers from high absorption limiting the sample volume probed. Due to the high storage ring energy of the third generation synchrotron sources, insertion devices can be designed to produce high brilliance beams of X-rays with an energy 10 times that of conventional X-ray scattering techniques. By using such high energy X-rays the bulk of the sample can be probed as the absorption length of such X-rays is typically a few centimetres, even in heavily absorbing samples. Chapter 2 reports studies of the charge stripe phases in $La_{2-x}Sr_xNiO_{4+\delta}$ for $x = 0.33$, one of the special commensurate values of hole concentrations. Surprisingly the inverse correlation lengths measured in the bulk of the material are different from the near surface region despite the increase in instrumental res-

olution obtained by going to higher energies. Indeed the inverse correlation length measured is different from that measured by corresponding neutron techniques which may indicate that the charge distribution (charge stripes) is behaving in a different way to the corresponding nuclear displacements measured by the neutron scattering.

Charge and spin stripes are not the only types of ordering process in strongly correlated perovskites. The manganite compounds were thought to display charge ordering processes for some time, as predicted by Goodenough (1955). Recently however, again through the use of third generation synchrotron sources, by exploiting the tunability of the incident X-ray energy the charge ordering pattern has been confirmed by resonant diffraction (von Zimmermann *et al.*, 2001). By a combination of high energy X-ray scattering and resonant scattering Chapters 3 and 5 present the study of the charge and orbital ordering phases in the $Bi_{1-x}Ca_xMnO_3$ and $La_{2-2x}Sr_{1+2x}Mn_2O_7$ perovskite manganite compounds respectively. Here the interplay between the charge orbital and spin degrees of freedom is studied. Resonant scattering is the only technique which can probe the orbital order as there is only appreciable intensity of the scattering close to an absorption edge of the material. The results in the $Bi_{1-x}Ca_xMnO_3$ system prove, conclusively the wavevector of the charge and orbital ordering. In addition they confirm that charge and orbital ordering is present in the hole-rich doping regime. The studies on the $La_{2-2x}Sr_{1+2x}Mn_2O_7$ system have clarified the ordering wavevector of the charge as there has been recently some disagreement in the literature. Previous studies have suggested that the phase transition is 're-entrant' but the data presented here proves that this is not the case. At low temperature

the charge and Jahn-Teller order remains in a weak, poorly correlated state. In addition the Jahn - Teller ordering is found to be incommensurate with the lattice in this temperature region.

Finally Chapter 6 reports the first results from a new technique developed by the author, single crystal soft X-ray scattering. In strongly correlated systems the spin correlations are often as important as the corresponding charge correlations, because the interplay between these determines the ground state of the system. Previously neutrons have been used to study the spin correlations but they often suffer from both poor resolution and low source intensities although neutron - spin scattering has a high cross-section. X-rays while they both have very high intensity and resolution, the cross-section for magnetic scattering, resulting from the interaction between the magnetic field of the X-ray and the spin of the electron is reduced by a factor of $\hbar\omega/mc^2$. This corresponds to an intensity reduction of $\tau \approx \frac{1}{60}$ compared with a single electron. Even with the high intensity available at a synchrotron source the intensity of the magnetic scattering is tiny, typically 10^8 times weaker. The key lies in using the wavelength tunability to resonantly enhance the scattered intensity in the vicinity of a absorption edge. While this has become a proven technique for probing magnetic states in the actinide compounds, the large resonant enhancements which have been predicted (Hannon *et al.*, 1988) at the L edges for the transition metals have failed to be used for scattering experiments as the energy of the resonances lies in the soft X-ray region ($\hbar\omega \leq 2$ keV). Scattering at such energies had previously been thought not to be possible due to high absorption and the restrictively small Ewald sphere. Results on the $La_{2-2x}Sr_{1+2x}Mn_2O_7$ bilayer

manganite system have found that at the soft energies the magnetic scattering intensities are over 10 times greater than the charge scattering, far higher than intensities reported at $\sim$ 3 keV on actinide compounds. The future possibilities using this technique for the study of spin correlations in transition metal containing compounds are exciting and unlimited, indeed it may provide a new probe for the interplay between copper magnetism and superconductivity using the element specificity inherent in the technique as has been attempted previously (Hill *et al.*, 2000) at the K-edge.

Chapter 2

Observation of a Glassy Charge Stripe Phase in $La_{2-x}Sr_xNiO_4$, $x = 0.33$

2.1 Introduction

The nickelate class of compounds have attracted much interest since the discovery of high temperature superconductivity in the isostructural cuprate family. The parent, undoped, compounds La_2CuO_4 and La_2NiO_4 are antiferromagnetic Mott insulators with a layered perovskite, K_2NiF_4, structure. It is however the partially substituted compounds that have generated considerable excitement. Replacement of La^{3+} ions by alkaline earth ions, for example Sr^{2+}, adds holes to the material. These holes are mobile and account for dramatic changes in the physical properties of the material, and complex structural ordering at low temperatures. It has been thought that copper

oxygen planes are vital for the presence of superconductivity. The nickelate system, being iso-structural displays the same crystal structure but instead has nickel - oxygen planes. No superconductivity has been found to date in the nickelate compounds.

The crystal structure of lanthanum nickelate is shown in Figure 2.1, where the nickel - oxygen octahedra are shown as shaded blue octahedra with the red oxygen at the apexes and blue nickel atoms at the centre. The lanthanum / strontium sites are shown as the yellow spheres. Upon substitution of strontium for lanthanum, mobile holes are introduced into the system (this can also be achieved by the addition of excess oxygen). At high temperature the holes are distributed randomly within the lattice. What happens as the temperature is lowered? Figure 2.2 shows the resistivity of $La_{2-x}Sr_xNiO_{4+\delta}$ with $0.2 \leq x \leq 0.4$ by Cheong *et al.* (1994). Here a distinct anomaly at a temperature of $\sim$ 240 K can be seen in some samples, with the strongest anomaly appearing in samples with a composition of $x = 0.33$. Conductivity, being a measurement of the mobile charge carriers in a material provides insight into what may be happening in these materials upon cooling. In addition to the conductivity measurements Figure 2.2 also shows the magnetic susceptibility, $\mathrm{d}\chi/\mathrm{d}T$, as a function of temperature. Again, an anomaly can be seen at a temperature of $\sim$ 240 K, maximising at a composition of $x = 0.33$.

Below the charge ordering temperature, T_{CO}, the holes segregate to form stripes, and below a further temperature, T_N, the spins order into stripes. Figure 2.3 shows a schematic representation of such charge and spin stripes. The spacing between the stripes is dependant on the hole concentration, n_h. The hole-rich stripes act as π-domain walls for the local antiferromagnetic

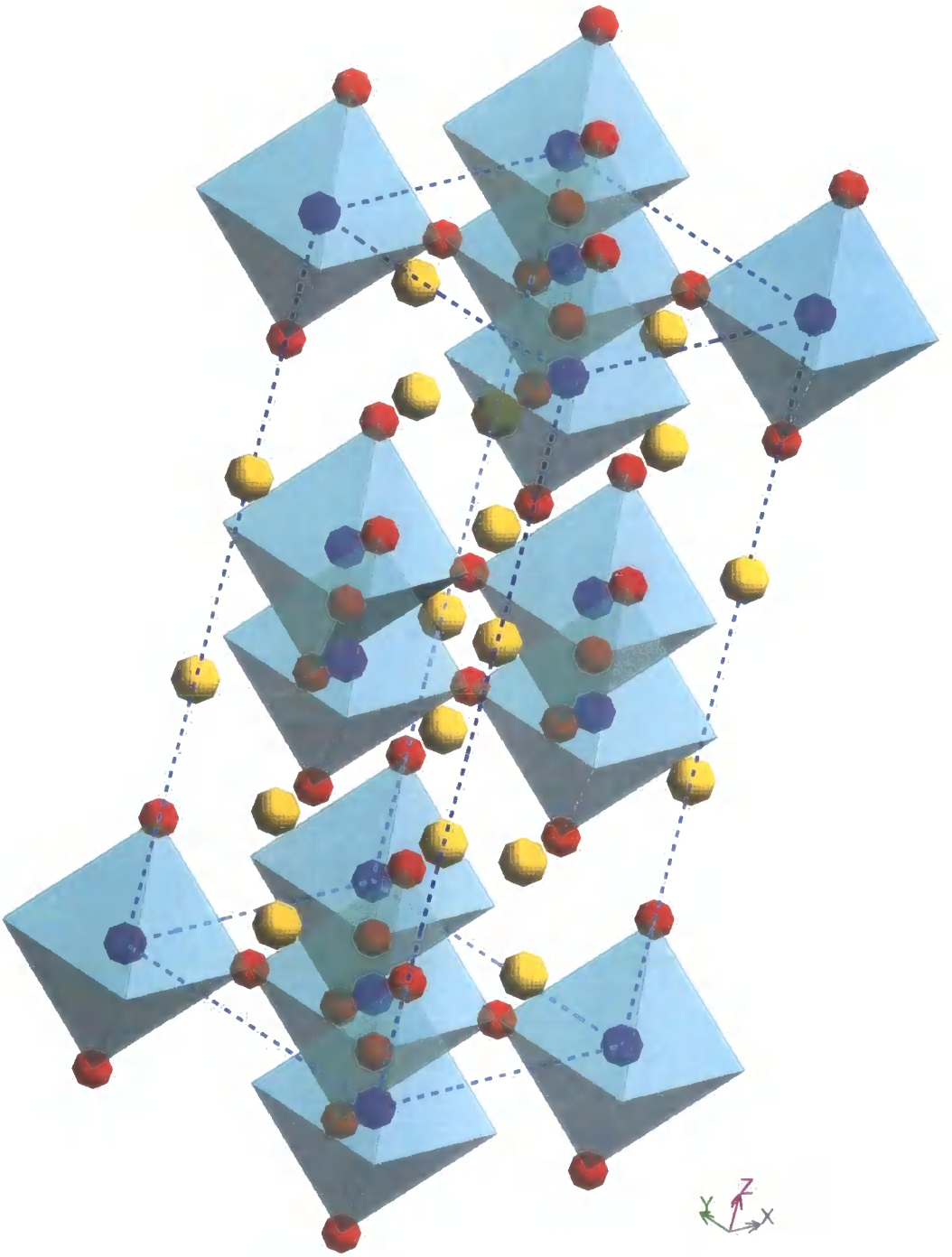

Figure 2.1: Crystal Structure of $La_{2-x}Sr_xNiO_{4+\delta}$. The red, light blue and yellow spheres represent the oxygen, nickel and lanthanum / strontium sites respectively.

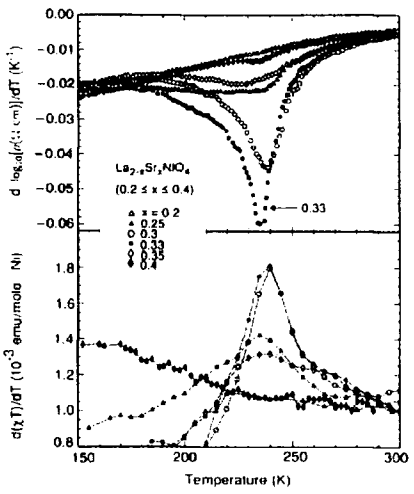

Figure 2.2: Temperature derivative of logarithmic resistivity (upper panel) and susceptibility multiplied by temperature (lower panel) verses temperature for Sr concentrations of $0.2 \leq x \leq 0.4$. Taken from Cheong *et al.* (1994)

order, aligned parallel to the stripe direction, induced between the hole-deficient regions. Such charge and spin stripes form within the $a - b$ plane of the material, and due to the tetragonal nature of the unit cell are found to be two dimensional in nature.

Initial studies started on the study of these materials using neutron scattering techniques. They found superlattice reflections from both the stripe and charge order. The wavevectors for the charge and spin stripes respectively were found to be $\boldsymbol{Q}_{CO} = (2\varepsilon,\ 0,\ 1)$ and $\boldsymbol{Q}_{SO} = (\varepsilon,\ 0,\ 1)$. The composition $x = 0.33$ was thought to be a special case as it was revealed that the charge and spin stripes are coincident in reciprocal space. A study of $La_{2-x}Sr_xNiO_{4+\delta}$ $x = 0.33$ with neutron scattering was reported by Lee and Cheong (1997). They reported charge and spin stripe ordering temperatures

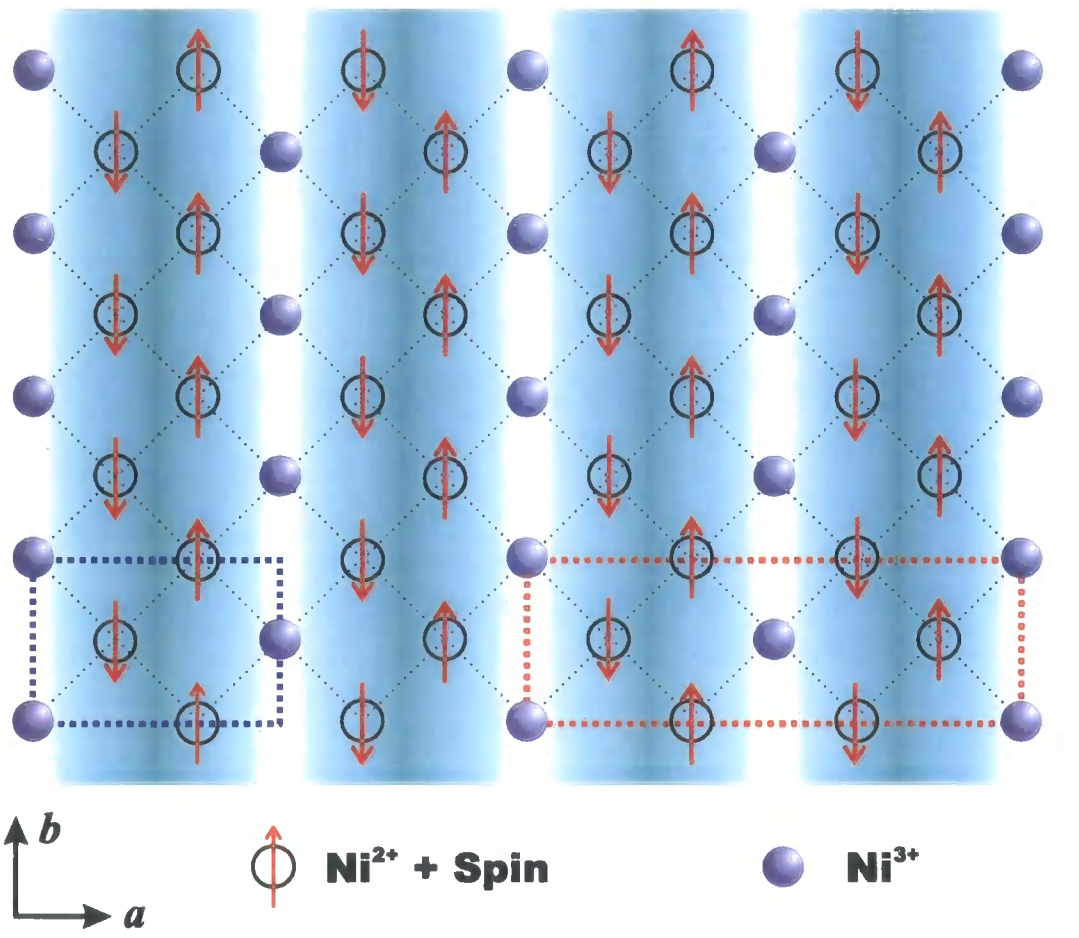

Figure 2.3: Schematic representation of the charge and spin stripes in $La_{2-x}Sr_xNiO_{4+\delta}$ ($x = 0.33$). Ni^{3+} ions are represented as filled blue circles, whereas Ni^{2+} ions are represented as open circles with the associated spin as a red arrow. The dotted red and blue lines indicate the super-cell from the spin stripes and charge stripes respectively.Only nickel ions are shown for clarity. The blue shading shows the charge density distribution.

of $T_{CO} \approx 239$ K and $T_{SO} \approx 190$ K respectively, and the correlation lengths of the charge stripes within the $a-b$ plane was ~ 3 times larger than that of the corresponding spin stripes. This lead them to the conclusion that it was the charge correlations which drive the spin ordering. The incommensurability of the stripes ,ε, measured from fundamental Bragg reflections was found to

be constant at a value of $\varepsilon = 0.33$ over the whole temperature range, which in fact corresponds to a commensurate value of the lattice. Such a modulation indicates that direct space ordering of the charge and spin stripes is $d_{co} = \frac{3a}{2}$ and $d_{so} = 3a$ respectively, where a is the lattice parameter in the $F4/mmm$ tetragonal setting ($a_t = \sqrt{2}a_p$ where a_t and a_p are the tetragonal and perovskite unit cell parameters respectively). This is consistent with the model displayed schematically in Figure 2.3.

More recent neutron scattering studies of $La_{2-x}Sr_xNiO_{4+\delta}$ over a larger range of hole doping with $0.289 \leq x \leq 0.5$ display results that confirm the anomalies with the $x = 0.33$ system hinted at by the previous resistivity studies of Cheong *et al.* (1994). Figure 2.4 displays the transition temperature of the charge and spin stripes, T_{CO} and T_{SO} respectively as a function of the hole concentration calculated using $n_h = x + 2\delta$ where x is the strontium concentration and δ is the excess oxygen concentration. In the doping region around $n_h = 0.33$ the charge and spin stripe transition temperatures were observed to maximise and the incommensurability was found to 'lock into' a value of $\varepsilon = 0.33$. Away from this doping level in both directions of the stoichiometry suppression of the transition temperatures is observed and the stripes become increasingly incommensurate. Yoshizawa *et al.* (2000) concluded that in the $n_h = 0.33$ system, because the charge and spin stripes coincide with each other in reciprocal space, the strong electron - lattice coupling here helped to stabilise the stripe ordering. In Nuclear Magnetic Resonance (NMR) studies Yoshinari *et al.* (1999) found that the magnetic ordering temperature is suppressed by $\sim$ 30 K when measured on the microsecond timescale of the NMR measurements, as opposed to the

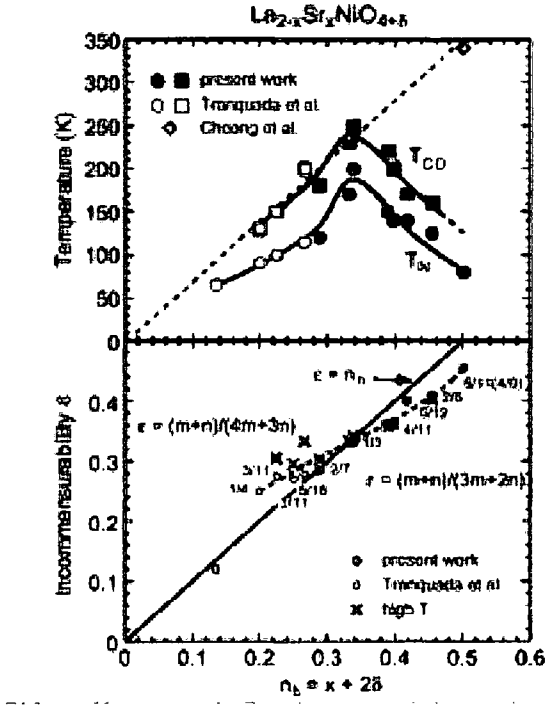

Figure 2.4: Transition temperatures T_{CO}, T_N and the incommensurability ε as a function of the hole concentration n_h. Taken from Yoshizawa *et al.* (2000)

nanosecond timescale of neutron measurements. They attributed this to a glassy - like character of the charge and spin stripe ordering.

With such stripe phases existing, one question which becomes apparent is of where do the holes reside? The results to date are conflicting. X-ray absorption spectroscopy at the oxygen edge by Kuiper *et al.* (1991) have suggested that the holes have a high oxygen $2p$ character. However Tan *et al.* (1993), reporting on measurements at the nickel K edge have found that the holes have a high degree of mixed nickel $3d$ and oxygen $2p$ character. With such results Tranquada *et al.* (1997) has suggested that above the spin ordering temperature, T_N, the stripes are oxygen-centred and below this

temperature the stripes are nickel-centred, with a shift of the domain walls onto the oxygen sites.

Previous studies by Du *et al.* (2000) centred on studying $La_{2-x}Sr_xNiO_{4+\delta}$ with $x = 0.33$ using high resolution X-ray scattering. Experiments were carried out at an incident X-ray energy of 12.4 keV and a germanium (1, 1, 1) analyser was used to increase the experimental resolution. A comparison with these data will be presented later in this chapter.

2.2 High Energy X-ray Scattering

High Energy X-ray Scattering (HEXS) has become recently available due to the availability of high energy synchrotron sources which have sufficient flux available in the high energy range. HEXS is defined as scattering using energy which is above an energy of $\hbar\omega = 80$ keV. X-rays of this energy are available by using either asymmetric multipole wigglers or superconducting wavelength shifters. On the high energy beamline at the ESRF, Grenoble where the storage ring energy is 6 GeV, X-rays in the range 15 keV to 450 keV are available with the permanent magnet wiggler and 17 keV to 800 keV using the superconducting wavelength shifter.

The advantages of HEXS for performing monochromatic scattering and diffraction are three-fold. Firstly, there is a large decrease in absorption, secondly there is an increase in resolution and finally as the extinction depth is large and the scattering becomes weaker so the conditions for perfect kinematical diffraction are approached. Lets us consider the absorption case first.

The absorption by a material of thickness x is given by.

$$I(\omega) = I_0 \, e^{-\mu(\omega)x} \tag{2.1}$$

Where I and I_0 are the final and initial intensities and $\mu(\omega)$ is the linear absorption coefficient. A calculation of the total absorbtion from the effects of photo-electron, Compton and pair-production for various elements is shown in Figure 2.5. Here we can see that at an energy of above 80 keV the effects of photo-electric absorption are drastically reduced. The photo-electron cross-section in fact decreases proportional to $(\hbar\omega)^{-3}$. Therefore with such weak attenuation above 80 keV other processes such as Compton and pair-production dominate in this regime, which have a very weak dependance with

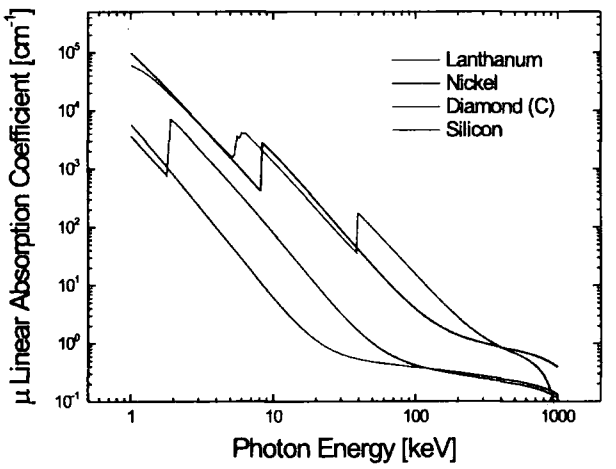

Figure 2.5: Linear absorption coefficient (μ) for diamond (red line), silicon (magenta line), nickel (blue line) and lanthanum (green line) calculated from the DBAX tables by the XOP programme (Sanchez del Rio and Dejus, 2001).

energy in the range 80 keV $\leq \hbar\omega \leq$ 500 keV. Such a decrease in absorption causes the sample gauge volume probed to dramatically increase. The main effect of the increase in sample volume is an increase in the intensity of the scattering which enables HEXS to be used for the study of weak reflections which would otherwise not be seen with X-ray scattering using traditional energies ($\sim$ 10 keV). In addition, the measurements using HEXS probe the bulk of the sample, integrating over much of the crystal, and therefore can often see mixed phases, multi domains and very short range correlations. Such measurements remove the problems with X-ray scattering in the region 3 keV $\leq \hbar\omega \leq$ 20 keV where only a small sample volume is probed, due to a depth penetration of only a few microns, and surface effects are all too apparent. In addition the volume of reciprocal space which can be probed is governed by the size of the Ewald sphere, the radius of which is equal to $2\pi/\lambda$. Therefore as the energy is increased the size of the Ewald sphere increases allowing a much greater volume of reciprocal space to be probed. This is shown in the diagram of reciprocal space shown in Figure 2.6 with Ewald spheres for 10 keV and 100 keV. In addition, many experiments can be performed in Laue transmission geometry which allows greater access to reflections in reciprocal space removing the condition that the sample angle θ has to be in the range $0 \leq \theta \leq 2\theta$ where 2θ is the scattered beam angle relative to the incident beam.

The second main advantage of HEXS is the increase in wavevector resolution which is available. For perfect crystals obeying dynamical diffraction conditions the angular width of the reflection is given by (derived from Als-

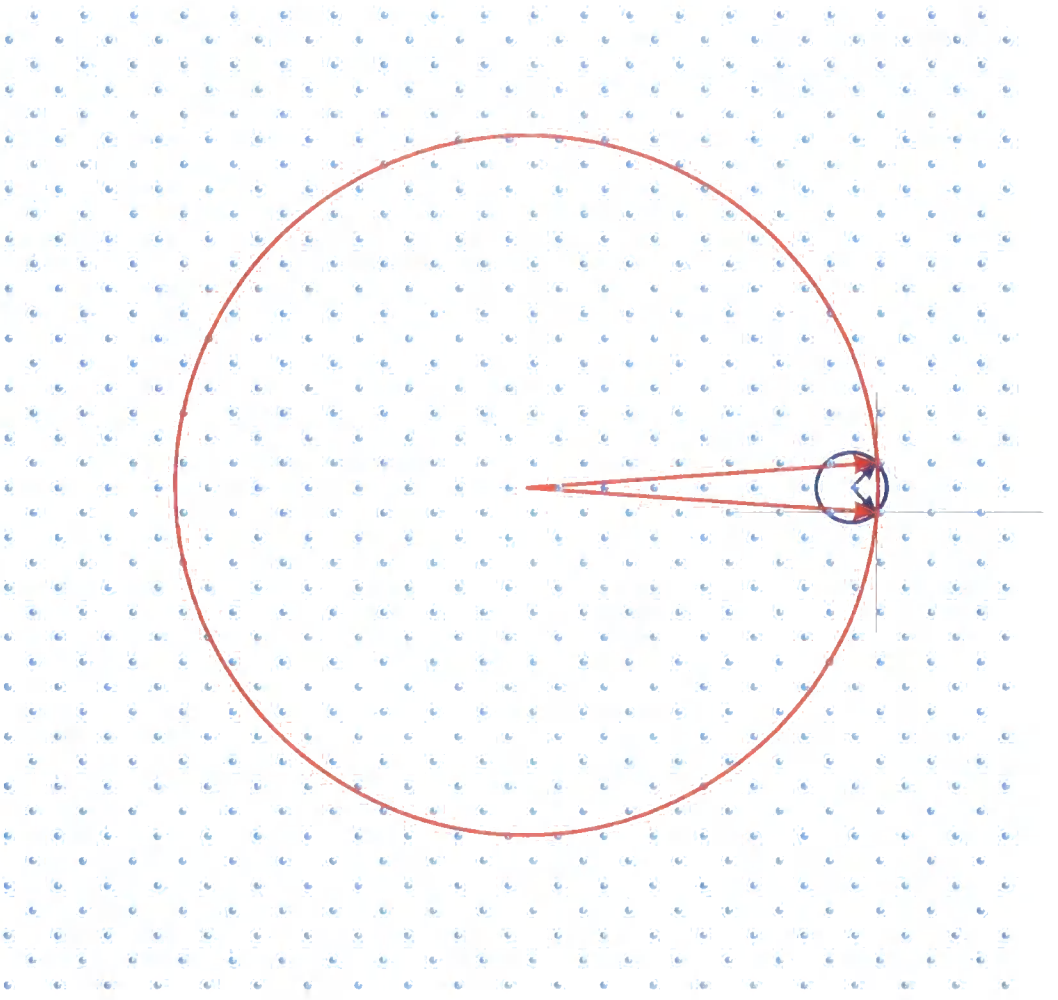

Figure 2.6: Schematic representation of the Ewald sphere in a 2-D plane for an energy of 10 (blue) and 100 keV (red).

Nielsen and McMorrow, 2001):

$$\kappa_{darwin}^{FWHM}(\boldsymbol{Q},\omega) = \left(\frac{6d^2 r_0}{\sqrt{2}\pi m^2 v_c}\right)\tan(\theta_B) f(\omega) \sum_{r_j} e^{i\boldsymbol{Q}\cdot\boldsymbol{r_j}} \qquad (2.2)$$

Where d, m and θ_B are the familiar expressions in Bragg's law ($m\lambda = 2d\sin\theta_B$), v_c is the volume of the unit cell, and r_0 is the Thompson scat-

tering length. The factor,

$$F(\boldsymbol{Q},\omega) = \sum_{r_j} f(\omega)\, e^{i\boldsymbol{Q}\cdot\boldsymbol{r}_j} \tag{2.3}$$

can be remembered as the structure factor for the unit cell with the factor $f(\omega)$ being the resonant scattering term[1]. As we now increase the energy both the resonant scattering $f(\omega)$ and the Bragg angle θ_B decrease. This has the effect to decrease the Darwin width of the reflection. Figure 2.7 shows the angular width of the (1, 1, 3) reflection in silicon for both 12 keV and 130 keV for the symmetrical Bragg case. Here we can see that there is a dramatic decrease in the width of the reflection which increases the resolution if such crystals are used as a monochromator and analyser set.

We also need to consider the extinction depth which defines the attenuation of the incident beam under the conditions of dynamical diffraction. The extinction length, Λ, at the point of the maximum in the rocking curve is given by:

$$\Lambda = \frac{mv_c}{4dr_o} \cdot \frac{1}{|F(\boldsymbol{Q},\omega)|} \tag{2.4}$$

Where $F(\boldsymbol{Q})$ is the structure factor defined by Equation 2.3. Recalling the results from above we know that $F(\boldsymbol{Q},\omega) \propto f(\omega)$, therefore as the energy is increased the contribution to the structure factor of the resonant scattering terms is reduced. This has the effect that the extinction depth increases as the incident energy is increased. Therefore, for weak reflections, where the

[1]This factor is often called the anomalous scattering term which has historical basis. Strictly speaking however, anomalous scattering occurs when $dn/d\omega < 0$ for an index of refraction n and angular frequency ω. Throughout this thesis the distinction is ignored as resonant and anomalous scattering have taken on the same meaning.

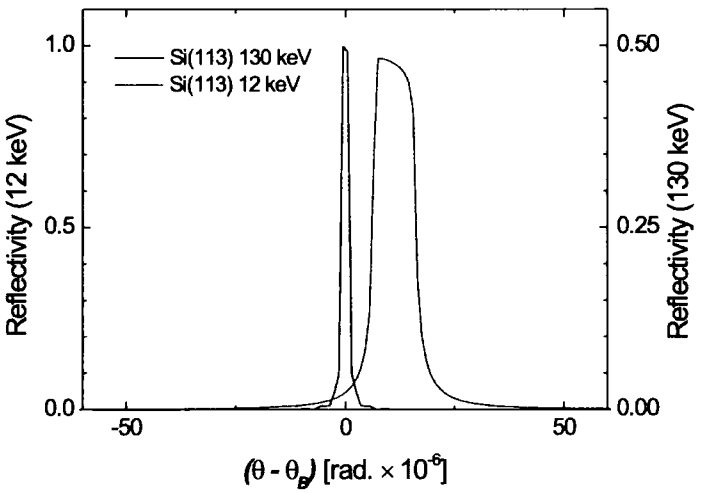

Figure 2.7: Angular Darwin widths for the (1, 1, 3) reflection of silicon at 12 keV (red line) and 130 keV (blue line), calculated by the XOP programme (Sanchez del Rio and Dejus, 2001).

$\sum e^{i\boldsymbol{Q}\cdot\boldsymbol{r}_j}$ part of the structure factor is small, the extinction depth will be much larger than the absorption length (which only depends on $f''(\omega)$). This has the effect that in HEXS weak reflections approach the conditions for ideal kinematic diffraction faster.

We can conclude therefore that for the study of weak superlattice reflections and in cases where a higher resolution is required HEXS is an ideal technique that allows bulk sensitive, high resolution, high intensity measurements which can be interpreted in the kinematical regime.

2.3 Experimental Details

Experiments were carried out on the high energy X-ray scattering beamline (ID15A) at the European Synchrotron Radiation Facility (ESRF), Grenoble, France. The beamline and experimental setup have been described by Liss *et al.* (1998) and Suortti and Tschentscher (1995). The beamline is on the end of a wiggler insertion device with a critical energy $E_C = 45$ keV. To reduce the heat load on the optics the beam is permanently attenuated by 4 mm aluminium, 3.5 mm beryllium and 1 mm carbon, upstream to downstream respectively. The incident white beam was initially monochromated in the optics hutch by means of two bent silicon crystals to form a polychromatic beam. The bending was necessary to increase the Darwin width of the reflections to allow a greater band-pass through the system. Then the partly monochromatic beam was then further monochromated by use of a (1, 1, 3) Si oxygen precipitated crystal. The oxygen precipitation is used, like the bending of the pre-monochromator crystals, to increase the Darwin width of the crystal. The reflected monochromatic beam was then incident on the sample stage. The sample was mounted on a closed cycle He refrigerator enclosed in an aluminium dome. The helium refrigerator was in turn mounted on a Huber 511 Eulerian cradle on the diffractometer's θ axis. The analyser crystal used for the triple axis measurements was a (1, 1, 3) silicon crystal identical to the monochromator. The X-rays were then detected by means of a Ge solid state detector. Higher order harmonics were removed electronically by the use of pulse height analysis. The monochromator, sample and analyser axes are encoded by the use of a laser interferometer. This

enabled the absolute position of each axis to be read to an accuracy better that 0.05 arc seconds.

Figure 2.8 shows a geometrical representation of diffraction in reciprocal space. Scattering is observed when the scattering vector (or momentum transfer) is coincident with a reciprocal lattice point. The length of the scattering vector is given by $|\boldsymbol{Q}| = \frac{4\pi}{\lambda} \sin \frac{2\theta}{2}$ and it can be shown to reduce to Bragg's law. The radius of the Ewald sphere is the magnitude of the incident wavevector given by $|\boldsymbol{k_i}| = \frac{2\pi}{\lambda}$, therefore as the energy is increased this becomes larger.

When performing diffraction in reciprocal space at high energy, the greatest resolution is found when measuring parallel to the scattering vector, such

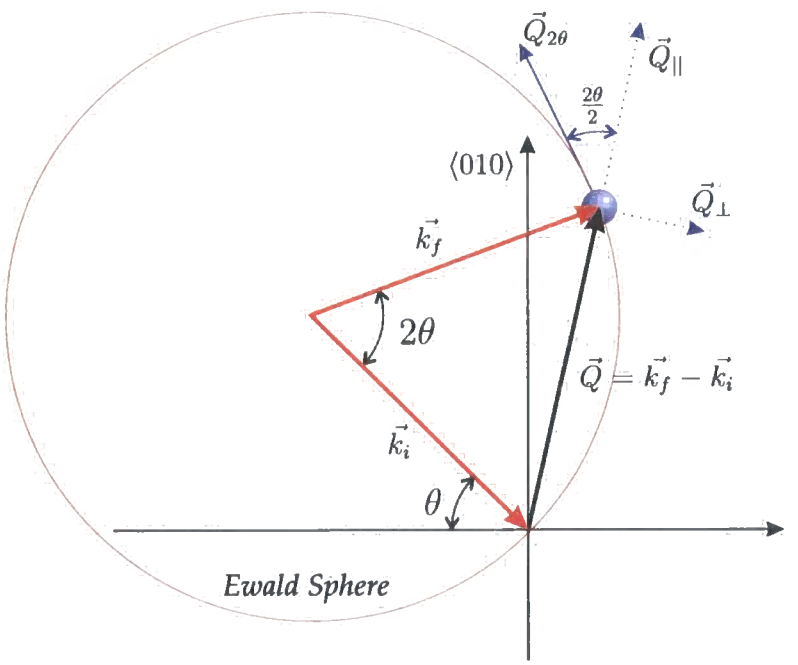

Figure 2.8: Geometrical representation of diffraction in reciprocal space (see text for details)

a scan is often performed by moving the detector at twice the sample speed, the so called 'theta - two theta' coupled scan. However, at high energy it is possible to scan just the detector angle, or the equivalent analyser angle. A scan in this direction can be shown to be geometrically (by Figure 2.8) at an angle of $\frac{2\theta}{2}$ with respect to the $\boldsymbol{Q}_{||}$ direction. At high energy, due to the small scattering angles involved, this direction is equivalent and has the advantage that the sample does not have to be moved, ensuring that the sample stays on one crystallite and the sample gauge volume does not change.

Two crystals of $La_{2-x}Sr_xNiO_{4+\delta}$ with $x = 0.33$ were studied. The first was grown at Bell Laboratories, USA and the second in the Department of Physics, University of Oxford, UK (Prabhakaran *et al.*, 2002). The crystals were indexed in the *F/4mmm* setting with polarised lattice parameters $a_t = \sqrt{2}a_p = 5.4145$ Å and $c = 12.71$ Å. An incident energy of 130 keV was selected. This selection was based on the energy dependance of the linear absorption coefficient, the results of which are displayed in Figure 2.5 for various elements. At this point, further increases in energy do not dramatically reduce the linear absorption coefficient therefore there are no major gains to be made by increasing the incident photon energy past 130 keV. No structural phase transition was observable in the temperature region under study. Both crystals were of high quality and displayed rocking curve widths of $\sim 0.05°$. The sample was mounted in the $\langle 1,\ 0,\ 1 \rangle$ / $\langle 0,\ 1,\ 0 \rangle$ zone of reciprocal space. The Bragg reflections (4, 0, 4) and (4, 2, 0) were located after alignment of the sample by use of the $\boldsymbol{UB}$ matrix. Figures 2.9 and 2.10 show scans taken in the $\boldsymbol{Q}_{||}$ direction by scanning the analyser crystal in the θ_A direction. The Bragg peaks were found to be sharp and well correlated.

The (4, 2, 0) Bragg reflection and to a lesser extent the (4, 0, 4) reflection show two distinct peak values in the $\boldsymbol{Q}_{||}$ direction. This is due to twinning in the $a-b$ plane caused by a slight orthorhombic unit cell with $a \neq b$, causing two different d-spacings. This was not apparent when initially aligning the crystal using the $\boldsymbol{UB}$ matrix.

Having located the Bragg reflections, a search for superlattice reflections corresponding to the charge stripe modulations was undertaken. Charge stripe reflections were expected at a modulation of $\boldsymbol{Q}_{CS} = (2\varepsilon, 0, 1)$ surrounding fundamental Bragg reflections. Weak superlattice reflections were located at (4.667, 0, 5), (3.333, 0, 3) and (4.667, 0, 3) surrounding the (4, 0, 4) Bragg peak. High resolution, triple-axis measurements were taken at a temperature of 100 K on the (4.667, 0, 5) peak. Figure 2.11 shows a scan taken in the H-direction displaying both the superlattice reflection and the (4, 0, 4) Bragg reflection for comparison. Figure 2.12 shows also a scan of the (4.667, 0, 5) superlattice and (4, 0, 4) Bragg reflections but taken in the $\boldsymbol{Q}_{||}$ direction by rocking the analyser crystal.

The Bragg reflection provides an upper limit on the resolution of the measurement in the corresponding direction. In both the H- and $\boldsymbol{Q}_{||}$ directions we can observe that the resolution of the measurement is much greater than the width of the superlattice reflections. This enables the calculation of the inverse correlation length and integrated area to be measured without the need to perform a de-convolution of the instrumental resolution function. The inverse correlation length was calculated from the half width at half

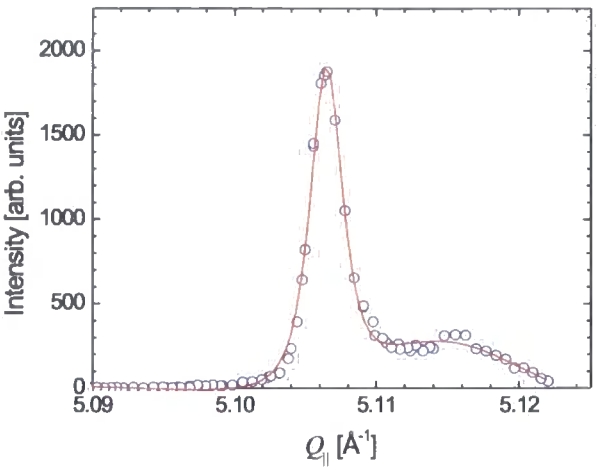

Figure 2.9: Scan through the (4, 0, 4) Bragg reflection in the $\boldsymbol{Q}_{||}$ direction, measured by rocking the analyser crystal. The solid line is a fit to the data assuming a Lorentzian squared lineshape for the main peak. FWHM = $2.6519 \pm 0.07 \times 10^{-3}$ Å^{-1}

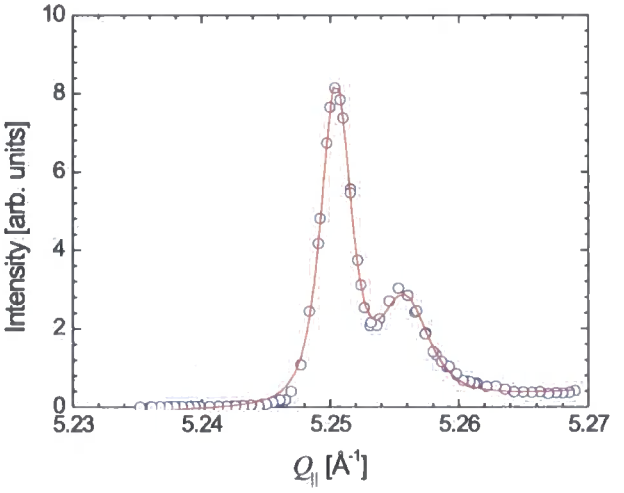

Figure 2.10: Scan through the (4, 2, 0) Bragg reflection in the $\boldsymbol{Q}_{||}$ direction, measured by rocking the analyser crystal. The solid line is a fit to the data assuming a Lorentzian squared lineshape for the main peak. FWHM = $2.719 \pm 0.0406 \times 10^{-3}$ Å^{-1}

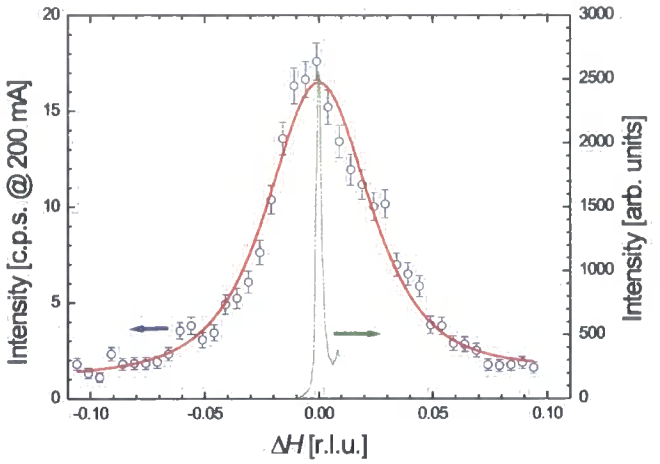

Figure 2.11: Scan in the H-direction through the (4.667, 0, 5) charge stripe superlattice reflection (blue circles). The red line is a Lorentzian squared fit to the experimental data. For comparison the (4, 0, 4) Bragg reflection is also shown, measured in the same direction (dark green).

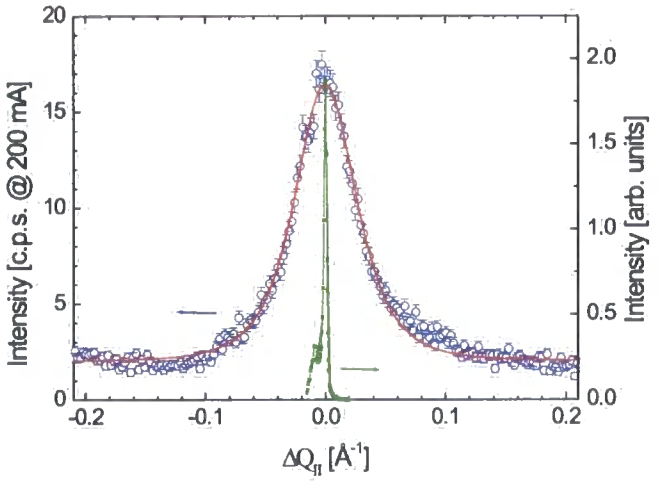

Figure 2.12: Scan in the $Q_{||}$ direction through the (4.667, 0, 5) charge stripe superlattice reflection (blue circles). The red line is a Lorentzian squared fit to the experimental data. For comparison the (4, 0, 4) Bragg reflection is also shown, measured in the same direction. (dark green).

maximum, w, of the peak using the relationship

$$\xi_d^{-1} = \frac{2\pi}{d} w \tag{2.5}$$

where d is the direct space lattice parameter along the direction of the measurement, which is consistent with the model presented in Appendix A.

The superlattice reflection (4.557, 0, 5) was measured in the temperature region 100 K to 250 K. Figure 2.13 shows the inverse correlation length measured in the H-direction. Here we can see firstly that the inverse correlation length starts to increase at a temperature of ~240 K, consistent with the melting of the charge stripes at this temperature. However, also noticeable from these data is a decrease in the inverse correlation length in the region 140 K $\leq T \leq$ 160 K. If we look at the integrated area measured in the same temperature range variations can be seen at the two same regions as shown in Figure 2.14. Here the integrated area increases in the same 140 K $\leq T \leq$ 160 K temperature region in which the inverse correlation length decreases. Past 160 K upon warming the integrated intensity then falls until a temperature of $\sim$ 250 K at which point the reflection is not visible above the background.

Taking the behaviour of the charge stipes on warming from 100 K, the increase in temperature has no effect on the inverse correlation length until the temperature region 140 K $\leq T \leq$ 160 K at which point the inverse correlation length drops. However, the integrated area up until this point increases. The increase in the integrated area with no change in inverse correlation length suggests that upon warming the contrast between the charge

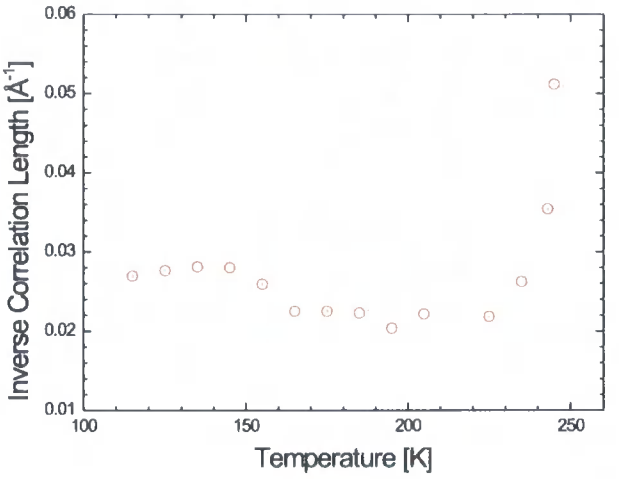

Figure 2.13: Inverse correlation length of the (4.667, 0, 5) charge stripe superlattice reflection as a function of temperature. Error bars from the fitting are smaller than the displayed symbols.

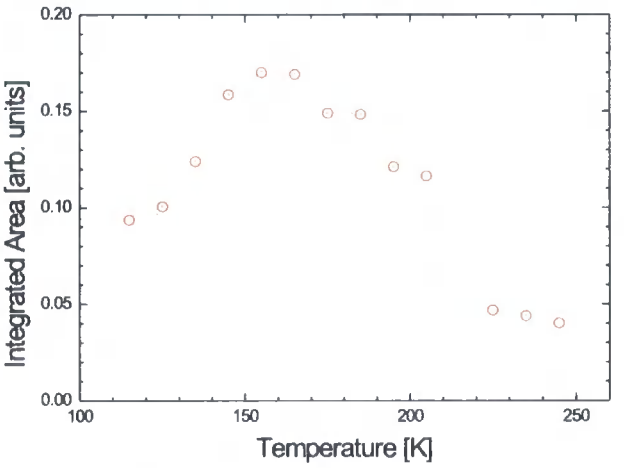

Figure 2.14: Integrated area of the (4.667, 0, 5) charge stripe superlattice reflection as a function of temperature. Error bars from the fitting are smaller than the displayed symbols.

stripes and therefore their hole concentration per stripe is increasing. After 160 K the degree of correlation between the charge stripes increases while the integrated area starts to fall. This indicates that even as the stripes become more correlated to each other, the hole concentration of the stripes starts to fall off with increasing temperature.

We can now compare the inverse correlation length measured in the bulk of the crystal with high energy X-ray scattering and the inverse correlation length previously measured in the near surface region by Du *et al.* (2000) and Ghazi (2002). Figure 2.15 shows the comparison in the H-direction for the (4.667, 0, 5) charge stripe reflection. Here we can see that at $\sim$ 100 K

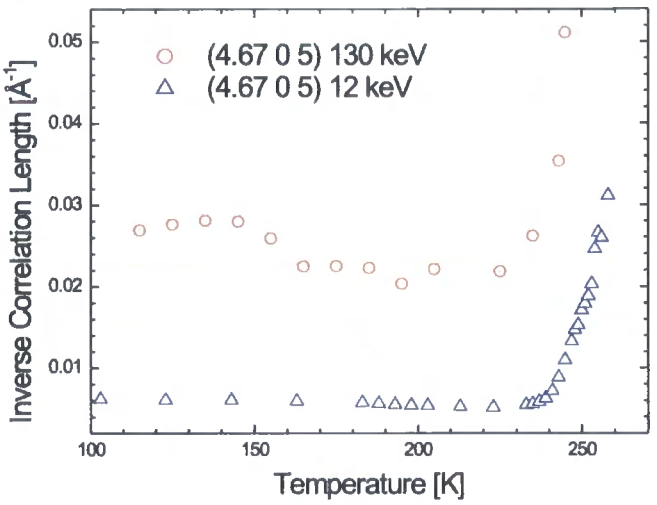

Figure 2.15: Inverse correlation length along the H-direction of the (4.667, 0, 5) charge stripe superlattice reflection measured at 130 keV (circles) and 12 keV (triangles). The 12 keV data is taken from Ghazi (2002).

the difference in the inverse correlation lengths is equal to:

$$\frac{\xi^{-1}_{12\text{ keV}}}{\xi^{-1}_{130\text{ keV}}} = 0.2314$$

In both cases the instrumental resolution of each measurement is much greater that the peak width. The 12 keV data does not show the anomaly at $\sim$ 150 K which is visible in the high energy data.

It appears that in the bulk of the material the charge stripes are more disordered than in the near surface region as measured at 12 keV. At such an energy the penetration depth of the crystal is estimated as 19.3 μm, in comparison to 2.3 mm at 130 keV.

Turning to the anomaly at 150 K, such a temperature does not appear to agree with any transition in the material. However the Nuclear Magnetic Resonance (NMR) by Yoshinari *et al.* (1999) found that the spin ordering transition temperature T_N was suppressed on the timescale of the measurement. They proposed a more glassy nature of the stripe ordering with a suppression of the spin ordering temperature by $\sim$ 30 K. If we re-examine the inverse correlation length in the 180 K region the 12 keV data shows the same decrease. Is it possible that the high energy X-ray scattering is seeing the glassy nature of the stripe ordering? The X-ray scattering measurements operate on a timescale of femto seconds far shorter than that of the NMR measurements therefore it is unlikely that the X-ray scattering observes the same glassy state.

Extracting correlation lengths from the measurements, consistent with the model in Appendix A for a Lorentzian squared lineshape, yields a in-

plane value of $\xi_H = 25.7 \pm 0.87$ Å. These correlation lengths are less than those presented by neutron diffraction measurements of Lee *et al.* (2001) and Yoshizawa *et al.* (2000) where correlation lengths of $\sim$ 200 Å are reported for the charge stripes. In fact the correlation lengths measured in the HEXS experiment for the $x = 0.33$ sample are similar to that of hole concentrations, x far away from the commensurate $x = \frac{1}{3}$ value. Using the results of Yoshizawa *et al.* (2000) and results presented by Ghazi (2002) the correlation length measured here is more like the charge stripe glass phase in $x = 0.2$ and $x = 0.5$ samples.

However, high energy X-ray scattering should sample the same bulk of the crystal that neutron scattering samples. Kivelson *et al.* (1998) have theoretically proposed that the charge stripes can be though of as vibrating strings of charge within the $a - b$ plane, similar to the behaviour of liquid crystals. This in turn could explain why the X-ray data does not agree with the neutron diffraction data. For the study of the charge stripes, the X-ray scattering is primarily sensitive to the time average of the charge distribution of each atom, whereas the neutron diffraction is sensitive to the perturbation of the position of the nucleus. In a model where the stripes are fluctuating and vibrating such motion will, in the X-ray case, mean that the time average size of the stripe is larger whereas in the neutron case, because the nuclei are more massive than the electrons the motion of the nucleus will be damped resulting in a smaller effective time average size. Indeed, this could explain the smaller correlation length of the spin stripes observed by Lee and Cheong (1997). As neutron scattering is sensitive to the magnetic moment from the outer shell electrons their effective size will be as large as the charge stripes in

the X-ray case and will result in a smaller correlation length than measured by the neutrons for the charge stripes.

This difference in the correlation lengths between the bulk and near surface regions in perovskite materials has previously been reported in the study of $SrTiO_3$ by HEXS. The work of Neumann *et al.* (1995) found that the second length scale seen in the near surface region was not observed in the bulk of the crystal. In addition, returning to the model of Kivelson *et al.* (1998) such vibrating stripes could be effectively pinned by surface defects and strain fields in the near surface region. For the 12 keV measurements the surface of the crystal was cut and polished with 100 μm diamond paste. Such preparation damages the near surface region and could lead to the effects mentioned above.

2.4 Conclusions

By using high resolution measurements with an incident energy of 130 keV we have confirmed the existence of modulation of the charge density in $La_{2-x}Sr_xNiO_{4+\delta}$ $x = 0.33$ consistent with charge stripe modulations. The charge stripes appear to exist in a glassy state with a increased inverse correlation length compared with previous near surface measurements by Ghazi (2002) and Du *et al.* (2000). In addition a decrease in the inverse correlation of the charge stripes is found to occur at $T = 150$ K which is consistent with the reduced spin stipe transition temperature proposed by NMR measurements by Yoshinari *et al.* (1999). This indicates that in the glassy state of the charge ordering the associated spin stripes cause a disruption of the

charge stripe patterns.

2.5 Future Work

The results presented here display a difference where the inverse correlation length measured in the bulk of the sample is more reminiscent of that measured in doping levels away from $x = 0.33$. By studying the range of doping levels at high energy by Ghazi (2002) it would be possible to ascertain if either; (1) in the bulk of the samples the inverse correlation length is static over the doping region, with the charge stripes being pinned at the surface or (2) In the bulk of the samples the inverse correlation length is always greater than that at the surface. This would result in a further increase of the inverse correlation length as the hole concentration is varied away from $x = 0.33$. Such results would both strengthen the data presented in this chapter and obtain a greater insight into the behaviour of charge stripes over the whole doping region.

Chapter 3

Charge and Orbital Ordering in $Bi_{1-x}Ca_xMnO_3$, $x = 0.76$

3.1 Introduction

The manganite series of compounds with the perovskite related structures have received much attention in recent years. Although first studied and theorised about in the early 1950's they have attracted much recent attention principally due to the discovery of a large magnetoresistance effect (MR) in materials such as $Nd_{1/2}Pb_{1/2}MnO_3$ and $La_{2/3}Ba_{1/3}MnO_3$. This effect has been cited as being a candidate for future high-sensitivity magnetic sensors. In addition they have attracted much attention as they provide an especially illuminating demonstration of the interplay between spin, charge and orbital degrees of freedom.

These materials display many phenomena such as metal-insulator transitions, charge ordering, orbital ordering and a variety of structural distortions

caused by varying the parameters of the system by relatively small amounts. In such materials it is often difficult to perform theoretical calculations as the degree of correlation between all the parameters is high and often varying only one by a small amount can change dramatically the properties of the material.

The manganite compounds form the general structure $R_{1-x}A_xMnO_3$ where R is a tri-valent rare-earth cation and A is a bi-valent alkali earth element. The parent compounds $RMnO_3$ are all insulators at all temperatures. The electronic structure of the manganese ions is $[Ar]3d^4$ and within these compounds the manganese has an oxidation state of +3 corresponding to four electrons in the $3d$ level, which are all spin aligned due to Hund's rules of maximum multiplicity. As the manganese ion sits in a octahedral environment the $3d$ level is split due to the crystal field into a doubly degenerate e_g state, and a triply degenerate t_{2g} level (which is lower in energy). The higher energy e_g orbitals point towards the oxygen $2p$ orbitals and are therefore strongly hybridised. The e_g electrons cannot be easily considered to be localized. It is these de-localized states which are thought to cause the conduction (Dessau and Shen, 2000).

In addition to the crystal field splitting of the $3d$ band caused by the Mn octahedra there also exists a distortion of the octahedra called the Jahn-Teller effect. Manganese, or more specifically Mn^{3+}, is one of the ions which displays strong Jahn - Teller distortions along with Cu^{2+}, Ni^{3+} in its low spin state and Cr^{2+}. The distortion occurs to lift the degeneracy of the e_g levels, as it is these which have charge density directed towards the ligands (see Figure 3.1). To lower the total energy of the system the structure distorts

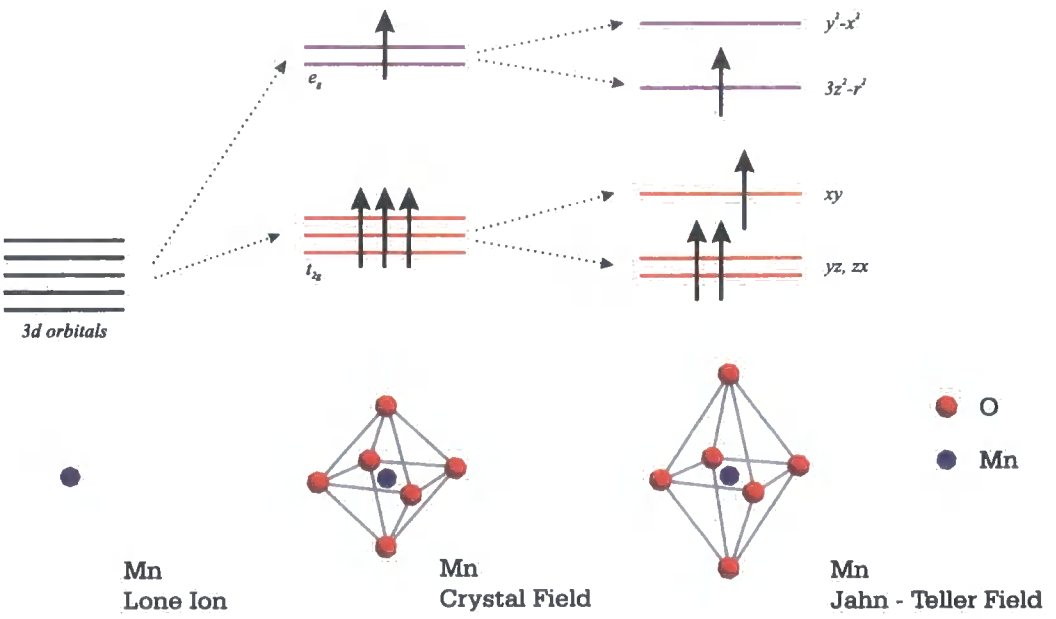

Figure 3.1: Schematic diagram of the $3d$ band energy levels within a lone manganese ion (left), a octahedral crystal field (centre) and a Jahn - Teller distorted octahedral crystal field (right).

elongating the octahedra in one direction. The degree of elongation is often known as the 'c over a' ratio (c/a) with an undistorted octahedra having a ratio of 1. As the distortion increases, c/a becomes greater than 1. It is important to note that the terms c and a are axes within the frame of the octahedra and are not to be confused with the structural lattice parameters.

The doping of holes into the system, by the substitution of the bi-valent alkali earth element, introduces more charge carriers into the system. The addition of holes provides a degree of freedom within the valence state of the manganese which is found to exist in an intermediate region between Mn^{3+} and Mn^{4+}. In this case a number of differing states can be observed effecting the spin degree of freedom. Such magnetic structures as ferromagnetic

(FM), anti-ferromagnetic (AFM) and paramagnetic are readily realised with a strong correlation between the conduction electrons and the magnetic alignment. In the ferromagnetic state the double exchange process is favoured, requiring mobile electrons. However, phases do exist where the charge segregates into Mn^{3+} and Mn^{4+} like regions. This charge ordered state was first observed by Wollan and Koehler (1955). In such a state the dominant magnetic coupling is through the super-exchange interaction and the magnetic ordering can be either ferromagnetic or anti-ferromagnetic, depending on the orbital of the mobile electron.

In such a charge ordered state the segregation of holes to form Mn^{3+} and Mn^{4+} like regions will result in distortions of the MnO_6 octahedra around the Mn^{3+} sites but no distortions will be evident on the Mn^{4+} sites due to their inactivity to the Jahn - Teller effect.

If we take the case where the the doping level is $x = 0.5$ resulting in a ratio of Mn^{3+} to Mn^{4+} of 1:1, one possible structure is to segregate the holes into a checker-board type ordering pattern with each Mn^{3+} ion being surrounded by a Mn^{4+} ion. In this configuration two magnetic sublattices are realised from the Mn^{3+} and Mn^{4+}. In this configuration there is also an associated cooperative Jahn - Teller distortion, which due to the lifting of the degeneracy of the e_g state causes the e_g orbitals to order, the so-called orbital ordered state. Such a state was predicted by Goodenough (1955). In this model the e_g orbitals form zig-zag chains within the $a - b$ plane of the crystal. The Jahn - Teller effect causes an increase in the Mn - O bond length of the populated e_g orbital and subsequently this leads to a movement of the Mn^{4+} ions within the lattice. The Mn^{3+} ions continue to form a square

lattice.

Figure 3.2 displays such a co-operative Jahn - Teller effect in a half - doped sample. In this schematic the Mn^{3+} e_g orbitals are represented in blue. Ordering of these causes a lengthening of the Mn - O bonds which are along the e_g orbital direction. The result is the motion of the Mn^{4+} ions in the direction indicated by the red arrows. Such a motion of the Mn^{4+} ions in half doped manganites, such as $La_{0.5}Ca_{0.5}MnO_3$, has been confirmed using X-ray and neutron powder diffraction methods by Radaelli *et al.* (1997).

$La_{0.5}Ca_{0.5}MnO_3$ is an example of a manganite material with a doping level of $x = 0.5$ displaying charge order due to the 1:1 ratio of Mn^{3+} to Mn^{4+}

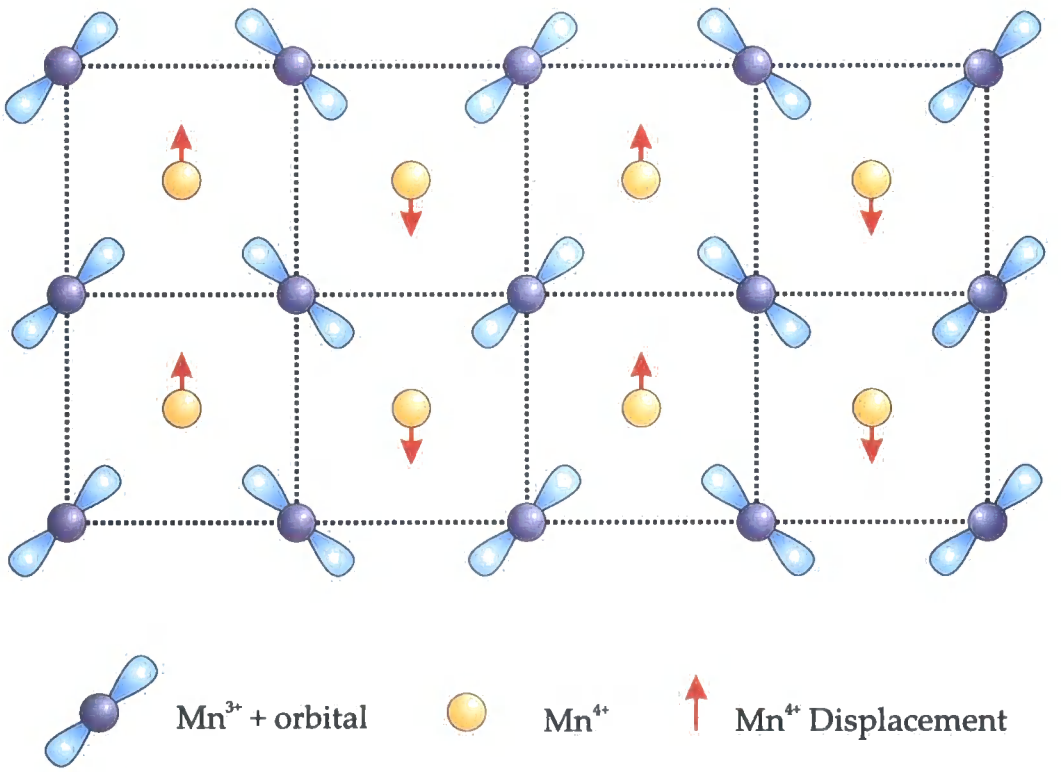

Figure 3.2: Displacement of the Mn^{4+} ions in a system with a Mn^{4+} / Mn^{3+} ratio of 1:1. The displacements are shown by the red arrows.

and cooperative Jahn - Teller ordering (orbital order). At room temperatures $La_{0.5}Ca_{0.5}MnO_3$ is a paramagnetic insulator and upon cooling it first becomes ferromagnetic at a temperature $T_C \sim 225$ K and then antiferromagnetic at $T_N \sim 115$ K. Such a variety of phases is thought to be due to the competition between double exchange and superexchange from the antiferromagnetic and ferromagnetic ordering.

Recent experimental evidence for charge ordering in half doped manganites started with the study of $La_{0.5}Ca_{0.5}MnO_3$. Radaelli *et al.* (1995) reported neutron and bulk magnetization data on polycrystalline samples of $La_{0.5}Ca_{0.5}MnO_3$ and $La_{0.75}Ca_{0.25}MnO_3$. They reported varied magnetic structures associated with structural transitions linked with the Jahn - Teller distortion of the MnO_6 octahedra.

Chen and Cheong (1996) found superlattice reflections in electron diffraction patterns occurring at a wavevector of $\boldsymbol{q} = (2\pi/a)\left(\frac{1}{2} - \epsilon, 0, 0\right)$. Figure 3.3 shows the electron diffraction pattern obtained from such a material below the charge ordering temperature T_{CO} with the corresponding model of the charge and orbital order. The incommensurability of such reflections was found to vary spatially over the sample under study.

However, since the discovery of charge order by electron diffraction, as described above, there has been notable X-ray and neutron powder diffraction studies of the charge, magnetic and orbital order. Radaelli *et al.* (1997) through powder diffraction analysis, found that the superlattice reflections previously associated with charge order by electron diffraction were due to the motion of the Mn^{4+} ions. No such superlattice reflections were found due to the charge ordering.

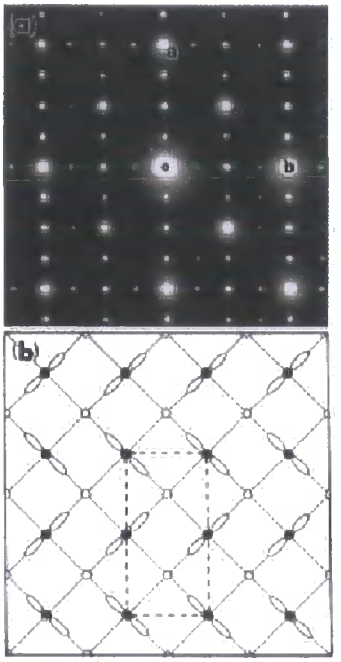

Figure 3.3: [0, 0, 1] Zone diffraction pattern from $La_{0.5}Ca_{0.5}MnO_3$ (top) and proposed charge order model (bottom). Taken from Chen and Cheong (1996)

Single crystal X-ray diffraction lends itself as an ideal tool for the study of charge and orbital order being a direct probe of the charge density of such materials. However, $La_{0.5}Ca_{0.5}MnO_3$ is inappropriate for such studies as it is very difficult to grow single crystals. The manganite $Nd_{0.5}Sr_{0.5}MnO_3$ easily forms single crystals large enough for the study using X-ray and neutron techniques. $Nd_{0.5}Sr_{0.5}MnO_3$ is similar to the $La_{0.5}Ca_{0.5}MnO_3$ system undergoing similar phase transitions upon cooling from room temperature. It undergoes a transition from a paramagnetic state to a ferromagnetic ordered state at a temperature of $T_C \approx 255$ K and, upon further cooling, undergoes a transition into an insulating, antiferromagnetic charge ordered

state at $T_{CO} = T_N \approx 160$ K. Neutron diffraction has confirmed the magnetic ordering present in this system.

The technique of resonant X-ray scattering allows for the study of the charge and orbital order. Nakamura *et al.* (1999) have applied resonant X-ray diffraction at the Mn K edge to study the charge and orbital phases of $Nd_{0.5}Sr_{0.5}MnO_3$. The techniques by which resonant X-ray scattering is sensitive to the charge and orbital order is discussed later in the Chapter in Sections 3.3.2 and 3.3.1. Figure 3.4 displays the X-ray energy resonance detected on superlattice reflections corresponding to the charge order (at a wavevector of $(0,\ k,\ 0)$) and orbital order (at $\left(0,\ \frac{k}{2},\ 0\right)$) with the corresponding temperature dependance. They found, consistent with the model of orbital order, that below 140 K upon cooling the material enters into a charge and orbitally ordered phase. At 140 K they reported a strongly first-order transition. The resonance from the charge order obtained fits a model for the segregation of Mn^{3+} and Mn^{4+} on alternate Mn sites and not due to any structural modulation from e.g. the motion of the oxygen or manganese ions. The orbital ordering reflection however is ascribed to be due to a $(d_{3x^2-r^2}/d_{3y^2-r^2})$ orbital ordering pattern and appears at twice the direct space periodicity as compared with the charge order. This is again consistent with the model shown in Figure 3.2. No mention in this paper is made to the relative widths of the charge and orbital order reflections which would give an indication of the degree of long-range order.

One major disadvantage of the $Nd_{1-x}Sr_xMnO_3$ system is, while it displays a fairly rich phase diagram of many magnetic phases, it only displays charge ordering over a very narrow range centred on the $x = 0.5$ composition.

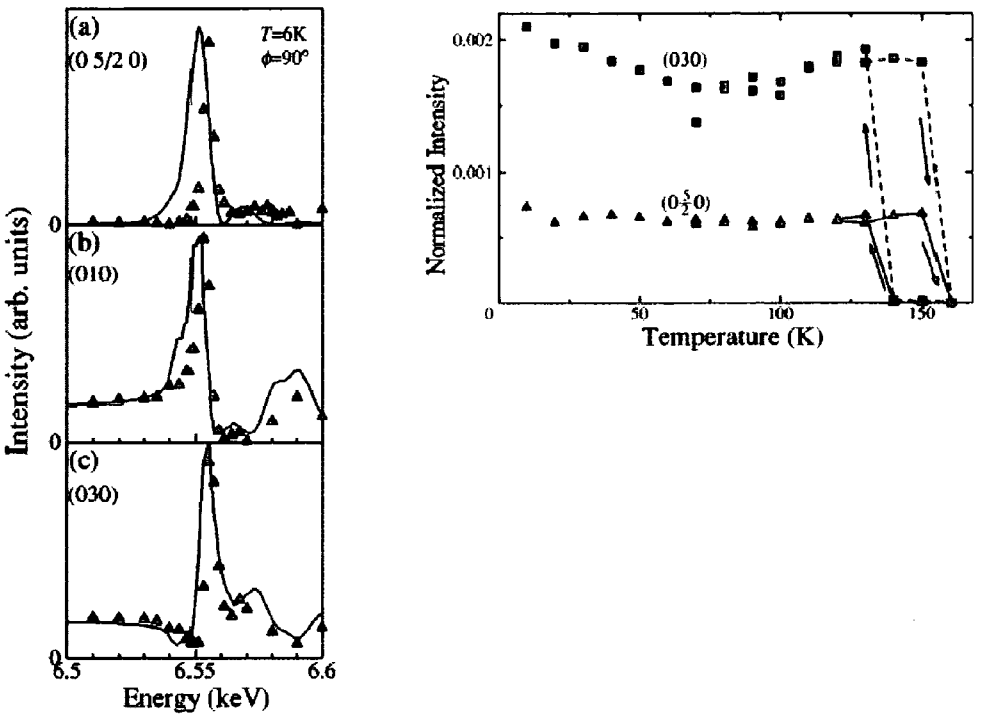

Figure 3.4: Resonance (left) and temperature dependance of the integrated intensity (right) of the charge $(0,\ k,\ 0)$ and orbital $\left(0,\ \frac{k}{2},\ 0\right)$ superlattice reflections in $Nd_{0.5}Sr_{0.5}MnO_3$. (Taken from Nakamura *et al.* (1999))

Figure 3.5 displays the phase diagram of the $Nd_{1-x}Sr_xMnO_3$ system. The narrow region of charge ordering around $x = 0.5$ is shown in black. With such a system it is difficult to test what occurs as the doping is moved away from the $x = 0.5$ region. One question which is apparent is that the model presented previously relies on a composition which has a equal ratio of Mn^{3+} to Mn^{4+}. What happens when the composition is varied away from $x = 0.5$?

The $Pr_{1-x}Ca_xMnO_3$ system, the phase diagram of which is shown in Figure 3.6, shows charge and orbital ordering over a much wider range of hole doping levels. The parent compound $PrMnO_3$ is thought to show a

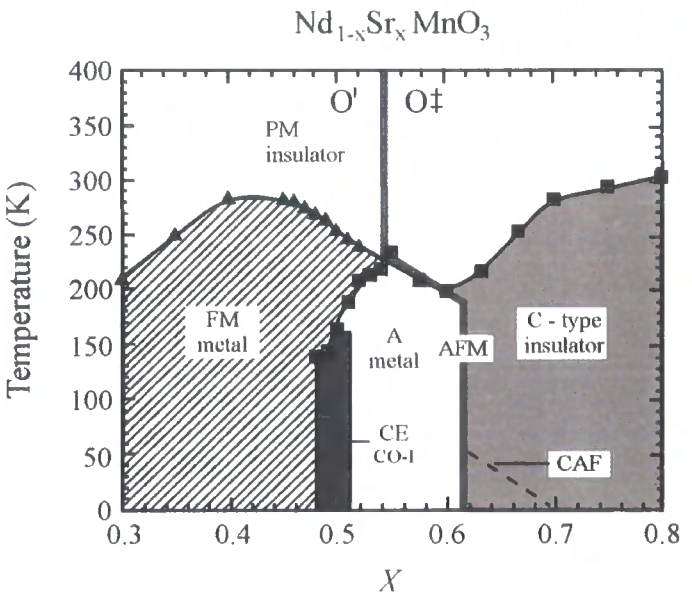

Figure 3.5: Phase diagram of $Nd_{1-x}Sr_xMnO_3$. PM : Paramagnetic insulator; FM : ferromagnetic; AFM : antiferromagnetic; CE : 'CE' type charge/magnetic ordering; A : A-type antiferromagnetic; C : C-type antiferromagnetic; CAF : canted antiferromagnetic. Taken from Kajimoto *et al.* (1999)

orbitally ordered ground state similar to that of $LaMnO_3$ discovered experimentally by Murakami *et al.* (1998). When doped in the region $0.3 \leq x \leq 0.7$, $Pr_{1-x}Ca_xMnO_3$ becomes an antiferromagnetic insulator at temperatures below room temperature. It is accompanied with the display of colossal magnetoresistance upon the application of an applied magnetic field. It is in this region that charge and orbital order are thought to be apparent.

$Pr_{1-x}Ca_xMnO_3$ with doping levels of $x = 0.25$, 0.4 and 0.5 was studied by von Zimmermann *et al.* (1999) and von Zimmermann *et al.* (2001). In the case of the $x = 0.25$ doping no charge ordering was observed but orbital ordering in the $(d_{3x^2-r^2})/(d_{3y^2-r^2})$ pattern was found, occurring at a

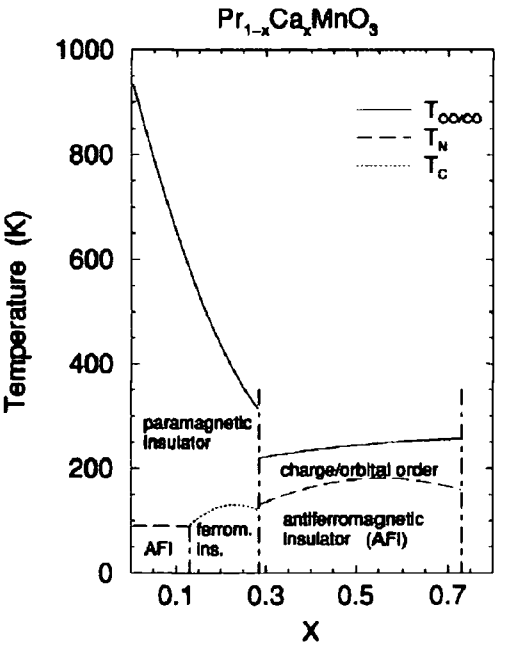

Figure 3.6: Phase diagram of temperature verses composition for $Pr_{1-x}Ca_xMnO_3$ in zero magnetic field. The full lines represent the charge / orbital transition temperature. Dashed lines represent antiferromagnetic transitions and dotted lines mark ferromagnetic transitions. Taken from von Zimmermann *et al.* (2001)

direct space periodicity half that which would be expected if charge ordering was present. Such an orbital ordering pattern requires each Mn ion to have a valence approaching +3. In the $x = 0.4$ and 0.5 cases charge and orbital ordering was again found using resonant X-ray techniques. Here in both cases charge and orbital superlattice reflections similar to those observed in $Nd_{1-x}Sr_xMnO_3$, were found consistent with the model presented in Figure 3.2. One major advantage of X-ray scattering is the high (wavevector) resolution available by the use of crystal analysers. Upon performing high resolution measurements on the charge and orbital order superlattice peaks

in the $x = 0.4$ and 0.5 samples and on the orbital order superlattice peaks in the $x = 0.25$ sample they found some surprising results. For the charge order they found that the correlation length (measured using $\xi = d/2\pi\Delta k$ where d is the lattice parameter and Δk is the peak half-width at half maximum in reciprocal lattice units) for the charge order in both cases was greater than 2000 Å. The correlation of the orbital order in the $x = 0.25$ sample was found to be approximately as well correlated as the lattice resulting in diffraction peaks of approximately the same width. For the $x = 0.4$ and 0.5 samples however, the orbital reflections were found to be considerably broader allowing an estimation of the correlation length of 320 ± 10 Å and 160 ± 10 Å respectively. They proposed that while long range order exists on the Mn^{4+} sublattice the orbital order exists in a domain type structure, with the long range order broken by orbital type domain walls. In addition the increase in x of the doping seems to lead to a disorder in the orbital order.

One possible explanation cited by the authors centres on the neutron diffraction results by Jirák *et al.* (2000) and Kajimoto *et al.* (1998) where different correlation lengths were found on the magnetic sublattices for the Mn^{3+} and Mn^{4+} where a vast difference of correlation lengths of $\xi_{3+}^{mag}/\xi_{4+}^{mag} \approx$ 4 to 8 is observed. Such a model also relies on disordered e_g orbitals on the Mn^{3+} sublattice to break the magnetic correlation. This result again highlights the strong interplay between the charge, orbital and spin degrees of freedom present in such samples.

Again moving further away from the $x = 0.5$ special composition the $La_{1-x}Sr_xMnO_3$ system with its parent compound $LaMnO_3$ has been studied. $LaMnO_3$, as has been discussed previously, has been found to be orbitally

ordered at high temperature, which has been confirmed by Murakami *et al.* (1998) using resonant X-ray diffraction. Upon the doping of holes into the system by the substitution of Sr for La a varied phase diagram is realised. An example of such a phase diagram is shown in Figure 3.7. Endoh *et al.* (1999) studied a single crystal of $x = 0.125$ which showed interesting results. Two transitions were observed upon cooling, first at a temperature of $T_{JT} = 291$ K the system underwent a transition into a Jahn - Teller distorted phase realised by a structural phase transition into an orthorhombic phase. Upon further cooling at a temperature of $T_{OO} = 145$ K the sample displayed a transition into an orbitally ordered state accompanied by a structural transition back into a tetragonal state, suggesting the collapse of the cooperative Jahn - Teller

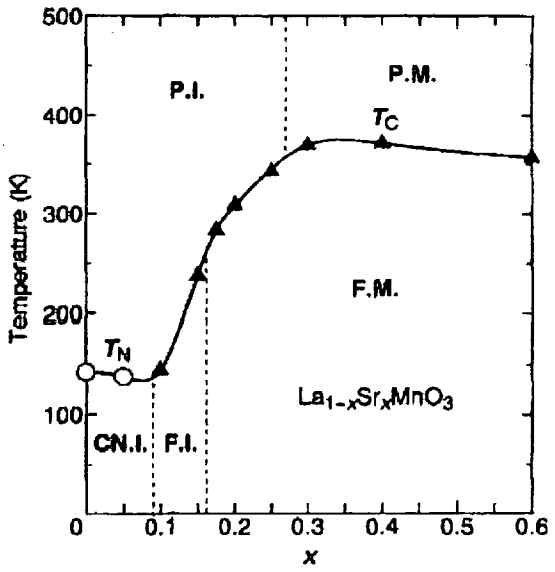

Figure 3.7: Phase diagram of the $La_{1-x}Sr_xMnO_3$ manganite system. P.I. : Paramagnetic Insulator; P.M. : Paramagnetic Metal; F.M. : Ferromagnetic Metal; F.I. : Ferromagnetic Insulator.

effect. By performing resonant diffraction they showed energy resonances on the superlattice reflections due to orbital ordering.

Niemöller *et al.* (1999) studied crystals of $La_{1-x}Sr_xMnO_3$ with $x = 0.06$, 0.125 and 0.15 using high energy X-ray diffraction. They found satellite reflections corresponding to the charge ordering occurring at wavevectors of $\boldsymbol{q} = (h \pm 0.25,\ k,\ 0)$ and $(h,\ k \pm 0.25,\ 0)$ in the $x = 0.125$ sample consistent with the doping level. Superlattice reflections were also found at the same locations in reciprocal space in the $x = 0.15$ sample. They agreed with the work of Endoh *et al.* (1999) with the same Jahn - Teller distorted phase in the intermediate temperature range. The observation of orbital order at a wavevector of $\boldsymbol{q} = (1,\ 0,\ 0)$, identical to the case for $LaMnO_3$ suggests that there is no disproportionation of the charge into Mn^{3+} and Mn^{4+} regions, but the high energy data with a charge ordering at $\boldsymbol{q} = (0.25,\ 0,\ 0)$ would require a different orbital order wavevector. This is one of the few systems which show charge and orbital order away from the $x = 0.5$ compositions. With such an anomaly effects such as phase segregation could be possible but clearly further work is required.

In summary it appears that by varying the sample doping away from the $x = 0.5$ composition by small amounts, the checkerboard pattern, as shown in Figure 3.2, is realised. The work of Niemöller *et al.* (1999) suggests that charge ordering appears at a different periodicity, but seems to disagree with the orbital ordering suggested by Endoh *et al.* (1999). One main question which has to be addressed is the possibility of charge ordering away from $x = 0.5$ with the checkerboard pattern, with long range orbital order. If we again return to the $La_{1-x}Ca_xMnO_3$ system, the phase diagram

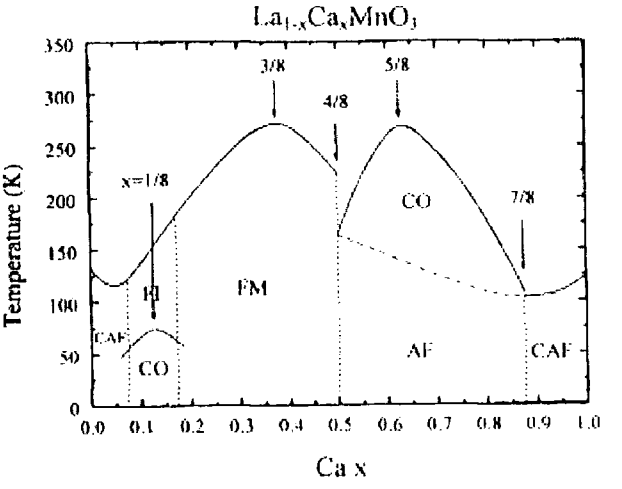

Figure 3.8: Phase diagram of the $La_{1-x}Ca_xMnO_3$ manganite system. CO : Charge Ordered; AF : Antiferromagnetic; CAF : Canted Antiferromagnetic; FM : Ferromagnetic; CO Charge Ordered; FI : Ferromagnetic Instulator.

of which is shown in Figure 3.8, the charge ordered region can be seen extending from $x = 0.5$ to 0.85. Such a doping can be thought of as electron doping, or the doping of holes with $x > 0.5$. However, single crystal samples of $La_{1-x}Ca_xMnO_3$ have not been grown to date but $Bi_{1-x}Ca_xMnO_3$ readily grows, and is iso-structural with the $La_{1-x}Ca_xMnO_3$ system displaying the same phase diagram. The $Bi_{1-x}Ca_xMnO_3$ $x = 0.76$ sample was chosen to be studied to observe whether it shows the 'checkerboard' type of charge order or forms 'stripes' of Mn^{3+} regions separated by Mn^{4+} rich regions. Previous studies by Su *et al.* (1999) have studied the cooperative Jahn - Teller distortion associated with charge ordering occurring at a wavevector of $Q_{JT} = (0.25, 0, 0)$ characteristic of charge ordering with double the direct space periodicity of the $x = 0.5$ doped samples. Bao *et al.* (1997) performed both electron diffraction and single crystal neutron scattering on

samples of $Bi_{1-x}Ca_xMnO_3$ with $x = 0.74$, 0.76 and 0.84. They reported on the magnetic structure of the system along with its similar properties to $La_{1-x}Ca_xMnO_3$. Again, they reported observing structural modulations consistent with a charge ordered model occurring at twice the direct spacing seen the $x = 0.5$ system for the $x = 0.76$ composition.

3.2 Charge Ordering Model

The $Bi_{1-x}Ca_xMnO_3$ system upon cooling from room temperature, starts in a paramagnetic state and then undergoes a transition into a ferromagnetic state at a temperature of $T_C \approx 240$ K which is proposed to be charge ordered. The material then undergoes a further transition into an antiferromagnetic state at a temperature of $T_N \approx 120$ K.

The charge ordering model that we propose for the $Bi_{1-x}Ca_xMnO_3$ system with $x = 0.76$, is one in which 'stripes' of Mn^{3+} are separated by Mn^{4+} regions. Figure 3.9 shows a representation of the model of charge ordering. Here the Mn^{4+} is represented by the yellow circles, the Mn^{3+} by blue circles with their associated e_g electron orbital direction. The suggested motion of the Mn^{4+} ions which cause the Jahn - Teller distortion superlattice reflections is shown by red arrows.

In this model the charge ordering occurs at a wavevector of $\boldsymbol{Q_{CO}} = \left(\frac{1}{2}, 0, 0\right)$, the orbital order at $\boldsymbol{Q_{OO}} = \left(\frac{1}{4}, 0, 0\right)$ along with the Jahn - Teller order which occurs at the same modulation wavevector $\boldsymbol{Q_{JT}} = \left(\frac{1}{4}, 0, 0\right)$.

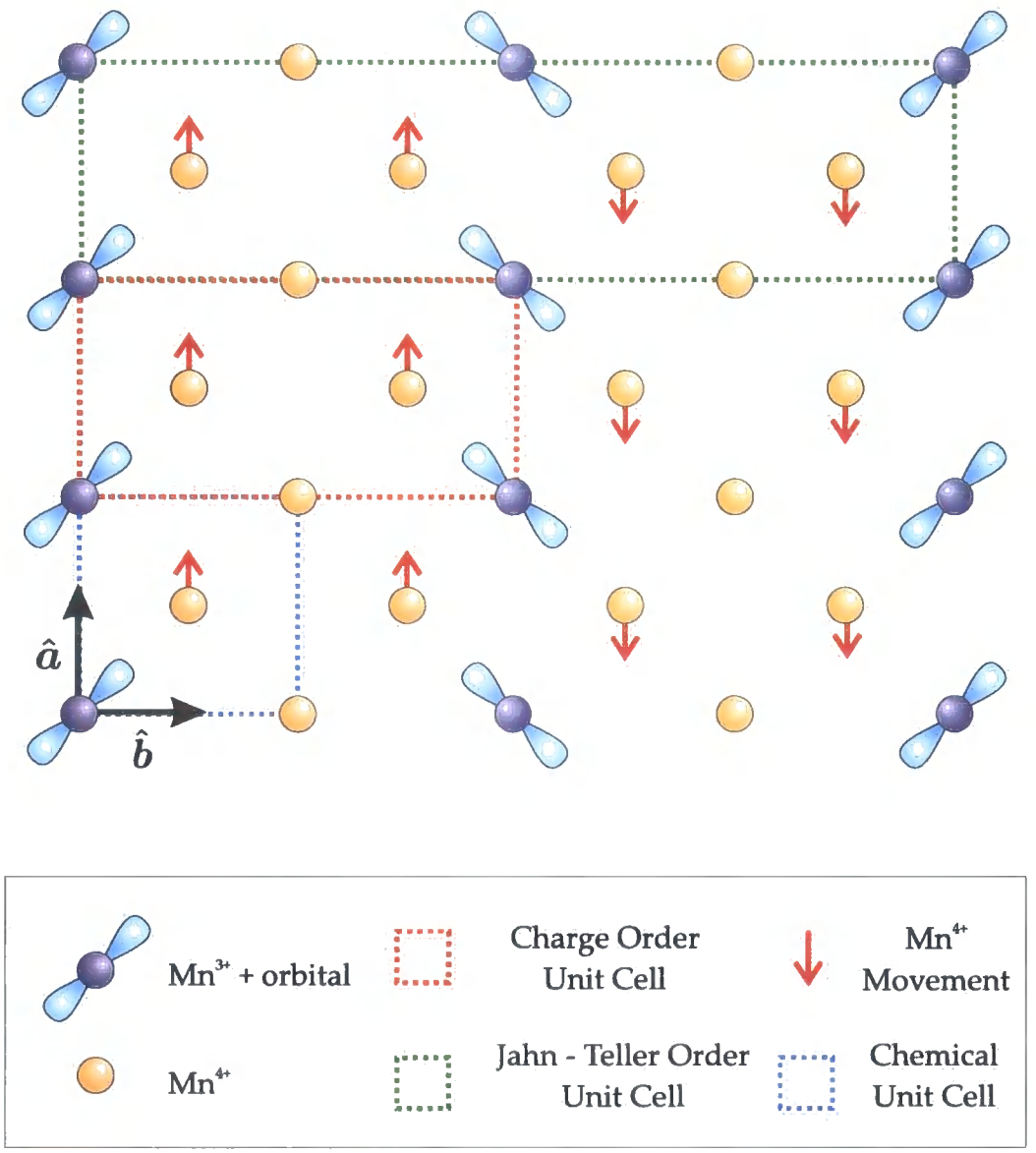

Figure 3.9: Proposed charge and orbital ordering model for the $Bi_{1-x}Ca_xMnO_3$ $x = 0.76$ system.

3.3 X-Ray Resonant Scattering

3.3.1 Resonant Scattering from Charge Ordering

X-ray scattering is primarily sensitive to the charge distribution in a solid and is an ideal technique for the study of charge based modulations. However, it is difficult to separate scattering from a structural modulation occurring at the same wavevector from the actual Mn^{3+} / Mn^{4+} ordering pattern. The answer to this problem lies in the use of resonant X-ray scattering. This technique has become possible only due to the tunability of synchrotron radiation sources. We can write the resonant scattering contribution to the cross-section as:

$$f(\boldsymbol{Q}, \hbar\omega) = f_0(\boldsymbol{Q}) + f'(\hbar\omega) + if''(\hbar\omega) \tag{3.1}$$

Where the terms $f'(\hbar\omega)$ and $f''(\hbar\omega)$ are the real and imaginary parts of the resonant scattering factors and f_0 is the non resonant scattering factor. If we now consider the case where we have a mixture of Mn^{3+} and Mn^{4+} present in the sample, the energy of the absorption edge will be different in the two cases due to the effects of the chemical shift. Figure 3.10 shows EXAFS spectra taken on samples of $LaMnO_3$ (containing only Mn^{3+}) and $CaMnO_3$ (containing only Mn^{4+}). Figure 3.11 shows the same data differentiated to exaggerate the difference in the absorption edge position. From these data a clear difference of the absorption edge position of approximately 2.5 to 3 eV can be seen clearly.

If we now return to the case from scattering from a charge ordered unit

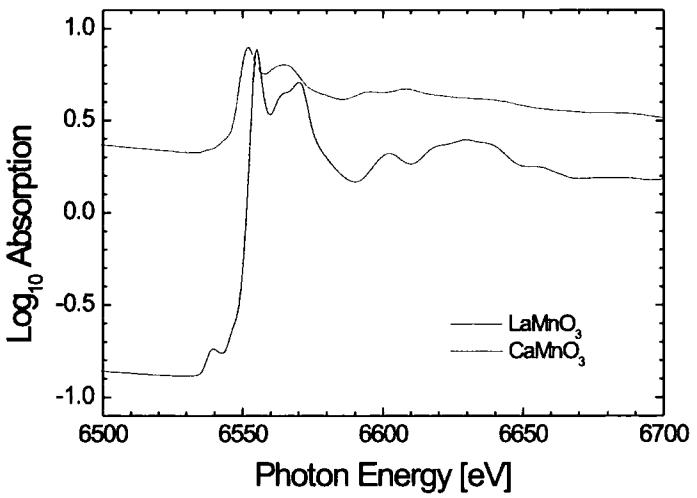

Figure 3.10: EXAFS Absorption spectrum from $LaMnO_3$ (red line) and $CaMnO_3$ (blue line)

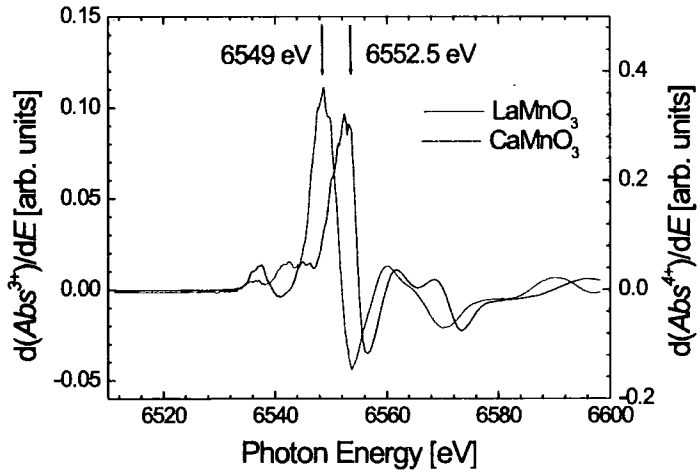

Figure 3.11: Differentiated ($\frac{\mathrm{d}Abs}{\mathrm{d}E}$) absorption spectra from $LaMnO_3$ (red line) and $CaMnO_3$ (blue line) to highlight the difference in absorption edge position.

cell composed of both Mn^{3+} and Mn^{4+} the resonant scattering contribution to the structure factor will be of the form:

$$F_{CO} \propto f_{CO}(\hbar\omega) = \left(f'^{3+}(\hbar\omega) + if''^{3+}(\hbar\omega)\right) - \left(f'^{4+}(\hbar\omega) + if''^{4+}(\hbar\omega)\right) \quad (3.2)$$

Therefore, if we tune the incident X-ray energy to an energy between the two edge positions $E^{3+} < \hbar\omega < E^{4+}$ a large contrast will exist between the Mn^{3+} and Mn^{4+} ions and an enhancement in the scattered intensity will be obtained.

3.3.2 Resonant Scattering from Orbital Ordering

The observation of orbital ordering at non-resonant energies relies solely on the asymmetry between the electron density distributions of neighbouring Mn^{3+} ions. Such an effect is extremely small and would not be expected to be observable by traditional X-ray diffraction techniques. It is possible however to enhance this signal by tuning the X-ray energy close to an absorption edge.

In the case of resonant scattering at the Mn K edge the transition involved is $1s \rightarrow 4p$. In the case of the manganese ions the $4p$ band is unoccupied. However the model assumes that the $4p_{x,y,z}$ states are initially unoccupied but split due to the orbitally ordered state. Figure 3.12 shows the energy level diagram which displays such a splitting of the $4p$ levels.

For a reflection consisting of the difference between the two split $4p$ states

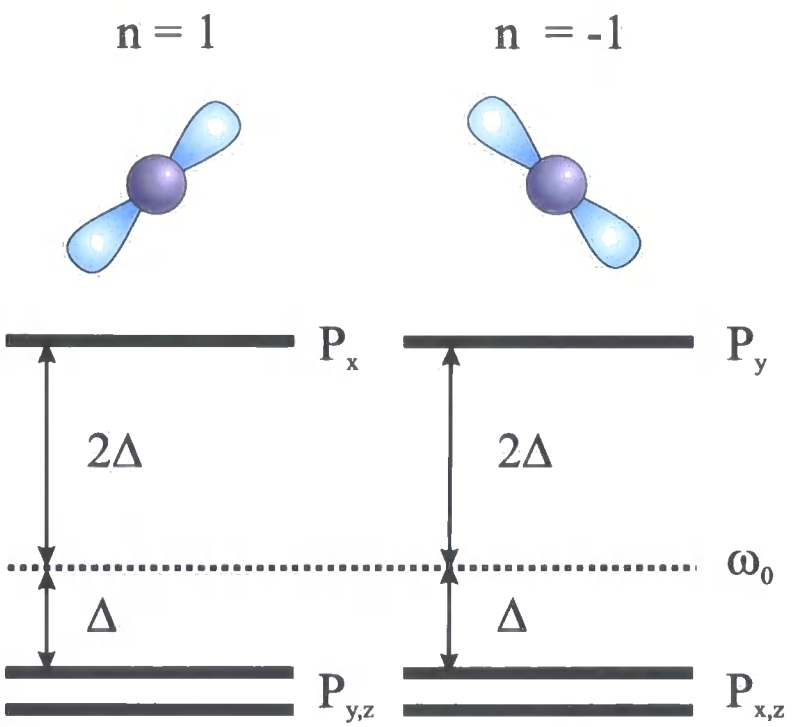

Figure 3.12: Schematic energy level diagram of the splitting of the $4p$ band due to the orbital ordering

the resonant scattering can be written as:

$$I^{RES} = \sum_{x,y,z,n=\pm 1} n \frac{\langle s|P^{\alpha}|p\rangle\langle p|P^{\beta}|s\rangle}{\omega - \omega_0 - \delta\omega_m^n + i\Gamma/2} \epsilon'^{\alpha}\epsilon^{\beta} \tag{3.3}$$

where the coordinate system ensures x and y are along the direction of the elongation of the e_g orbitals and z lies perpendicular to a plane defined by x and y. $|s\rangle$ and $|p\rangle$ are the wavefunctions of the Mn $1s$ and $4p$ orbitals respectively. P^{α} is the dipole operator, ω is the incident photon energy with ω_0 being the energy of the unperturbed $4p$ levels. The photons are incident (emitted) with a polarisation defined by ϵ (ϵ') and Γ is the lifetime in the excited state. n labels the orbitals directions with $n = 1$ ($n = -1$)

corresponding to an elongation along the x (y) axis.

To evaluate Equation 3.3 we can make some substitutions, namely from Figure 3.12 we can write the terms $\delta\omega_m^n$ as $\delta\omega_m^{-1} = 2\Delta$ with $m = x, z$ and $\delta\omega_m^1 = 2\Delta$ with $m = y$.

Within this model no reference is made to the origin of the splitting, Δ, within the $4p$ band. This matter has caused some controversy within the field of resonant studies of orbital order. The work of Castleton and Altarelli (2000) have suggested that the only direct probe of the orbital order is to perform resonant scattering not at the K edge but at the L_{III} and L_{II} edges, which are due to the $2p \rightarrow 3d$ electronic transition, and directly probe the e_g level. However, various models to account for the signal have been proposed. One possible method for the splitting is due to the Coulomb coupling between the Mn $3d$ and $4p$ levels, either directly or indirectly, through hybridization of the Mn($3d$) - O($2p$) and O($2p$)-Mn($4p$) states as suggested by Ishihara and Maekawa (1998). Both these cases lead to the same sign of Coulomb interaction but the latter would be expected to be weaker.

The second proposed model centres on the motion of the oxygen atoms away from high charge density caused by the distortion of the Mn octahedra due to the Jahn - Teller effect. Such an interaction will serve to lower the level of the $4p_m$ levels which lie along the extension of the octahedra while rasing the level along a compressed direction. Qualitatively, it is also worth noting that the p orbital spherical harmonics yield a shape which is very similar for the type of d orbitals which are though to be ordered. This effect has an opposite sign to the Coulomb interaction discussed above, but from the study of the scattered intensity it is not possible to distinguish between

these two processes. However, to observe a resonant signal at the K edge for a dipole transition, all that is required is the case that $\Delta \neq 0$.

3.4 Experimental Details

3.4.1 XMaS : The UK CRG

Experiments were carried out at the XMaS (X-ray Magnetic Scattering) beamline at the European Synchrotron Radiation Facility (ESRF), Grenoble, France (see Brown *et al.*, 2001). The beamline is situated on a bending magnet (BM28) which has a critical energy of $\sim$ 10 keV and is aligned on the soft sector to increase the flux available in the 3 - 4 keV region (The actinide M edges).

Situated 24.5 m from the source is the monochromator, which is the first optical element. The monochromator consists of two silicon (1, 1, 1) crystals which are water cooled to dissipate the heat load from the incident white beam radiation. Focusing of the X-ray beam is provided by a Zeiss focusing mirror of length 1.2 m and width 0.12 m machined from a single crystal of silicon into a cylindrical cross section of radius 116 mm and coated with rhodium. Focusing is provided by bending the mirror by means of pneumatic benders to provide 1:1 focusing at the sample position. The beam is incident onto the mirror at an angle of 4.5 mrad which leads to a cutoff in energy of $\sim$ 15 keV. The monochromator and mirror are housed in the first (optics) hutch and are all in a UHV environment.

The second (experimental) hutch houses the diffractometer and the inci-

dent beam optics. All flight paths are evacuated to reduce the effects of air absorption. Within the experimental hutch there exists a pair of harmonic contamination mirrors. The mirrors are formed from pyrex and coated with palladium. It is especially important to eliminate the effects of harmonic contamination from $\frac{\lambda}{2}$, $\frac{\lambda}{3}$, $\frac{\lambda}{4}$, $\cdots$ when studying superlattice positions such as $\left(\frac{1}{2}, 0, 0\right)$ as Bragg reflections from incident beam harmonics will exist at the same diffractometer angles. However, the primary focusing mirror has a cutoff of approximately $\sim$ 15 keV and will act to suppress harmonics occurring at energies above this value.

The end station of the beamline consists of an 11-axis 4-circle triple axis diffractometer constructed by Huber. The diffractometer circles are accurate in angular position to 1 arcsecond and the sphere of confusion is 30 μm. Within the ϕ circle of the diffractometer it is possible to mount a 'Displex' type cryostat capable of cooling the sample to 10 K with two beryllium domes or approximately 20 K by removing the inner Be dome which acts as a radiation shield. It is possible to perform diffraction in either horizontal or vertical geometries. Such flexibility is important so as to be able to control the direction of the polarisation of the incident beam.

Upon the 2θ axis it is possible to mount both a conventional two circle analyser stage or an in-vacuum polarisation analyser. The X-rays are detected by the use of a NaI scintillation detector which is electronically gated using pulse height analysis to the incident photon energy. Some limited form of harmonic rejection is available.

3.4.2 Polarisation Analysis

Until sources of synchrotron radiation were available, most diffraction was performed using laboratory sources which consist of an unpolarised source of X-rays. For the study of crystal structures where the primary scattering mechanism is Thompson scattering at an incident energy far from any absorption edge this does not prove any disadvantage. However, the incident polarisation does have an effect on the scattered intensity from an electron.

For a classical description of the effect of the incident polarisation we can assume that an incident electromagnetic wave will cause the electron to oscillate along the direction of the electric field. The electron will then reradiate a spherical wave centred on the mean position of the electron. We now consider an observer located at two positions as displayed in Figures 3.13 and 3.14. In the case where the observer is located in a plane normal to the incident electric field (Figure 3.13) at any angle, ψ, the full acceleration of the electron will be seen by the observer and there will be no dependance of the scattered intensity on ψ. However, in the case where the observer is in the plane of the electric field polarisation (Figure 3.14) the component of acceleration of the electron will vary as $\cos\psi$ and therefore the scattered intensity will vary by the same factor.

Consider now Bragg diffraction from a crystal for the two conditions where the incident polarisation vector is either within a plane defined by the incident beam wavevector ($\boldsymbol{k}$) and the scattering vector ($\boldsymbol{q}$), the so-called π polarisation and the case where the incident electric field is perpendicular to this plane, the so-called σ polarisation case. By the above argument

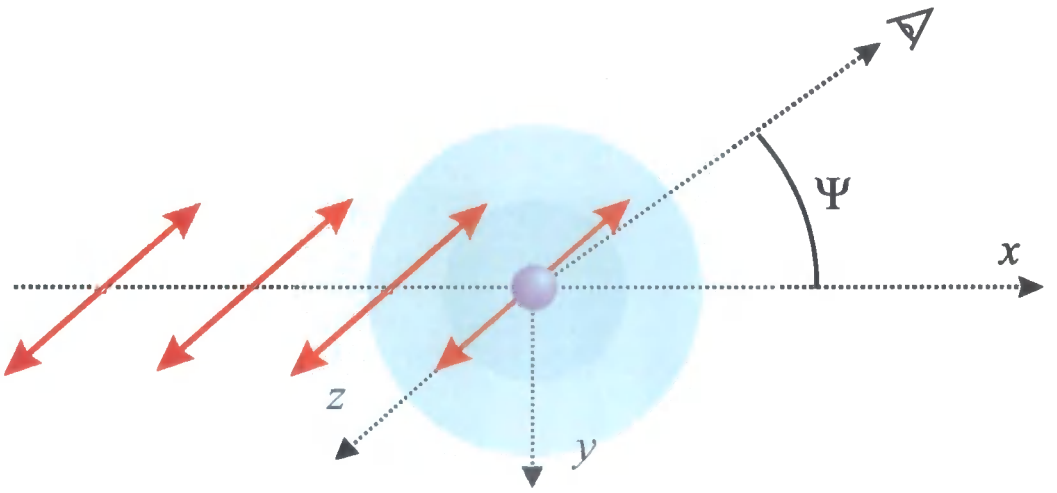

Figure 3.13: Schematic representation of a plane electromagnetic wave incident on a single electron. In this case the observer is in a direction normal to the incident beam polarisation and no dependance on the scattering with the angle ψ is observed.

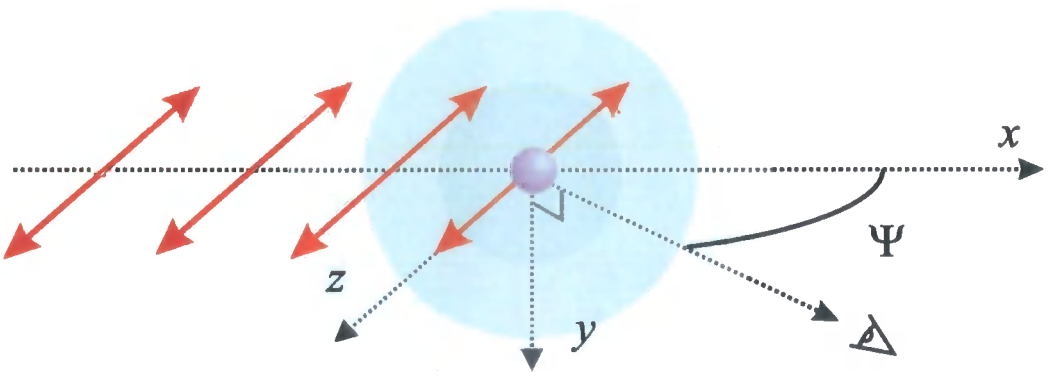

Figure 3.14: Schematic representation of a plane electromagnetic wave incident on a single electron. In this case the observer is located within the plane of the incident beam polarisation and a $\cos\psi$ dependance on the scattered amplitude is observed.

therefore, for an incident σ polarised wave there will be no reduction in the intensity of the scattering due to the incident polarisation. However for the π case the scattered intensity will be reduced by a factor of $\cos\theta_B$ where θ_B is the Bragg angle of the reflection.

We can therefore use this as a basis for polarisation analysis. If we arrange for our analyser crystal to have a Bragg angle of approximately $\sim 90°$. The angle which allows for the greatest degree of selection of the polarisation is known as Brewster's angle and is given by:

$$\theta_P(\omega) = \frac{\pi}{4} - \frac{\delta(\omega)}{2} \tag{3.4}$$

where the parameter $\delta(\omega)$ comes from the refractive index change in the material n given by $n(\omega) = 1 - \delta(\omega) + i\beta(\omega)$. The parameter $\delta(\omega)$ is given by:

$$\delta(\omega) = \frac{n_a r_e \lambda^2}{2\pi} f'(\omega) \tag{3.5}$$

Figure 3.15 shows the arrangement of a polarisation analyser. By rotating the analyser crystal around the axis of the incident beam (the η axis) it is possible to select the polarisation state measured by the detector. The two configurations for measuring σ and π polarised light are shown.

The efficiency of the polarisation analyser depends upon the choice of Bragg reflection. Often it is not possible to arrange for a suitable analyser crystal which, at the energy of the diffraction, will give a reflection with a Bragg angle equal to the Brewster angle. Therefore, one has to choose a reflection which gives a Bragg angle which is close to the Brewster angle. The result of this is that we remove some the efficiency of the analyser to

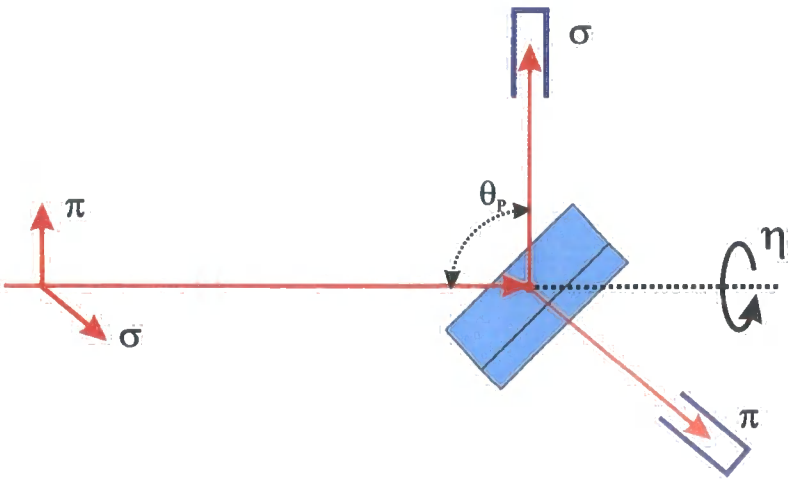

Figure 3.15: Diagram of a polarisation analyser using a crystal analyser. The incident beam enters from the left and is incident on the analyser crystal. By rotating the crystal around the axis of the incident beam (η) it is possible to select the component of polarisation which is observed in the detector.

pass the opposite polarisation and some 'leak through' will be detectable.

3.5 Experimental Procedure

3.5.1 Introduction

A high quality crystal of $Bi_{1-x}Ca_xMnO_3$ with $x = 0.76$ was grown at Bell Laboratories and was cut to give the $\langle 1,\ 1,\ 0 \rangle$ direction surface normal. The doping level of $x = n_h = 0.76$ can be though as electron doping to a level of $n_e = 0.24$. The crystal was indexed in the *Pbnm* setting with the lattice parameters $a_o \approx b_o \approx \sqrt{2a_p}$ and $c_o = 2a_p$ where p and o represent the cubic perovskite and orthorhombic lattice parameters respectively. Initial measurements were conducted on the in-house diffractometer as described by Wilkins *et al.* (2002) and in Chapter 4. The mosaic spread of the crystal was

found to be $\sim 0.1°$. The sample was mounted on the 11-axis diffractometer in a closed cycle He refrigerator capable of cooling to 20 K as described in Section 3.4.1. The sample was orientated with the $\langle 1,\ 1,\ 0 \rangle$ and $\langle 0,\ 0,\ 1 \rangle$ directions lying within the scattering plane.

Initially the sample was cooled to 20 K, the base temperature of the cryostat, and a search for superlattice reflections corresponding to the Jahn - Teller, charge and orbital ordering were undertaken. Reflections corresponding to the orbital order were found to occur at a modulation of $\boldsymbol{Q_{OO}} = \left(\frac{1}{4},\ 0,\ 0\right)$ surrounding the (2, 0, 0) Bragg peak. Charge order superlattice reflections were found at a wavevector of $\boldsymbol{Q_{CO}} = \left(\frac{1}{2},\ 0,\ 0\right)$ again surrounding the (2, 0, 0) Bragg peak. Jahn - Teller distortions were found at $\boldsymbol{Q_{JT}} = \left(\frac{1}{4},\ 0,\ 0\right)$ surrounding the (2, 2, 0) Bragg peak.

3.5.2 Polarisation Analysis

Introduction

Polarisation analysis was undertaken on the Jahn - Teller, Charge and Orbital ordering superlattice reflections. The (2, 2, 0) reflection from a single crystal of copper was used to provide the polarisation analysis as discussed in Section 3.4.2. This selection of reflection provides optimum polarisation analysis at 6.869 keV giving a 2θ angle of 90°. At the Mn K edge of $\hbar\omega = 6.556$ keV, as measured from the fluorescence of the sample, the 2θ angle is 95.63° which is close enough to the theoretical value to be suitable for the experiment. It is worth noting that the (0, 0, 4) reflection of silicon would provide a more perfect polarisation analyser at a 2θ angle of 88.31° but was not used due

to the very small rocking curve width of the reflection. The rocking curve width of the Cu analyser as measured on a Bragg reflection was $\sim 0.3°$.

Jahn - Teller Ordering

Figure 3.16 shows a energy scan in the range 6.52 keV $< \hbar\omega <$ 6.58 keV through the (1.75, 2, 0) reflection at fixed wavevector. Also shown for comparison is the fluorescence spectrum taken over the same energy range. The

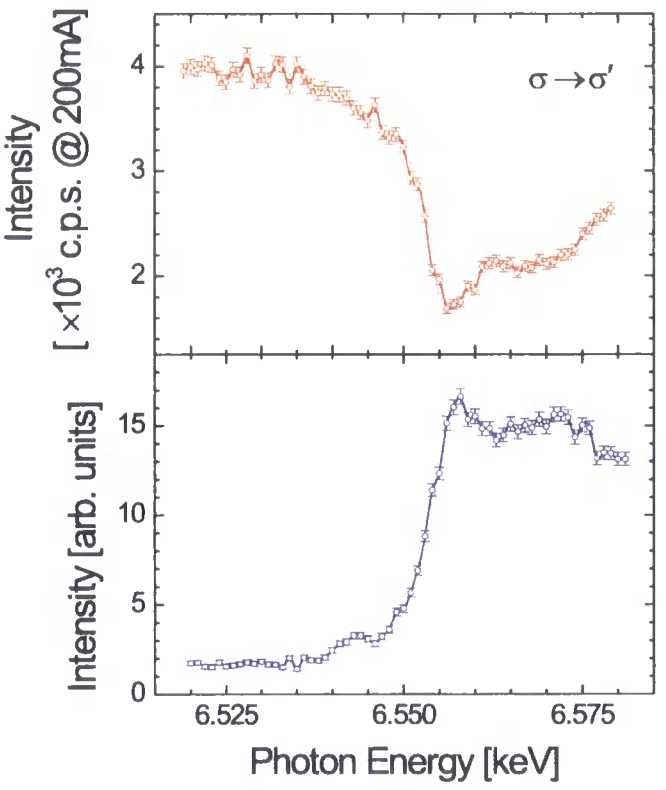

Figure 3.16: Energy scan at fixed wavevector through the (1.75, 2, 0) Jahn - Teller ordering reflection (top panel). Fluorescence measurement on the sample measured with an open detector (lower panel).

intensity of the Jahn - Teller reflection can be seen to be quantitatively inversely proportional to the fluorescence intensity. This is consistent with the intensity modification of the reflection being due to the variation in the resonant scattering factors $f'(\hbar\omega)$ and $f''(\hbar\omega)$ resulting in a variation in the absorption, μ, which is inversely proportional to the fluorescence. The reduction in intensity after the edge with respect to the value before the edge is most likely due to the increase in absorption at energies higher than the edge which serves to reduce the sample volume probed. Such an energy profile, displaying no resonance, is consistent with the origin of the scattering being from a structural modulation or distortion due to the Jahn - Teller ordering. In fact, identical results would be expected by performing similar scans on Bragg reflections.

Charge Ordering

Turning to the charge ordering, Figure 3.17 displays an energy scan at a fixed wavevector through the charge ordering superlattice reflection (3.5, 0, 0). Here a resonance can be observed in the $\sigma \rightarrow \sigma'$ channel, peaking at an energy of 6.556 keV. There is no resonance observed at this energy in the $\sigma \rightarrow \pi'$ channel and the intensity observed in this channel can be attributed to be due to the leak-through from the signal in the σ' channel which is $\sim 1\%$. The observation of the signal in the un-rotated σ' channel is consistent with the assumption that the origin of the scattering is from charge distribution.

To confirm the origin of the resonance was of the form suggested in Section 3.3.1, simulations of the resonant scattering were undertaken. The absorption EXAFS spectra for $LaMnO_3$ and $CaMnO_3$ were obtained by kind

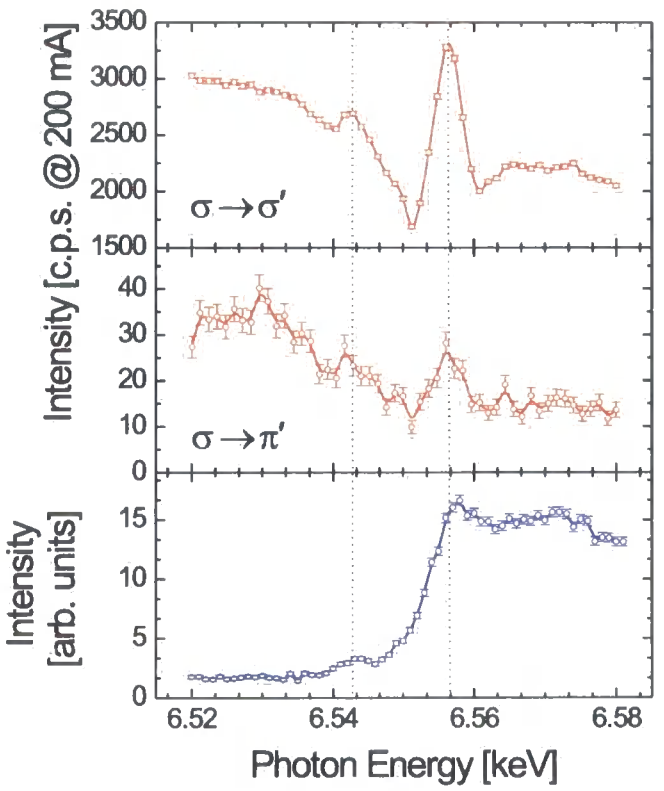

Figure 3.17: Energy scan at fixed wavevector through the (3.5, 0, 0) charge ordering reflection in the $\sigma \rightarrow \sigma'$ channel (top panel) and the $\sigma \rightarrow \pi'$ channel (middle panel). Fluorescence measurement on the sample measured with an open detector (bottom panel).

permission A. Dent, CLRC Daresbury Laboratory. These data are shown in Figure 3.10 and have been discussed previously in Section 3.3.1. $LaMnO_3$ will have an average manganese valence of 3 while $CaMnO_3$ will have an average manganese valence of 4 allowing the absorption spectra of Mn^{3+} and Mn^{4+} to be measured.

The absorption, $\mu(E)$, is related to the resonant scattering term f''

through the optical theorem by:

$$\mu(E) = \left(\frac{4\pi N\hbar e^2}{mE}\right) f''(E) \tag{3.6}$$

where N is the atomic number density, e is the electronic charge and m the electronic mass. Therefore from the absorption spectra it is possible to calculate the resonant scattering term f''. However, in the calculation of the charge order resonance, both the parameters f' and f'' are required. If we ignore any $\boldsymbol{Q}$ dependance then f' is related to f'' through the dispersion relations and can be written using the Kramers-Krönig transform (Kittel, 1996) as:

$$f'(E) = \frac{2}{\pi} P \int_0^\infty \frac{E' f''(E')}{E^2 - E'^2} \mathrm{d}E' \tag{3.7}$$

Such an integral is very difficult to perform on actual data due to the range of the integral being over $0 \rightarrow \infty$. Therefore to calculate both f'' and f' the differential method outlined by Cross *et al.* (1998) using the *DIFFKK* software.

In this method the resonant scattering parameters $f'(\hbar\omega)$ and $f''(\hbar\omega)$ are calculated for a lone resonant atom using the Cromer and Liberman functions (Cromer and Liberman, 1970). This data is then broadened using a Lorentzian of 1 eV to allow for the energy resolution ($\Delta E/E$) of the experiment. $f'(\hbar\omega)$ is then calculated from $f''(\hbar\omega)$ (the measurement of μ) and f'_{CL} from the Cromer and Liberman calculations. The Kramers-Krönig transform then separates to:

$$f'(E) = f'_{CL}(E) + \frac{2}{\pi} P \int_0^\infty \frac{E'[f''(E') - f''_{CL}(E')]}{E^2 - E'^2} \mathrm{d}E' \tag{3.8}$$

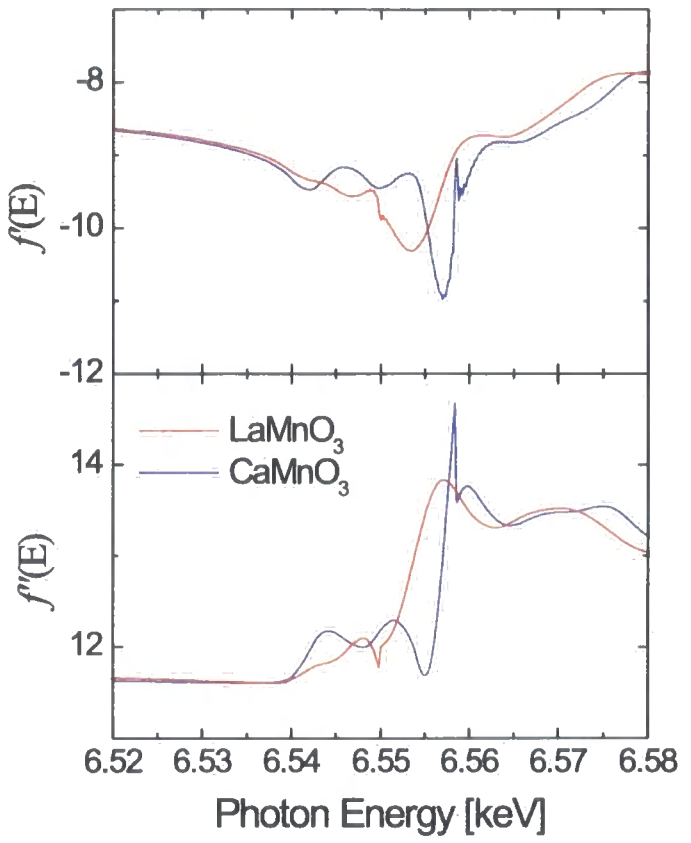

Figure 3.18: f' and f'' calculated from EXAFS data using the differential Kramers-Krönig technique (see text) for $LaMnO_3$ (red) and $CaMnO_3$ (blue)

So to calculate the resonance for the charge order, the parameters $f'(\hbar\omega)$ and $f''(\hbar\omega)$ for both $LaMnO_3$ and $CaMnO_3$ were calculated from the experimental data for the case of Mn^{3+} and Mn^{4+} respectively. Figure 3.18 shows both f' and f'' as calculated using the data above.

To estimate the resonance condition for the charge order the parameter f_{CO} was calculated from the difference between the resonant scattering

parameters for the two valence states by

$$f_{CO}(\hbar\omega) = f'^{3+}(\hbar\omega) - f'^{4+}(\hbar\omega) + if''^{3+}(\hbar\omega) - if''^{4+}(\hbar\omega) \qquad (3.9)$$

Figure 3.19 shows the results of computing f_{CO} compared with the actual measurement of the energy resonance. It can be seen that the main feature centred on an energy of $\hbar\omega = 6.556$ eV fits the resonance well with the correct width which is dependant on the difference in edge positions between Mn^{3+} and Mn^{4+}. The pre-edge feature at an energy of $\hbar\omega = 6.543$ keV is also displayed in both the experimental data and the fit. The emergence of such a feature in the fit can be explained as follows. If we look again at the EXAFS

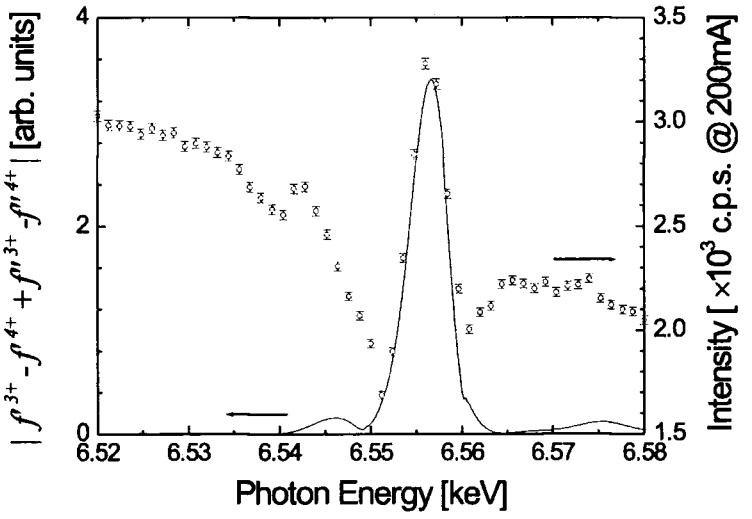

Figure 3.19: Energy scan at fixed wavevector through the (3.5, 0, 0) charge ordering reflection in the $\sigma \rightarrow \sigma'$ channel (open circles) with the fit from the EXAFS data (see text, solid line).

data presented in Figure 3.10 the $CaMnO_3$ data (Mn^{4+}) shows a pre-edge feature which is not present in the $LaMnO_3$ (Mn^{3+}) data. Therefore, when taking the difference between the two, the pre-edge feature will be visible within both the model and the experimental data. The post edge features are present due to the difference in $f'(\hbar\omega)$ and $f''(\hbar\omega)$ for the two species due to the EXAFS oscillations of the two ions. This would not be expected for lone ions. From Figure 3.10 it is clearly seen that the post edge structure is different in $LaMnO_3$ to $CaMnO_3$.

Orbital Ordering

Superlattice reflections corresponding to the proposed measurement of orbital order in Section 3.3.2 were located at 20 K at (1.75, 0, 0) and (2.25, 0, 0) surrounding the (2, 0, 0) Bragg peak. Figures 3.20 and 3.21 show energy scans at fixed wavevector through the (1.75, 0, 0) and (2.25, 0, 0) reflections respectively. Here we can see a resonant signal occurring at an energy of $\hbar\omega = 6.556$ keV in the rotated, $\sigma \rightarrow \pi'$ channel. Comparing the resonance in the $\sigma \rightarrow \pi'$ channel with the fluorescence signal measured on the sample the resonance is found to occur at an energy corresponding to the white-line of the fluorescence. Such a resonance at this energy is consistent with a dipole transition at the K edge from a $1s \rightarrow 4p$ state. The resonance is found to occur at the same energy at both wavevectors of (1.75, 0, 0) and (2.25, 0, 0).

Turning to the signal observed in the un-rotated $\sigma \rightarrow \sigma'$ channel, at the (1.75, 0, 0) reflection a resonance is observed at an energy of $\hbar\omega = 6.528$ keV, whereas for the (2.25, 0, 0) reflection a resonance is observed at $\hbar\omega = 6.532$ keV. If we look at the fluorescence signal shown in both figures

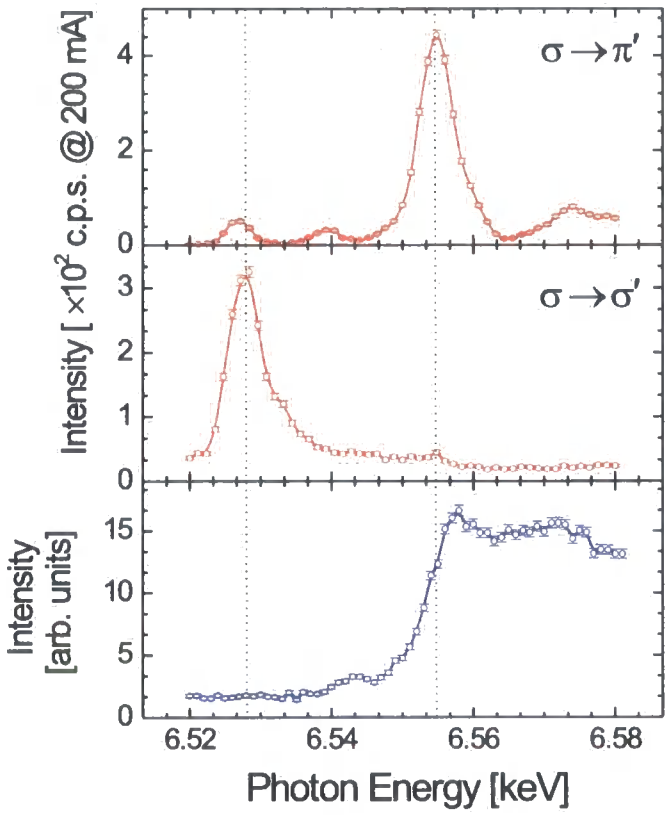

Figure 3.20: Energy scan at fixed wavevector through the (1.75, 0, 0) orbital ordering reflection in the $\sigma \rightarrow \pi'$ channel (top panel) and the $\sigma \rightarrow \sigma'$ channel (middle panel). Fluorescence measurement on the sample measured with an open detector (bottom panel).

there is no feature at such energies which correspond to core-hole atomic transitions. We have attributed such reflections to be due to multiple scattering or Renniger type scattering. Such reflections were found also to have a strong dependance with the azimuthal angle ψ which corresponds to a rotation around the scattering vector, $\boldsymbol{Q}$. Here for a normal charge (Bragg) reflection no dependance would be expected upon rotating the sample around

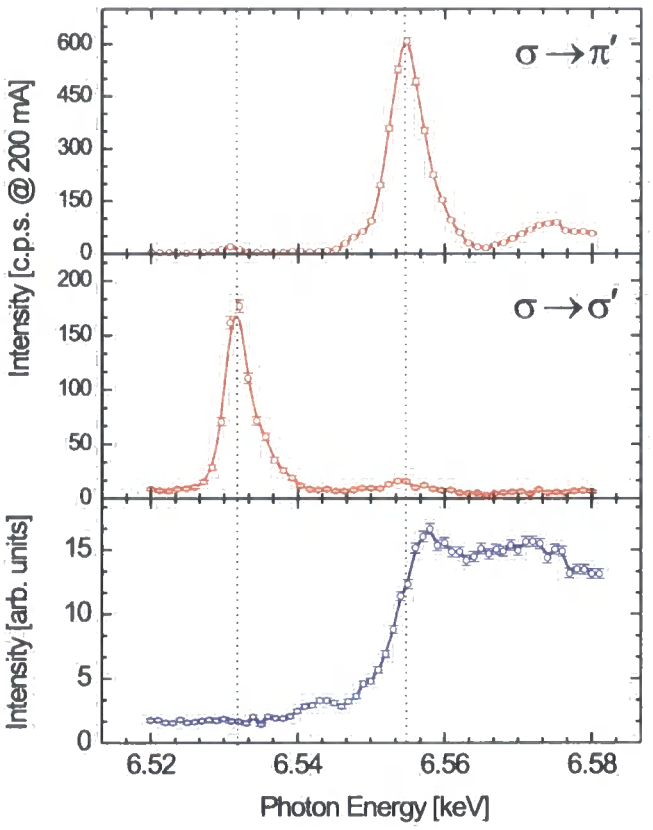

Figure 3.21: Energy scan at fixed wavevector through the (2.25, 0, 0) orbital ordering reflection in the $\sigma \rightarrow \pi'$ channel (top panel) and the $\sigma \rightarrow \sigma'$ channel (middle panel). Fluorescence measurement on the sample measured with an open detector (bottom panel).

the scattering vector. In reciprocal space, such a rotation ensures that the scattering vector still touches a reciprocal lattice point. However, by rotating around the scattering vector the Ewald sphere is found also to rotate within reciprocal space and will come into contact with other reciprocal lattice points. This then leads to a ψ dependence on the scattering. Secondly

the radius of the Ewald sphere is equal to $r_e = |\boldsymbol{k}| = \frac{2\pi}{\lambda}$ where $\boldsymbol{k}$ is the incident wavevector. As the energy is changed, although the scattering vector does not change to achieve this both $\boldsymbol{k}$ and $\boldsymbol{k}'$ have to change. This results in the Ewald sphere changing size and position which is why a resonance type condition is observed.

Figure 3.22 shows the resonances observed in the $\sigma \rightarrow \pi'$ channel for both the (1.75, 0, 0) and (2.25, 0, 0) orbital order reflections. From this we can confirm that the resonance energy of the orbital order is not dependant on $\boldsymbol{Q}$ whereas the resonance seen below the edge is consistent with the assumption of multiple scattering, as it has a $\boldsymbol{Q}$ dependance on the resonant energy.

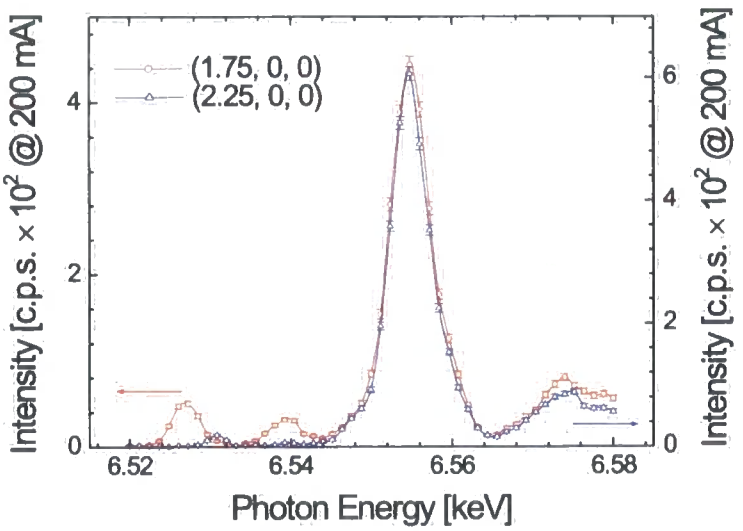

Figure 3.22: Comparison of energy scans at fixed wavevector through the (1.75, 0, 0) and (2.25, 0, 0) orbital ordering reflections in the $\sigma \rightarrow \pi'$ channel.

3.5.3 High Resolution Measurements

High resolution measurements were conducted using the same experimental setup as discussed previously but the polarisation analyser was exchanged for a conventional two-circle analyser stage. The analyser stage was fitted with a single crystal of germanium and the (1, 1, 1) reflection was used which resulted in a 2θ angle of $\sim 32°$. At such an angle the polarisation factor for the 90° rotated (π') channel results in a reduction of the intensity of a factor of $\sim 43\%$.

In the H-direction the Bragg, charge and orbital order superlattice reflections were fitted with a Lorentzian squared function discussed in Appendix A. The superlattice reflections were measured along the H direction as this corresponded to the high resolution direction parallel to the scattering vector in addition to being along the direction of the modulation. Figure 3.23 shows a fit to a Lorentzian squared lineshape to the (2, 0, 0) Bragg reflection in the H direction. Figure 3.24 shows a fit to the orbital order reflection and Figures 3.25 and 3.26 show the charge order reflection in the on-resonant ($\hbar\omega = 6.556$ keV) and off-resonant ($\hbar\omega = 6.556$ keV) cases respectively. From the peak widths in the H direction it is possible to estimate the inverse correlation length of each type of long range order. The inverse correlation length is estimated from the peak half width at half maximum, w, by

$$\xi_d^{-1} = \frac{2\pi}{d} w \tag{3.10}$$

where d is the direct space lattice parameter and ξ_d^{-1} is the inverse correlation length along the direction of the lattice parameter d. Table 3.1 shows the

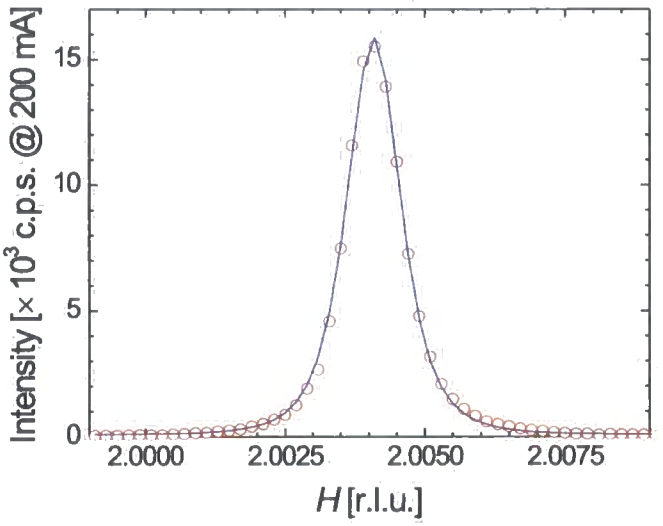

Figure 3.23: Lorentzian squared fit to the (2, 0, 0) Bragg peak in the H-direction. Note : error bars are smaller than the symbols for the raw data.

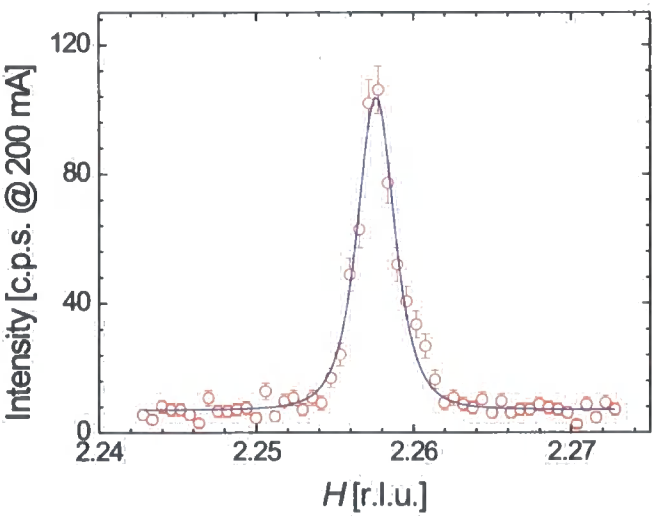

Figure 3.24: Lorentzian squared fit to the (2.25, 0, 0) orbital order superlattice peak in the H-direction at an energy of $\hbar\omega = 6.556$ keV.

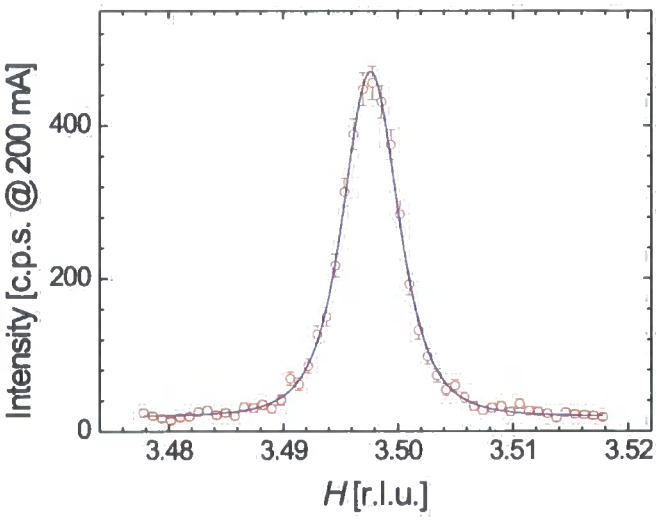

Figure 3.25: Lorentzian squared fit to the (3.5, 0, 0) charge order superlattice peak in the H-direction at an energy of $\hbar\omega = 6.556$ keV.

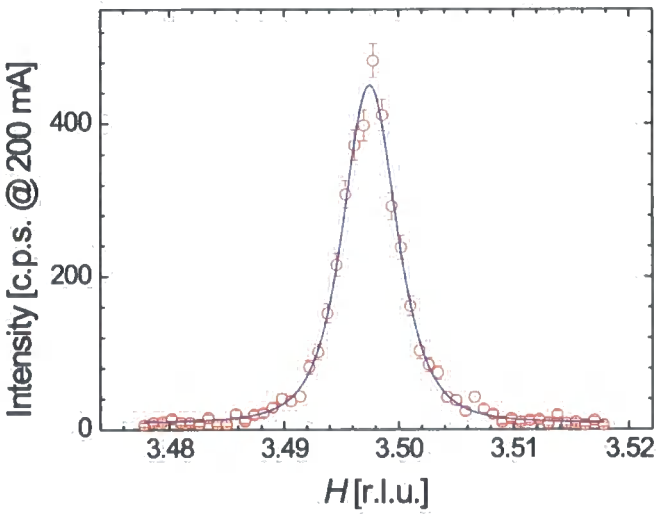

Figure 3.26: Lorentzian squared fit to the (3.5, 0, 0) charge order superlattice peak in the H-direction at an energy of $\hbar\omega = 6.520$ keV.

estimated inverse correlation lengths for the Bragg, orbital and on- and off-resonant charge order super-lattice reflections with Figure 3.27 showing the difference in diffraction peak widths in reciprocal lattice units for the same reflections.

Reflection	Inverse Correlation Length [Å^{-1}]
(2, 0, 0) Bragg	$7.042\times10^{-4} \pm 6\times10^{-6}$
(2.25, 0, 0) Orbital Order	$1.708\times10^{-3} \pm 7\times10^{-5}$
(3.5, 0, 0) Charge Order ($\hbar\omega = 6.556$ keV)	$3.497\times10^{-3} \pm 5\times10^{-5}$
(3.5, 0, 0) Charge Order ($\hbar\omega = 6.520$ keV)	$3.378\times10^{-3} \pm 7\times10^{-5}$

Table 3.1: Inverse correlation lengths estimated from the width of the fitted Lorentzian squared functions (From Equation 3.10) to the Bragg, charge and orbital order superlattice reflections.

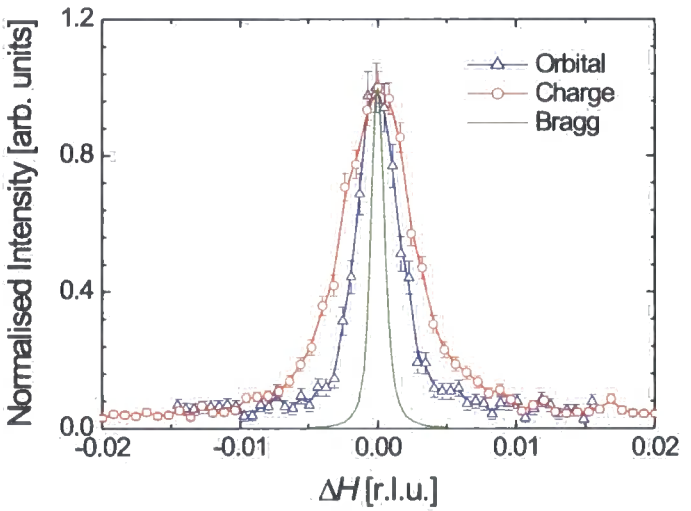

Figure 3.27: Comparison of the peak widths of the Charge (open circles), Orbital (open triangles) and Bragg peak widths (solid line) in the H direction.

From the inverse correlation lengths we can see that the charge order is less correlated than the orbital order which in turn is less correlated than the crystal lattice as measured on the (2, 0, 0) Bragg Peak. The charge ordering superlattice reflection was measured as a function of temperature along the three principal directions H, K and L. The results are shown in Figures 3.28 and 3.29. No quantitative measurement of the width was obtained in the K and L directions due to the much larger experimental resolution in these directions.

Figure 3.28 shows the integrated intensity, half width at half maximum (calculated width from fitting to a Lorentzian squared lineshape), and peak position, as a function of temperature in the H direction. In addition Figure 3.30 shows the estimated correlation length as a function of temperature in the H direction. Firstly it can be seen that the behaviour of the charge order reflection is identical, within the experimental error, when measured on- and off-resonance. While the resonant enhancement gives a indication of the origin of the scattering the underlying off-resonant scattering behaves identically. Upon warming from 10 K it can be seen that the charge order exists in a highly correlated state with a constant amplitude until a temperature of 210 K. This indicates two main points. Firstly, as the integrated intensity remains constant this suggests that the contrast of the Mn^{3+} to the Mn^{4+} is not changing and that there is no change in the difference in the valence state of the manganese ions. Secondly, as the inverse correlation length is constant in this region there is no change in the ordering of the Mn^{3+} and Mn^{4+} in the pattern suggested in Figure 3.9. After 210 K, the integrated intensity starts to fall and the correlation length decreases

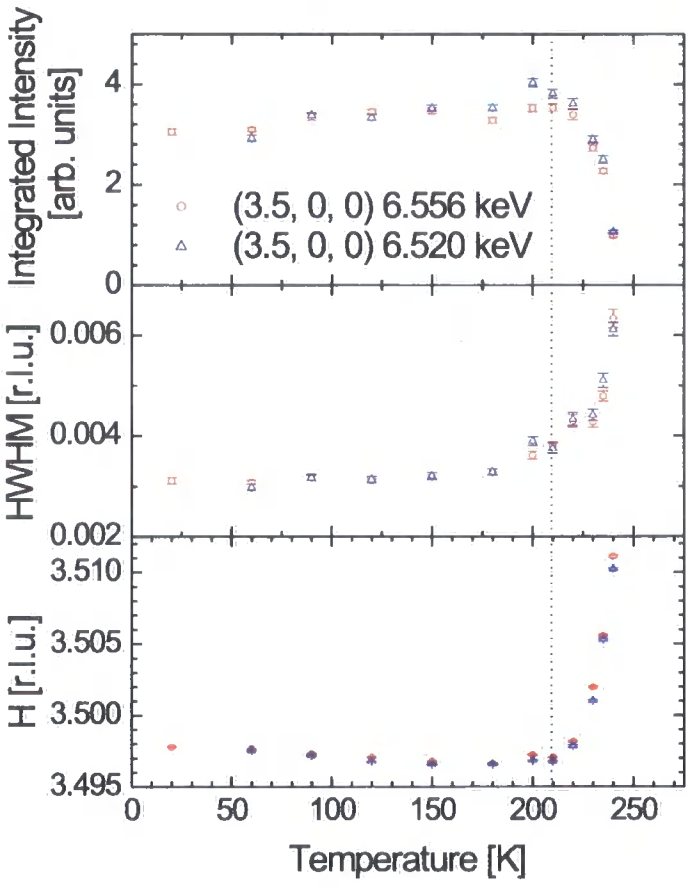

Figure 3.28: Integrated intensity (top panel), half width at half maximum (centre panel) and peak position (lower panel) for the charge order reflection (3.5, 0, 0) for both the on- and off-resonant cases. (circles and triangles respectively))

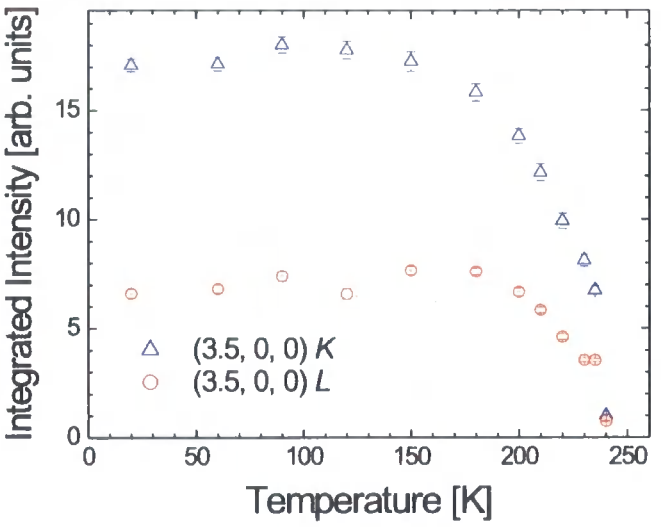

Figure 3.29: Integrated area along the K and L directions of the (3.5, 0, 0) charge order reflection on resonance ($\hbar\omega = 6.556$ keV).

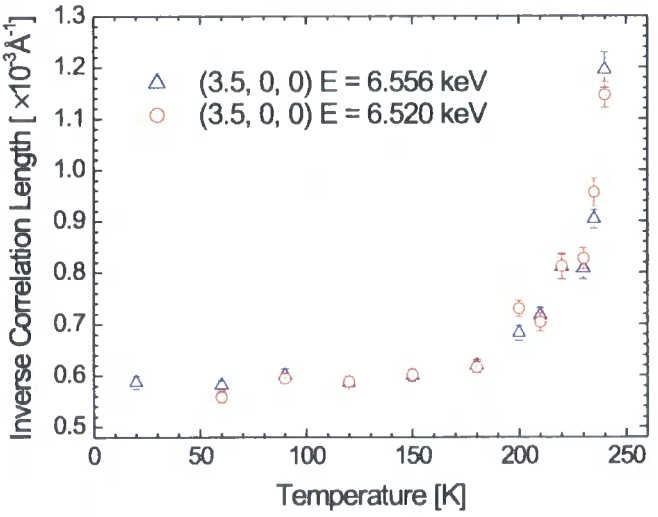

Figure 3.30: Inverse Correlation length as estimated from the fitted peak width to a Lorentzian squared line shape using Equation 3.10.

also. Such an effect is consistent with the difference in valence state of the manganese ions decreasing, i.e. the valence of the manganese ions is now approaching 3.5. In addition to this, the correlation of the charge ordered pattern decreases. At 240 K no superlattice reflections corresponding to the charge or orbital order were detected.

3.6 Discussions and Conclusions

In this study of the manganite $Bi_{1-x}Ca_xMnO_3$ ($x = 0.76$) we have proved the ordering pattern of both the charge and orbital order is of the form proposed initially in Figure 3.9. In this model the system exists in a Mn^{4+} rich state with stripes of Mn^{3+} regions separated by 2 unit cells in the a direction, i.e. one Mn^{3+} every 4 manganese ions. In addition the e_g orbitals are ordered, at least in the sense that a perturbation is placed on the $4p$ bands which results in a signal at the orbital ordering wavevector. Each Mn^{3+} along the chain in the a direction is alternatively ordered, realising a direct space ordering of the orbitals of four unit cells or each 8 manganese ions. This result seems to be in direct opposition to recent studies by Renner *et al.* (2002) using scanning tunnelling microscopy where they conclude that the charge ordering is half this direct space periodicity, i.e. the same as in the case for $x = 0.5$.

The energy resonance of the charge order reflection is consistent with the difference in resonant scattering factors for both the Mn^{3+} and Mn^{4+} sub-lattices upon tuning the incident X-ray energy. It is worth noting that the size of the resonance is less than has been observed in the half doped manganites as has been reported by von Zimmermann *et al.* (1999). Such

a resonance confirms the Mn^{3+} / Mn^{4+} ordering pattern present, and the polarisation dependance ($\sigma \rightarrow \sigma'$) confirms that the signal arises from charge based scattering.

Turning to the orbital order reflection, it is found to occur at twice the direct space periodicity of the charge order consistent with the model proposed. However, such a signal from resonant scattering does not arrise directly from the $3d$ band structure, but due to a perturbation of the $4p$ band. The polarisation dependance ($\sigma \rightarrow \pi'$) is consistent with dipole scattering from the $1s \rightarrow 4p$ bands. However, recent studies by Castleton and Altarelli (2000) have suggested that experiment should be carried out at the L_{III} and L_{II} absorption edges which correspond to transitions into the $3d$ band. By observing the difference in the resonances at the L_{II} and L_{III} edges it is possible to distinguish between the $3d_{3x^2-r^2}/3d_{3y^2-r^2}$ orbital order pattern or the $3d_{x^2-z^2}/3d_{z^2-y^2}$ orbital order pattern. The latter is due to a cooperative Jahn - Teller effect or Jahn - Teller ordering. Such an ordering is strong in these materials and indeed as has been displayed in this Chapter, strong symmetry forbidden reflections are found due to such ordering at similar types of wavevectors. Clearly further work is required to solve this problem. However, the K edge experiments do give us an initial insight into the orbital ordering states and do confirm that some form of long range cooperative order is present.

The high resolution measurements, performed with a Ge (1, 1, 1) analyser provide quantitative measurements of the degree of correlation of the different ordering processes observed. Here we find that by estimating the correlation length of the charge and orbital order, as compared with the Bragg

peak correlation, that the charge order is less correlated than the orbital order. Such an effect where $\xi_{CO} < \xi_{OO}$ has been reported by Wakabayashi *et al.* (2001) in the $La_{1-x}Sr_{1+x}MnO_4$ system performing similar experiments using a high resolution analyser. von Zimmermann *et al.* (2001; 1999) observed however that in $Pr_{1-x}Ca_xMnO_3$ for $x = 0.4$ and 0.5 that $\xi_{CO} > \xi_{OO}$. Their model to explain such an effect relies on the system displaying orbital domains which, while causing a reduction in the orbital correlation, does not effect the correlation of the charge order. It is difficult therefore form a model for a system whereby the charge ordering correlations are disturbed but the correlations on the Mn^{3+} e_g orbitals are kept intact.

3.7 Further Work

Drawing on the work undertaken on the $Bi_{1-x}Ca_xMnO_3$ system in this Chapter for a sample of $x = 0.76$ there are many opportunities for further work on this system.

As has been said previously, the $Bi_{1-x}Ca_xMnO_3$ system is iso-structural with the $La_{1-x}Ca_xMnO_3$ system, the phase diagram of which is shown in Figure 3.8. This material displays a large charge ordered region from $0.5 \leq x \leq 0.875$. By performing studies on different doping, x, there should be a transition from the checkerboard type ordering seen in half doped manganites to the stripe like charge order seen as this doping level of $x = 0.76$. In addition Wakabayashi *et al.* (2001) have shown that as the composition is moved away from such commensurate (or almost commensurate) values the ratio ξ_{CO}/ξ_{OO} tends to 1. A value of 0.49 ± 0.02 was measured in the current experiments.

Here in addition to observing a transition in the period of the charge and orbital ordering with doping it would be possible to see what happens to the correlations of the charge and orbital order.

Further work needs to be undertaken on the temperature dependance of the charge, orbital and Jahn - Teller order. In this chapter the dependance of the charge order has been systematically studied, clearly further studies on the orbital and Jahn - Teller ordering superlattice reflections should be studied in a similar fashion to compare the effects of temperature on each ordering process.

Finally, strong superlattice reflections are observed in this material below the charge ordering temperature. By performing either powder diffraction or single crystal structural analysis of this material it should be possible to calculate the positions of the oxygen ions along with the Mn^{4+} position to measure both the degree of Jahn - Teller distortion (The extension of the Mn - O bond) and the degree to which the Mn^{4+} ions move. Such an experiment reveals information about the cooperative Jahn - Teller effect which is closely linked to the orbital ordering process.

Chapter 4

Development and Testing of A Focused Laboratory Diffractometer

4.1 Introduction

During the last twenty years there has been a tremendous qualitative improvement in experimental X-ray scattering techniques. This has principally been due to technical advances in synchrotron radiation sources. The advent of second and third generation machines with ever-lower source sizes and beam divergences, insertion devices with optimised intensities, etc. has allowed researchers to undertake experiments with extremely high resolution or very high intensities to enable the detection of very weak scattering phenomena. Examples of very high-resolution diffraction measurements include studies of very long period multilayers (Hu *et al.*, 1999), as well as meV

inelastic X-ray scattering (Scopigno *et al.*, 2001). Alternatively, the very high intensities have allowed the detection of resonant magnetic scattering in holmium (Gibbs *et al.*, 1988), cuprates (von Zimmermann *et al.*, 1998) and many other materials. Such improvements are likely to continue with the advent of fourth-generation synchrotrons such as the TESLA machine (*The TESLA Project*, 2002). However, during the same period, advances in laboratory-based sources have been much less spectacular. Continued improvements in X-ray tube design have gradually improved source stability, lifetime and power output for fixed tubes, micro-focus sources and rotating anode generators, but these gains have been relatively modest compared to the advances using synchrotron radiation. However, there is still a need for laboratory-based instrumentation. Time at national or international synchrotron facilities is limited and expensive. It is therefore imperative that as much training, sample alignment and initial experimentation as possible be undertaken using in-house instrumentation.

The major focus of this thesis is spin, charge and orbital correlations in transition metal oxides. The interplay between these correlations leads to such phenomena among which Colossal Magneto-Resistance (CMR) and high temperature superconductivity (Mills, 1996; 1998*b*;*a*; Tranquada *et al.*, 1994; Tranquada, 1995) are noted. In these systems a multitude of phenomena can be studied including charge stripes, charge ordering and charge density waves. However, the superlattice reflections that appear due to such ordering are incredibly weak, typically 10^4 to 10^5 times weaker than corresponding Bragg peaks and require a high incident flux to perform high quality measurements. In addition, the diffractometer system has to include

cryogenic cooling, as these phenomena occur at low temperatures. Typically, experiments studying charge ordering involve measurement of the wavevector (diffraction peak position), integrated intensity and inverse correlation length (peak width) to be measured as a function of temperature, requiring accurate, stable, temperature control. Until recently this has required that measurements of such systems be undertaken exclusively at synchrotron X-ray sources which intrinsically have the high wavevector resolution and high intensity required. In this Chapter the design, construction and initial results obtained with a focusing optics diffractometer operating on a rotating anode X-ray generator are described. The success of this now makes it possible to study charge ordering at low temperatures using a laboratory based diffractometer. This system was designed to give the maximum flux possible for the observation of weak X-ray scattering from oxide crystals. Typically these crystals, which are grown using flux growth, have rocking curve widths no better than 0.05° - 0.5°. These are much larger than those encountered typically in semiconductor samples such as silicon or germanium. Such samples are often employed as monochromator or analyser materials giving a wavevector resolution of $\sim 10^{-4}$ Å^{-1}. This has been standard on synchrotron sources as the rocking curve width of Si (111) is close to that of the natural vertical beam divergence. However, on a standard laboratory-based source the X-rays emerge from the target with a very large divergence and the use of such monochromators results in a well conditioned parallel beam, but a large intensity penalty, as the beam conditioner passes only a fraction of the X-rays from the source. Traditionally, other wider-band pass monochromators such as pyrolytic graphite (0001) have been used instead. However,

the rocking curve width is approximately 0.3° which is sufficiently large that measurement of intrinsic inverse correlation lengths is impossible; rather, the peak widths are then dominated by the instrumental resolution rather than by the sample. Simultaneously high intensities (so that weak charge scattering can be observed) and higher resolution are required so that intrinsic peak widths can be measured. The result of this Chapter is a diffractometer which has been optimised for the study of such systems providing a factor of 10 increase in intensity and a factor of 7.5 improvement in resolution. The result is a diffractometer that is close in performance to that of an unfocussed diffractometer at a second-generation synchrotron.

The great increase in intensity is obtained by focusing the largely divergent source from the target onto the sample. Recently, advancements in thin film growth techniques have enabled the development of graded d-spacing parabolic mirrors, which act as focusing devices for a point source of X-rays. These Göbel mirrors (Schuster and Gobel, 1995), named after the researcher who popularised their use, collect X-rays over a much greater solid angle from the source and focus the X-rays into a quasi-parallel beam. The resultant beam can be further conditioned by means of a Bragg diffracting crystal. To retain a higher beam divergence it is possible to cut a single crystal asymmetrically to increase the band-pass. We have used an asymmetric, channel-cut germanium crystal to condition the beam, with a resultant divergence close to that of the mosaic spread of the sample under study. In addition, for triple crystal experiments the analyser crystal acceptance angle used should match the incident beam divergence, but at the same time have an angular acceptance small enough to allow the true width in momentum space to be

measured, without the need for deconvolution. This can be obtained by again using an asymmetric channel-cut crystal with a rocking curve width that is of the order of the incident beam divergence. A layout of the diffractometer optics system is shown in Figure 4.1.

4.2 Crossed Mirror System

Grazing incidence graded *d*-spacing parabolic mirrors have been utilised as beam conditioning optics in the diffractometer system, collimating the X-rays generated by an Enraf-Nonius FR571 rotating anode generator with a electron beam spot size of 3 mm $\times$ 300 μm impinging upon a copper target. By employing two such mirrors, one mounted vertically and the other horizontally, the mirrors accept a highly divergent X-ray beam and produce a parallel X-ray beam in both dimensions. Due to the small sample size of our single crystals, two mirrors were employed in a crossed fashion to collimate the beam into a relatively small spot size $\sim$ 1 mm in cross section at the sample position 500 mm from the second mirror. Multilayer mirrors produced by Osmic Inc. were mounted in a custom alignment system similar to that previously reported by Matyi *et al.* (2000). In our mirror box design the incident angles of both the horizontal and vertical mirror are adjusted by tangent arms, moved by micrometers driven by stepper motors. The displacements of both mirrors are adjusted by means of manual translation stages. In addition, the distance of both mirror assemblies from the source can be adjusted.

Figure 4.2 shows the mirror alignment system. The first mirror, type

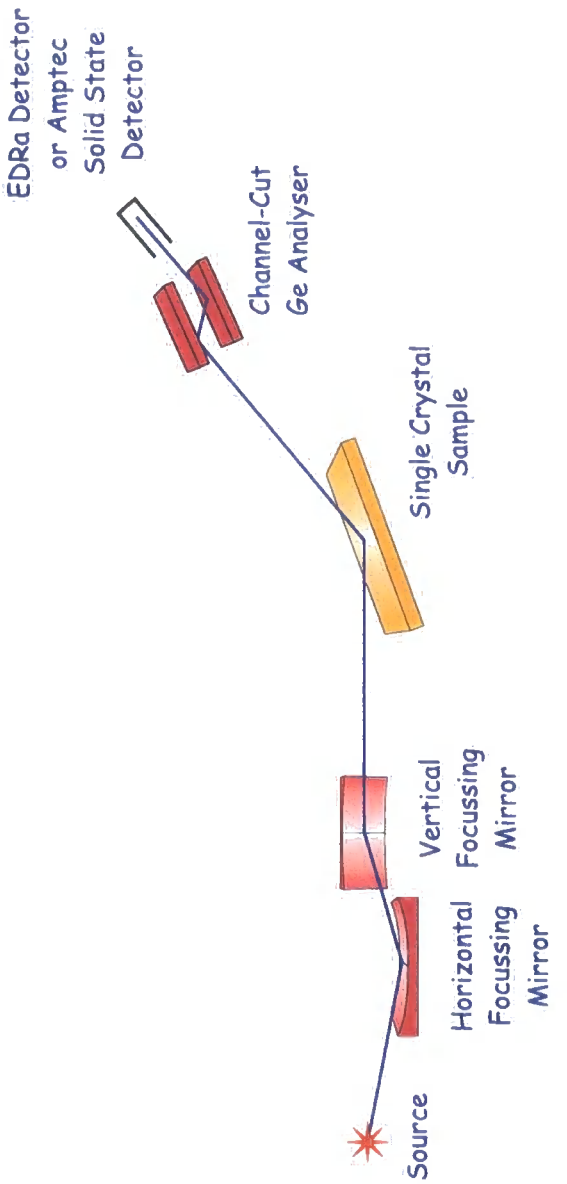

Figure 4.1: D^3 Diffractometer optical layout.

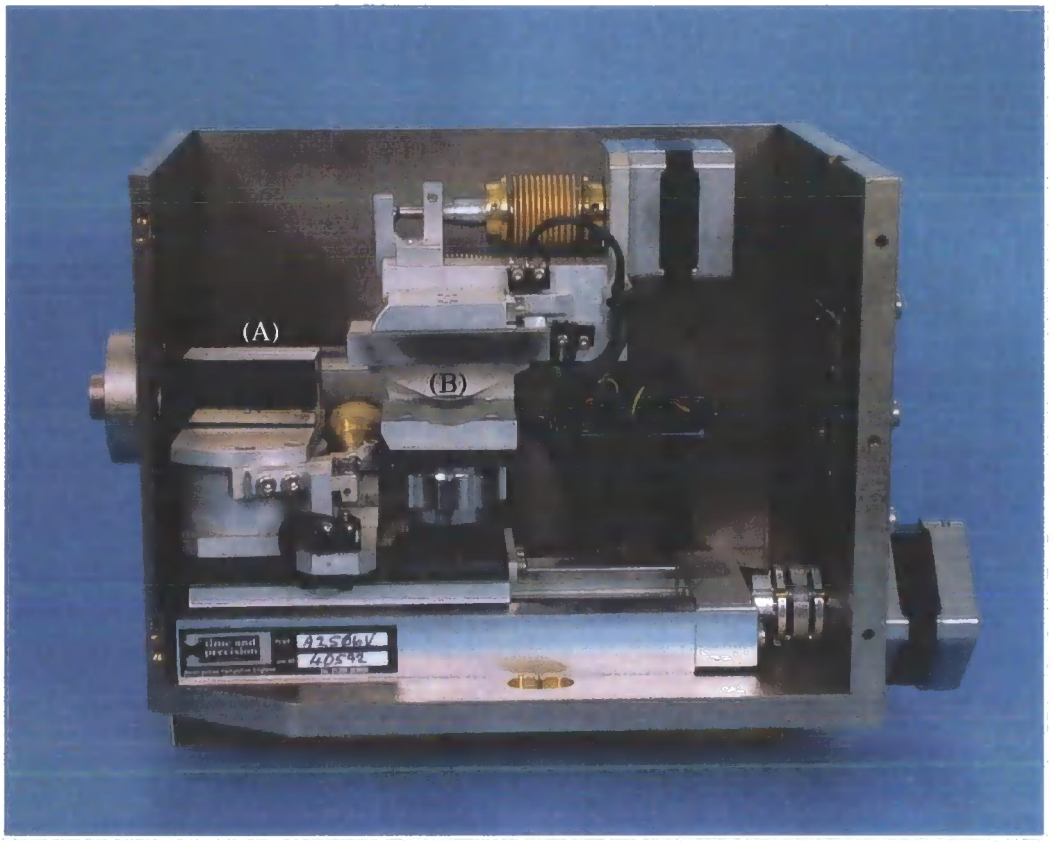

Figure 4.2: Mirror mounting and alignment system. From this picture the first mirror (GO 13) and second mirror (GO 11) are labelled (A) and (B) respectively. Divergent X-rays enter from the left of the picture from the rotating anode X-ray source and a monochromatic parallel X-ray beam emerges through a pinhole on the right hand side.

GO 13 with a central d-spacing of 45 Å and an average reflectivity of 74.6% is a W/B_4C multilayer and serves to focus the beam in the horizontal direction, diffracting the beam at a Bragg angle of 1°. The second mirror, type GO 11, has a central d-spacing of 34.88 Å and an average reflectivity of 63.4% and is a W/B_4C multilayer which focuses in the vertical plane diffracting with a Bragg angle of 1.3°. The final collimated beam emerging from the mirror system is deflected at 2.6° downwards. Alignment is made simple using a

high resolution X-ray imager produced by Photonic Science Ltd., consisting of a phosphor screen coupled to an image intensifier incident on a CCD which is capable of determining the spatial distribution of the X-ray intensity. After such initial adjustments are made, with the X-ray detector it is possible to further optimise the intensity of the X-ray beam by fine-tuning the angular settings of both mirrors. This process is achieved very easily due to the motorisation of the angular adjustments of the mirrors. In addition, this allows for further optimisation at a later date, without the need to dismantle any equipment.

The beam divergence in the diffraction plane was measured by measuring the full width at half maximum of the (0, 0, 4) rocking curve on a silicon [0, 0, 1] wafer, the results of which are shown in Figure 4.3. From this, it is apparent that the spectral purity of the beam is high, with only the $K\alpha_1$ and $K\alpha_2$ characteristic lines present. By fitting the measured rocking curve to two Gaussian peaks, the divergence of the incoming beam was determined to be 0.0626° as measured on the $K\alpha_1$ peak.

4.3 Beam Conditioning Optics

Upon commissioning the diffractometer system, the measured beam divergence in the diffraction plane was found to be adequate without the need for further beam conditioning. This has several advantages over the traditional use of further beam conditioning crystals that would substantially decrease the beam flux at the sample. One major disadvantage apparent from Figure 4.3 is the presence of $K\alpha_2$ in the incident beam which causes

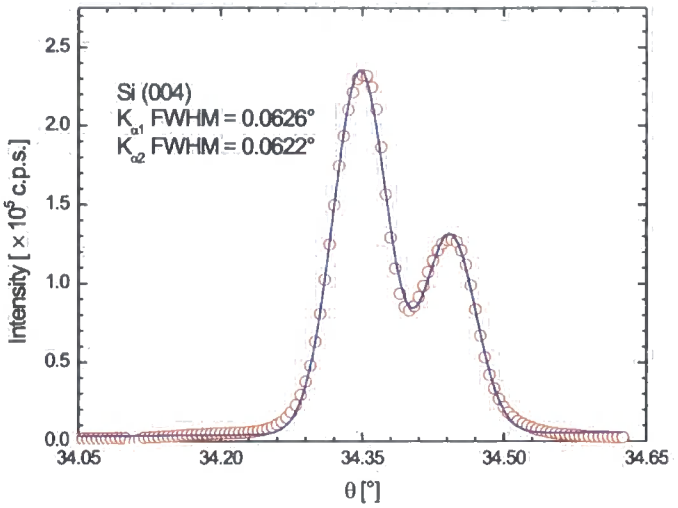

Figure 4.3: Silicon (0, 0, 4) rocking curve measurement to measure the beam divergence. The solid line is a fit to two Gaussian lineshapes.

doublets to appear in diffraction patterns. However, this can be reduced for double crystal measurements by the addition of a 500 μm slit before the detector. For triple crystal measurements an asymmetric channel-cut Ge crystal in non-dispersive (+,-) geometry was used, the theoretical rocking curve of which is shown in Figure 4.4 calculated using the XOP (Sanchez del Rio and Dejus, 2001) suite of programs. The intrinsic rocking curve width of symmetrical (2, 2, 0) germanium is too low to be of utility for our system. By cutting the crystal with an off-cut angle of 19.7°, resulting in an incident angle of 3°, the rocking curve full width at half maximum is increased by a factor of ~ 4. This results in a vastly greater intensity. The crystal was prepared by Crystal Scientific Limited.

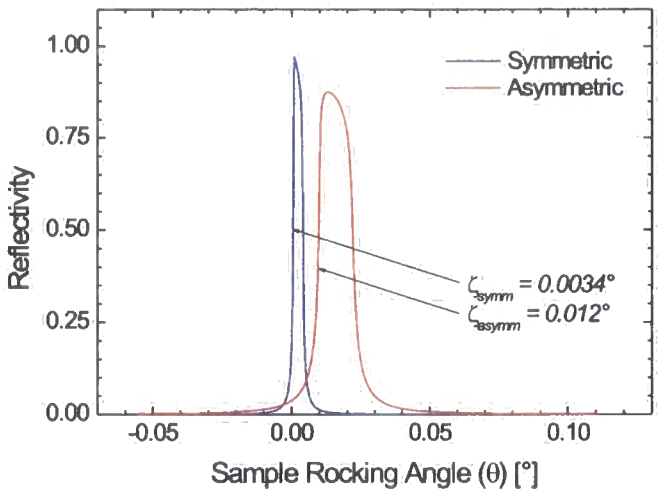

Figure 4.4: Theoretical prediction of Ge (2, 2, 0) analyser rocking curve.

4.4 Diffractometer System

The goniometer system was a modified Bede Scientific Instruments Ltd. D^3 system. This system consists of a four-circle triple crystal goniometer operated under computer control via a Minicam 3 and Unidex motor control units. The 2θ- and θ-axes are driven using encoded servo-motors allowing for rapid movements with a precision of $\pm$ 0.055". Other axes are driven by means of 4-phase and 5-phase stepper motors. Novel to this instrument is the addition of a cryostat sample stage. Using a micro-miniature refrigerator developed by MMR Ltd., temperatures down to 90 K are possible using high-pressure argon gas, cooling by means of Joule-Thompson expansion. This cryostat system cools to a base temperature of 90 K in approximately 30 minutes including the added heat-load of the Cu sample mounts. The temperature

can be controlled via a standard temperature controller to $\sim$ 0.1 K, stable over the typical time-frame of an experiment.

4.5 Detector System

Gains in signal and thus in the smallest detectable signal, can not only be obtained by increasing the incident flux but also by the lowering of the intrinsic shot noise limit within the detector. This can be achieved in two main ways. Firstly, it is possible to shield heavily the incident beam using collimators and slit assemblies resulting in only the reflected beam incident upon the sample. However, the main problem of fluorescence from the sample cannot be reduced in this fashion. Secondly, traditional laboratory-based systems have relied heavily on the use of scintillation detectors, which while offering high dynamic range, suffer from a relatively high intrinsic noise level. In addition, the level of incident X-ray energy discrimination is poor, leaving it difficult to differentiate between elastic scatter from the sample and fluorescence from the sample excited by the high flux from the incident beam. Solid-state germanium detectors offer an ideal solution as they have very high energy resolution coupled with a very low background level; however, the need for liquid nitrogen coolant restricts their use due to their physical size. In the last few years there have been a number of Peltier cooled solid-state detectors available on the market. Due to their small size (comparable with that of scintillation detectors) they can be easily integrated into a laboratory diffractometer. We have used a detector developed by Amptek Ltd. that offers an energy resolution of 186 eV with a physical size of 123 x 44

x 23 mm. The Amptek detector has been found to reduce the background by a factor of $\sim$ 10 with no detrimental effect on the peak intensity when gated with a single channel analyser. Another advantage of energy gating the detector system by employing pulse height analysis is that harmonic signals such as $\frac{\lambda}{2}, \frac{\lambda}{3}$ etc. can be excluded. This is of particular importance in the study of superlattice reflections existing at commensurate wavevectors where harmonic contamination from Bragg reflections may be severe.

To provide an indication of the system intensity, a scan was carried out on the weak silicon (222) reflection using the Amptek detector to eliminate harmonic interference from the Si (111) reflection. The rocking curve is shown in Figure 4.5. The Si (222) reflection had an intensity of $\sim$ 1400 counts per second in double-crystal mode, when the generator was operating at 40 kV and 75 mA.

4.6 Software

Using in-house software which employs the use of the $\boldsymbol{UB}$ matrix, first described by Busing and Levy (1967) it is possible to transform between direct space diffractometer angles (2θ, θ, χ and ϕ) and reciprocal lattice vectors (H, K and L). The addition of a $\boldsymbol{UB}$ matrix allows for the efficient collection of diffraction data by scanning in reciprocal space. Such measurements, often being more physically relevant, allow for the easy analysis of data collected by the diffractometer system. Using in-house software we have coded the H, K and L directions for any crystal and the Q_x and Q_z directions as pseudo motors. This enables scans to be taken as easily in these directions as scan-

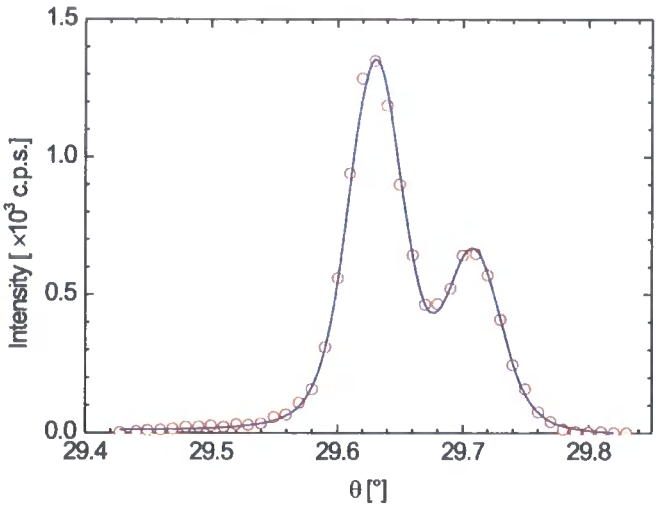

Figure 4.5: Silicon (2, 2, 2) rocking curve measured with the Amptek solid state detector measured in double crystal geometry (no analyser crystal).

ning a traditional motor axis. In addition to the traditional one-dimensional scans, by the method of loop scanning (i.e. scanning in one direction and then subsequently incrementing in another) it is possible to collect efficiently two-dimensional reciprocal space maps. Such maps are very useful for a visual representation of the scattering in reciprocal space.

4.7 Charge Ordering

To test the performance of the system, measurements were made on a previously studied sample of $Bi_{0.24}Ca_{0.76}MnO_3$ (Su *et al.*, 1999). This sample was indexed in the orthorhombic *Pbnm* setting, with $a \approx b \approx \sqrt{2}a_p$ and $c \sim 2a_p$ where a_p is the cubic perovskite unit cell with lattice parameters

of $a \approx b = 5.335$ Å and $c = 7.512$ Å. The sample was mounted with the $\langle 1,\ 1,\ 0 \rangle$ direction normal to the scattering plane. This class of compounds undergoes a charge ordering phase transition below a characteristic temperature $T_C \approx 240$ K. Due to the segregation of mobile holes, superlattice reflections appear below T_C at a modulation wavevector of $(\epsilon,\ 0,\ 0)$ due to a distortion associated with the charge order and at $(2\epsilon,\ 0,\ 0)$ due to the Mn^{3+} / Mn^{4+} ordering pattern. In the sample $\epsilon = 0.25$, related to the hole density via the sample stoichiometry and superlattice reflections are seen at modulations of $\left(\frac{1}{4},\ 0,\ 0\right)$ and $\left(\frac{1}{2},\ 0,\ 0\right)$ for the structural modulation and the real charge ordering respectively. A fuller description of this is given in Chapter 3 which uses polarised synchrotron radiation to study the charge and orbital ordering.

The sample was mounted in the $\langle 1,\ 1,\ 0 \rangle$ / $\langle 1,\ \bar{1},\ 0 \rangle$ zone and was cooled to 90 K in the Joule-Thompson cryostat. The rotating anode generator was operated at 40 kV and 75 mA, resulting in a power output of the generator of 3 kW with a focal spot of 0.3 mm × 3 mm (fine focus). The source was focused using the crossed parabolic mirrors and no further monochromation was used. For the triple crystal measurements the asymmetric channel-cut Ge (2, 2, 0) analyser was used with two 2 mm slits in front of the detector and analyser crystal to reduce the background. Measurements were carried out using a Bede Scientific Instruments EDRa scintillation detector as described by Cockerton *et al.* (1995) except in stated instances where the Amptek detector was used for the higher performance available. To demonstrate the suitability of the system for our crystals, a comparison of the widths of the silicon (0, 0, 4) Bragg peak and the $Bi_{0.24}Ca_{0.76}MnO_3$ (2, 2, 0) Bragg peak

in the $Q_{\|}$ direction, in triple-crystal geometry is shown in Figure 4.6. In order to maximise the intensity we aimed to match the incident beam divergence to the rocking curve width of transition metal oxide crystals. This allows the observation of weak superlattice peaks without significant broadening. Figure 4.6 demonstrates that the instrumental resolution is less than the sample rocking curve width, allowing a determination of inverse correlation lengths after suitable deconvolution of the resolution function. To compare the differences between the system presented here and our previous diffractometer employing a graphite monochromator and analyser set, scans were undertaken on the (2, 2, 0) Bragg peak in the ⟨ 1, 1, 0 ⟩ direction which

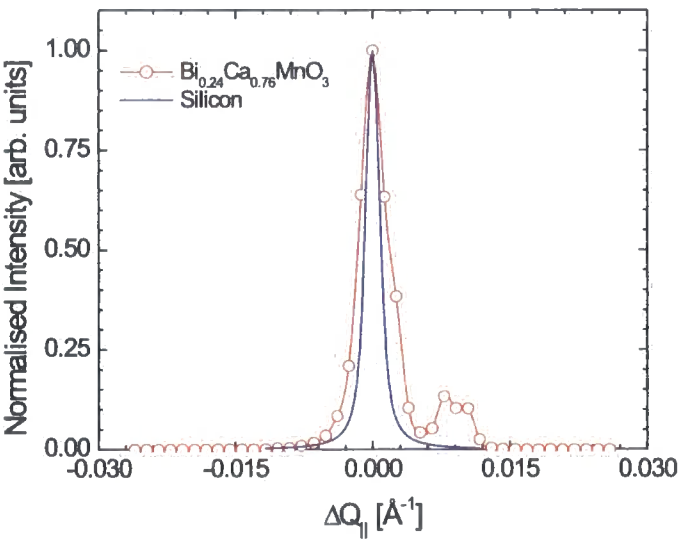

Figure 4.6: Comparison between the widths of the silicon (0, 0, 4) peak (blue) and the $Bi_{0.24}Ca_{0.76}MnO_3$ (2, 2, 0) Bragg peak (red) measured in the $Q_{\|}$ direction

corresponded to the longitudinal direction ($Q_{\|}$). The measured width of the (220) reflection with the graphite optics was found to be $Q_{\|} = 0.03$ Å^{-1} whereas the measured width on the new diffractometer was found to be $Q_{\|} = 0.004$ Å^{-1}, an increase in resolution of a factor of 7.5. This comparison is shown in Figure 4.7.

In addition, the peak lineshape measured with the graphite optics is a Gaussian function whereas the peak lineshape measured on the new system employing mirrors is a Lorentzian shape. This indicates that the previous measurements were resolution limited whilst the new measurements are not heavily dominated by the resolution function.

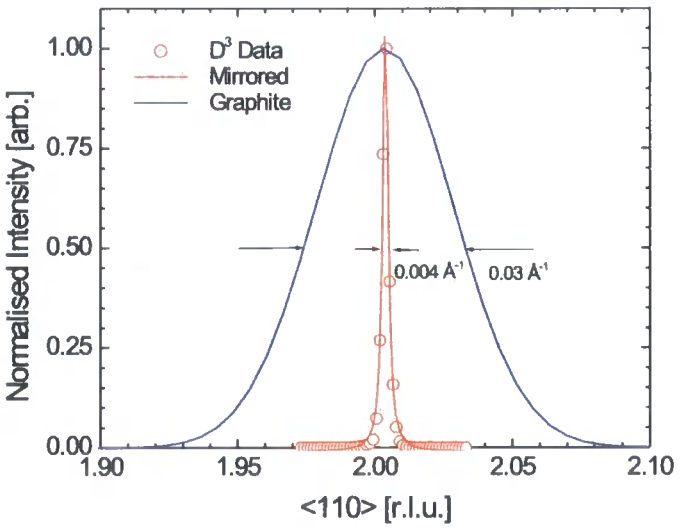

Figure 4.7: Comparison of the widths of the (2, 2, 0) Bragg peak in BCMO. The red line shows a fit of the measured width with the mirrored diffractometer. The blue line is a fit to previous data measured using a diffractometer with graphite optics (CPEX) .

Superlattice reflections were located at (2.25, 2, 0), (1.75, 2, 0)), (2, 1.75, 0) and (2, 2.25, 0) and the intensity and width of each was measured. The strongest was found to be at (2, 1.75, 0) and the temperature dependence of the integrated intensity and width of the satellite was measured in the temperature range 90 K to 250 K, the results of which are shown in Figure 4.8.

A reciprocal space map around the (2, 2, 0) Bragg peak was constructed in the $\langle 0,\ k,\ 0 \rangle$ / $\langle h,\ 0,\ 0 \rangle$ plane of reciprocal space with scans being carried out in the K direction while incrementing in H. The resultant reciprocal space map covering the range 1.7 to 2.3 reciprocal lattice units is shown in Figure 4.9, and the four satellite reflections can be seen clearly surrounding

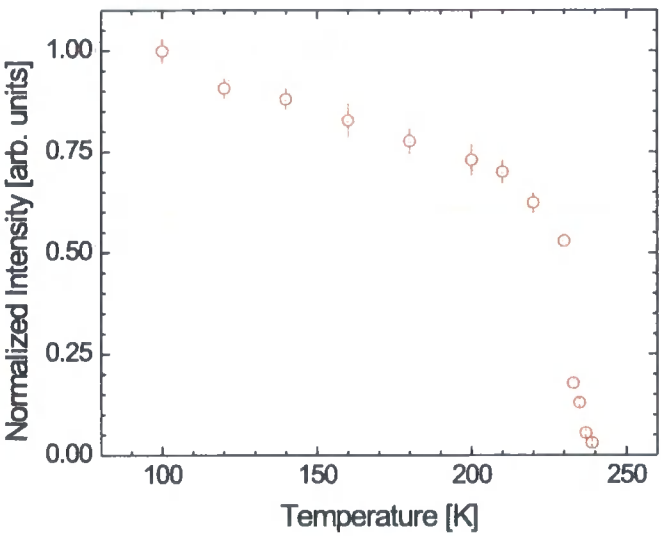

Figure 4.8: Temperature dependence of the (2, 1.75, 0) Jahn - Teller distortion superlattice peak.

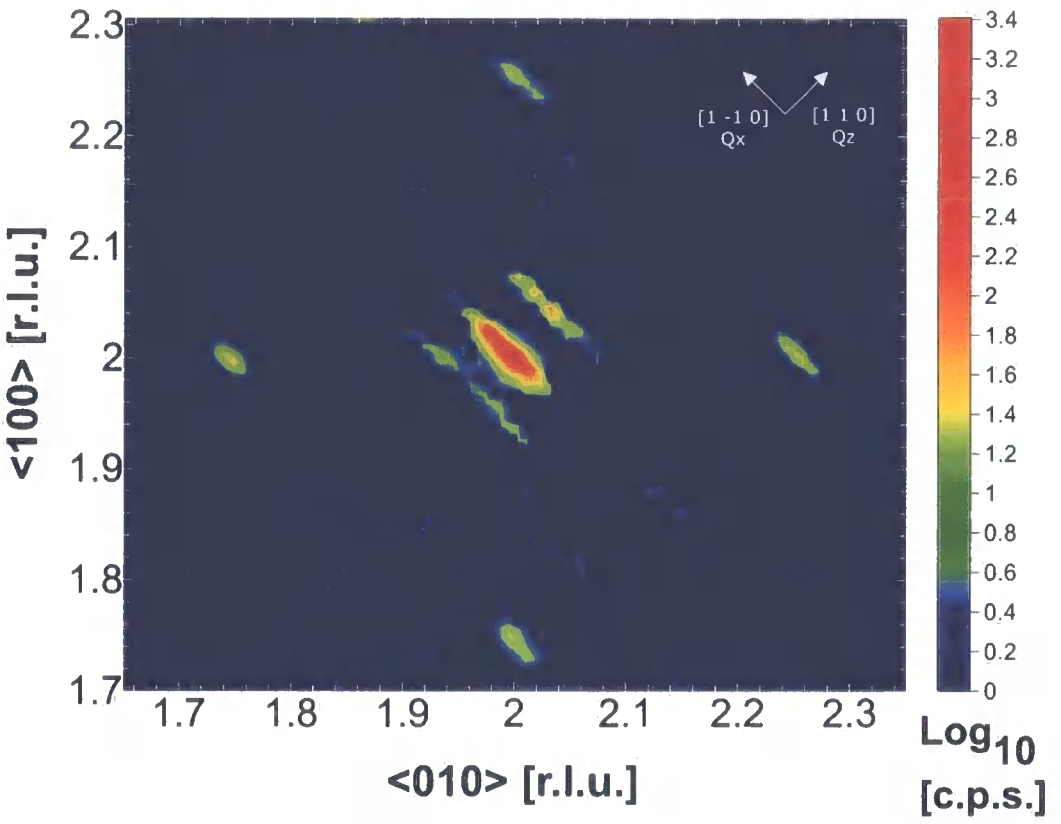

Figure 4.9: Reciprocal space map of the charge distortion superlattice peaks surrounding the (2, 2, 0) Bragg peak from $Bi_{0.24}Ca_{0.76}MnO_3$. The intensities are displayed on a pseudo-logarithmic scale as shown on the right of the map.

the central Bragg peak both vertically (at (1.76, 2, 0) and (2.24, 2, 0) and horizontally (at (2, 1.76, 0) and (2, 2.24, 0)). In addition satellites due to the twinning of the crystal in its low temperature orthorhombic phase can be seen next to the central Bragg peak. Figures 4.10 and 4.11 show the central portion of the map in Figure 4.9 on the (2, 2, 0) Bragg peak as a function of temperature. The transition from the low temperature orthorhombic phase into the tetragonal phase can be seen to evolve.

In addition to the weak structural modulation present in these samples,

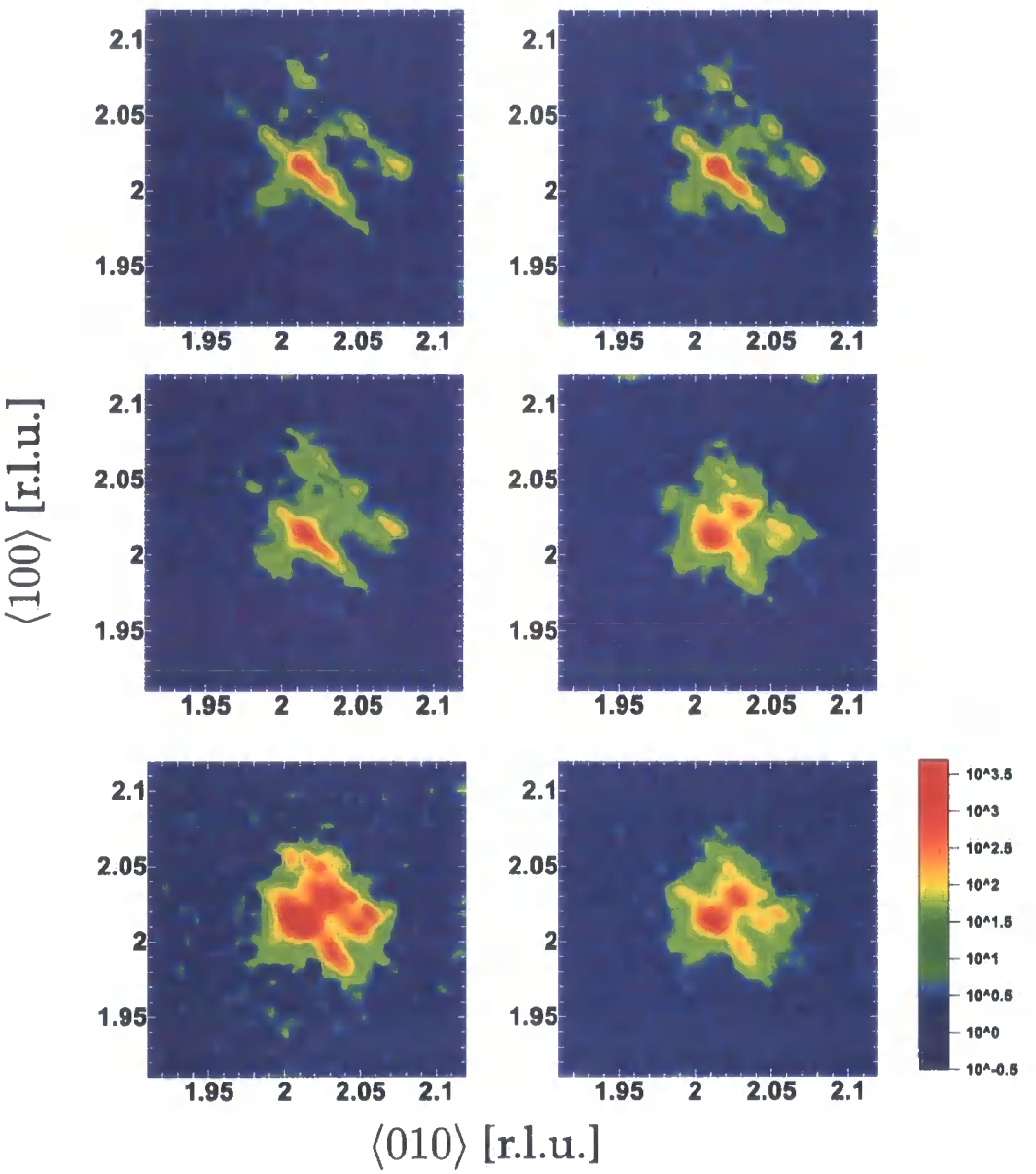

Figure 4.10: Reciprocal space maps in the ⟨1, 0, 0⟩ / ⟨0, 1, 0⟩ zone of reciprocal space on the (2, 2, 0) Bragg reflection. The temperature of the maps is (from top left to bottom right) 225 K, 230 K, 234 K, 236.5 K, 237.5 K and 238.5 K.

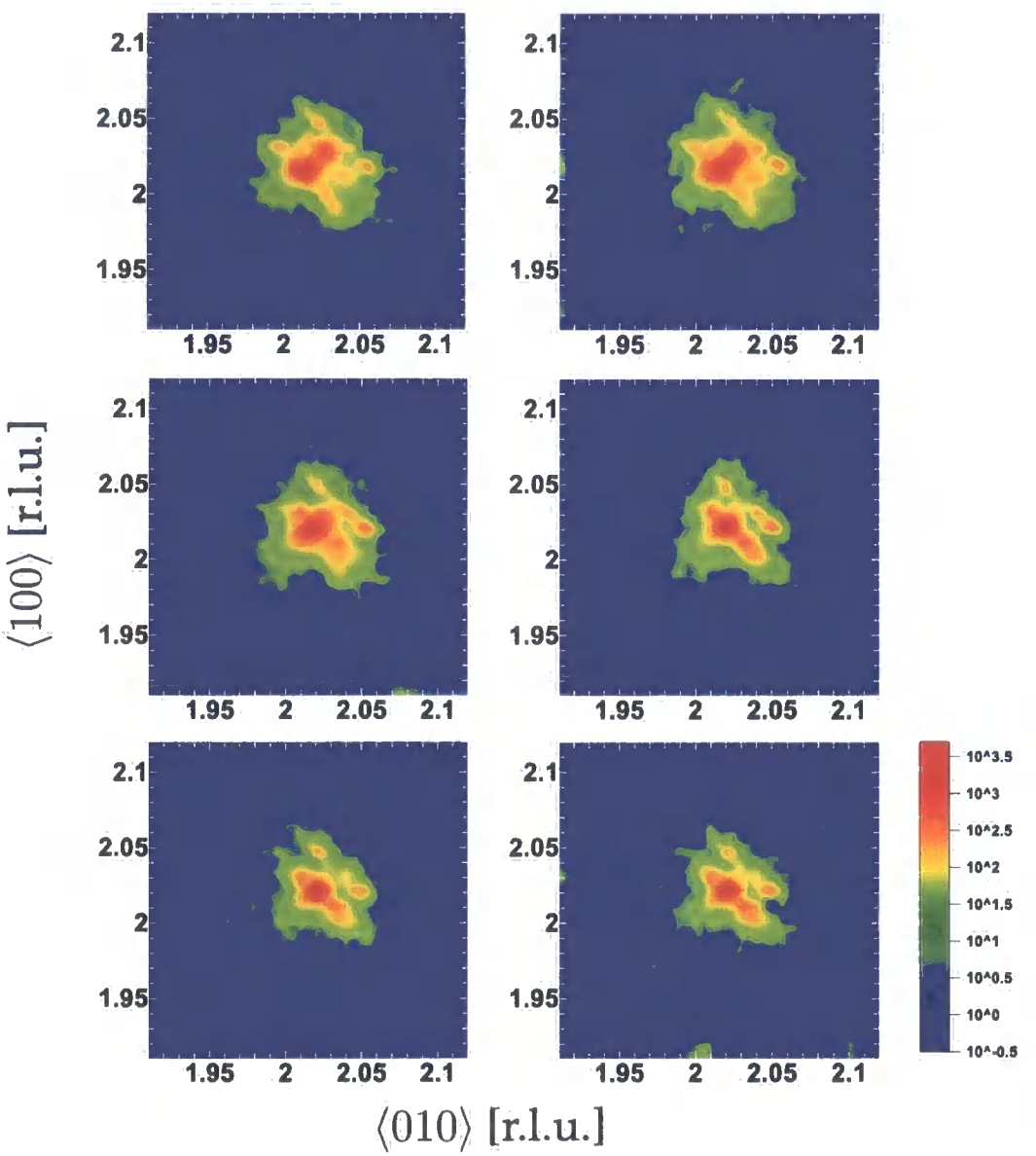

Figure 4.11: Reciprocal space maps in the ⟨1, 0, 0⟩ / ⟨0, 1, 0⟩ zone of reciprocal space on the (2, 2, 0) Bragg reflection. The temperature of the maps is (from top left to bottom right) 239.5 K, 241 K, 242 K, 247 K, 250 K and 255 K.

there exist superlattice reflections due to the charge ordering, resulting from the Mn^{3+} / Mn^{4+} ordering pattern. The scattering at such reflections is, at maximum, due to one electron difference in the scattering factors. Such measurements have only been possible using resonant X-ray scattering at third generation synchrotron sources before now. The observation of such weak phenomena provides a unique challenge for laboratory based X-ray facilities. Having previously located such reflections (Su *et al.*, 1999) we have undertaken measurements using the diffractometer system presented in this paper. Figure 4.12 shows a scan taken on the (2, 1.5, 0) superlattice reflection corresponding to the charge order. Such a peak was found to be very weak ($\sim$ 0.4 counts per second) but using both the asymmetrically cut

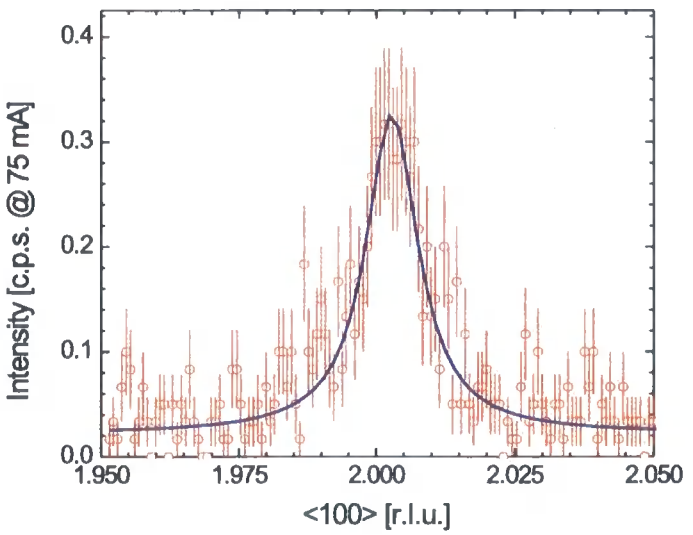

Figure 4.12: Scan along the $\langle 1,\ 0,\ 0 \rangle$ direction through the charge order superlattice peak at (2, 1.5, 0). The solid line is Gaussian a fit to the experimental data.

Ge analyser and the Amptek solid state detector it has been possible to reduce the background sufficiently to observe comfortably the reflection with signal to noise greater that 3σ.

4.8 Conclusions

This Chapter has presented the development of a novel laboratory-based diffractometer optimised for high-intensity and resolution matched to that of flux grown single crystal transition metal oxide samples under study in this thesis. This has been implemented using crossed graded d-spacing parabolic multilayer mirrors, a severely off-cut asymmetric analyser crystal and a micro-miniature cryostat. It has been demonstrated that the wider bandpass of the multilayer mirrors provides a significant increase in intensity compared to the use of silicon and germanium optics, but still provides the necessary resolution to obtain accurate measurements for inverse correlation lengths. The increase in flux allows the observation of features that were previously only visible with third generation synchrotron X-ray sources, shown by the observation of the very weak charge order peak without the use of a synchrotron source. Results on samples previously studied show an increase of a factor of 10 in intensity, coupled together with a factor of 7.5 increase in resolution over the previous system employed using a rotating anode source and flat pyrolytic graphite (0001) crystals. With such a diffractometer it has been now possible to carry out detailed studies of charge ordering in transition metal oxides in the laboratory and the benefits of this are three-fold. Firstly, this will improve the quality of any preparation work, for subsequent

experiments at synchrotron sources. This has the advantage of maximising the efficiency of synchrotron measurements. Secondly, the enhanced intensity and resolution will allow experiments to be conducted in the laboratory which previously required access to synchrotron sources. Thirdly, it will allow for synchrotron time to be used for its unique properties i.e. wavelength tunability and polarisation, which is necessary for the observation of magnetic reflections and orbital ordering by means of resonant enhancements and polarisation analysis. This means that laboratory based measurements are easily incorporated with synchrotron data, maximising the potential of both techniques and receiving a net gain in data output.

Chapter 5

An X-Ray Diffraction Study of Charge and Jahn - Teller Order in $La_{2-2x}Sr_{1+2x}Mn_2O_7$, $x = 0.475$

5.1 Introduction

The layered manganite materials $(La,Sr)_{n+1}Mn_nO_{3n+1}$ ($n = 2$) exist as a modification to the basic perovskite structure previously studied in Chapter 3, which can be classed as the $n = \infty$ type. These materials show a variety of novel phenomena due to the decrease in dimensionality of the system.

The dimensionality of these systems is reduced by the introduction of a rock-salt-type layer ($(La,Sr)_2O_2$) every n MnO_2 sheets, resulting in the structure $(La,Sr)_{n+1}Mn_nO_{3n+1}$. The $n = 1$ system forms a K_2NiF_4 type structure, with the $n = 2$ system forming a "bilayer" structure. By varying

the ratio of La to Sr it is possible to dope in holes to the system by the substitution of Sr ions onto the La sites.

Magnetic and resistivity measurements by Moritomo *et al.* (1996) on samples of $La_{1.55}Sr_{0.45}MnO_4$ and $La_{1.1}Sr_{1.9}Mn_2O_7$ found very surprising results. For the $n = 2$ bilayer system with a doping level of $n_h \approx x = 0.4$, where n_h is the concentration of holes, there exists a magnetic phase transition from a paramagnetic to a ferromagnetic state at a temperature of 150 K. This was in stark contrast to the $n = \infty$ system where the paramagnetic - ferromagnetic phase transition occurs at a temperature of 350 K in $La_{0.6}Sr_{0.4}MnO_3$. Further, the resistivity measurements show a drop greater than two orders of magnitude at the transition from the paramagnetic phase into the ferromagnetic phase. There exists a large anisotropy of the charge carriers, indicated by a difference of approximately two orders of magnitude in the resistance in the $a-b$ plane and in the perpendicular direction along the c-axis. Figure 5.1 shows the resistivity of a number of manganite compounds as a function of temperature. (taken from Kubota *et al.*, 1999)

Measurements of the magneto resistance (MR), the ratio of the change in resistance upon the application of a magnetic field ($\rho_{ab}(H)/\rho_{ab}(0)$) on the $n = 2$ system at 129 K show a very large MR effect, over two orders of magnitude. This is far greater than that observed in the $n = \infty$ series of compounds, which is shown in Figure 5.1. However, it is worth noting that this increase in MR is achieved at the cost of a decrease in T_c, but the magnetic field required to 'switch' the system is greatly reduced in the $n = 2$ system. This suggests that the $n = 2$ reduced dimensionality systems could have possible technological possibilities as a magnetic sensor.

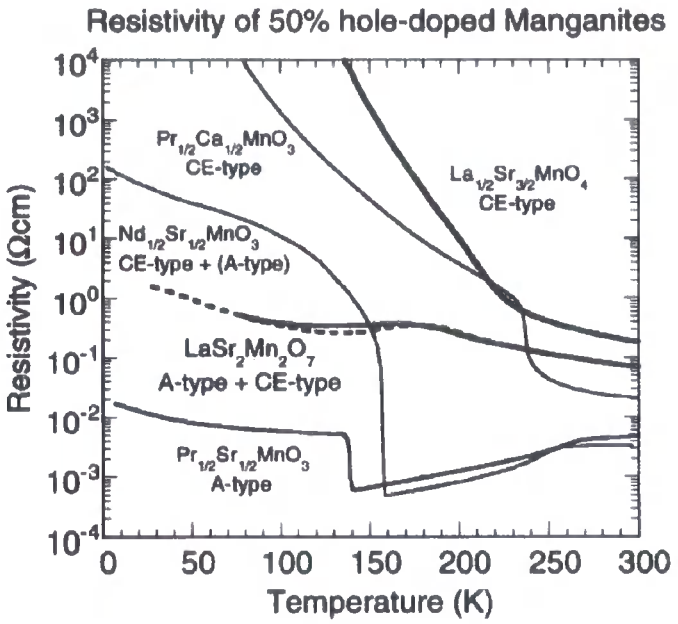

Figure 5.1: Resistivity vs. temperature for a number of perovskite manganite compounds. (Taken from Kubota *et al.*, 1999)

Since the discovery of the MR effect in these systems many theories have been suggested as the cause. The MR is strongest when the temperature of the system is just above T_C. It is at this point that the system is subject to competing instabilities involving the double-exchange interaction. Possible mechanisms which have been suggested include antiferromagnetic superexchange, electron lattice interactions which includes the Jahn-Teller effect and charge ordering interactions. With such a vast array of possible mechanisms it is clear that much research has to be undertaken to solve some of the questions posed. For a general introduction to the manganite series of compounds the reader is referred to the introduction of Chapter 3.

The structure of the bilayer manganite $La_{2-2x}Sr_{1+2x}Mn_2O_7$ is shown in

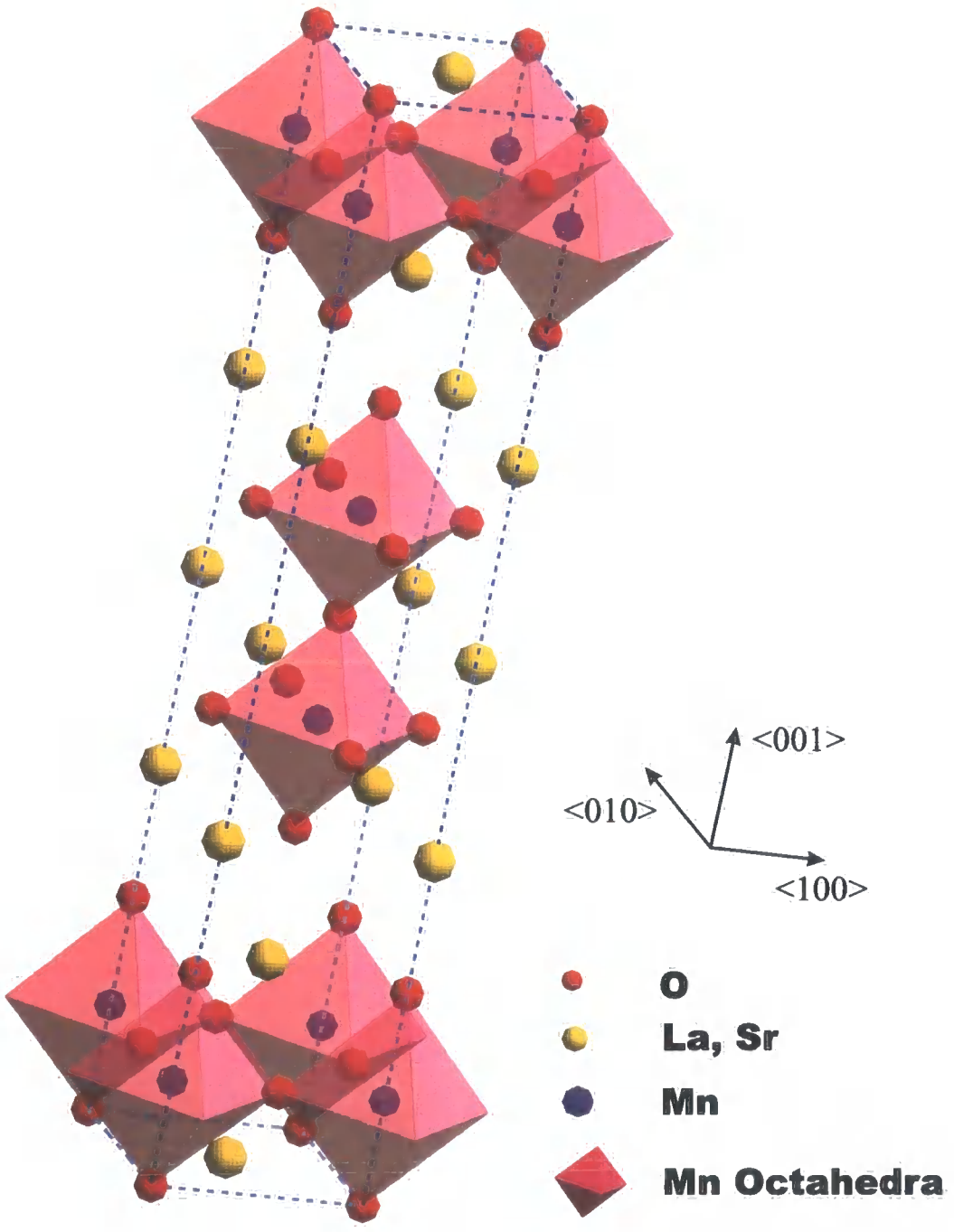

Figure 5.2: Crystal structure of the Ruddelston-Popper bilayer manganite $La_{2-2x}Sr_{1+2x}Mn_2O_7$.

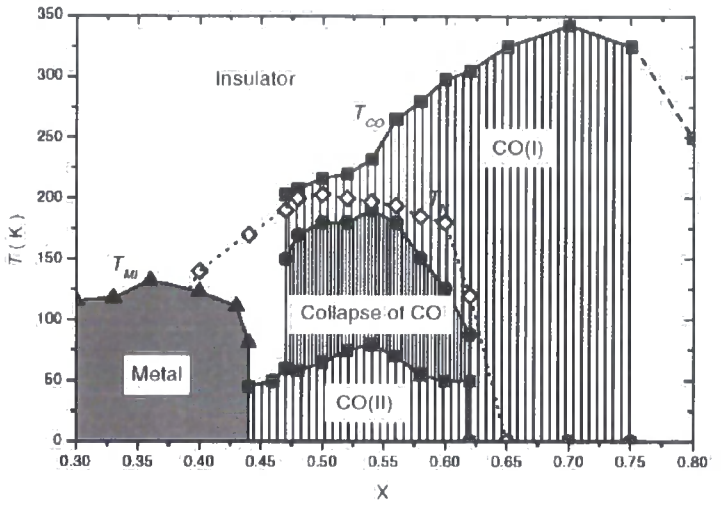

Figure 5.3: The phase diagram of $La_{2-2x}Sr_{1+2x}Mn_2O_7$ as a function of temperature and composition, x. Filled symbols are from transport data and open symbols are from previously reported values. Filled squares and triangles represent T_{CO} and T_{MI}, respectively. Taken from Dho *et al.* (2001)

Figure 5.2. The manganese - oxygen octahedra are shown by the purple polyhedra with the oxygens as the red spheres at the apices. The lanthanum / strontium sites are shown as the yellow spheres.

A comprehensive study of the transport and magnetic behaviour of the $La_{2-2x}Sr_{1+2x}Mn_2O_7$ series of compounds was undertaken by Dho *et al.* (2001). They measured both the charge order and metal-insulator transition temperatures as a function of the hole doping, x. They found that in the region $0.47 \leq x \leq 0.75$ the bilayer manganite displayed, upon cooling below a transition temperature T_{CO}, charge ordering indicated by a upturn in the resistivity verses temperature behaviour. The transition temperature indicated by this method for the $x = 0.5$ sample is consistent with X-ray diffraction data by Wakabayashi *et al.* (2000) which will be discussed later. In addition

in the doping region $0.47 \leq x \leq 0.62$ a 're-entrant' form of the charge order was found which coincides with the region of A-type antiferromagnetic order, indicated on Figure 5.3 by open diamonds.

Li *et al.* (1998) reported both electron diffraction measurements and direct space imaging of a single crystal of $La_{2-2x}Sr_{1+2x}Mn_2O_7$ with $x = 0.5$. The electron diffraction at low temperature displayed superlattice reflections at positions $\boldsymbol{Q} = \left(\frac{1}{4}, \frac{1}{4}, 0\right)$ surrounding each reciprocal lattice point. These superlattice peaks appeared to be commensurate in nature and appeared when the sample was cooled below 200 K. They attributed these superlattice reflections to be due to charge ordering. Figure 5.4 shows the electron diffraction images obtained. In Figure 5.4(c) two sets of diffraction spots can be seen running along the $\langle 1, 1, 0 \rangle$ and $\langle \bar{1}, 1, 0 \rangle$ directions which they suggested to be two charge ordered domains which had previously been seen in various manganite systems by electron diffraction. They reported re-entrant behaviour of the charge order, with the superlattice reflections appearing first at 220 K and then disappearing upon further cooling to 100 K. In addition they report resistivity measurements which showed a similar type of re-entrant behaviour of the resistivity.

The work of Kimura *et al.* (1998) reported the same findings as Li *et al.* (1998) with superlattice reflections appearing at $\boldsymbol{Q} = \left(\frac{1}{4}, \frac{1}{4}, 0\right)$ which are re-entrant in behaviour over the same temperature range.

The attributation of the superlattice peak at $\boldsymbol{Q} = \left(\frac{1}{4}, \frac{1}{4}, 0\right)$ to CO raises a number of problems when trying to fit it to the model proposed by Goodenough (1955). Here the superlattice reflections due to the CO should appear at a modulation of $\boldsymbol{Q} = \left(\frac{1}{2}, \frac{1}{2}, 0\right)$, corresponding to the 'checkerboard' type

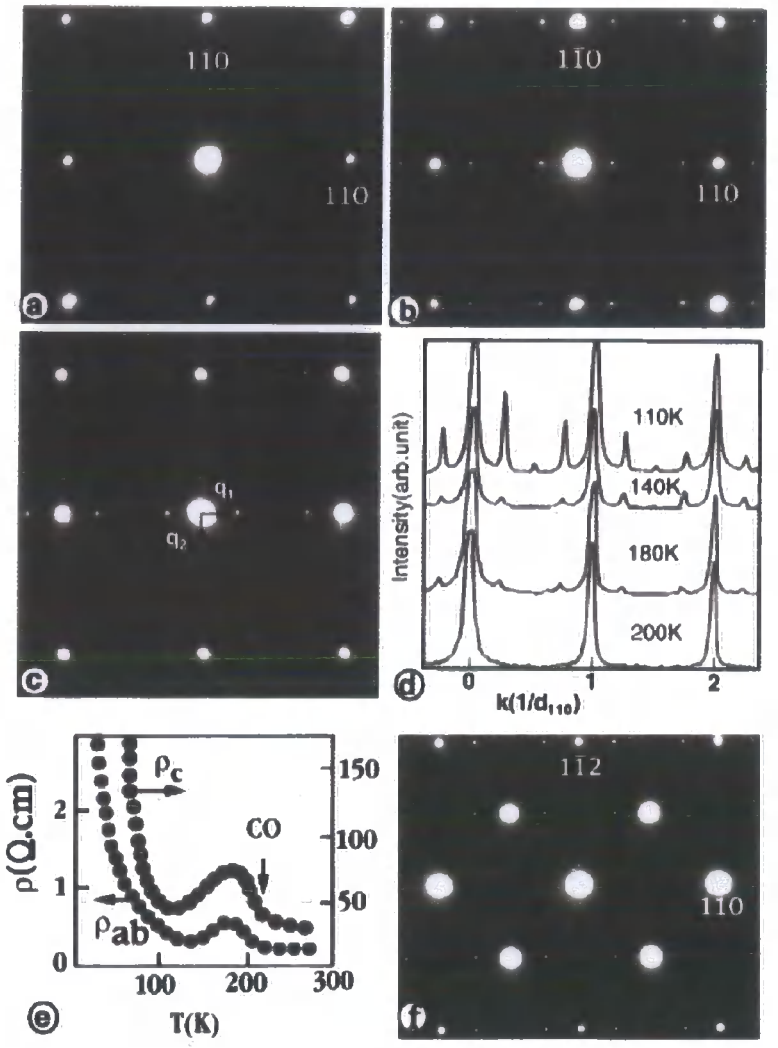

Figure 5.4: [001] zone-axis electron diffraction patterns of $LaSr_2Mn_2O_7$ obtained at (a) 300 K and (b) 110 K, respectively. (c) Electron diffraction image at 110 K showing twin domains. Microphotometric density curves along the a^* b^* direction. (e) Temperature dependance of the resistivity of $LaSr_2Mn_2O_7$ (f) [111] zone-axis diffraction pattern. (Taken from Li *et al.*, 1998)

ordering in direct space of the Mn^{4+} / Mn^{3+} species.

Chatterji *et al.* (2000) reported both high energy and resonant X-ray diffraction studies on a sample of $La_{2-2x}Sr_{1+2x}Mn_2O_7$ with $x = 0.5$. Building on the electron diffraction work previously, they reported finding superlattice reflections at a modulation of $\boldsymbol{Q} = \left(-\frac{1}{4}, \frac{1}{4}, 0\right)$ observable at 100 keV. Figure 5.5 shows the observed temperature dependance for the (0.75, 1.25, 0) reflection upon warming and cooling the sample. Again, 'the re-entrant' type behaviour of the superlattice reflections can be seen. They however, found that the reflection reappeared at approximately 40 K upon further cooling and commented that the intensity of the reflection never reached zero.

In agreement with Li *et al.* (1998) and Kimura *et al.* (1998) they at-

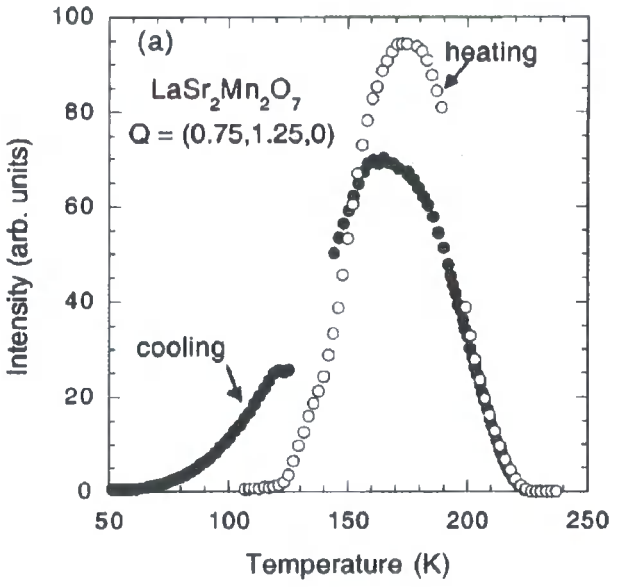

Figure 5.5: Temperature dependance of the (0.75, 1.25, 0) superlattice reflection. Taken from Chatterji *et al.* (2000).

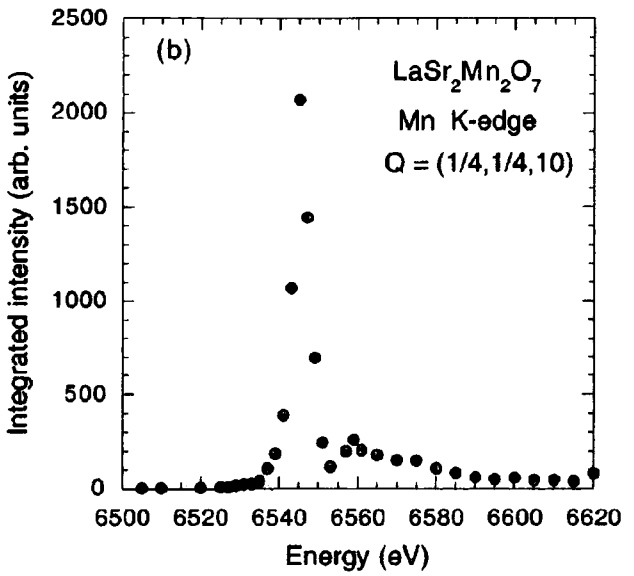

Figure 5.6: Energy resonance of the (0.25, 0.25, 10) superlattice reflection at the manganese K edge. Taken from Chatterji *et al.* (2000).

tributed the superlattice reflections at $\boldsymbol{Q} = \left(\frac{1}{4}, \frac{1}{4}, 0\right)$ to be due to the charge ordering in the sample. To account for the discrepancy between the observed wavevector for the charge order and the model proposed by Goodenough, they suggest a model in which a form of 'narrow stripe ordering' with alternating stacking along the b axis of a chain of the form Mn^{3+} - Mn^{3+} - Mn^{4+} - Mn^{4+} previously suggested by Li *et al.* (1998).

Resonant scattering at the Mn K edge was also reported on the same sample (Figure 5.6). Chatterji *et al.* (2000) found that the $\left(\frac{1}{4}, \frac{1}{4}, 10\right)$ reflection displayed a resonance when scattered $\sigma \rightarrow \pi'$. There was no observed signal away from the resonance condition. Scattering of this form is usually attributed to orbital order, as in previous work by von Zimmermann *et al.* (1999) and Murakami *et al.* (1998), being only non-zero at the absorption

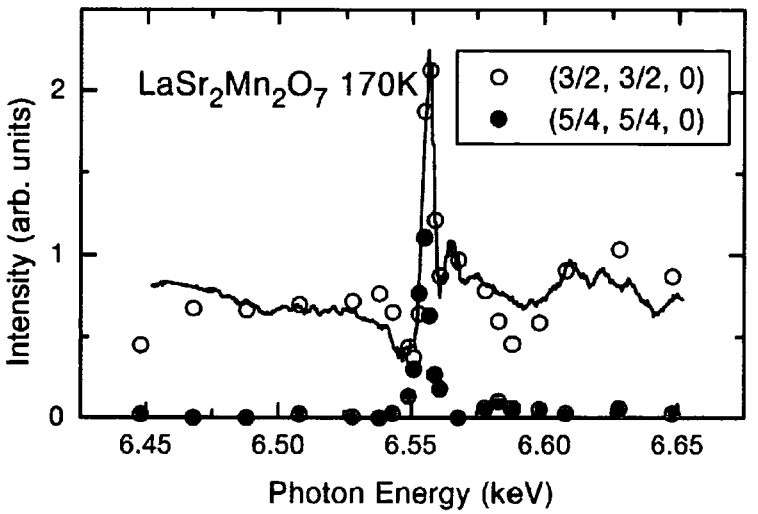

Figure 5.7: Energy dependance of the integrated intensity of charge (1.5, 1.5, 0) and orbital (1.25, 1.25, 0) superlattice reflections at 170 K at an azimuthal angle $\psi = 90°$. The solid line represents the calculated intensity of the (1.5, 1.5, 0) peak. Taken from Wakabayashi *et al.* (2000).

edge, which has no cross-section at 100 keV being far from any resonance condition. No definite conclusion as to the origin of this reflection was made. However, if this reflection is due to the orbital order then this would be in agreement with the model of Goodenough.

Wakabayashi *et al.* (2000) studied a similar sample of $La_{2-2x}Sr_{1+2x}Mn_2O_7$ with $x = 0.5$ using resonant X-ray scattering. Their investigations centred around a study of orbital and charge ordering. They presented results on resonant scattering of the charge order using the Anisotropy Tensor Susceptibility technique (ATS) previously used by the author in Chapter 3, in addition to studies of the orbital order at the Mn K-edge.

Contrary to the results of Chatterji *et al.* (2000) they reported the modulation wavevectors for the charge and orbital order are $\boldsymbol{Q_{CO}} = (\frac{1}{2}, \frac{1}{2}, 0)$

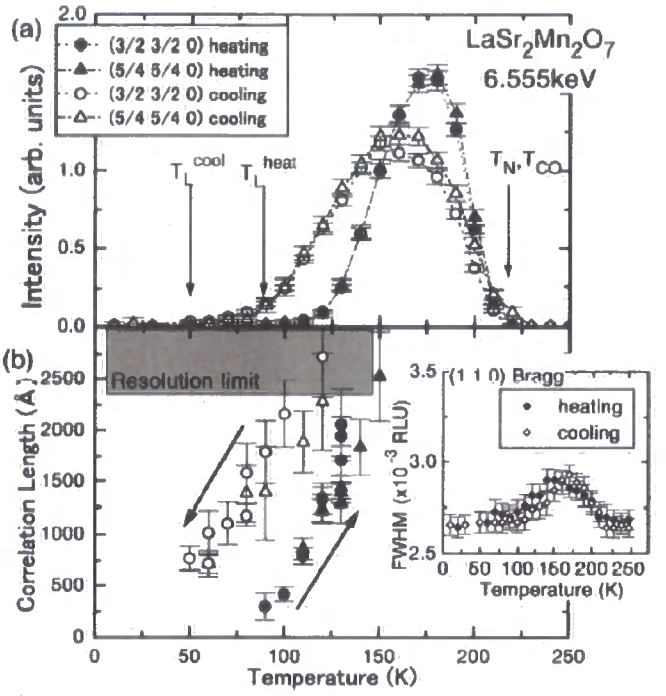

Figure 5.8: (a) Integrated intensity of the (1.5, 1.5, 0) and (1.25, 1.25, 0) superlattice reflections as a function of temperature. (b) Temperature dependance of the correlation length of the charge and orbital order. Taken from Wakabayashi *et al.* (2000).

and $\boldsymbol{Q_{OO}} = \left(\frac{1}{4}, \frac{1}{4}, 0\right)$ respectively. However it does agree with the resonant X-ray scattering that they report. Figure 5.7 shows the energy resonances obtained on their orbital and charge order reflections. They found that the charge order was scattered $\sigma \rightarrow \sigma'$ and the orbital order was scattered $\sigma \rightarrow \pi'$. This is consistent with other manganite systems as studied by von Zimmermann *et al.* (1999), Murakami *et al.* (1998) and the author in Chapter 3. The wavevectors are also consistent with the Goodenough model presented in Section 5.3.

Figure 5.8 shows the temperature dependance of the integrated intensity

of both the charge and orbital order superlattice reflections. Wakabayashi *et al.* (2000) observed the same re-entrant behaviour seen by Chatterji *et al.* (2000) with the charge and orbital order reaching a maximum at 180 K. They however did not observe any intensity below 75 K as in the case of Chatterji *et al.* (2000) or the re-emergence of the charge order below 40 K.

5.2 Summary of Previous Studies

To summarise the previous studies of charge and orbital order in $La_{2-2x}Sr_{1+2x}Mn_2O_7$ there appears to be some inconsistency in the wavevector for the orbital and charge ordering. In addition no work has been reported to date on the Jahn-Teller ordering introduced in Chapter 3 which occurs at the same wavevector as the orbital order. It appears that the work of Wakabayashi *et al.* (2000) is at least consistent with previous half-doped manganites. The superlattice reflection studied by Chatterji *et al.* (2000) at $\boldsymbol{Q} = \left(\frac{\overline{1}}{4}, \frac{1}{4}, 0\right)$ with high energy, claimed to be charge order is at variance with the claim of Wakabayashi *et al.* (2000) who attribute this due to orbital order. However, the resonant scattering by Chatterji *et al.* (2000) is consistent with the work of Wakabayashi *et al.* (2000). Is it possible that the reflection seen by Chatterji *et al.* (2000) is in fact Jahn - Teller order? Chatterji *et al.* (2000) mentions that there is a measurable intensity of the reflection at low temperature. This would indicate that the system is not re-entrant, however previous measurements have failed to see any weak ordering. Is it possible then, that these systems are not in fact re-entrant but there is a transition at 180 K which causes the reduction in the charge and

orbital order? Finally, no work has been carried out using X-ray scattering to date on compositions away from $x = 0.5$. Are these compounds charge ordered? If we again return to the phase diagram of Dho *et al.* (2001), shown in Figure 5.3, there is a wide ($0.47 \leq x \leq 0.62$) range at which, according to transport measurements, is charge ordered in the same 're-entrant' fashion as the $x = 0.5$ sample. X-ray diffraction measurements provide a much more detailed probe of the charge, orbital and Jahn - Teller ordering present in such samples and is thus the technique used.

5.3 Charge Ordering Model

Within the $a - b$ plane the bilayer manganite has the same structure as the single layer manganites. For this reason the material would be expected to display the same type of charge and orbital ordering pattern seen previously in the $n = \infty$ class of compounds.

Figure 5.9 show a schematic of a section of the $a - b$ plane for the $x = 0.5$ sample. The $d_{3x^2-r^2}$ / $d_{3y^2-r^2}$ orbital ordering with the orbitals pointing alternatively along the $\langle 1,\ 0,\ 0 \rangle$ and $\langle \bar{1},\ 0,\ 0 \rangle$ is shown with the accompanying charge order. The motion of the Mn^{4+} ions, due to the Jahn-Teller distortions are shown by red arrows. It is worth noting that the bilayer ($n = 2$) series of compounds are often indexed as $a = b = a_p$ whereas the $R_{1-x}A_xMnO_3$ ($n = \infty$) is indexed with $a \approx b \approx 2\sqrt{a_p}$. This constitutes a rotation of the a and b axes by $\frac{\pi}{2}$. In this model superlattice reflections should occur surrounding Bragg peaks due to the charge and orbital order at:

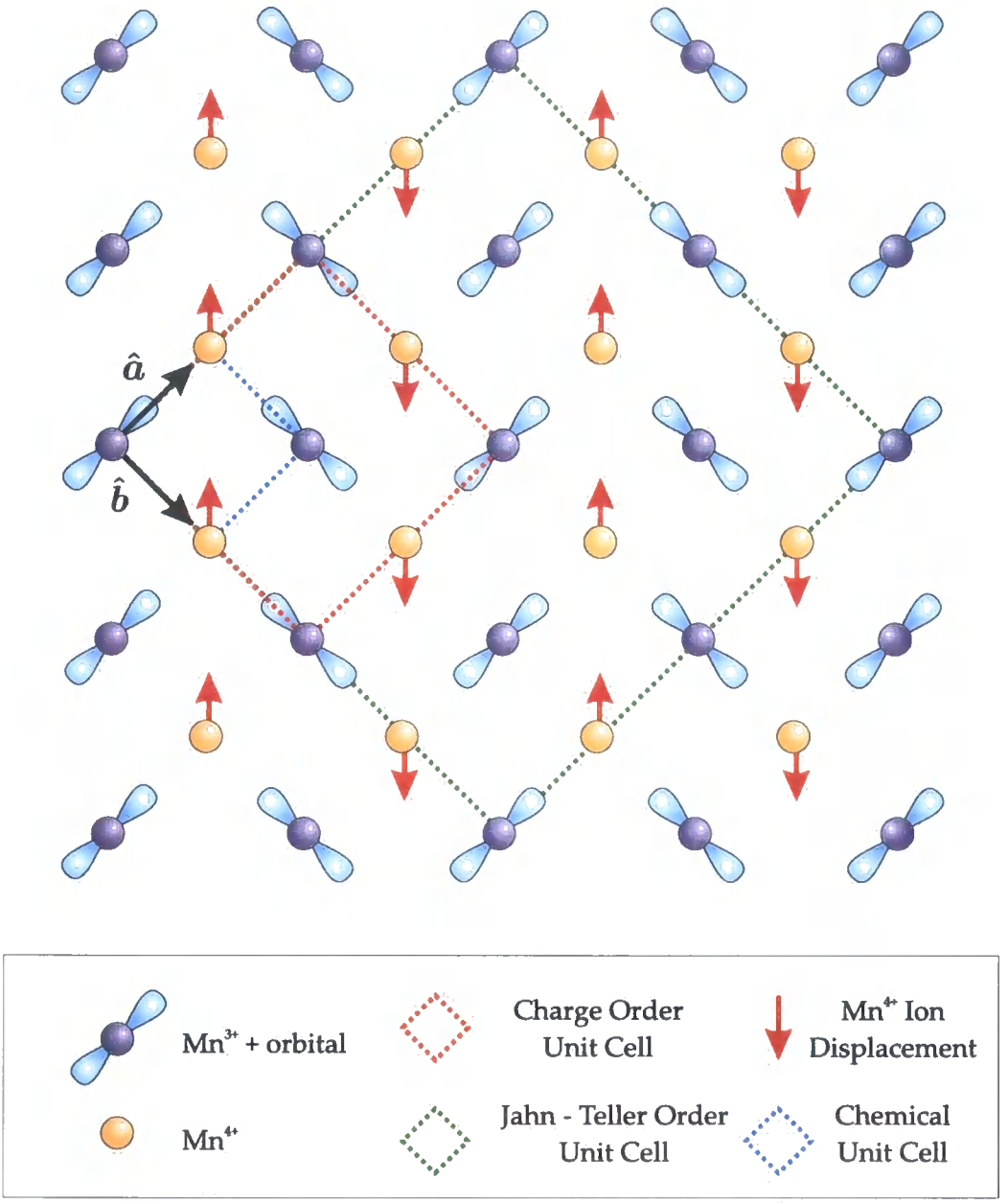

Figure 5.9: Schematic representation of the charge ordering model in the a - b plane in $La_{2-2x}Sr_{1+2x}Mn_2O_7$ $x = 0.5$. The Mn^{4+} ions are displayed as yellow circles, the Mn^{3+} ions as blue circles with the direction of the e_g orbital in light blue. The displacement of the Mn^{4+} ions, giving rise to the Jahn-Teller ordering signal are shown as red arrows.

Charge Order $\boldsymbol{Q_{CO}} = (\frac{1}{2}, \frac{1}{2}, 0)$

Orbital Order $\boldsymbol{Q_{OO}} = (\frac{1}{4}, \frac{1}{4}, 0)$

5.4 Experimental Details

Experiments were undertaken on the high-energy diffraction beamline BW5 (see Bouchard *et al.*, 1998) at the Hamburger Synchrotronstrahlungslabor (HASYLAB), Germany. This beamline is situated on the 17 period high field wiggler, with a critical energy of $E_c = 26.5$ keV making it ideal for the use of high energy X-rays. To filter out the low energy components of the beam a water cooled 1.5 mm copper filter is placed upstream of the experimental hutch. The resultant usable spectral range is 60 - 200 keV. This beam then passes into the experimental hutch where it is monochromated by a $Si_{1-x}Ge_x$ gradient crystal. These crystals are formed with a constant compositional gradient along their length which enables the value of x to be chosen by translating the crystal with respect to the beam, allowing the user to change the bandpass of the monochromator. This allows the experimental resolution of the diffractometer to be varied to match the mosaic spread of the sample, maximising the diffracted intensity. This feature is especially important in the study of flux grown crystals at such high energies. Typically monochromators are fashioned from single crystal Si or Ge, however at these high energies the resultant beam divergence from such a monochromator is extremely low. This is advantageous for high resolution measurements but in the study of very imperfect crystals, such as used in this thesis, intensity is wasted because the mosaic spread of the sample is much higher than that of

the incident beam. If the incident beam divergence is increased to approach that of the mosaic spread then the sample couples into the incident beam better (see Chapter 4) an increase of intensity is achieved.

A closed cycle He cryostat was used to allow the sample temperature to be varied in the range from 10 K to 300 K. The cryostat was mounted on a Huber 512.1 Eulerian cradle which was mounted on a Huber 430 rotation stage to form the θ-axis. A second $Si_{1-x}Ge_x$ gradient crystal was used as an analyser with the X-rays being detected using a solid state Ge detector. Higher order harmonics were removed by pulse height analysis of the detector signal. A photograph of the BW5 beamline is shown in Figure 5.10 and a schematic representation of the diffractometer is shown in Figure 5.11. At 100 keV the flux available at the sample is typically 1.7×10^{11} photons $\cdot$ second^{-1} $\cdot$ mm^{-2}

A high quality single crystal sample of $La_{2-2x}Sr_{1+2x}Mn_2O_7$ ($x = 0.475$) grown at the Department of Physics, University of Oxford was mounted on the diffractometer. The sample was mounted in the $\langle 0,\ 0,\ 1 \rangle$ / $\langle 1,\ 1,\ 0 \rangle$ zone on the end of the cold finger of the closed cycle He cryostat. The experiment was performed in transmission geometry with an incident beam size of 2 mm $\times$ 2 mm. The crystal was indexed in the *I4/mmm* setting with lattice parameters $a \simeq b = 3.873$ Å, $c = 19.9$ Å and the incident photon energy was selected to be $E = 94.8362$ keV ($\lambda = 0.1306$ Å). Although the sample was mounted in a certain zone, the additional degrees of freedom provided by the χ- and ϕ-axes, coupled with the use of transmission geometry, allowed for a large area of reciprocal space to be accessed.

The sample was initially orientated by rocking the sample using the θ-axis of the diffractometer whilst observing the diffracted beam on a fluorescent

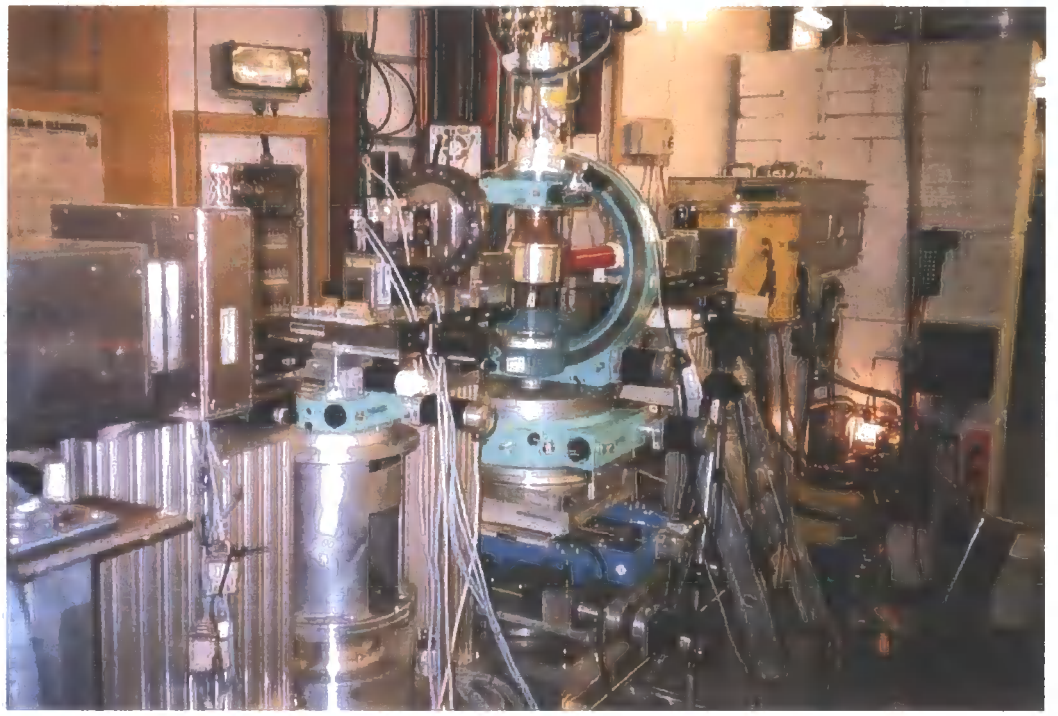

Figure 5.10: Photograph of the high energy X-ray diffractometer installed on beamline BW5 at HASYLAB

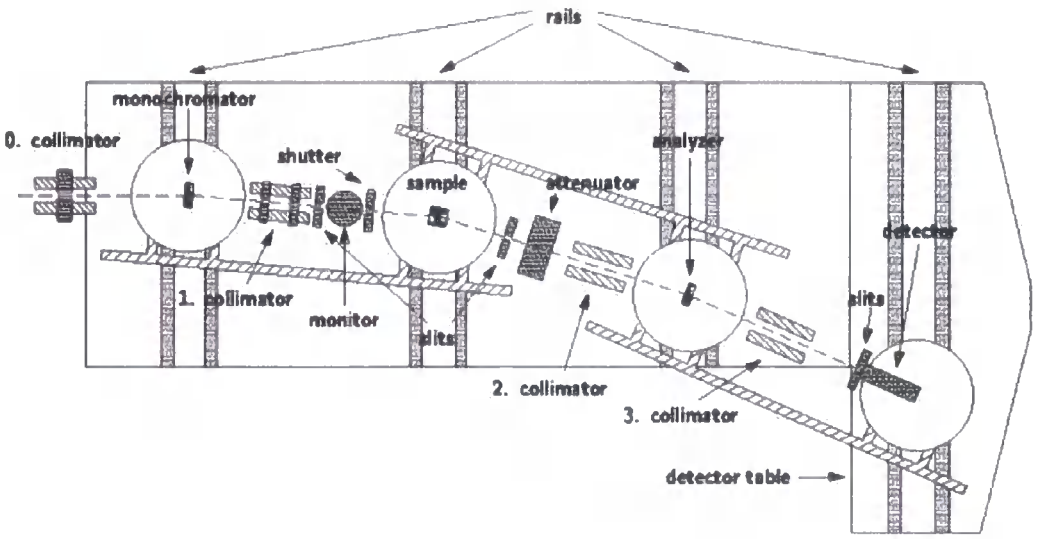

Figure 5.11: Schematic representation of the 4-circle diffractometer installed on BW5. Diagram courtesy of M. von Zimmermann, *HASYLAB*

screen. Using this approach it was easy to find the $(0,\ 0,\ l)$ diffraction peaks, as their 2θ angle was much smaller than in the other directions due to the very large c lattice parameter. Once diffraction was observed on the fluorescent screen the peak was centred in the detector and the setting angles entered into the calculation of the $\boldsymbol{UB}$ matrix. The same process was applied once the sample had been rotated 90° in the ϕ axis to search for the orthogonal $\langle 1,\ 1,\ 0 \rangle$ direction. This was then added to the $\boldsymbol{UB}$ matrix as the secondary direction.

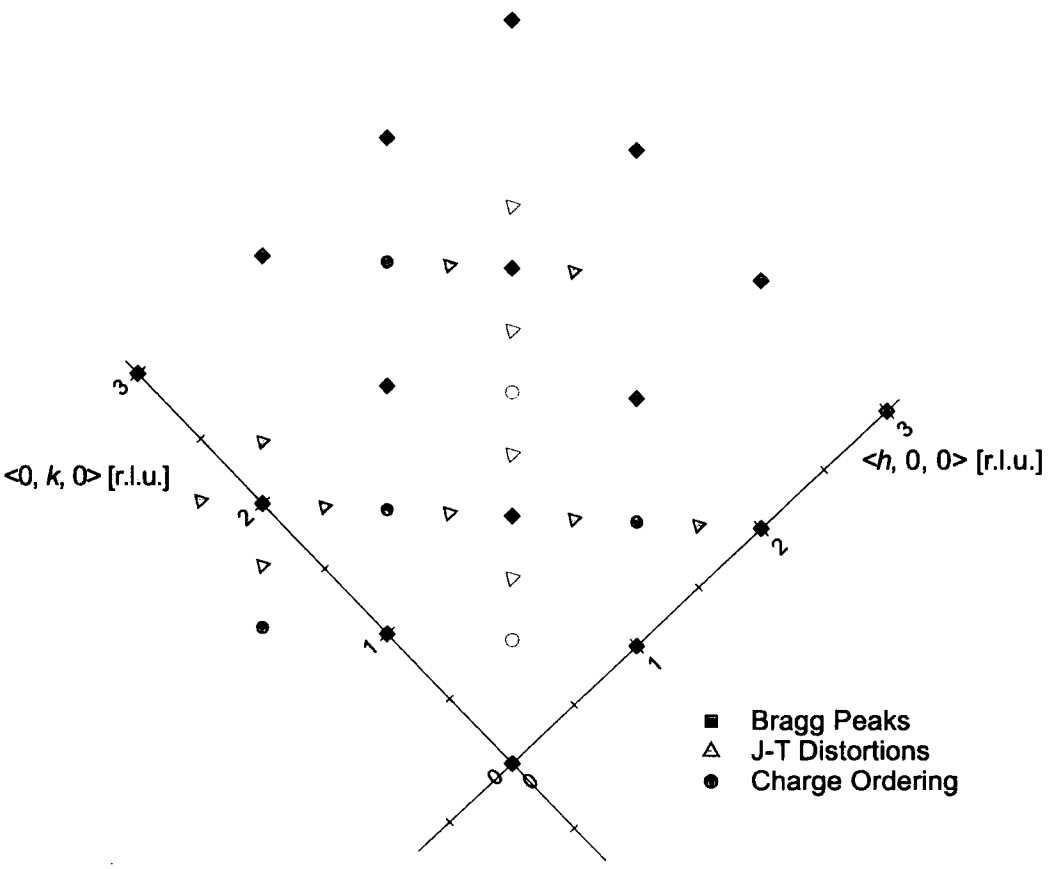

Figure 5.12: Location of the Bragg peaks (squares), charge ordering (circles) and Jahn-Teller distortions (triangles). Closed and open symbols indicate locations where strong or weak reflections were located respectively.

Once the sample orientation was solved and the $\boldsymbol{UB}$ matrix refined the sample was cooled to a temperature of $T = 180$ K, which previous diffraction studies had shown to be the maximum in superlattice intensity. A search for superlattice reflections at modulation wavevectors of $Q_{JT} = (\pm\frac{1}{4}, \pm\frac{1}{4}, 0)$ and $Q_{CO} = (\pm\frac{1}{2}, \pm\frac{1}{2}, 0)$ surrounding fundamental Bragg peaks was then made. Intense reflections were found at $Q_{JT} = (\frac{1}{4}, -\frac{1}{4}, 0)$ and $Q_{JT} = (-\frac{1}{4}, \frac{1}{4}, 0)$ with very weak reflections found at modulations of $Q_{JT} = (+\frac{1}{4}, +\frac{1}{4}, 0)$ and $Q_{JT} = (-\frac{1}{4}, -\frac{1}{4}, 0)$. The charge ordering was found to mirror the JT order in the intensity of reflections. The intensity of scattering on the $(\frac{5}{4}, \frac{3}{4}, 0)$ J-T peak was found to be $\sim 24 \times 10^3$ counts per second after correcting for the attenuators used. The corresponding charge order reflection at $(\frac{3}{2}, \frac{1}{2}, 0)$ was found to be $\sim 1 \times 10^3$ counts per second. Figure 5.12 shows the location of the superlattice reflections in the $(h, k, 0)$ plane of reciprocal space. The closed symbols represent locations which strong scattering was observed and open circles represent locations where weak scattering was observed. From this diagram it can be seen that the strong superlattice reflections run along the $\langle \bar{1}, 1, 0 \rangle$ direction.

The superlattice reflections (1.75, 0.25, 0) and (0.5, 1.5, 0) were studied as a function of temperature to measure the charge and Jahn-Teller order respectively. Scans were undertaken in the three principal directions in reciprocal space, H, K and L in triple-axis mode.

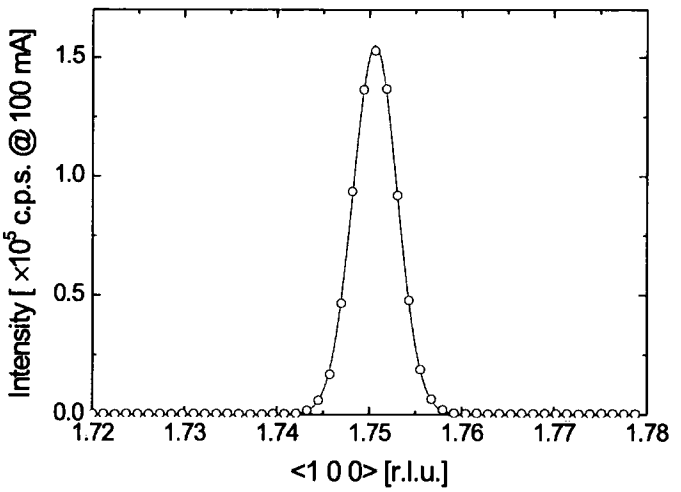

Figure 5.13: Scan through the H direction of the (1.75, 0.25, 0) J-T order peak at $T = 180$ K. The solid line is a fit to the experimental data assuming a Gaussian lineshape.

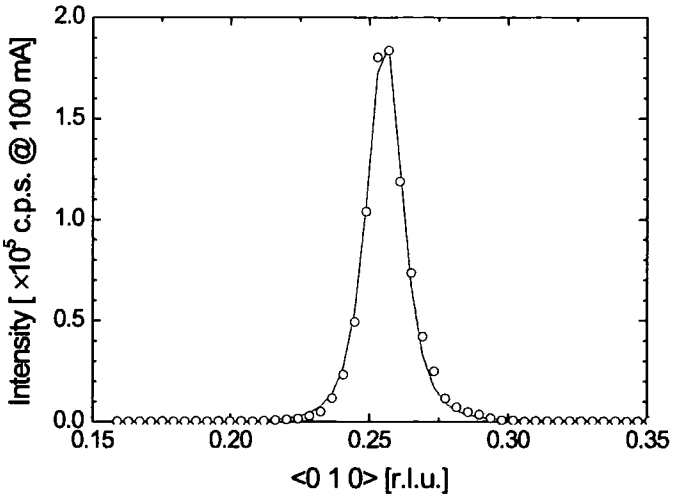

Figure 5.14: Scan through the K direction of the (1.75, 0.25, 0) J-T order peak at $T = 180$ K. The solid line is a fit to the experimental data assuming a Lorentzian squared lineshape.

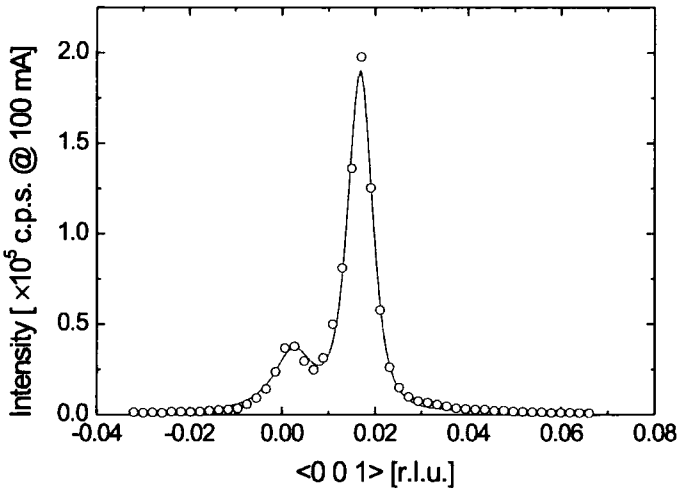

Figure 5.15: Scan through the L direction of the (1.75, 0.25, 0) J-T order peak at $T = 180$ K. The solid line is a fit to the experimental data assuming two convolved Lorentzian squared lineshapes.

5.4.1 Jahn-Teller Ordering

In the H-direction the Jahn-Teller peaks were found to be Gaussian in profile and in the K-direction to be of Lorentzian squared lineshape. In the L-direction two peaks were visible due to the mosaic spread of the sample (The sample was rotated by 90° in ϕ from the orientation above) and therefore the data was fitted to two Lorentzian squared peaks.

Figures 5.13, 5.14 and 5.15 show the resultant fits at $T = 180$ K in the H, K and L-directions. The parameters used for these fits were used as the starting points for the other fits to the experimental data at different temperatures. The inverse correlation lengths (related to the peak width) measured in the H, K and L-directions are shown in Table 5.1. The sample

was then cooled to the base temperature of the cryostat, $\sim$ 10 K, and a search was undertaken for the J-T order peak.

As at 180 K, superlattice reflections due to the J-T ordering were located at 10 K. Figures 5.16, 5.17 and 5.18 show the fits to the experimental data in the H-, K- and L-directions respectively. Similar to the case at T = 180 K the H-scans were fitted to a Gaussian lineshape with the K and L directions fitting a Lorentzian squared lineshape the latter displaying the obvious mosaic structure. Table 5.1 gives the measured inverse correlation length at 180 K and 10 K, calculated using the model outlined in Appendix A using the equation

$$\xi^{-1}_{(hkl)} = \frac{2\pi}{d_{(hkl)}}\kappa_{(hkl)} \tag{5.1}$$

where $\xi^{-1}_{(hkl)}$ is the inverse correlation length, $\kappa_{(hkl)}$ is the half width at half maximum of the diffraction peak and $d_{(hkl)}$ is the lattice parameter along the direction (hkl).

	Inverse correlation length [$\times 10^{-3}$ Å^{-1}]		
Temperature	H	K	L
10 K	2.677 ± 0.06	13.69 ± 0.03	6.59 ± 0.02
180 K	1.934 ± 0.007	4.690 ± 0.008	0.3977 ± 0.002
Ratio $\xi^{-1}_{10\text{ K}}/\xi^{-1}_{180\text{ K}}$	1.384	2.919	16.57

Table 5.1: Inverse correlation lengths measured on the (1.75, 0.25, 0) Jahn-Teller ordering peak at 10 K and 180 K.

Just by comparing the inverse correlation lengths at T = 180 K and 10 K it can be seen that along the L-direction there was a considerable broadening at low temperature. This is accompanied by a decrease in intensity. Along the H-direction there was not the same considerable broadening apparent

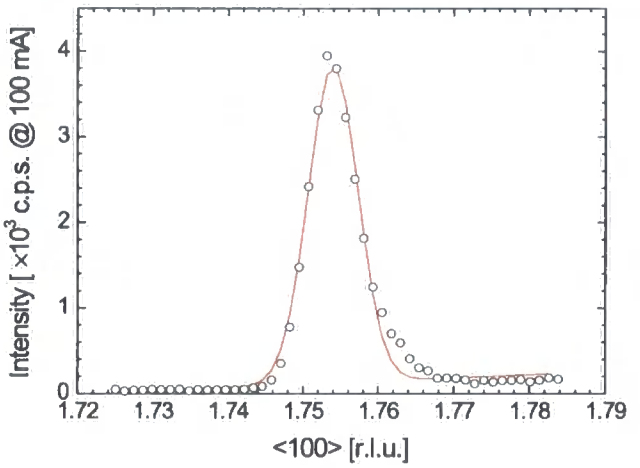

Figure 5.16: Scan along the H-direction of the (1.75, 0.25, 0) Jahn-Teller order peak at $T = 10$ K. The solid line is a fit to the experimental data assuming a Gaussian lineshape.

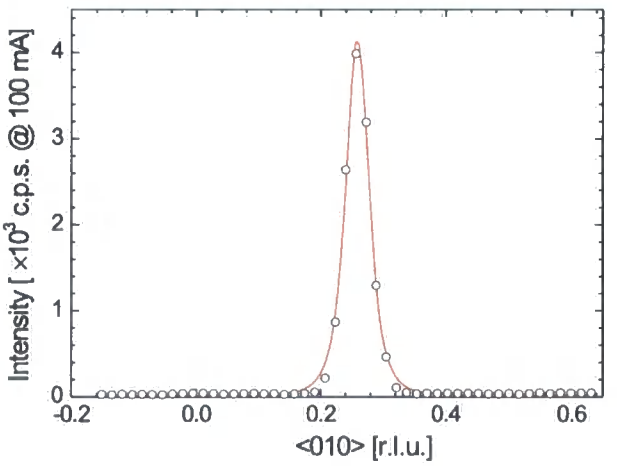

Figure 5.17: Scan along the K-direction of the (1.75, 0.25, 0) Jahn-Teller order peak at $T = 10$ K. The solid line is a fit to the experimental data assuming a Lorentzian squared lineshape.

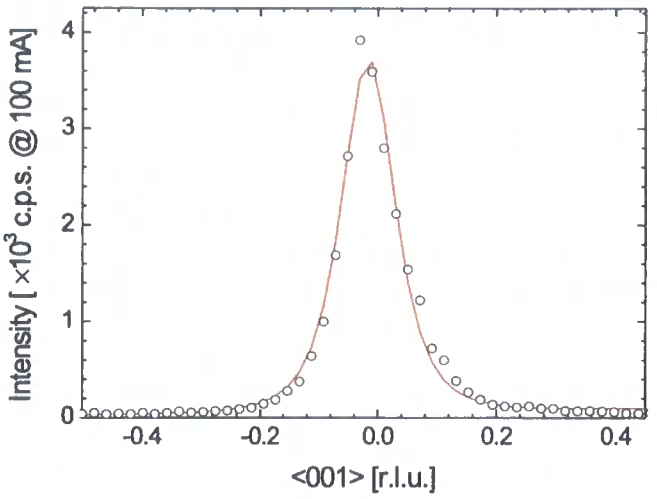

Figure 5.18: Scan along the L-direction of the (1.75, 0.25, 0) Jahn-Teller order peak at $T = 10$ K. The solid line is a fit to the experimental data assuming a Lorentzian squared lineshape.

when the sample is cooled to 10 K.

Figure 5.19 shows the temperature variation of the integrated intensity of the (1.75, 0.25, 0) Jahn-Teller (J-T) ordering superlattice reflection measured in the H- and K-directions. Here there appears to be two main regions of interest. As the sample is warmed from 10 K the integrated intensity stays at a constant low value until 100 K. At this temperature the integrated intensity starts to increase, reaching a maximum at 180 K which is ~ 6 times greater than that at 10 K. Further warming causes the integrated intensity to drop until 220 K where there is no observable peak above the background.

The integrated intensity can be thought of as a measure of the amplitude of the J-T distortion, as an increase in the distortion causes a greater

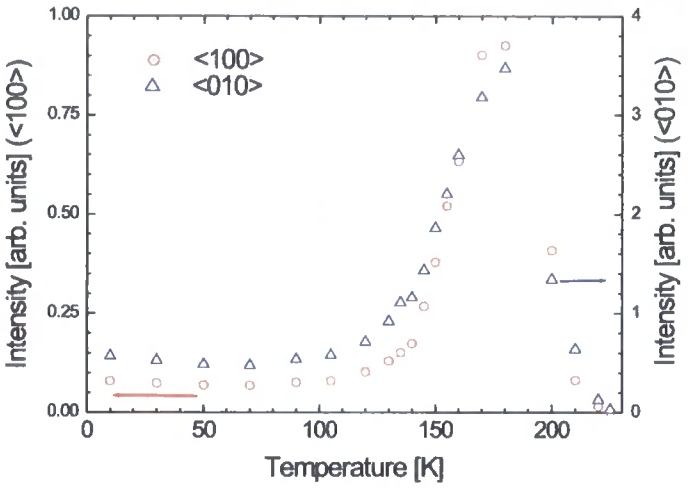

Figure 5.19: Integrated intensity of the (1.75, 0.25, 0) J-T ordering peak as a function of temperature measured in the H (circles) and K (triangles) directions upon warming the sample.

difference in the electron density, resulting in a greater amount of scattering at the wavevector of the J-T order. Using this we can postulate that upon cooling the sample it first enters a region at which the J-T order is strong, indicating that the c/a ratio within the Mn octahedra is large i.e. they become elongated along their c-axes as their Mn - O bond lengths increase. This in turn causes a greater displacement of the Mn^{4+} ion from their high temperature position. Such a movement of the Mn^{4+} ions has been observed by powder neutron diffraction in $La_{1-x}Ca_xMnO_3$ by Radaelli *et al.* (1997). Upon further cooling the integrated intensity drops, suggesting that the Mn octahedra's c/a ratio decreases, indicating that the J-T distortion of the octahedra decreases.

Figure 5.20 shows the integrated area measured in the L-direction on

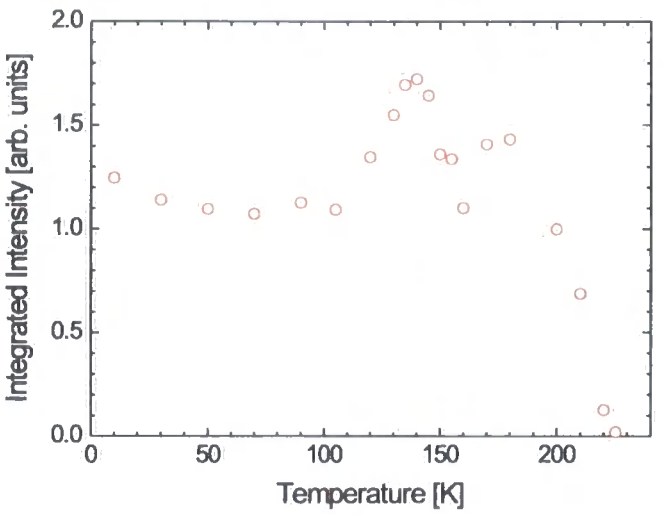

Figure 5.20: Integrated intensity of the (1.75, 0.25, 0) J-T ordering peak as a function of temperature measured in the L direction upon warming the sample.

the same peak. Here the integrated intensity appears not to have the large increase at 120 K seen in the H- and K-directions but an increase is visible. There is however a more dramatic drop in intensity at 220 K.

Turning to the measured widths of the J-T ordering superlattice reflections, Figures 5.21 and 5.22 show the inverse correlation length as a function of temperature measured along the H-, K- and L-directions in reciprocal space. Comparing the width in the H- direction to the K- and L-directions it can be seen that the inverse correlation length (the peak width) is much less in the H-direction. However, one has to be careful when performing scans in these three orthogonal directions to include the effects of the instrumental resolution. At the (1.5, 0.5, 0) reflection the highest experimental resolu-

tion will be along the $Q_{||}$ direction, the longitudinal direction, which for this sample is $\sim 18°$ from the H-direction. Referring to the sample orientation discussed previously, measurements along the L-direction will be equivalent to measuring in the $Q_{\perp}$ direction and scans along the K-direction will be at 72° to the $Q_{||}$ direction, almost equivalent to measurements out of the diffraction plane. Whilst it can be said that along the K- and L-directions there will be a greater contribution to the width from the instrumental resolution than along the H-direction, it is still possible to qualitatively look at the variation of the width as a function of temperature. However along the H-direction it is possible to quantitatively measure the associated correlation length. No deconvolution was performed on any of the data taken in the H, K and L directions, as the instrumental resolution of the experiment was much narrower than the widths of the diffraction peaks (see Bouchard *et al.*, 1998).

In X-ray scattering the inverse correlation length is a measurement of the amount of long-range correlation at the wavevector of the peak in reciprocal space, consistent with the model suggested in Appendix A. At the wavevector of the J-T order such a measurement indicates the correlation of the distortions of the Mn octahedra. Similar in fashion to the integrated intensity, in Figures 5.21 and 5.22 there are again two distinct temperature regions visible. At low temperature the degree of correlation measured remains at a steady value until 100 K. Upon warming further the J-T distortion becomes more correlated and finally reaches a maximum at 180 K. Past 180 K the degree of correlation then remains constant until 210 K after which the correlation sharply falls again.

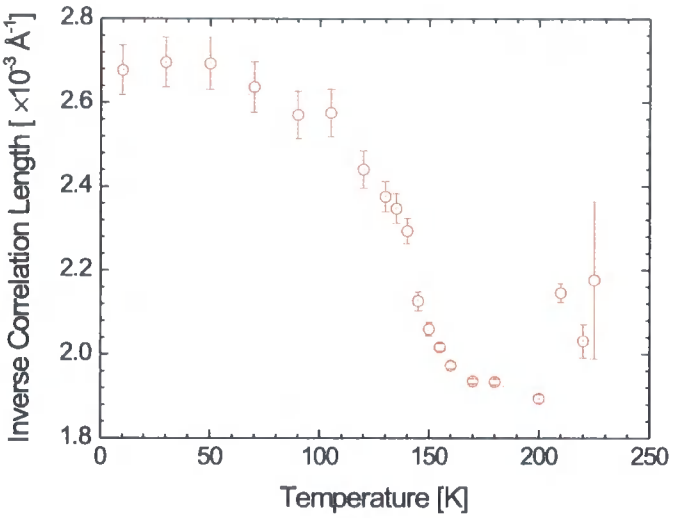

Figure 5.21: Inverse correlation length measured along the H direction as calculated from a Gaussian lineshape. Error bars are calculated from the error in fitting the width of the diffraction peak.

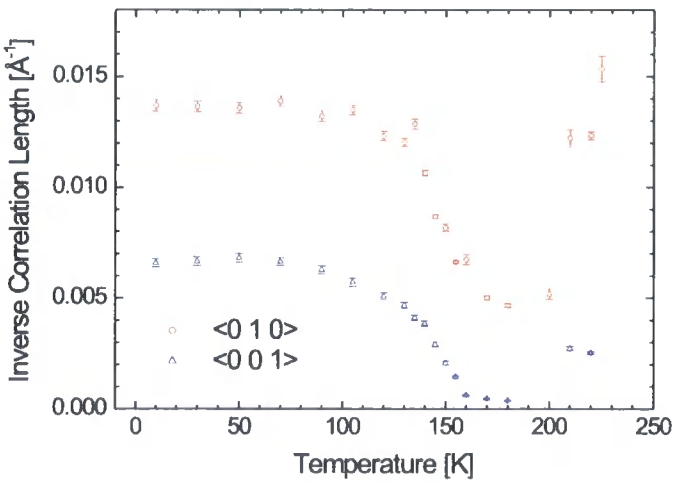

Figure 5.22: Inverse correlation length measured along the K and L directions as a function of temperature as calculated from a Lorentzian squared lineshape. Error bars are calculated from the error in fitting the width of the diffraction peak.

Such an increase in the width past 210 K observable in all three principal directions suggests that at the phase transition either the domain size of co-existing Jahn - Teller domains is decreasing (which will cause a increase in the inverse correlation length) or then there appears critical fluctuations into the Jahn - Teller distorted region. The latter requires a second order phase transition.

Jahn-Teller ordering, being a modulation of the lattice, would be expected to occur at commensurate positions in reciprocal space. In this system these occur at positions separated by (ε_{JT}, ε_{JT}, 0) where $\varepsilon_{JT} = \frac{1}{4}$. It is possible to measure the degree of commensurability by measuring the peak position in reciprocal space of the superlattice reflection relative to the Bragg peaks. Figure 5.23 shows the position of the (1.75, 0.25, 0) reflection as measured in the H-direction. No peak movement was detected in the K- or L- directions.

From Figure 5.23 we can see that as the sample is cooled the position of the peak in H is at the expected commensurate value of 1.75. However, at 140 K there is a transition at which the position in H starts to increase. Such a change in the H position shows that at 140 K the J-T ordering becomes incommensurate.

The incommensurability of the Jahn-Teller order ε can be calculated from the 10 K and 180 K values. This is found to be from $\varepsilon = 0.246 \pm 0.001$ to $\varepsilon \approx 0.25$ which corresponds to a difference value of 0.004 reciprocal lattice units suggesting a very long range period.

To summarise the results of the Jahn - Teller distortion Figure 5.24 shows the integrated intensity (top panel), Position of the peak along the H-direction (middle panel) and the inverse correlation length along the H-

direction (bottom panel). Here three distinct regions can be detected. If we take the case upon cooling the sample from 300 K, there is no detectable Jahn-Teller ordering present until a temperature of 220 K. At this temperature the intensity of the superlattice reflections due to the Jahn-Teller ordering start to grow. At 210 K there is a movement into a region (indicated by II on the graph) where the Jahn-Teller ordering grows in intensity and it becomes more correlated and 'locks in' to a commensurate value. Upon further cooling of the sample at 180 K the integrated intensity starts to drop, along with the correlation length, until 140 K at which point the Jahn-Teller order breaks the commensurate value and starts to become more incommensurate. Upon further cooling of the sample (indicated by region I) the Jahn-Teller order exists in a weak, poorly correlated state and the incommensurability

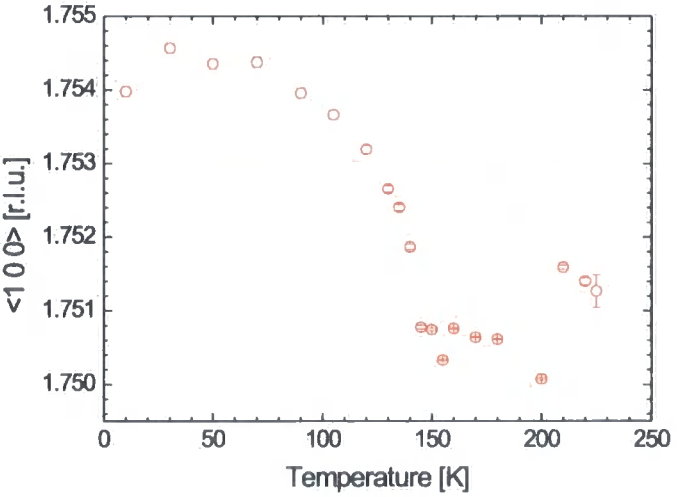

Figure 5.23: Position of the (1.75, 0.25, 0) J-T ordering peak in the H direction as a function of temperature.

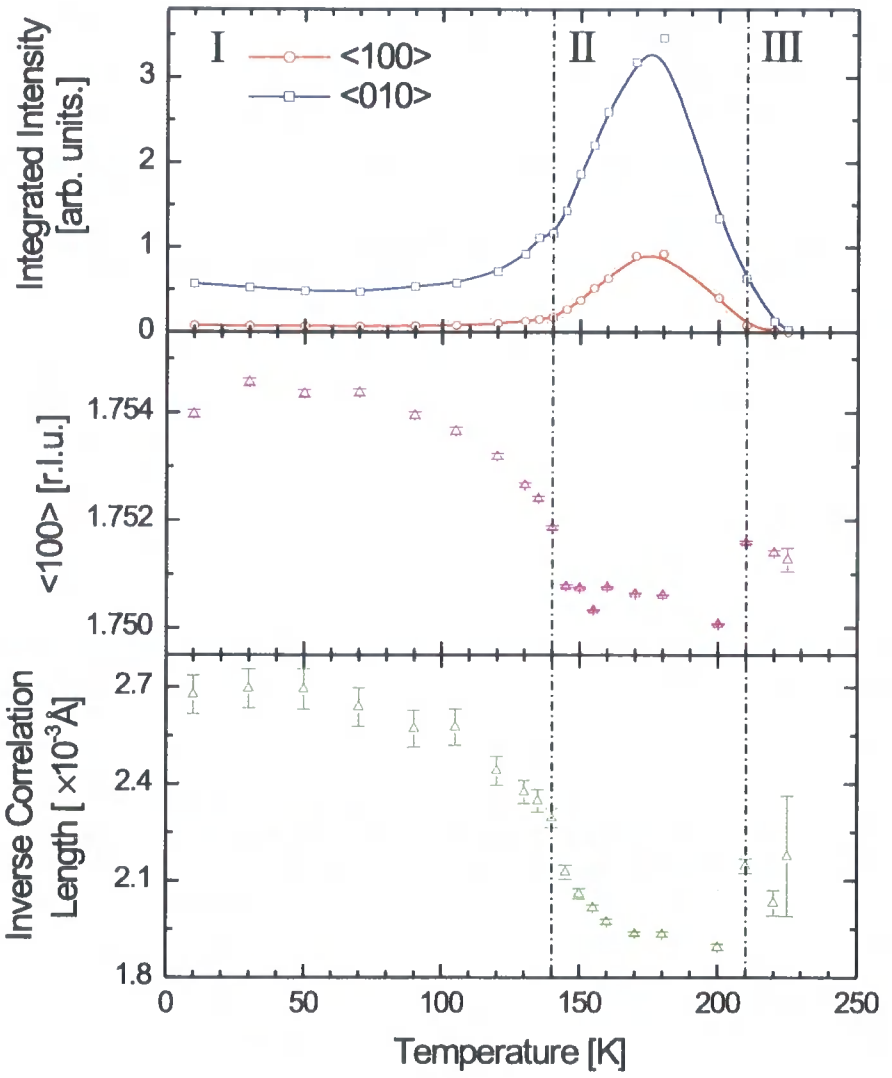

Figure 5.24: Integrated intensity, wavevector and inverse correlation length as a function of temperature. See text for details.

grows.

Therefore we conclude that there exist three main structural phases in this sample. In the temperature region 210 K to 140 K the Jahn-Teller order is highly correlated, commensurate with the crystal lattice and shows a high intensity, therefore there appears to be a large rotation of the Mn octahedra which is correlated over a long range. In the temperature region below 140 K the integrated intensity has dropped indicating that the degree of rotation of the Mn octahedra is much less and the rotation is correlated over a much shorter range. In addition there also appears a very long range modulation of the octahedra, indicated by the incommensurate value of the H position. Finally above 220 K the sample exists with no Jahn - Teller distortions and no observable charge order.

5.4.2 Charge Ordering

Similar to the previous section describing the J-T order the sample was cooled to $T = 180$ K and scans along the H-, K- and L-directions in reciprocal space were undertaken upon the charge ordering reflection at a wavevector of (1.5, 0.5, 0).

Figures 5.25, 5.26, 5.27 show fits in the H-, K- and L-directions of reciprocal space with a Lorentzian squared lineshape. Along the L-direction two peaks were again detected. Due to the zone of reciprocal space that the measurements were taken in, it is likely that this is due to the mosaic structure of the sample, i.e. two distinct crystallites can be seen.

The superlattice reflections were found to exist in the temperature re-

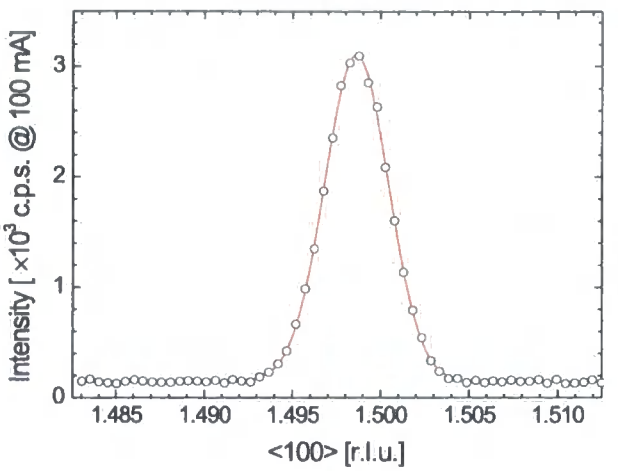

Figure 5.25: Scan along the H-direction of the (1.5, 0.5, 0) charge order peak at $T = 180$ K. The solid line is a fit to the experimental data assuming a Lorentzian squared lineshape.

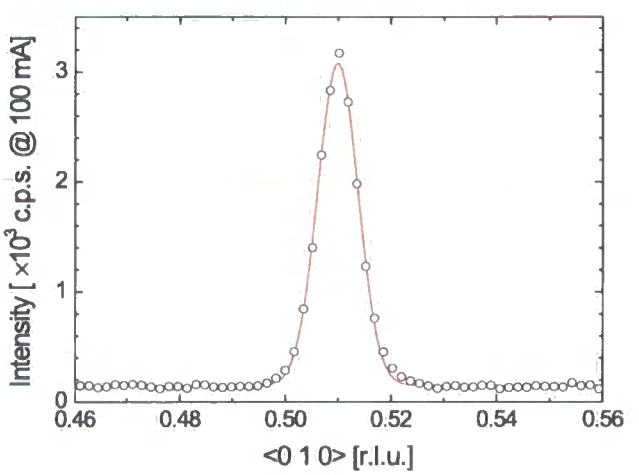

Figure 5.26: Scan along the K-direction of the (1.5, 0.5, 0) charge order peak at $T = 180$ K. The solid line is a fit to the experimental data assuming a Lorentzian squared lineshape.

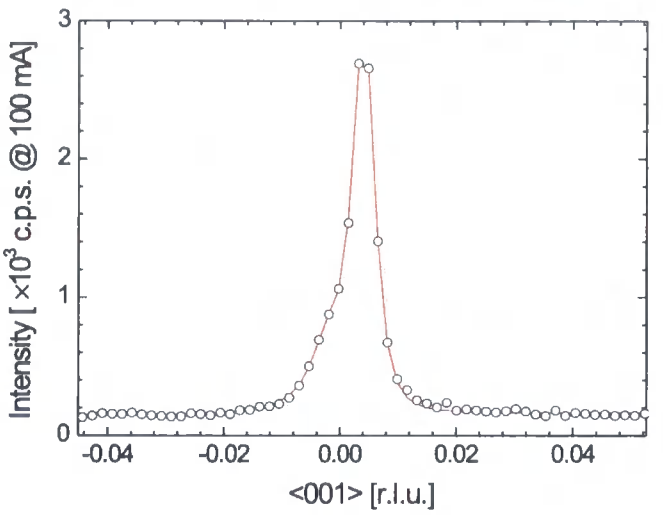

Figure 5.27: Scan along the L-direction of the (1.5, 0.5, 0) charge order peak at $T = 180$ K. The solid line is a fit to the experimental data assuming two Lorentzian squared lineshapes.

gion between 120 K and 210 K. Below 120 K no appreciable intensity was detected above background at the wavevector corresponding to the charge order. Table 5.2 show the inverse correlation lengths measured by fitting of the diffraction peaks at 180 K.

	Inverse correlation length [$\times 10^{-3}$ Å^{-1}]		
Temperature	H	K	L
180 K	2.939 ± 0.013	6.360 ± 0.050	0.706 ± 0.028

Table 5.2: Inverse correlation length measured on the (1.5, 0.5, 0) Jahn - Teller ordering peak at 180 K.

Figure 5.28 shows the integrated intensity as a function of temperature for the charge order superlattice reflection. Here the temperature dependance

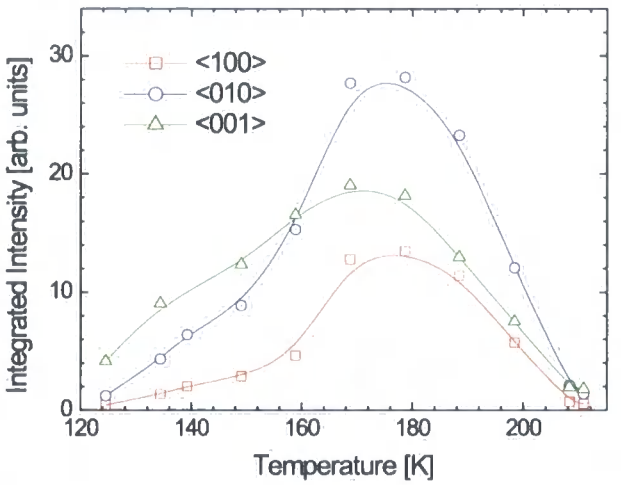

Figure 5.28: Integrated area of the (1.5, 0.5, 0) charge order superlattice reflection in the H (squares), K (circles) and L direction (triangles). The solid lines are a guide to the eye.

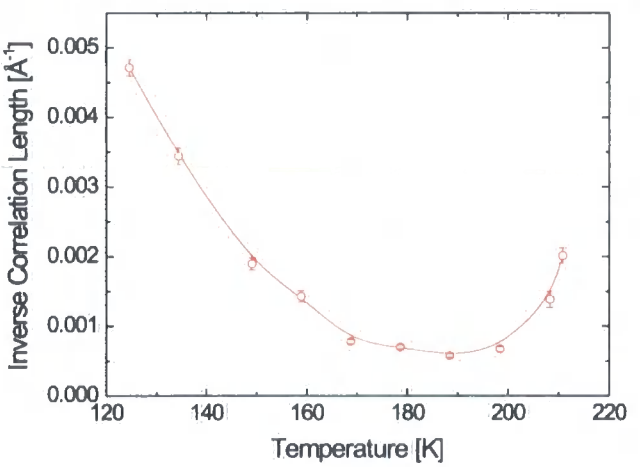

Figure 5.29: Inverse correlation length measured in the L-direction on the (1.5, 0.5, 0) charge ordering reflection after fitting to a Lorentzian squared lineshape. The solid line is a guide to the eye.

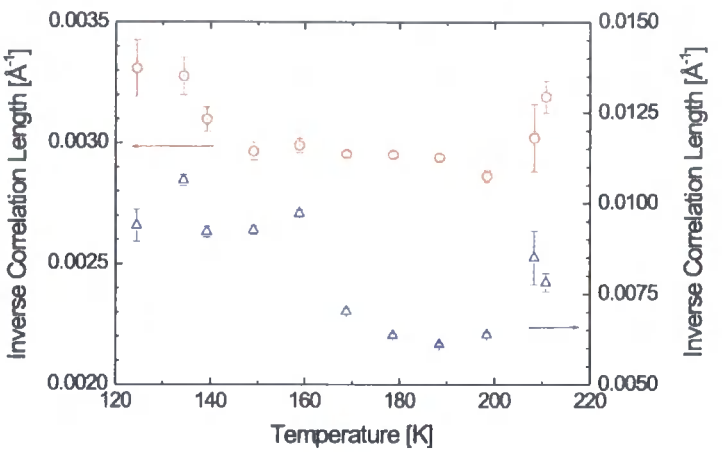

Figure 5.30: Inverse correlation length measured in the H- and K-direction on the (1.5, 0.5, 0) charge ordering reflection.

can be seen to be similar to that found in the region II for the Jahn - Teller order shown in Figure 5.24. Again, the intensity maximises at 180 K, as did the Jahn-Teller order.

Figure 5.29, shows the inverse correlation length measured along the L-direction. Here a significant change in the inverse correlation length can be seen. It again was found to maximise around 180 K corresponding to the maximum in integrated intensity. Figure 5.28 however, shows the inverse correlation length along H- and K-directions as a function of temperature as measured from the FWHM of the superlattice peak in the H and K-directions. Here no appreciable variation in the inverse correlation length can be detected. One possible explanation for the decrease in the correlation length in the L-direction only could be that as the temperature is decreased below 180 K the charge ordering becomes more two dimensional, not signif-

icantly changing in correlation along the H- and K-directions but changing more dramatically along the L-direction.

5.5 Conclusions

Previous measurements on the $x = 0.5$ system using X-ray diffraction by Chatterji *et al.* (2000) and Wakabayashi *et al.* (2000) have focused mainly on the charge and orbital ordering present. In this study we have found that the modulation wavevector for the charge and J-T order appears at $Q_{JT} = (\pm\frac{1}{4}, \pm\frac{1}{4}, 0)$ and $Q_{CO} = (\pm\frac{1}{2}, \pm\frac{1}{2}, 0)$ respectively. In this respect we agree with the charge order wavevector found by Wakabayashi *et al.* (2000). The charge ordering referred to in Chatterji *et al.* (2000) occurs at a wavevector identical to that observed by ourselves for Jahn - Teller order. Their wavevector appears at $Q = (\pm\frac{1}{4}, \pm\frac{1}{4}, 0)$ which is hard to reconcile with the model for the charge and orbital ordering presented in Figure 5.9. If the charge ordering was to appear at $Q = (\pm\frac{1}{4}, \pm\frac{1}{4}, 0)$ then one would expect a J-T modulation at a wavevector of $Q = (\pm\frac{1}{8}, \pm\frac{1}{8}, 0)$. This would indicate a direct space spacing between the Mn^{3+} / Mn^{4+} of 4 unit cells which is inconsistent with the checkerboard type charge ordering that would be expected from samples with $n_h \approx 0.5$. We can therefore conclude that the ordering detected by Chatterji *et al.* (2000) is not charge ordering but Jahn - Teller ordering.

High energy X-ray scattering is very insensitive to orbital ordering, as such a signal would require the detection in the asymmetry of the electron density in a super-cell created by the orbital order. It is here that resonant

X-ray scattering, as previously discussed in Chapters 3 and 6, becomes useful, as it is able to detect the modulation in the electronic structure of the Mn ions due to the ordering. However, this poses a problem with the data presented here. Wakabayashi *et al.* (2000) presented a modulation for the orbital ordering of $Q_{OO} = \left(\pm\frac{1}{4},\ \pm\frac{1}{4},\ 0\right)$ which coincides with the Jahn - Teller ordering signal present.

The Jahn - Teller signal detected in this high energy data is not that of the orbital order as the cross-section for such at high energy is negligible as we are so far away in energy from any absorption edge (resonance). Such a strong signal detected here with high energy X-ray scattering should be also detectable at normal X-ray energies as the origin is a lattice distortion. If we return to the reciprocal space diagram (Figure 5.12) we can see that the Jahn - Teller is only detectable along the $\langle\,\bar{1},\ 1,\ 0\,\rangle$ direction. Such an orbital order peak, if it exists, here would be undetectable under the Jahn - Teller order peak. The weak modulations observed along the $\langle\,1,\ 1,\ 0\,\rangle$ direction are most probably due to twin domains of the sample and are detectable because the high energy X-ray scattering probes a very large sample volume compared with X-rays at ≈ 6.5 keV. It must be noted however that no twinning of the lattice in the a - b plane was detected. At normal X-ray energies these twin domains would probably be undetectable due to the small sample volume probed. Is it possible that the orbital order signal can be detected along the $\langle\,1,\ 1,\ 0\,\rangle$ direction where there is no Jahn - Teller ordering?

Comparing the inverse correlation lengths of the Jahn-Teller and charge order given in Tables 5.1 and 5.2 respectively we can see that the degree of correlation of both is approximately the same with slightly less correlation

in the case of the charge order. Both show a sharp decrease in correlation along the L direction through the transition into the low temperature region. This again suggests a low temperature 2-D ordering mediated by the highly 2-D crystal structure.

Wakabayashi *et al.* (2000) suggested that the charge and orbital ordering is 're-entrant' in behaviour. Whilst we detect no noticeable signal below 120 K for the charge order (see Figure 5.28) there is appreciable intensity of the Jahn - Teller order below 120 K. We can therefore postulate that the charge order signal should exist below 120 K in the sample but the drop in intensity from 180 K is too great and the measurement has insufficient intensity to detect the weak charge ordering. The presence of the Jahn - Teller ordering in the sample at the wavevector of $Q_{JT} = (\pm\frac{1}{4}, \pm\frac{1}{4}, 0)$ confirms that the sample must be charge ordered to obtain a direct space ordering quadrupling the chemical unit cell. In the absence of charge order the J-T order would be expected to appear at a modulation of $Q = (\pm\frac{1}{2}, \pm\frac{1}{2}, 0)$. We can therefore conclude that the charge and Jahn - Teller ordering is not re-entrant but undergoes a phase transition which starts at 180 K causing a decrease in the intensity and correlation of the charge and Jahn - Teller order. Contrary to the work of Wakabayashi *et al.* (2000) we propose that charge and Jahn - Teller order exists in the sample down to 10 K.

5.6 Future Work

Using the Resonant X-Ray Scattering (RXS) technique it is possible to distinguish between lattice, charge and orbital ordering. By measuring the

dependance of the intensity of scattering as a function of incident photon energy and the resultant polarisation, dependance three distinct differing cases can be observed similar to that displayed in Chapter 3. Recent data collected on XMaS, the UK CRG, at the ESRF Grenoble France, has shown that the charge ordering signal, at a modulation of $Q_{CO} = \left(\pm\frac{1}{2}, \pm\frac{1}{2}, 0\right)$ show a resonance in the $\sigma \rightarrow \sigma'$ channel. In addition, orbital ordering type reflections have been located at $Q_{OO} = \left(\frac{1}{4}, \frac{1}{4}, 0\right)$ along the $\langle 1, 1, 0 \rangle$ direction and show a resonance in the $\sigma \rightarrow \pi'$ channel. These results confirm the origin of these peaks discussed in this thesis.

High energy X-ray scattering, with its very low absorption through materials, allows for the use of many sample environments where only aluminium is needed for transmission of the incident and scattered X-ray beam. This benefit would allow for the measurement of the charge order transition as a function of magnetic field by placing the sample in a cryo-magnet system. With the magnetic ordering playing an important part of the transition between the highly correlated region and the weak poorly correlated region in which A-type AFM order is formed. By using a magnetic field it should be possible to force the A-type order within the $a - b$ plane to observe whether a change in the amplitude or correlation is observed.

Chapter 6

Soft X-Ray Magnetic Scattering from $La_{2-2x}Sr_{1+2x}Mn_2O_7$, $x = 0.475$ and $x = 0.5$

6.1 Introduction

The use of X-ray scattering to probe the magnetic structure of crystalline solids started over 20 year ago with the study of NiO by de Bergevin and Brunel (1981). When X-rays incident upon electrons are scattered, the dominant process is charge scattering which represents the basis of crystallographic structure determination. However, the electric and magnetic fields both interact with the magnetic moment causing magnetic X-ray scattering. Such scattering is extremely weak, with the result that most magnetic scat-

tering studies have employed neutrons, where often the magnetic scattering is equal, if not greater that the nuclear scattering. It wasn't until the pioneering work of Gibbs *et al.* (1988), where during measuring the non-resonant magnetic scattering from holmium they tuned to the L_{III} edge of holmium and discovered a 50 fold enhancement in the scattered intensity. This technique, clearly a complication over the non-resonant case, occurs due to the strong spin-orbit split core states due to the magnetism present. It therefore follows that the largest resonant enhancement will occur when the incident photon energy corresponds to the energy of the optical transition which probes the band split due to the magnetism. This was dramatically demonstrated by McWhan *et al.* (1990) where a resonant enhancement of approximately six orders of magnitude at the uranium M_{IV} edge in a crystal of UAs which lead to diffraction intensities of many thousands of counts per second, almost one percent of the dominant charge scattering.

These results made two very important points regarding the future of X-ray magnetic scattering. Firstly, one of the key factors is the resonant enhancement of an otherwise weak signal. Secondly, it is important to choose the absorption edge which displays strong enough spin-orbit coupling which can be separated by the resolution of the incoming probe. Taking the second point, the required absorption edges are the $3d$-bands in the transition metal oxides, the $4f$-bands in the lanthanides and the $5f$ states in the actinides. The energy corresponding to the optical transitions involving these bands and states is largely in the soft X-ray region with $E = \hbar\omega < 2$ keV. The exception is the actinides where the energies are higher, e.g. for uranium the M_{IV} edge is at 3.728 keV with the result that to date most resonant magnetic

X-ray scattering has been carried out on actinide compounds. Unfortunately the largest class of magnetic materials in technological applications and fundamental research contain the $3d$ transition metals.

For the transition metals the K edges appear in the energy range 4 keV to 20 keV and are easily accessible by most synchrotron diffractometers. There have been a number of key experiments performed at the K edge using either the dipole transition from the $1s \rightarrow 4p$ or a quadropole transition from the $1s \rightarrow 3d$ levels. Fernandez *et al.* (1998) and Hill *et al.* (1997) performed studies on single crystals of NiO, with Neubeck *et al.* (1999) and Stunault *et al.* (1999) studying CoO and $RbMnF_3$ respectively. Here however, a detectable quantity of off-resonant magnetic scattering was present, indicating that there was initially a strong magnetic signal. The resonant enhancements obtained were very weak, the dipole transitions do not probe the bands containing the magnetic information, and the quadropole transitions of the transition metal oxides at the K edge are very weak, leading to a very small resonant enhancement, which was indeed observed. The experiments on the $PrBa_2Cu_3O_{(7-\delta)}$ system by Hill *et al.* (2000) have proven it is possible to study the magnetism in a "real" system, with more dilute moments, but again the resonant enhancement was weak and a substantial amount of non-resonant magnetic scattering was present. To probe systems where there exists dilute magnetisation a larger resonance of the size predicted by Hannon *et al.* (1988) and Carra *et al.* (1989) on both anti-ferromagnetic and ferromagnetic systems is required, using transitions that probe the bands containing the magnetic information.

The close link between X-ray diffraction and absorption processes still

allow magnetic information to be yielded despite the low X-ray energy. Indeed, MXCD (Magnetic X-ray Circular Dichroism) measurements have over the past years solved many problems in condensed matter physics. As this technique relies solely on the absorption spectra of the material under study, performing experiments at the soft energies of, say, the transition metal oxides makes the experiment technically difficult but does not effect the physics under study. Experiments performed using MXCD on transition metal oxides have observed very large effects when tuning through the absorption edge. Would it be possible to perform Soft X-Ray Magnetic Diffraction?

Two main factors cause problems when trying to perform diffraction at soft X-ray energies. Firstly, and the most significant is, that with such a low energy the corresponding Ewald sphere is very small, limiting the range of reciprocal lattice points which can be accessed. Secondly the relatively high absorption of soft X-rays makes the technique quite surface sensitive. The first soft X-ray magnetic diffraction experiments were carried out on pseudo-crystals consisting of thin films of metal grown onto a substrate. Such crystals involve relatively large d-spacings which are greater than tens of Ångstroms and are accessible at the soft energies. There have been successful experiments carried out previously to probe the magnetic alignment of coupled layers in metallic spin valves (see Hase *et al.*, 2000) and magnetic domain structures in FePd alloys (see Dudzik *et al.*, 2000). However, such experiments have been confined to such pseudo-crystals. The challenge is to perform soft X-ray diffraction on bulk single crystals.

In this chapter the results of the first attempt at soft X-ray diffraction from a bulk single crystal of $La_{2-2x}Sr_{1+2x}Mn_2O_7$ will be described. This

sample was used for a trial experiment as it has a large c axis lattice parameter of $\sim$ 20 Å which allows access out to the (0, 0, 2) reflection at the Mn L edge at $\sim$ 640 eV.

6.1.1 Theory of Resonant Magnetic Exchange Scattering

Following the work of Hannon *et al.* (1988), the total coherent scattering amplitude for a magnetic ion can be written as:

$$f(\boldsymbol{Q}, \hbar\omega) = f_0\boldsymbol{Q} + f'(\hbar\omega) + if''(\hbar\omega) + f_{spin}(\hbar\omega) \tag{6.1}$$

Here $f_0 = Zr_0$ is the term due to the Thompson scattering. $f'(\hbar\omega)$ and $f''(\hbar\omega)$ are the anomalous dispersion corrections due to the bound nature of the electrons and $f_{spin}(\hbar\omega)$ is the scattering from the interaction between the spin of the electron and the X-ray.

Far from a resonance condition $f'(\hbar\omega)$ and $f''(\hbar\omega)$ only contribute terms proportional to the spin and angular momentum and the non-resonant magnetic scattering amplitude is (Blume and Gibbs, 1988; Blume, 1985)

$$f_{non-res}^{(mag)} = ir_0 \left(\frac{\hbar\omega}{mc^2}\right) f_D \left[\frac{1}{2}\boldsymbol{L}(\boldsymbol{Q}) \cdot \boldsymbol{A} + \boldsymbol{S}(\boldsymbol{Q}) \cdot \boldsymbol{B}\right] \tag{6.2}$$

where f_D is the Debye-Waller factor, $\boldsymbol{Q} = \boldsymbol{k'} - \boldsymbol{k}$ is the momentum transfer, $\boldsymbol{L}(\boldsymbol{Q})$ and $\boldsymbol{S}(\boldsymbol{Q})$ are the Fourier transforms of the orbital and spin densities

respectively. Here $\boldsymbol{A}$ and $\boldsymbol{B}$ are given by

$$\begin{aligned}\boldsymbol{A} &= 2(1-\hat{k}\cdot\hat{k}')(\hat{\varepsilon}'\times\hat{\varepsilon}) - (\hat{k}\times\hat{\varepsilon})(\hat{k}\cdot\hat{\varepsilon}') + (\hat{k}'\times\hat{\varepsilon}')(\hat{k}'\cdot\hat{\varepsilon}) \\ \boldsymbol{B} &= (\hat{\varepsilon}'\times\hat{\varepsilon}) + (\hat{k}'\times\hat{\varepsilon}')(\hat{k}'\cdot\hat{\varepsilon}) - (\hat{k}\times\hat{\varepsilon})(\hat{k}\cdot\hat{\varepsilon}') \\ &\quad -(\hat{k}'\times\hat{\varepsilon}')\times(\hat{k}\times\hat{\varepsilon})\end{aligned}$$

where $\hat{\varepsilon}$ and $\hat{\varepsilon}'$ are the incident and scattered polarisation vectors respectively and $\hat{k}$ and $\hat{k}'$ are unit vectors along the incident and scattered wavevectors respectively. It is worth noting here that the non-resonant magnetic scattering amplitude is reduced by a factor of $\tau = \hbar\omega/mc^2 = \hbar k/mc$ with respect to the charge scattering. For 8 keV X-rays the magnetic scattering amplitude is weaker by a factor of $\tau \approx \frac{1}{60}r_0$ compared with a change scattering amplitude of $\sim Zr_0$. This means that the intensity approaches $\left(\frac{1}{60}\right)^2 \approx 2\times10^{-4}$ weaker than the charge scattering from a single electron. In addition, the spin scattering amplitude scales with the net spin, which is small even for strongly magnetic systems. This results in non-resonant magnetic scattering amplitudes being very weak compared to the dominant charge scattering.

If we look to the f' and f'' terms as we approach an absorption edge the contribution due to electric dipole transition in a magnetic ion is given by (Hannon *et al.*, 1988)

$$f_{EL}(\omega) = \left(\frac{4\pi}{|\boldsymbol{k}|}\right) f_D \sum_{M=-L}^{L} \left[\hat{\varepsilon}'^{*}\cdot\boldsymbol{Y_{LM}}(\hat{k}')\boldsymbol{Y^{*}_{LM}}(\hat{k})\cdot\hat{\varepsilon}\right] F_{LM}(\omega) \qquad (6.3)$$

where $\boldsymbol{Y_{LM}}(\hat{k})$ are the vector spherical harmonics. The strength of the resonance is given by the term $F_{LM}(\omega)$ which is governed by atomic properties

and is given by

$$F_{LM}(\omega) = \sum_{\alpha,\eta} \frac{[P_\alpha P_\alpha(\eta)\Gamma_x(\alpha M\eta; EL)]}{\Gamma(\eta)\,[x(\alpha,\eta) - i]} \tag{6.4}$$

where η is the excited state, α is the initial state and P_α is the probability of the ion existing in the initial state α and $P_\alpha(\eta)$ is the probability for a transition from α to the final state η. Γ_x/Γ is the ratio of the partial line width of the excited state due to a pure electric dipole radiative decay to that from all processes including, say Auger decay. Finally the term x is given by $(E_\eta - E_\alpha - \hbar\omega)/(\Gamma/2)$, the deviation from the resonance condition in units of the total half-width. This form of scattering amplitude is valid for any isotropic system where the symmetry is broken only in one direction.

The term in square brackets in Equation 6.3 can be evaluated for an electric dipole transition at the L_{III} edge (for example the $2p_{3/2} \rightarrow 5d_{1/2}$ transition in Ho). The spherical harmonic terms can be written for $L = 1, M = \pm 1$:

$$\begin{aligned}\left[\hat{\varepsilon}'^* \cdot \boldsymbol{Y_{1\pm1}}(\hat{k}')\boldsymbol{Y^*_{1\pm1}}(\hat{k}) \cdot \hat{\varepsilon}\right] &= \left(\frac{3}{16\pi}\right)\Big[\hat{\varepsilon}' \cdot \hat{\varepsilon} \mp i(\hat{\varepsilon}' \times \hat{\varepsilon}) \cdot \hat{z_n} \\ &\quad - (\hat{\varepsilon}' \cdot \hat{z_n})(\hat{\varepsilon} \cdot \hat{z_n})\Big]\end{aligned} \tag{6.5}$$

and for $L = 1, M = 0$;

$$\left[\hat{\varepsilon}'^* \cdot \boldsymbol{Y_{10}}(\hat{k}')\boldsymbol{Y^*_{10}}(\hat{k}) \cdot \hat{\varepsilon}\right] = \left(\frac{3}{8\pi}\right)\left[(\hat{\varepsilon}' \cdot \hat{z_n})(\hat{\varepsilon} \cdot \hat{z_n})\right] \tag{6.6}$$

where $\hat{z_n}$ is a unit vector pointing in the direction of the magnetic moment

of the nth ion. We can group these terms as a resonant amplitude f^{XRES} which calculates f' and f'' given in Equation 6.1 as:

$$f_{nE1}^{XRES} = \Big[(\hat{\varepsilon}' \cdot \hat{\varepsilon})F^{(0)} - i(\hat{\varepsilon}' \times \hat{\varepsilon}) \cdot \hat{z_n}F^{(1)} + (\hat{\varepsilon}' \cdot \hat{z_n})(\hat{\varepsilon} \cdot \hat{z_n})F^{(2)}\Big] \quad (6.7)$$

with

$$F^{(0)} = (3/4k)[F_{11} + F_{1-1}] \quad (6.8)$$

$$F^{(1)} = (3/4k)[F_{11} - F_{1-1}] \quad (6.9)$$

$$F^{(2)} = (3/4k)[2F_{10} - F_{11} - F_{1-1}] \quad (6.10)$$

where the F_{LM} terms are given by Equation 6.4. The first term in Equation 6.7 has no dependance on the symmetry broken condition $\hat{z}_n$ and only contributes to the total charge scattering. It is through this term that the classical anomalous dispersion corrections f' and f'' enter into the resonant scattering amplitude. The second term contributes to first order magnetic satellite reflections for an incommensurate anti-ferromagnet and is proportional to the magnetization. The third term contributes to second order satellites in a incommensurate anti-ferromagnet and contains two powers of the magnetic moment. It is worth noting that it is the second term which can be used in a difference experiment with circularly polarised light to perform measurements on ferromagnetic systems.

For evaluation of the magnetic scattering intensities in an experimental setup Hill and McMorrow (1996) represented the polarisation terms in

Equation 6.7 by a 2×2 matrix with the polarisation states either being perpendicular or parallel to the scattering plane. Figure 6.1 schematically shows the coordinate system used in this description. We can define two polarisation states σ and π which correspond to the polarisation being either perpendicular or parallel to the scattering plane respectively. In this form the four possible configurations for incident and scattered polarisation are included in the matrix as:

$$\begin{pmatrix} (\sigma \rightarrow \sigma') & (\pi \rightarrow \sigma') \\ (\sigma \rightarrow \pi') & (\pi \rightarrow \pi') \end{pmatrix} \tag{6.11}$$

In this formulation the resonant scattering amplitude is given by (Hill and

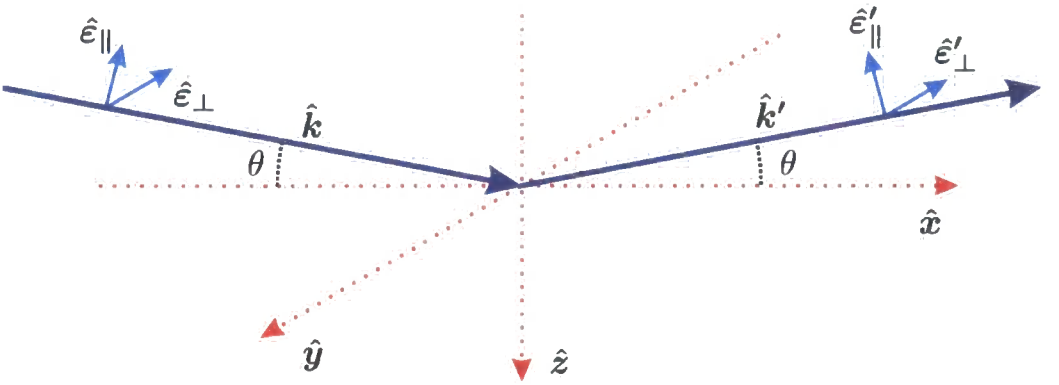

Figure 6.1: Coordinate system for a resonant X-ray scattering experiment.

McMorrow, 1996):

$$
\begin{aligned}
f_{E1}^{XRES} &= F^{(0)} \begin{pmatrix} 1 & 0 \\ 0 & \cos 2\theta \end{pmatrix} \\
&\quad - iF^{(1)} \begin{pmatrix} 0 & z_1 \cos\theta + z_3 \sin\theta \\ z_3 \sin\theta - z_1 cos\theta & -z_2 \sin 2\theta \end{pmatrix} \\
&\quad + F^{(2)} \begin{pmatrix} z_2^2 & -z_2 \left(z_1 \sin\theta - z_3 cos\theta\right) \\ z_2 \left(z_1 \sin\theta + z_3 \cos\theta\right) & -\cos^2\theta \left(z_1^2 \tan^2\theta + z_3^2\right) \end{pmatrix}
\end{aligned} \tag{6.12}
$$

Where θ is the Bragg angle. Analysing the three terms in the above equation leads us to the following results. The amplitude of the first term for $\sigma \rightarrow \sigma'$ scattering is unity whereas for the $\pi \rightarrow \pi'$ scattering there is a factor of $\cos 2\theta$. This term in $F^{(0)}$ contributes only to the charge scattering and these results are identical to the polarisation dependence of Thompson charge scattering from a single electron. For the terms where the polarisation is rotated the amplitude is zero and where the plane of polarisation is parallel to the scattering plane the amplitude is decreased by a factor of $\cos 2\theta$, the familiar term for the polarisation dependance of charge scattering. The two further matrices give the polarisation dependance of the first- and second-order magnetic satellites.

For magnetic scattering experiments using linear polarisation at synchrotron sources, diffraction is usually performed in the vertical direction with the incident X-ray beam polarised in the horizontal plane (the plane of orbit of the electron (or positron) beam), the so called σ polarisation state. For the case where polarisation analysis is possible the magnetic scattering

cross-section is to first-order:

$$\frac{d\sigma}{d\Omega}(\sigma \rightarrow \sigma') = 0 \tag{6.13}$$

$$\frac{d\sigma}{d\Omega}(\sigma \rightarrow \pi') = \left|-iF^{(1)}(z_3 \sin\theta - z_1 \cos\theta)\right|^2 \tag{6.14}$$

and to second-order;

$$\frac{d\sigma}{d\Omega}(\sigma \rightarrow \sigma') = \left|F^{(2)}(z_2^2)\right|^2 \tag{6.15}$$

$$\frac{d\sigma}{d\Omega}(\sigma \rightarrow \pi') = \left|F^{(2)} z_2(z_1 \sin\theta + z_3 \cos\theta)\right|^2 \tag{6.16}$$

where z_1 is the component of magnetisation along the incident beam and z_2 is the direction normal to the scattering plane. The term z_3 is given by the product $(z_1 \times z_2)$ as shown in Figure 6.1. In an experiment using σ polarised light the experiment is sensitive to the projection of the magnetization along the direction of the scattered beam $\hat{k}'$.

6.2 Experimental Background

6.2.1 Beamline

The experiments were carried out on the soft X-ray spectroscopy beamline 5U1 on the SRS synchrotron radiation source, Daresbury Laboratory, UK. The X-ray source at Station 5U.1 consists of a one meter long, ten period, variable gap permanent magnet undulator. With the maximum gap of 42 mm the fundamental energy is at 60 eV with quasi-continuous harmonics up to 2 keV. Figure 6.2 shows the calculated and measured flux as a function of

energy for the undulator (with kind permission of M.D. Roper, SRS Daresbury Laboratory, UK). The resultant polychromatic X-ray beam exits from the undulator and is incident upon the monochromator system. A schematic diagram of the optical layout is shown in Figure 6.3. The monochromator consists of three main optical elements. On the upstream side, closest to the source, the X-rays are reflected from a 250 mm long platinum coated plane mirror. The monochromation is provided by a 1200 line mm^{-1} platinum coated plane grating. Finally, the monochromatic X-rays are focused by a platinum coated spherical mirror. An ellipsoidal mirror is placed further downstream of the monochromator system which acts to refocus the X-rays onto the sample.

The energy resolution $\Delta E/E$ of the diffraction grating, and thus the

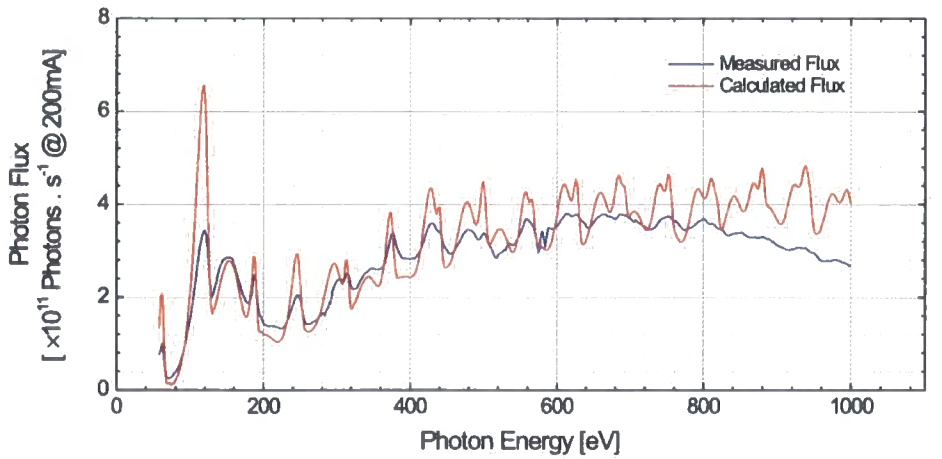

Figure 6.2: Calculated (red) and measured (blue) flux from the soft X-ray undulator on station 5U1 at a storage run current of 200 mA (data courtesy of M.D. Roper, CLRC Daresbury Laboratory).

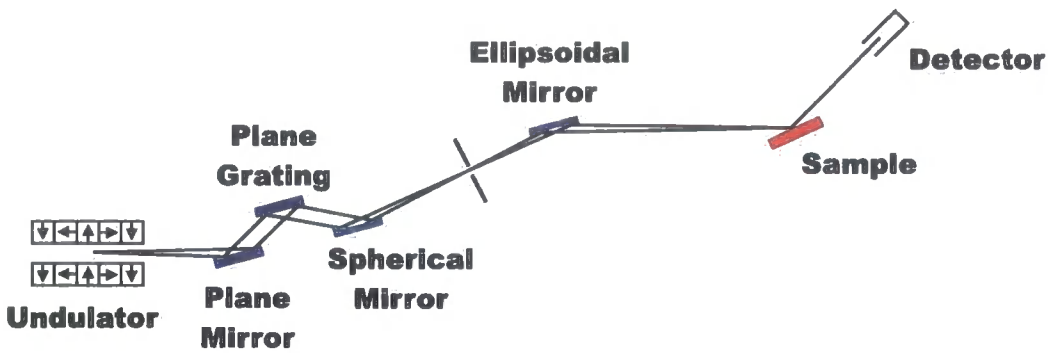

Figure 6.3: Schematic layout of the optical elements on beamline 5U1, SRS Daresbury Laboratory, UK.

resolution of the beamline, is strongly dependant on energy. Figure 6.4 shows the calculated energy resolution available of station 5U1 as a function of energy for different entrance slit sizes from the undulator.

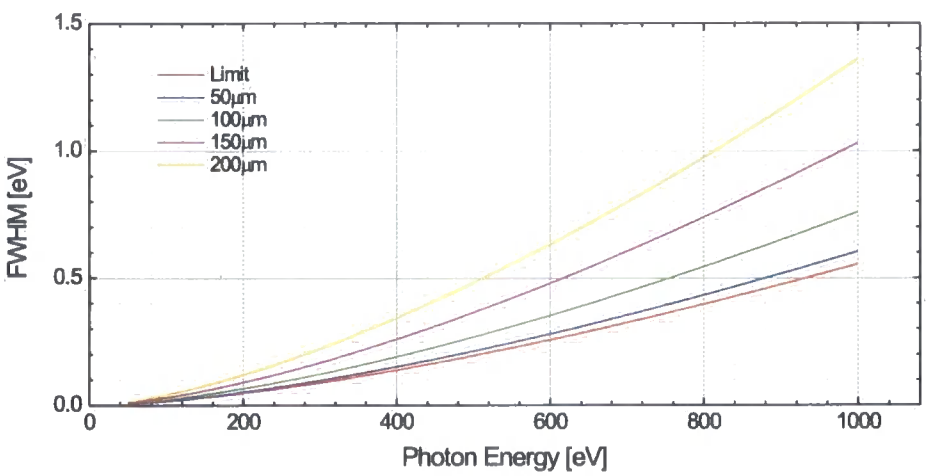

Figure 6.4: Measured resolution (FWHM $\Delta E/E$) from the soft X-ray beamline installed on 5U1 (data courtesy of M.D. Roper, CLRC Daresbury Laboratory).

6.2.2 Diffractometer

Due to the very short penetration depths of soft X-rays in air, the technical difficulties are far greater for performing diffraction at such energies than with conventional ($\sim$ 10 keV) X-ray. The experiments were carried out in the in-vacuum two-circle soft X-ray diffractometer available at the SRS. The diffractometer consists of two concentric circles (sample and detector) driven externally from stepper motors through pumped differential o-ring seals. A photograph of the diffractometer installed on the beamline is shown in Figure 6.5. X-ray detection is provided by measurement of the drain current from a silicon p-i-n diode, measured by amplification and current to voltage conversion. The voltage output is then input to a voltage to frequency converter with the output, a frequency proportional to the incident photon flux, input into the usual counting chain available at the beamline. The sample is mounted on a three point kinematic mount, upon which is mounted a copper χ arc which provides to allow for a small amount of sample alignment.

Samples were pre-aligned using a laboratory based diffractometer (see Wilkins *et al.*, 2002) using the copper χ arcs. These samples were then aligned in the diffractometer using a laser which was arranged to be coincident with the incident X-ray beam.

To cool the samples within the UHV environment of the diffractometer several modifications were made to the diffractometer by design of the author and Mr. M.D. Roper of Daresbury Laboratory. Figure 6.6 shows the inside of the vacuum chamber of the soft X-ray diffractometer with the modifica-

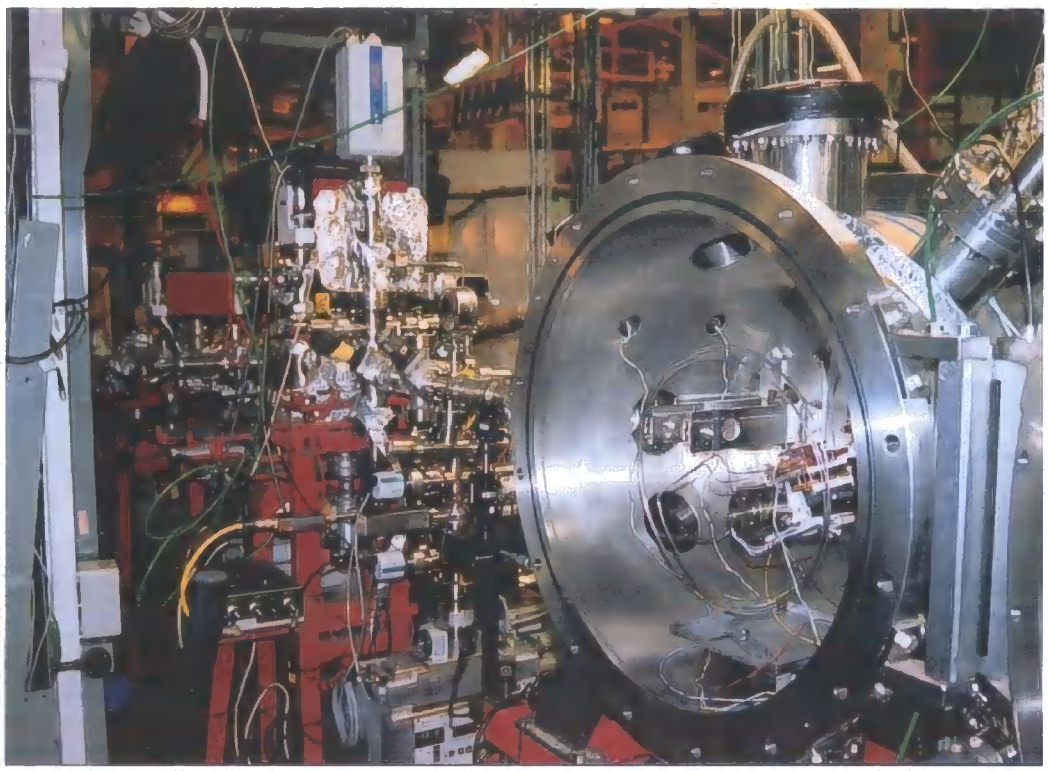

Figure 6.5: Picture of the two-circle soft X-ray diffractometer installed on station 5U1 on the SRS Daresbury Laboratory, UK

tions to allow the cooling of samples. Cooling power was provided by the use of a copper heat exchanger, upon the underside of which 0.5 mm bore stainless steel tubes were brazed. The stainless steel tubes were passed to the outside of the diffractometer through a UHV compatible flange. Liquid nitrogen from a pressurised dewar was re-liquified before entrance to the diffractometer by means of a exchange coil placed into a bath of liquid nitrogen. The re-liquified gas/liquid mixture was passed though the 0.5 mm bore tubes within the diffractometer. Once the gas/liquid mixture has passed through the system it was exhausted to the atmosphere. A film heater was attached to the copper heat exchanger and controlled by means of a Lakeshore

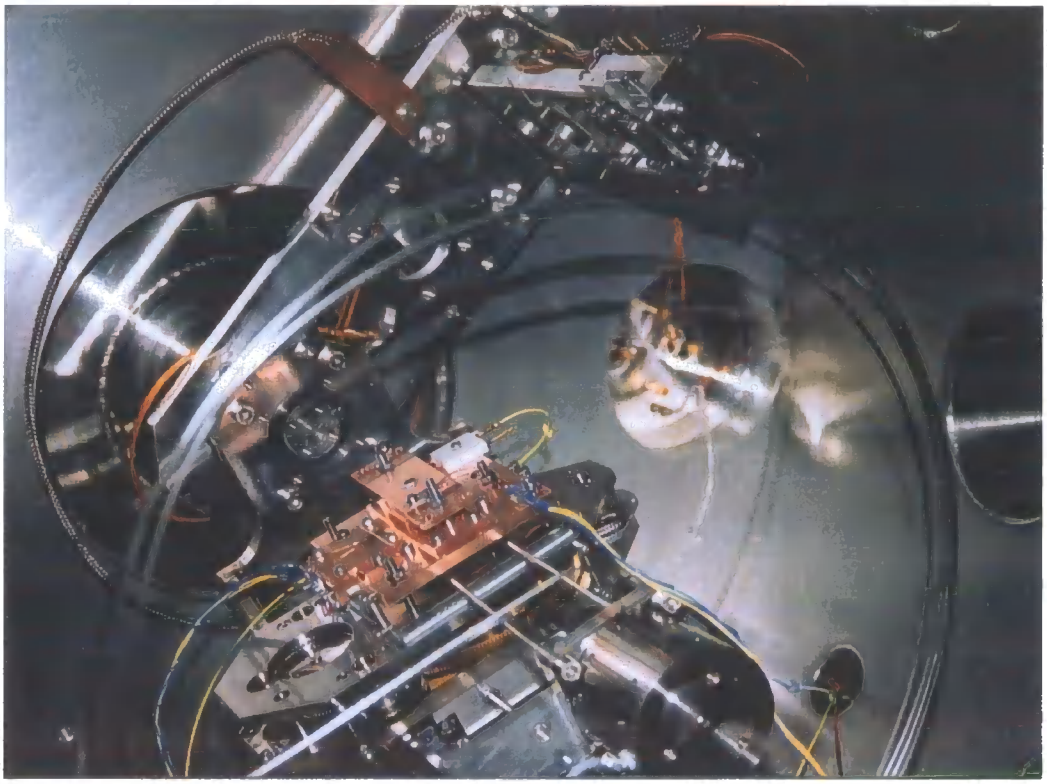

Figure 6.6: Inside picture of the soft X-ray diffractometer on station 5U1.

temperature controller. The sample and control temperature was monitored by silicon diodes and the temperature stability was $\sim \pm 0.05$ K. This is displayed in Figure 6.7 which displays the temperature dependance of the commensurate - incommensurate magnetic phase transition in $UAs_{1-x}Se_x$, $x = 0.15$ (Longfield *et al.*, 2001) measured on the soft X-ray diffractometer at the N_{IV} and N_V edges of uranium. The stability of the cryogenic cooling allowed the phase transition to be followed at small intervals of approximately 0.25 K. The performance of the liquid nitrogen cooling system was found to be similar, if not better, than that of commercial cryostat systems.

For quantitative measurements of the scattered photon flux the GaAsP

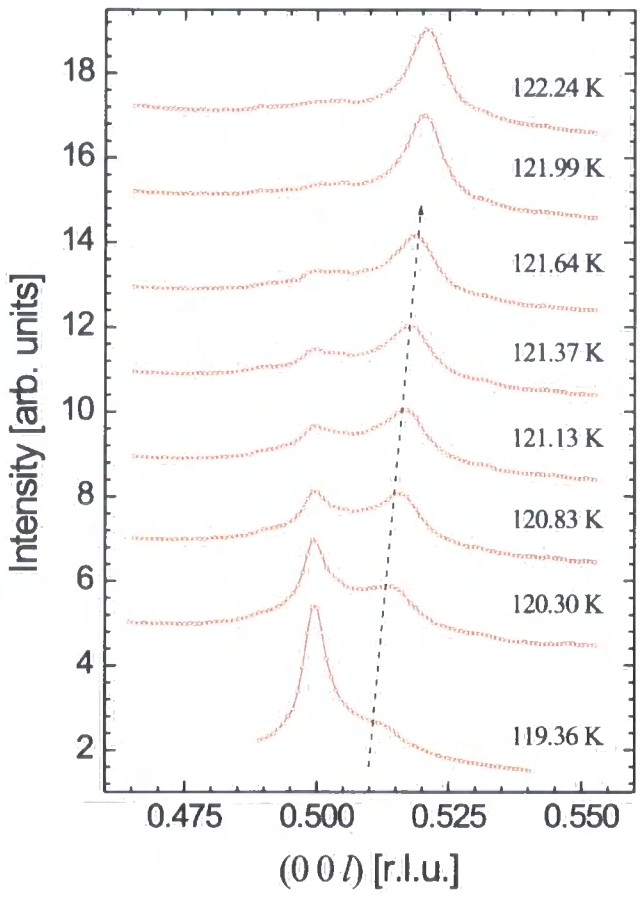

Figure 6.7: Temperature and wavevector dependance of the commensurate to incommensurate magnetic phase transition in $UAs_{1-x}Se_x$ measured on the diffractometer described in Section 6.2.2.

photodiode was calibrated (Roper, 2002), the energy dependance of which is shown in Figure 6.8. These data allowed for estimates of the photon flux scattered from the sample to be made. For most data the intensity was normalised to the beam monitor so no direct conversion to photon flux was made.

6.3 Samples

As discussed previously in Chapter 5, $La_{2-2x}Sr_{1+2x}Mn_2O_7$ with $x = 0.475$ and 0.45 undergoes magnetic transitions at $T_N \approx 180$ K and $T_N \approx 160$ K, respectively, into an anti-ferromagnetic state. In this state, superlattice reflections appear due to the AFM order at (0, 0, n) with $n = 1, 3, 5, \ldots$ as

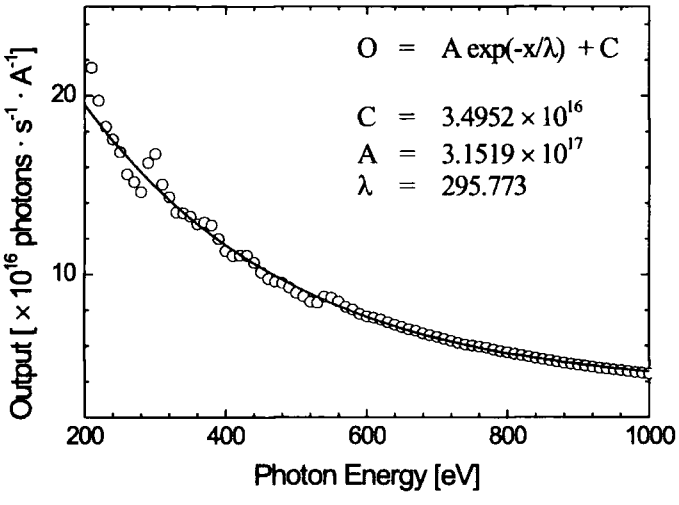

Figure 6.8: Measured output current per photon as a function of energy for the GaAsP photodiode used in the soft X-ray diffractometer.

previously reported by Chatterji *et al.* (2000). In this magnetic state the manganese spins align along the ⟨ 1, 1, 0 ⟩ direction. Figure 6.9 shows the magnetic and crystal structure of $La_{2-2x}Sr_{1+2x}Mn_2O_7$ at a temperature below T_N for $x = 0.475$ and $x = 0.45$. In the magnetic structure (schematic only) the spin on the manganese ions are shown. The magnetic order is of the A-type as defined by Goodenough (1955).

6.4 Experimental Details

Single crystal samples of $La_{2-2x}Sr_{1+2x}Mn_2O_7$ with $x = 0.475$ and 0.45 grown at the Department of Physics, University of Oxford by the floating zone method were pre-aligned and mounted on the two-circle diffractometer outlined in section 6.2.2. The crystal was indexed in the *I4/mmm* setting with lattice parameters $a = b = 3.87$ Å, $c = 20.1$ Å. The sample was mounted in the ⟨ 0, 0, 1 ⟩ / ⟨ 1, 1, 0 ⟩ zone with the ⟨ 0, 0, 1 ⟩ in the Q_z direction and the ⟨ 1, 1, 0 ⟩ along the incident beam. Initially the incident photon energy was set to $E = 900$ eV which allowed the (0, 0, 2) reflection to be accessed at an angle of $2\theta = 87.4°$. A 300 μm slit was placed in front of the detector to increase the experimental resolution.

Figure 6.10 shows a scan of the sample (θ) axis through the (0, 0, 2) Bragg reflection. The resultant peak was fitted to a Gaussian lineshape and gives a full width at half maximum of 0.0784°. A Gaussian lineshape is consistent with the broadening in this direction arising from the mosaic spread of the sample. Scans measured in the $\theta - 2\theta$ were transformed into

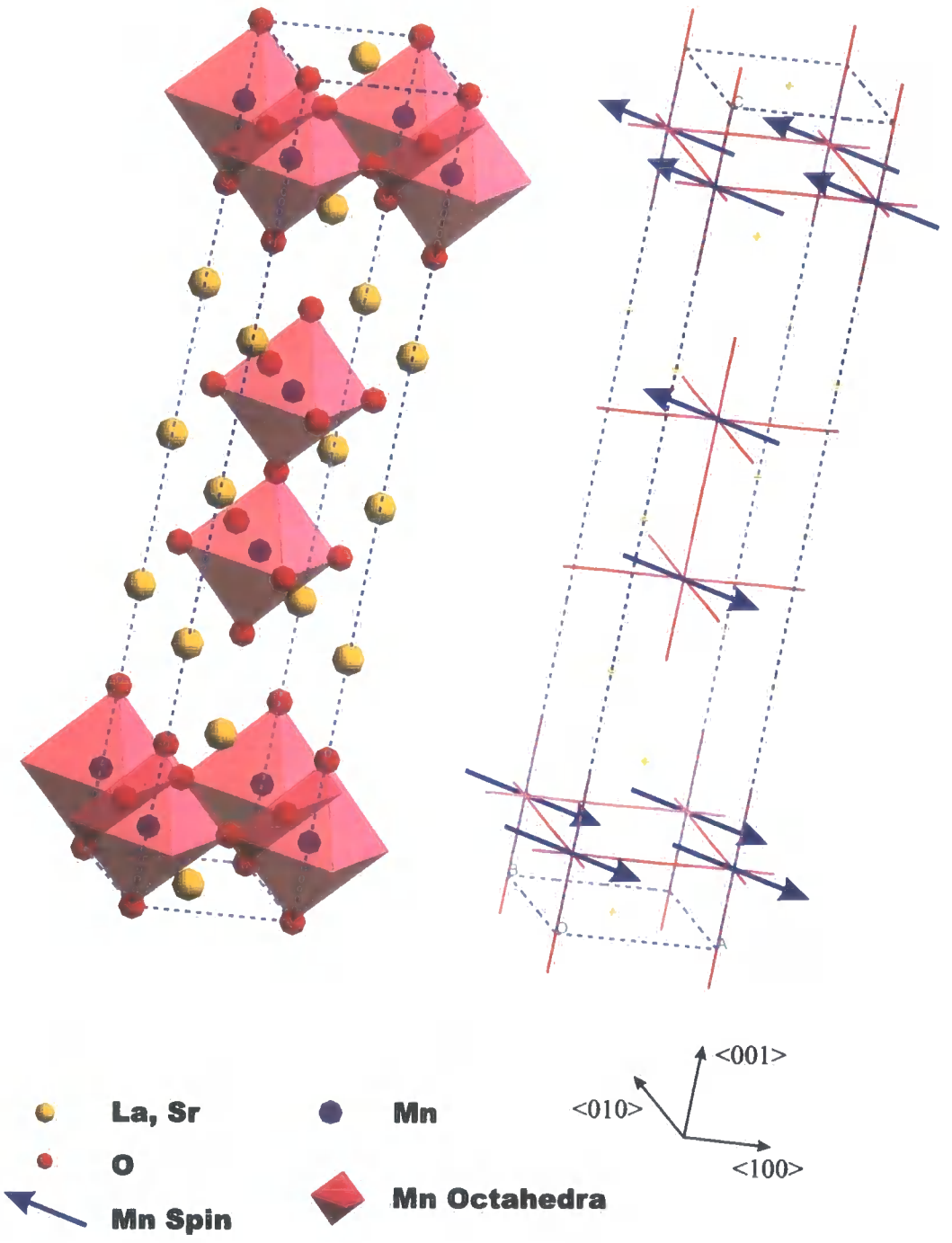

Figure 6.9: The crystallographic (left) and magnetic (right) structure of $La_{2-2x}Sr_{1+2x}Mn_2O_7$.

reciprocal space coordinates using

$$Q_z = \frac{4\pi}{\lambda} \sin \frac{2\theta}{2}$$

where 2θ is the detector angle. Figure 6.11 shows a scan taken through the (0, 0, 2) Bragg peak in the Q_z $(\theta - 2\theta)$ direction. The resultant peak was fitted to a Lorentzian lineshape with a width of $2.7074 \pm 0.015 \times 10^{-3}$ Å^{-1}.

With scattering at soft energies one question which is posed is whether the scattering is dynamical or kinematical. The extinction depth, measured at the point of total reflection in the rocking curve, is a measure of the attenuation of the X-ray beam as it is transmitted through the crystal. The

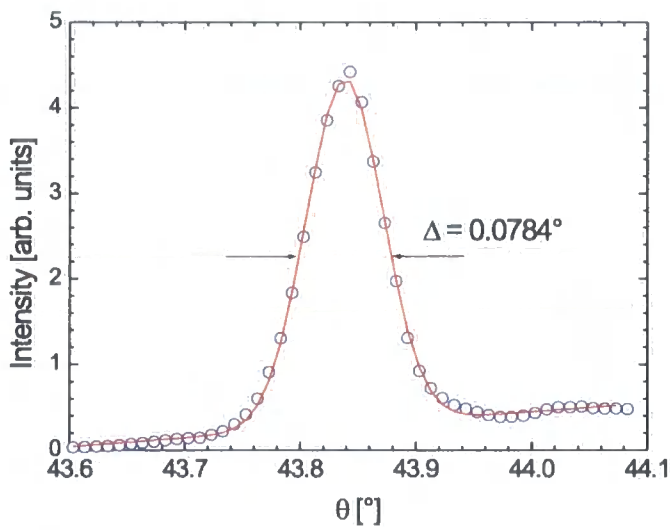

Figure 6.10: Scan in the θ direction through the (0, 0, 2) Bragg peak. The solid line is a Gaussian fit to the experimental data (open circles) with a linear background.

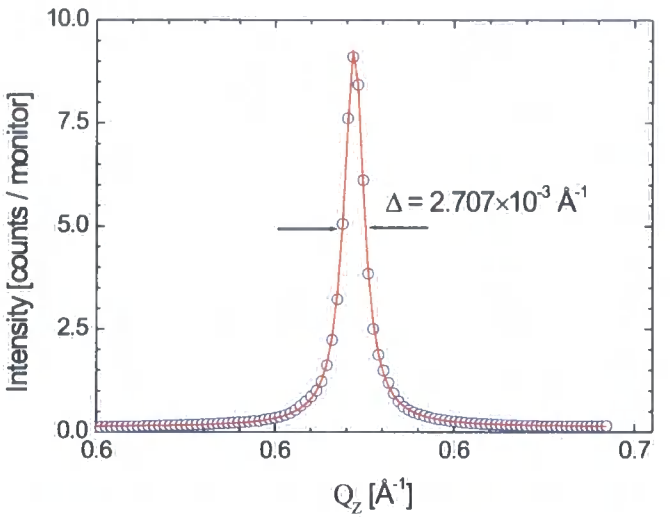

Figure 6.11: Scan in the Q_z ($\theta \rightarrow 2\theta$) direction through the (0, 0, 2) Bragg peak. The solid line is a Lorentzian fit to the experimental data (open circles).

length Λ_E is a measure of the distance required for the *intensity* to be reduced by a factor of $1/e$, and is given by

$$\Lambda_E = \frac{qv_c}{8\pi r_o} \cdot \frac{1}{|F(\boldsymbol{Q}, \hbar\omega)|} \tag{6.17}$$

where v_c is the volume of the unit cell, r_0 is the Thompson scattering length, q is the reciprocal lattice vector and $|F(\boldsymbol{Q}, \omega)|$ is the modulus of the structure factor given by

$$F_{hkl}(\boldsymbol{Q}, \hbar\omega) = \sum_j (f^0(\hbar\omega) + f'(\hbar\omega) + if''(\hbar\omega))\, e^{i\boldsymbol{r_j}\cdot\boldsymbol{q}}$$

where $f^0(\hbar\omega)$, $f'(\hbar\omega)$ and $f''(\hbar\omega)$ are the resonant scattering factors. For

an incident energy of $\hbar\omega = 900$ eV the structure factor gives a value of $F = 19.1336 - 10.1184i$ using the resonant scattering factors given in the Henke tables, described by Henke *et al.* (1993). Solving Equation 6.17 for this value of structure factor gives an extinction depth of $\Lambda_{\text{dynamical}} = 12304$ Å. The absorption can be calculated from solely the values of $f''(\hbar\omega)$ and for a given material can be calculated by

$$\mu(\hbar\omega) = \frac{2\lambda r_0}{v_c} \sum_j f''(\hbar\omega) \tag{6.18}$$

where λ is the incident wavelength, r_0 is the Thompson scattering length v_c is the volume of the unit cell. Performing this calculation gives a value of $\mu_{900\text{ eV}} = 8.0857 \times 10^{-4}\text{Å}^{-1}$ from which a penetration depth can be estimated using

$$\Lambda_{\text{abs}} = \frac{1}{\mu} \sin\theta$$

where θ is the sample angle. This gives a value for $\Lambda_{\text{abs}} = 770$ Å. From these calculations we can see that the penetration depth is far less than the extinction length confirming that the scattering from Bragg reflections can be modelled within the kinematical approximation.

From the fitted width of the Bragg peak in reciprocal space the inverse correlation length can be calculated, consistent with the model outlined in Appendix A for a Lorentzian lineshape. The inverse correlation length was calculated to be $1.354 \times 10^{-3}\text{Å}^{-1}$ which gives an estimate of 738.7 ± 4 Å for the correlation length consistent with the derivation in Appendix A. This value is in agreement with the absorption depth calculated above.

Having located a Bragg peak it was possible to calculate the location of the (0, 0, 1) peak in diffractometer coordinates. The diffractometer was moved to the angles corresponding to this wavevector and initially the energy was set to 625 eV, some distance away from the L edges of manganese. At this wavevector a peak was detected in both the θ and 2θ directions. The inverse correlation length measured from the FWHM was calculated to be 0.667×10^{-3} Å. This is much sharper than the (0, 0, 2) Bragg peak measured at 900 eV shown in Figure 6.11. What is the origin of this peak?

One major problem with the optical design of the beamline outlined in Section 6.2.1 is that of harmonic contamination. In the $\sim$ 625 eV region, the grating and mirrors pass a substantial proportion of second- and third-order light in addition to the first order. At an energy of 1250 eV (the second-order of 625 eV) the (0, 0, 2) reflection is accessible and will appear in the same point in angle space as the (0, 0, 1) reflection at 625 eV. Returning to the inverse correlation lengths (widths) calculated, if we now assume that the (0, 0, 1) peak originates from diffraction at $E = 1250$ eV the inverse correlation length is calculated to be 1.33×10^{-3} Å. If we compare this with the value of 1.354×10^{-3} Å^{-1} measured on the (0, 0, 2) peak at 900 eV we can see that the two values are almost identical, confirming the origin of the off-resonant peak. From this point forward, the second order contamination was subtracted as a background from the data collected.

The sample was cooled to 83 K, the base temperature of the cooling system, and energy scans were taken at the (0, 0, 1) position through the manganese L_I, L_{II} and L_{III} edges at 769.1 eV, 649.9 eV and 638.7 eV respectively. Figure 6.12 shows the energy scan at fixed wavevector through

the L_I edge showing no resonance at this energy. The L_I edge corresponds to a transition from the $2s \rightarrow 3p$ energy levels and thus does not probe the energy levels split due to the magnetic state of the ion, therefore no scattering due to the magnetic alignment would be expected. This is indeed what was observed.

Energy scans using the same method of fixing the wavevector were performed through the L_{II} and L_{III} edges of manganese in both the $x = 0.475$ and $x = 0.45$ samples. The results are shown in Figure 6.13 and Figure 6.14 respectively. Below the Neél temperature (T_N) a substantial resonance can be seen at the L_{III} edge with a weaker resonance at the L_{II} edge. The resonance appears to be split into a doublet with a separation of $\sim$ 2.5 eV.

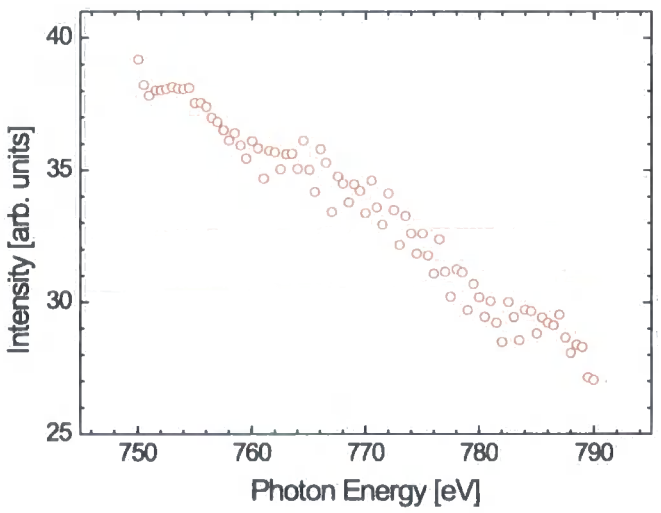

Figure 6.12: Energy scan through the L_I edge at constant Q on the (0, 0, 1) reflection. (Note : the background from the (0, 0, 2) is not subtracted)

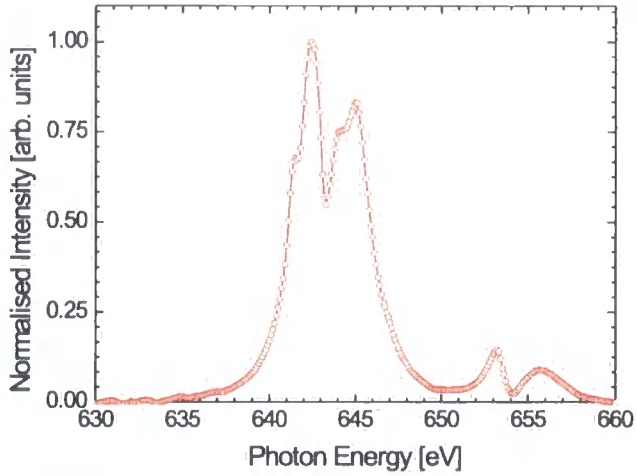

Figure 6.13: Energy scan at fixed wavevector, background subtracted, through the (0, 0, 1) AFM ordering superlattice reflection in the $n_h = 0.475$ sample. These data were taken in the high resolution mode of the beamline with a 30 μm slit giving a resolution of $\Delta E/E = 0.2849$ (calculated).

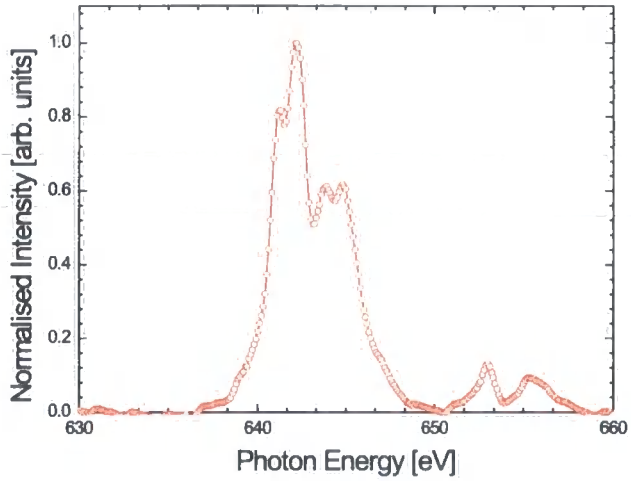

Figure 6.14: Energy scan at fixed wavevector, background subtracted, through the (0, 0, 1) AFM ordering superlattice reflection in the $n_h = 0.45$ sample. These data were taken in the high resolution mode of the beamline with a 30 μm slit giving a resolution of $\Delta E/E = 0.2849$ (calculated).

We attribute this resonance to be due to the resonant magnetic exchange scattering from the AFM order present in the sample.

To test the origin of the resonant scattering detected the sample was warmed to above the Neél (T_N) temperature and an energy scan was performed at $T = 300$ K. Figure 6.15 shows the energy scan obtained at high temperature above T_N showing no resonance at either the L_{II} or L_{III} edges. This result further confirms that the background peak is the (0, 0, 2) Bragg peak diffracting from second-order light. If the scattering was due to a (0, 0, 1) type peak at the first order energy, then the energy scan would show a substantial variation with energy. This is due to anomalous scattering effects from tuning through the manganese edge caused by a variation in the

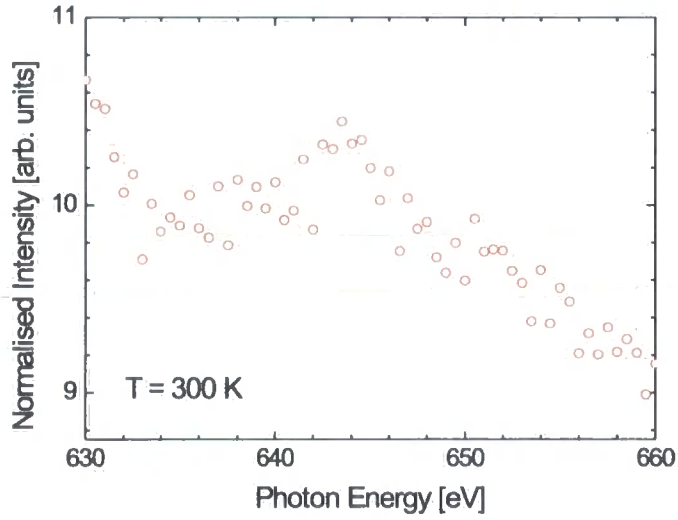

Figure 6.15: Energy scan at constant Q through the L_{II} and L_{III} edges of manganese at $T = 300$ K (Note : the background from the (0, 0, 2) is not subtracted)

anomalous scattering factors at the L edge. However, if the scattering is from second-order light then the energy range is really 1240 eV $< E <$ 1320 eV at which no absorption edges appear from elements present in the sample, therefore no variation would be expected.

The sample was re-cooled to the base temperature available (83 K) and scans through the (0, 0, 1) AFM superlattice reflection in the θ and $\theta - 2\theta$ direction were taken. Figure 6.16 shows a scan in the Q_z direction ($\theta - 2\theta$) and the corresponding fit to a Lorentzian lineshape is shown by the solid line, giving a value for the inverse correlation length to be 2.252×10^{-3} Å^{-1}. The inverse correlation lengths of the AFM spin order and the (0, 0, 2) Bragg peak were compared. A comparison of scans taken in the Q_z direction for both the (0, 0, 1) and (0, 0, 2) is shown in Figure 6.17.

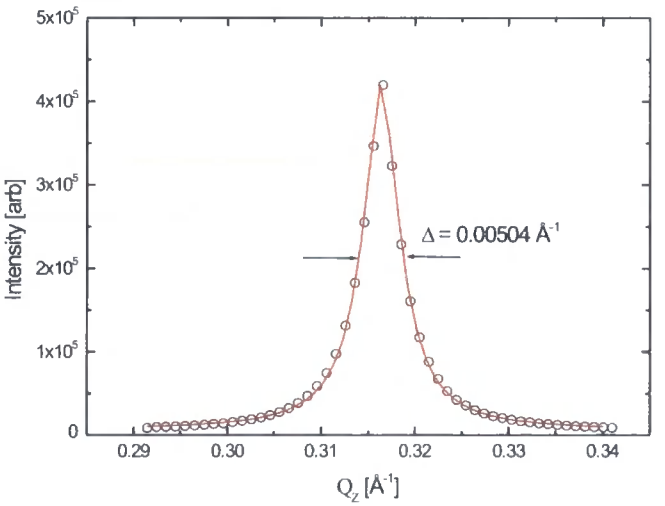

Figure 6.16: Scan through the (0, 0, 1) AFM ordering peak in the Q_z direction. The solid line is a Lorentzian fit to the experimental data.

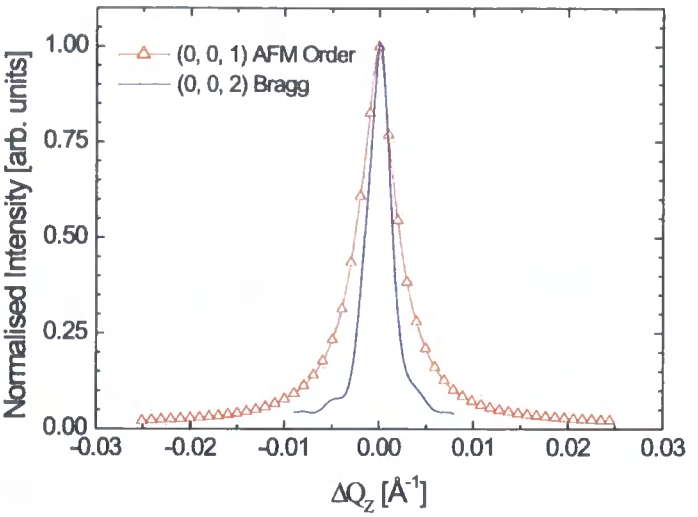

Figure 6.17: Comparison in the Q_z direction between the (0, 0, 2) Bragg peak (solid line) and the (0, 0, 1) AFM peak (open triangles).

The correlation length can be estimated using the model in Appendix A and gives a value of 444 Å, approximately half that of the correlation length estimated on the (0, 0, 2). The reason for the broadening on resonance is most likely due to the decrease in penetration depth on resonance because of the increased absorption at the L_{III} edge. Similar effects have been seen in multilayer samples using soft X-ray reflectivity by Hase (1998).

The temperature dependance of the (0, 0, 1) AFM peak was measured at $E = 641$ eV and $E = 644$ eV corresponding to the two main peaks in the energy scans at fixed wavevector (Figures 6.13 and 6.14). This was accomplished by fitting scans collected in the $\theta - 2\theta$ direction to a Lorentzian lineshape in the same manner as above. From the resultant fits of the data the integrated area was determined and Figure 6.18 and Figure 6.19 display this

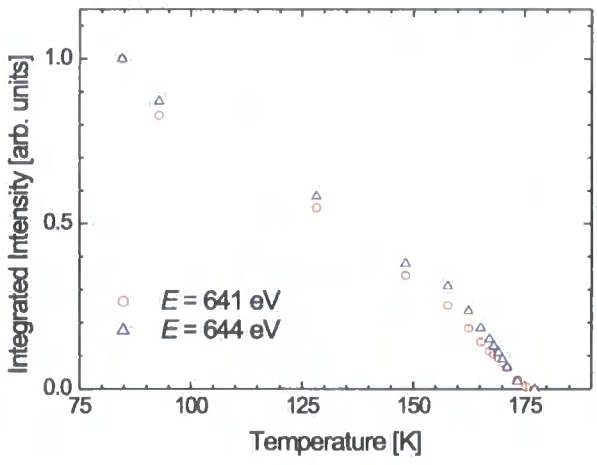

Figure 6.18: Integrated area of the (0, 0, 1) AFM superlattice reflection as a function of temperature in the $n_h = 0.475$ sample at $E = 641$ eV (red circles) and $E = 644$ eV (blue triangles). The non-resonant background has been subtracted.

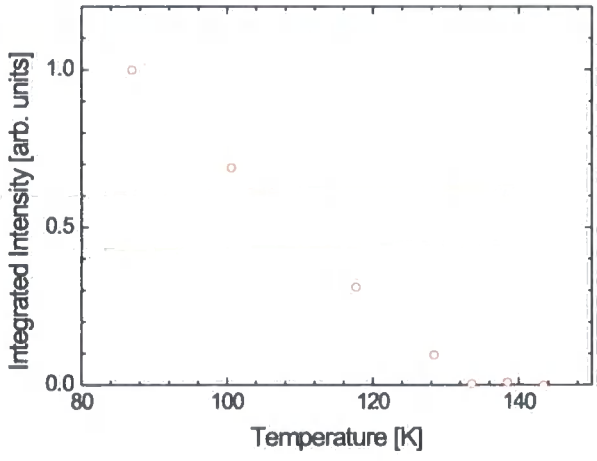

Figure 6.19: Integrated area of the (0, 0, 1) AFM superlattice reflection as a function of temperature in the $n_h = 0.45$ sample at $E = 641$ eV (red circles) and $E = 644$ eV (blue triangles). The non-resonant background has been subtracted.

as a function of temperature. The background from the (0, 0, 2) harmonic has been subtracted from these data. Initially apparent from these data is the identical shape at 641 eV and 644 eV showing that the ratio of the integrated areas measured at each energy does not change as a function of temperature. Both energies show a decrease in the intensity, and thus the AFM order as the temperature is increased. Such results are similar to those obtained by Chatterji *et al.* (2000) in their neutron diffraction study of the A-type AFM order on the $x = 0.5$ sample. The phase transition, from the intensity vs. temperature data, appears to look second-order in nature.

To search for other periods of magnetic ordering of the manganese, a long scan along the Q_z direction was performed at the L_{III} edge of manganese, the results of which are shown in Figure 6.20. In this scan the strong specular scatter can be seen as a decreasing background with increasing wavevector in addition to the very strong (0, 0, 1) AFM peak. In addition two peaks can be seen appearing around the (0, 0, 1.5) position ($Q_z \approx 0.6$ Å^{-1}). Figure 6.21 shows these two peaks in the Q_z direction around the (0, 0, 1.5) position. Scans of energy with a fixed wavevector were performed at both peak positions, the results of which are shown in Figure 6.22. The origin of these peaks is unclear and the resonance data do not compare with those of Figure 6.13 and 6.14.

In addition to measurements at the manganese L edges, the M_{IV} and the M_V edges of lanthanum at 853 eV and 836 eV respectively were studied. Here resonances were found at both the M_{IV} and M_V edges on the specular scatter from the sample. No superlattice reflections along the $\langle 0, 0, 1 \rangle$ direction were found but by setting θ to be half of the 2θ value, appreciable specular

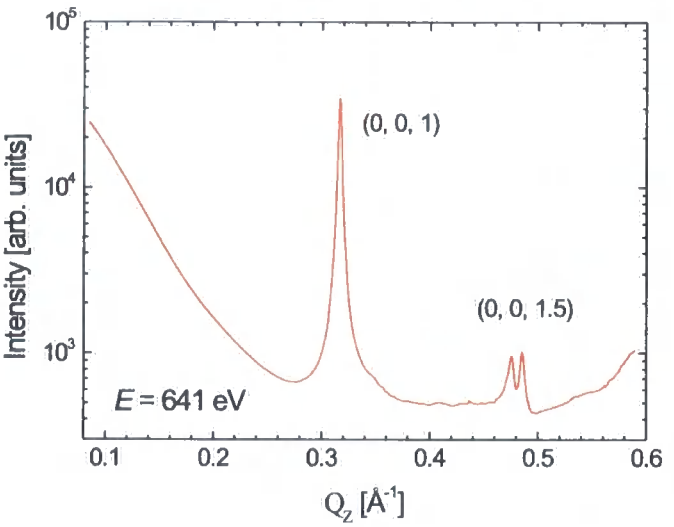

Figure 6.20: Scan along the Q_z direction with an incident photon energy of 641 eV, corresponding to the peak in resonance observed previously.

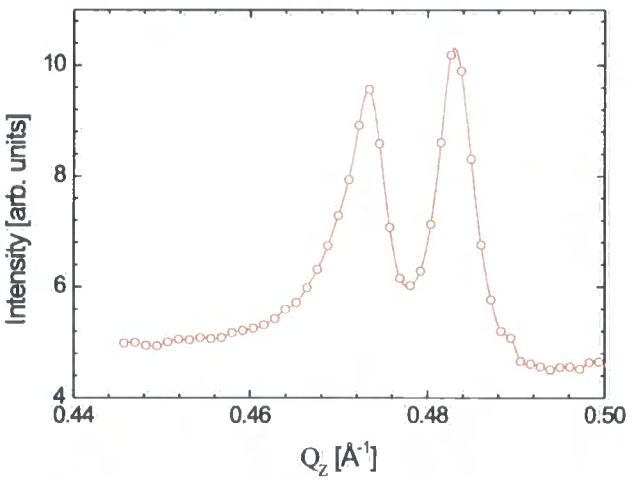

Figure 6.21: Q_z scan through around the (0, 0, 1.5) position showing the two peaks located at $E = 641$ eV.

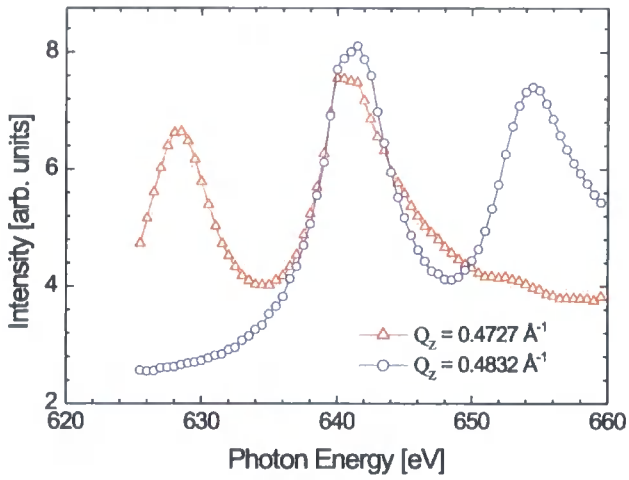

Figure 6.22: Energy scans at fixed wavevectors of $Q_z = 0.4727$ Å^{-1} (triangles) and $Q_z = 0.4832$ Å^{-1} (circles).

scatter was found similar to that found in thin-film reflectivity measurements. Such a resonance is most likely due to resonant charge scattering. With the indication that charge scatter may be resonantly enhanced the incident photon energy dependance of the (0, 0, 2) Bragg reflection was measured. Figure 6.23 shows these data. No measurement was taken below an energy of 635 eV as the 2θ angle of the reflection was larger than the maximum possible within the diffractometer. Here a large resonant enhancement of the charge can be seen at both the L_{III} and L_{II} edges. The resonance enters the scattering cross-section through modifications to the resonant scattering terms. The energy dependance of the resonance is different from that on the (0, 0, 1) magnetic reflection. Here there is not the same fine structure present from the splitting of the $3d$ band and the resonances are both approximately

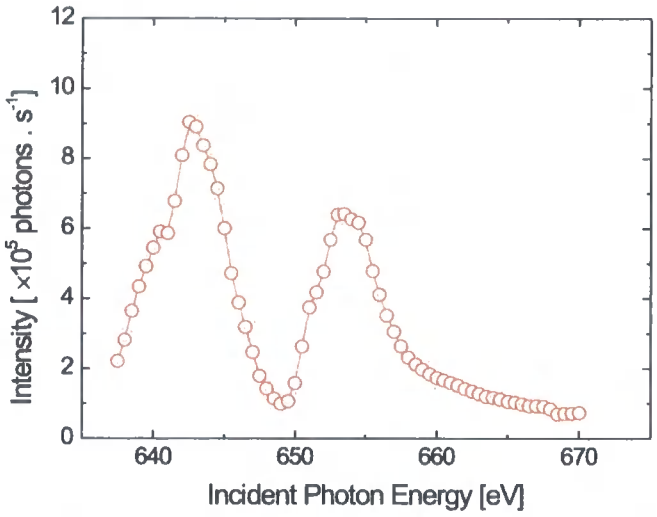

Figure 6.23: Scan of incident photon energy at constant wavevector on the (0, 0, 2) Bragg reflection at $T = 300$ K.

singular and broader in energy range with widths of approximately ~ 5 eV.

Turning to the integrated intensities of the AFM peak shown in Figure 6.18 and Figure 6.19 here our results follow the same trend that was observed by Chatterji *et al.* (2000) in their neutron diffraction results on a sample of $La_{2-2x}Sr_{1+2x}Mn_2O_7$, $x = 0.5$. As the lowest temperature available in the soft X-ray diffractometer is 80 K it was not possible to cool the sample further to see if the intensity eventually reaches a constant value at low temperature. Here we have to take into account the difference in the doping levels of the samples we have studied. This probably accounts for the difference in T_N observed in the soft X-ray scattering data coupled with the much greater intensity in the X-ray data allowing the scattering from the AFM order to be followed to higher temperatures. Some hysteresis was observed

in the AFM order, suggesting a first-order phase transition into the magnetic state, however, the gradual increase in intensity below T_N suggests that as the sample is cooled below T_N the A-type AFM order is not instantaneous but increases gradually on cooling the sample and the phase transition is more second-order like in nature.

If we recall the results from Chapter 5 on the same single crystal of $La_{2-2x}Sr_{1+2x}Mn_2O_7$, $x = 0.475$ we have measured the charge ordering and Jahn - Teller (J-T) ordering as a function of temperature. Here, the charge ordering (CO) is found to be re-entrant in nature, it reaches a maximum at a temperature of 180 K at which point upon cooling the system further caused the charge order to collapse. If we look also at the J-T order it follows a similar trend, peaking at a temperature of 180 K also, but upon further cooling it never collapses to zero intensity. As we have postulated in Chapter 5 the reason that the integrated intensity of the J-T does not disappear while the CO does is because in the experiment the J-T signal is many orders of magnitude greater at the maximum value. What causes the charge order to collapse?

Figure 6.24 shows the integrated intensity of the (1.5, 0.5, 0) CO reflection plotted with the (0, 0, 1) AFM superlattice reflection measured using soft X-ray magnetic scattering. Here we can see that at the onset of the AFM order at 180 K this point corresponds exactly to the maximum intensity from the charge order. Upon cooling the sample, the charge order is seen to grow in intensity below the charge ordering temperature $T_{CO} = 215$ K. However at 180 K the A-type AFM order starts to grow in intensity and there exists competition between the charge ordering, Jahn-Teller ordering and the A-

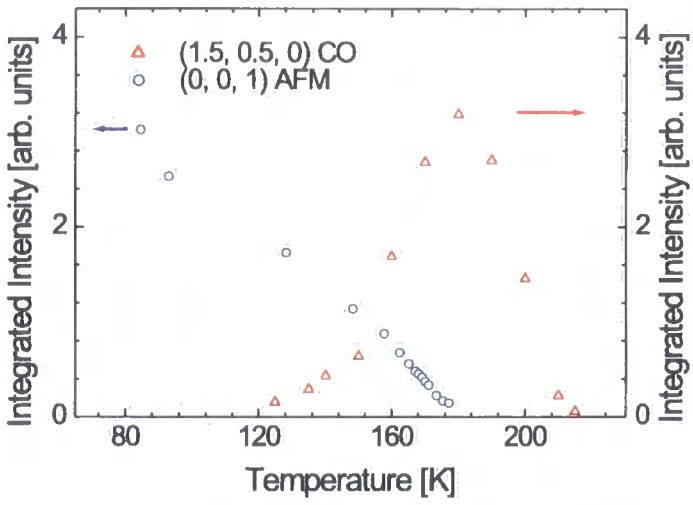

Figure 6.24: Integrated intensity of the AFM (0, 0, 1) superlattice reflection measured by soft X-ray diffraction (open circles) and the (0.5, 1.5, 0) charge order superlattice reflection measured by high energy X-ray diffraction (open triangles). For the latter see Chapter 5.

type AFM order. If we look at the magnetic structure of the A-type order shown in Figure 6.9 we see that the spins are aligned along the $\langle 1, 1, 0 \rangle$ direction and are anti-ferromagnetically aligned along the $\langle 0, 0, 1 \rangle$ direction. However in the a - b plane the manganese spins are aligned ferromagnetically. It is this FM order in the a - b plane which causes the collapse of the charge order. The very gradual onset of the A-type AFM order seen in Figures 6.18 and 6.19 indicates why the collapse of CO upon cooling is also gradual.

The detectable signal from the J-T order at low temperature suggests that the transition into the A-type AFM system in the $x = 0.475$ sample is not complete and some AFM order exists in the $a - b$ plane.

6.5 Conclusions

These results are, to date, the first X-ray diffraction measurements to perform resonant magnetic exchange X-ray scattering at the L edges of transition metals in bulk single crystal samples. These results prove that it is possible to perform diffraction with such samples at energies < 2 keV, opening a whole new technique, making it possible to probe the L edges of the transition metals. The very large resonance observed at the Mn L_{III} edge is conclusive proof that it is possible to obtain the same enhancements in signal that was previously only possible in the actinide compounds such as UAs (see McWhan *et al.*, 1990). By estimating the intensity of the magnetic scattering shown in Figure 6.13 with the off-resonant Bragg intensity measured in Figure 6.23 we find that the magnetic scattering signal is greater than 10 times that of the corresponding charge scattering. This is in stark comparison with the value of 1% obtained by McWhan *et al.* (1990) in UAs, indicating that soft X-ray magnetic scattering will become a very important technique in the future. Indeed soft X-ray scattering will open up a whole new method which provides for high intensity magnetic measurements on d-block transition metals. With such materials forming technologically important devices, it is clear that future studies will prove to be exciting.

Appendices

Appendix A

Fourier Analysis & Correlation Functions

A.1 Introduction

The *Fourier Transform* in its essence decomposes a spatially varying function into its different sinusoidal spatial frequency components. The Fourier transform of a function $f(x)$ is defined as

$$\mathcal{F}(s) = \int_{-\infty}^{\infty} f(x)\, e^{-i2\pi sx}\, \mathrm{d}x\,. \tag{A.1}$$

The inverse Fourier transform converts the function $\mathcal{F}(s)$ back to the spatially varying function $f(x)$ by

$$f(x) = \int_{-\infty}^{\infty} \mathcal{F}(s)\, e^{i2\pi sx}\, \mathrm{d}s\,. \tag{A.2}$$

For functions which are even the Fourier transform can be reduced to the cosine transform given by

$$\mathcal{F}_c(s) = 2\int_0^\infty f(x)\ \cos 2\pi sx\ \mathrm{d}x\,, \tag{A.3}$$

and similarly for odd functions the sine transform holds, given by

$$\mathcal{F}_c(s) = 2i\int_0^\infty f(x)\ \sin 2\pi sx\ \mathrm{d}x\ . \tag{A.4}$$

A.2 Scattering Theory

Fourier transforms can be used in scattering theory to transfer between direct space (the previous spatial domain) and reciprocal space (the spatial frequency domain). Let us start by considering the scattering in a classical fashion from a distribution of charge given by its number density $\rho(\boldsymbol{r})$, a schematic of which is shown in Figure A.1. The incident wavevector $\boldsymbol{k}$ scatters from the charge distribution into the direction $\boldsymbol{k}'$. The scattering is defined by the momentum transfer or scattering vector $\boldsymbol{q}$ which is given by

$$\boldsymbol{q} = \boldsymbol{k} - \boldsymbol{k}'\,, \tag{A.5}$$

where the magnitude of each wavevector is $|\boldsymbol{k}| = \frac{2\pi}{\lambda}$. Each volume element at $\boldsymbol{r}$ will contribute an amount $-r_0\rho(\boldsymbol{r})\mathrm{d}\boldsymbol{r}$, where r_0 is the Thompson scattering factor, and will include a phase factor given by $e^{i\boldsymbol{q}\cdot\boldsymbol{r}}$. The total scattering

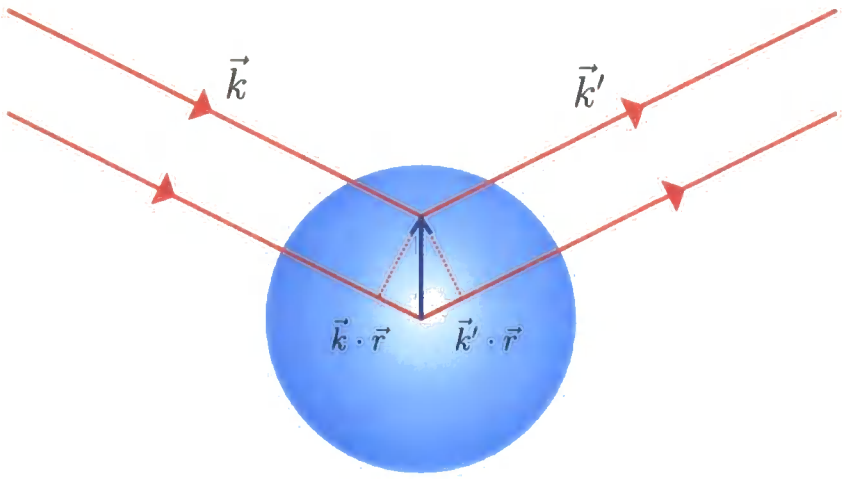

Figure A.1: Schematic representation of scattering from a charge distribution $\rho(\boldsymbol{r})\,\mathrm{d}\boldsymbol{r}$

from the charge distribution will therefore be given by

$$-r_0 f^0(\boldsymbol{q}) = -r_0 \int \rho(\boldsymbol{r})\, e^{i\boldsymbol{q}\cdot\boldsymbol{r}}\,\mathrm{d}\boldsymbol{r}\,. \tag{A.6}$$

Comparing the integral in Equation A.6 with the Fourier transform given by Equation A.1 we can see that the atomic scattering factor $f^0(\boldsymbol{q})$ is equal to the Fourier transform of the charge density $\rho(\boldsymbol{r})$.

One important property of Fourier transforms is the property of convolution. If we consider the convolution of a function $f(x)$ with a function $g(x)$ the convolution integral is given by:

$$h(x) = \int_{-\infty}^{\infty} f(x_1)g(x - x_1)\,\mathrm{d}x_1\,. \tag{A.7}$$

If we now consider the fourier transform $\mathcal{F}[h(x)]$ of the convolution of the

function $f(x)$ with $g(x)$ the results are

$$\mathcal{F}[h(x)] = \int_{-\infty}^{\infty} f(x_1) \exp[iqx_1]\, \mathrm{d}x_1 \int_{-\infty}^{\infty} g(x_1 - x) \exp[iq(x_1 - x)]\, \mathrm{d}x_1 ,$$

which can be reduced to

$$\mathcal{F}[h(x)] = \mathcal{F}[f(x)]\, \mathcal{F}[g(x)] , \tag{A.8}$$

the result that the Fourier transform of a convolution is equal to the product of the individual Fourier transforms.

Such a result has important applications within scattering theory. For example, the crystal lattice can be considered to be, in direct space, a periodic array of atoms represented by Dirac delta functions. We can represent the system therefore, as the convolution of the charge density at each atom and the function representing the lattice. By the convolution theorem the Fourier transform of the system will just be the product of the Fourier transform periodic lattice and the Fourier transform of the charge density of a single atom. Each can therefore be calculated separately and with relative ease.

A.3 Correlation Functions

A.3.1 Introduction

For the analysis of real systems there will not be a perfect arrangement of the measured quantity, for example in a system containing a linear chain of magnetic moments a infinite degree of correlation would be obtained if

all the magnetic moments were aligned with respect to each other. If we consider disorder in the system where the magnetic moments are allowed to vary in orientation we can define a correlation function which represents the probability that a moment situated at x will be in the same orientation as the one at the origin. Such correlation functions, existing in direct space can be convolved into the Fourier transform as discussed previously. This section derives the Fourier transform of several direct space correlation functions.

A.3.2 Lorentzian

If we start by assuming that the correlation at a point x decays exponentially from an initial value, A, at $x = 0$ we can define a correlation function $C(x)$ which represents this as:

$$C_L(x) = A \exp(-\kappa|x|) \,. \tag{A.9}$$

Here the correlation if found to decrease by a factor of e in a length of $x = 1/\kappa$. The representation of such a correlation function in reciprocal space can be found by applying the Fourier transform

$$\mathcal{C}_L(q) = \int_{-\infty}^{\infty} C_L(x)\, e^{iqx}\, \mathrm{d}x \,. \tag{A.10}$$

Applying the fact that $C(x)$ is a symmetrical function this can be reduced using the cosine transform given by Equation A.3 to

$$\mathcal{C}_L(q) = 2A \int_0^{\infty} \exp(-\kappa x)\, \cos(qx)\, \mathrm{d}x \,.$$

The integral can be evaluated by the following substitution

$$\int_0^\infty \exp(-\kappa x)\, \cos(qx)\, \mathrm{d}x = Re\left\{\int_0^\infty \exp(-\kappa x)\exp(iqx)\, \mathrm{d}x\right\},$$

which gives the result

$$C_L(q) = 2A\ Re\left\{\int_0^\infty e^{-(\kappa - iq)x}\, \mathrm{d}x\right\}.$$

Evaluating the integral gives

$$C_L(q) = 2A\ Re\left\{\frac{1}{-(\kappa - iq)}\left[e^{-(\kappa - iq)x)}\right]_0^\infty\right\},$$

leading to the result

$$C_L(q) = 2A\ Re\left\{\frac{\kappa + iq}{\kappa^2 + q^2}\right\} = \frac{2A\kappa}{\kappa^2 + q^2}, \tag{A.11}$$

which is the equation for a Lorentzian centred at $q = 0$ with height $2A/\kappa$. If we now solve Equation A.11 to obtain the half width at half maximum (HWHM) by setting $C(q) = A/\kappa$ we get the result that the parameter κ is related to the HWHM by the relationship

$$\Delta q_{(\mathrm{HWHM})} = \kappa. \tag{A.12}$$

This illustrates the reciprocal nature of the transform between direct and reciprocal space. Figure A.2 show both the correlation function $C(x)$ and the Fourier transform $C(q)$, graphically for different values of κ. Here the

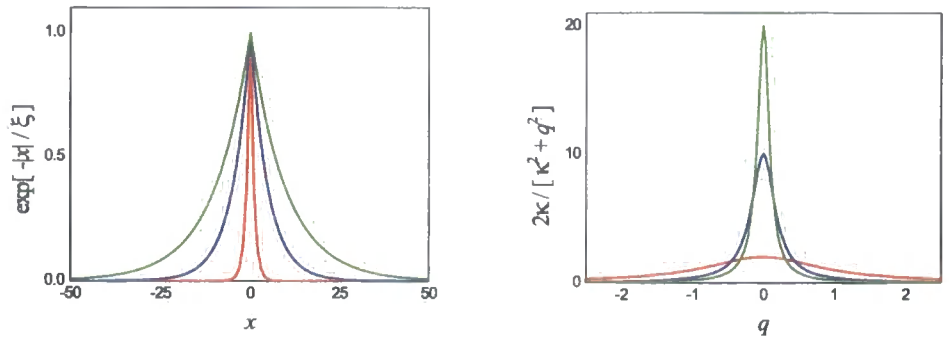

Figure A.2: The correlation function $C(x) = A\exp(-\kappa|x|)$ (left) and Fourier transform $\mathcal{C}(q) = \frac{2A\kappa}{\kappa^2+q^2}$ (right) for $\kappa = 1$ (red), 0.2 (blue) and 0.1 (green).

reciprocal nature of the transform can be seen. If there is a high degree of correlation in direct space the corresponding width in reciprocal space is small. If the object has very little correlation then the corresponding width in reciprocal space is large.

If we now turn to the integrated area (I) of a Lorentzian function, given by

$$I_{lorentz} = \pi\kappa H\,,$$

where H is the peak height. Substituting gives the result that the area of the Fourier transform of the correlation function is given by

$$I = \pi\kappa \cdot \frac{2A}{\kappa} = 2\pi A\,.$$

This shows that the integrated area of the peak in reciprocal space is proportional to the amplitude of the correlation function and is independent of the parameter κ, the inverse correlation length. This explains why diffraction is

primarily sensitive to long-range correlations. The peak height in reciprocal space is proportional to the correlation length, ξ, so the greater the degree of correlation the greater the intensity of scattering.

By analysis of the diffraction peak shape two main properties can be measured. The width of the diffraction peak in reciprocal space gives the degree of correlation while the integrated area gives the amplitude of the scattering with infinite correlation.

A.3.3 Gaussian

In the same manner as used previously we can derive the relationship for a Gaussian correlation function $C_G(x)$ given by

$$C_G(x) = A \exp\left[-\frac{x^2}{2\sigma_{ds}^2}\right], \tag{A.13}$$

where σ_{ds} is the standard deviation of the distribution. The Fourier transform of the Gaussian is found by applying

$$\mathcal{C}_G(q) = A \int_{-\infty}^{\infty} \exp(-x^2/(2\sigma^2)) \exp(iqx)\, \mathrm{d}x\,.$$

The Gaussian function is real, and symmetric about $x = 0$, therefore, the integral may be written as the real part of the integral given by

$$\mathcal{C}_G(q) = 2A\ Re\left\{\int_{-\infty}^{\infty} \exp\left(-x^2/(2\sigma^2) + iqx\right)\ \mathrm{d}x\right\}.$$

Completing the square gives the result

$$C_G(q) = 2A\exp(-\sigma^2 q^2/2)\ Re\left\{\int_{-\infty}^{\infty}\exp\left(-\left[\frac{x}{\sqrt{2}\sigma} - \frac{i\sqrt{2}\sigma q}{2}\right]^2\right)\ \mathrm{d}x\right\}.$$

Substituting the variable $k = (x/(\sqrt{2}\sigma) - i\sqrt{2}\sigma/2)$ and changing the subject of the integral to k gives

$$C_G(q) = 2A\sqrt{2}\sigma\exp(-\sigma^2 q^2/2)\ Re\left\{\int_{-\infty}^{\infty}\exp(-k^2)\ \mathrm{d}k\right\}.$$

Substituting for the standard integral

$$\int_{-\infty}^{\infty} e^{-y^2}\ \mathrm{d}y = \frac{\sqrt{\pi}}{2},$$

gives the Fourier transform of the Gaussian function given in Equation A.13 as

$$C_G(q) = A\sqrt{2\pi}\ \sigma\exp\left(-\frac{\sigma^2 q^2}{2}\right). \tag{A.14}$$

Figure A.3 shows the direct space Gaussian function (left side) and Fourier transform (right side) for σ = 1, 5 and 10. If we now look at the integrated area of a Gaussian which is given by

$$A = \sigma\sqrt{2\pi}\ H,$$

where A is the area and H is the peak height. Substituting into the Fourier

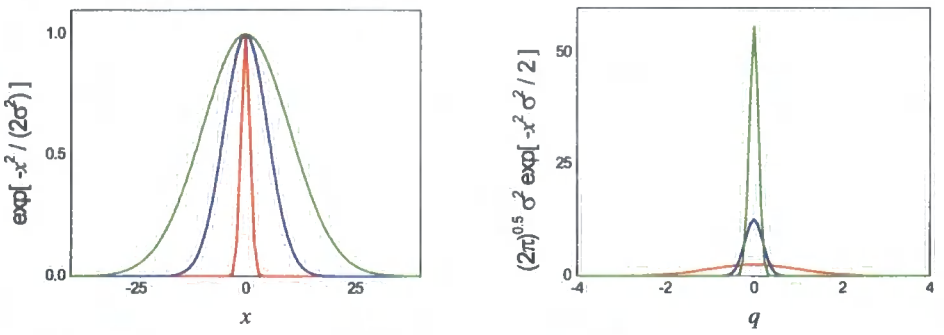

Figure A.3: The Gaussian function $C_G(x) = A\exp(-x^2/(2\sigma^2))$ (left) and Fourier transform $\mathcal{C}_G(q) = A\sqrt{2\pi}\ \sigma \exp\left(-\frac{\sigma^2 q^2}{2}\right)$ (right) for $\sigma = 1$ (red), 5 (blue) and 10 (green).

transformed function gives the result that the area is equal to

$$I = 2\pi A\,.$$

A.3.4 Lorentzian Squared

In identical fashion to the cases in Sections A.3.2 and A.3.3 we can define a correlation function $C(r)$ as

$$C_{\text{lorr}^2}(r) = A(1 + \kappa|x|)\exp(-\kappa|x|)\,, \tag{A.15}$$

which is found to fall off slower with the spacial variable x than the Lorentzian and Gaussian shapes discussed previously.

To find the lineshape from such scattering we can apply the cosine trans-

form to the function to give

$$\mathcal{C}_{\text{lorr}^2}(q) = 2\int_0^\infty (1+\kappa x)\exp(-\kappa x)\cos(qx)\,\mathrm{d}x\,. \tag{A.16}$$

Solving this integral using the symbolic integration in *Maple* gives the result

$$\mathcal{C}_{lorr^2}(q) = \frac{4A\kappa^3}{(\kappa^2+q^2)^2}\,. \tag{A.17}$$

Which is the case for a Lorentzian squared peak shape which has a height $2A/\kappa$ and area equal to $2\pi A$.

Figure A.4 shows the direct space correlation function for values of $\kappa =$ 1, 0.2 and 0.1 shown in red, blue and green respectively. Here again the reciprocal nature of the transform can be seen with the more correlated peak providing the sharpest, most intense in reciprocal space.

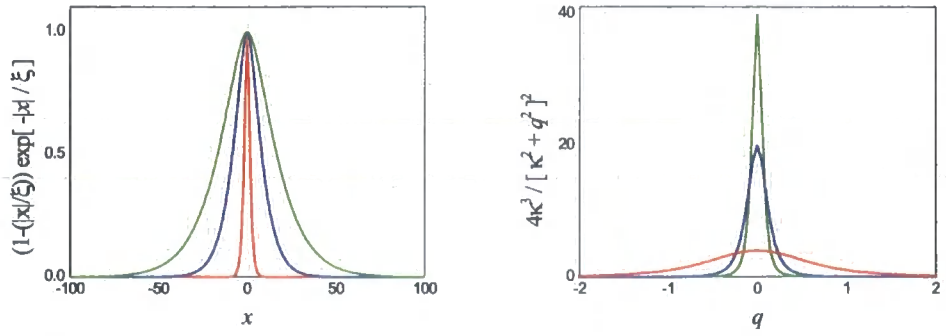

Figure A.4: The correlation function $C_{L2}(x) = A(1+|x|/\xi)\exp(-\kappa|x|)$ (left) and Fourier transform $\mathcal{C}_{L2}(q) = 4A\kappa^3/[q^2+\kappa^2]^2$ (right) for $\kappa = 1$ (red), 0.2 (blue) and 0.1 (green).

A.4 (Inverse) Correlation Lengths

A.4.1 Introduction

If we now consider the case of a scattering experiment in which the scattering is measured as a function of reciprocal space coordinates in one dimension, the result is a peak which may be fitted to one of the lineshapes described in this Appendix. As the measurement is made in reciprocal space we can define a quantity which is related to the measurement. The *inverse correlation length*, κ which is equal to the half width at half maximum, w, of the scattering. In direct space we can introduce a *correlation length* at which the degree of correlation has fallen to $1/e$ times its original value. Using the results of the Fourier transforms previously we can derive a relation between the inverse correlation length and correlation length.

If we compute the product $\Delta x \Delta q$, where Δq is the inverse correlation length and Δx is the point at which the correlation drops to $1/e$ its initial value we obtain a relation between the two in a method akin to the uncertainty principal.

The case of a Lorentzian is simple and is derived as follows.

A.4.2 Lorentzian

The half width at half maximum for the correlation function $C(r) = \exp(-\kappa x)$ and the reciprocal space Lorentzian lineshape, Δx and Δq re-

spectively, are given by

$$\begin{aligned} \Delta x_{1/e} &= \frac{1}{\kappa} \\ \Delta q_{(HWHM)} &= \kappa , \end{aligned}$$

using Equations A.9 and A.11 computing the product gives

$$\Delta x \Delta q = 1 . \tag{A.18}$$

Here again the reciprocal nature is displayed, with the correlation length begin just the simple inverse of the inverse correlation length.

A.4.3 Gaussian

The half width at half maximum of the Gaussian correlation function and Gaussian lineshape, Δx and Δq respectively, are given by

$$\begin{aligned} \Delta x_{1/e} &= \sigma\sqrt{2} \\ \Delta q_{(HWHM)} &= \frac{\sqrt{2\ln 2}}{\sigma} , \end{aligned}$$

using Equations A.13 and A.14. Computing the product of the widths gives

$$\Delta x \Delta q = 2\sqrt{\ln 2} . \tag{A.19}$$

Here the form is similar to that found for the Lorentzian in that the correlation length is proportional to the inverse of the inverse correlation length but there is a numerical factor of $2\sqrt{\ln 2}$.

A.4.4 Lorentzian Squared

Repeating again the above procedure the half width at half maximum, Δx, of the correlation function $C(r) = (1 + \kappa x)\exp(-\kappa x)$ can be numerically found using *Maple*. The corresponding half width at half maximum for the reciprocal space lineshape, Δq, can also be found analytically giving the result

$$\begin{aligned} \Delta x_{1/e} &= \frac{2.14619}{\kappa} \\ \Delta q_{(HWHM)} &= \kappa\sqrt{\sqrt{2}-1}\,, \end{aligned}$$

using Equations A.15 and A.17 which gives the product

$$\Delta x \Delta q = 1.38127(8)\,. \tag{A.20}$$

Which gives the same results as before but with a different numerical factor of 1.38127(8).

A.4.5 Conclusions

We can therefore arrive at a common definition of the relationship given by

$$\Delta x \Delta q = f\,, \tag{A.21}$$

where f is the factor which arrives from the reciprocal space lineshape and is found to be equal to 1, $2\sqrt{\ln 2} = 1.665(1)$ and 1.38127(8) for the Lorentzian, Gaussian and Lorentzian squared respectively.

The factor f forces the correlation functions to have a common value at the point $x = 1/e$. Figure A.5 displays the three direct space correlation functions for identical correlation length using the relationships in Equations A.18, A.19 and A.20. Here the common tie point at a value of $1/e$ can clearly be seen. However, what becomes immediately apparent from Figure A.5 is that although we can define a correlation length, this length is dependant on the lineshape in reciprocal space. In addition although there is a common tie point the variation of the correlation with x near the origin and far from the origin is very different. Such problems mean that there are two main problems with using correlation length.

Firstly, the reciprocal space lineshape must be accurately determined as

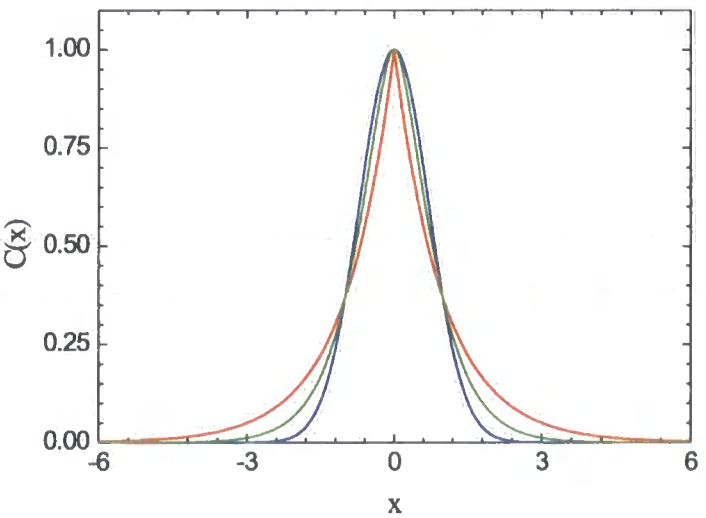

Figure A.5: Direct space correlation functions $C(x) = A\exp(-\kappa|x|)$ (red), $C(x) = A\exp(-x^2/(2\sigma^2))$ (green) and $C(x) = A(1+\kappa|x|)\exp(-\kappa|x|)$ (blue) for Lorentzian, Gaussian and Lorentzian squared lineshapes respectively.

it is from this which determines the factor f. In the absence of high enough quality data it is not possible to obtain a correlation length. Secondly, even though we have a correlation length it is not possible to compare correlation lengths between different lineshapes as each has a different spacial profile of the degree of correlation. However, the inverse correlation length, being a quantity in reciprocal space can be determined easily from the data upon peak analysis. Therefore, for comparisons between different sets of diffraction data their definitions are clearer and do not require any knowledge of the factor f.

References

Als-Nielsen, J. and McMorrow, D. (2001). *Elements of Modern X-ray Physics*, John Wiley & Sons Ltd., Chichester.

Bao, W., Axe, J., Chen, C. and Cheong, S.-W. (1997). *Impact of Charge Ordering on Magnetic Correlations in Perovskite (Bi,Ca)MnO_3*, Physical Review Letters **78**(3), 543–546.

Bednorz, J. G. and Muller, K. A. (1986). *Possible high-T_C superconductivity in the Ba-La-Cu-O system*, Zeitschrift für Physik B. **64**, 189–193.

Blume, M. (1985). *Magnetic scattering of X-rays*, Journal of Applied Physics **57**(1), 3615–3618.

Blume, M. and Gibbs, D. (1988). *Polarization dependence of magnetic X-ray scattering*, Physical Review B **37**, 1779–1789. Errata in **40**, 5218(E) (1989).

Bouchard, R., Hupfeld, D., Lippmann, T., Neuefeind, J., Neumann, H.-B., Poulsen, H., Rütt, U., Schmidt, T., Schneider, J. R., Süssenbach, J. and von Zimmermann, M. (1998). *A Triple-Crystal Diffractometer for High-Energy Synchrotron Radiation at the HASYLAB High-Field Wiggler Beamline BW5*, Journal of Synchrotron Radiation **5**, 90–101.

Brown, S. D., Bouchenoire, L., Bowyer, D., Kervin, J., Laundy, D., Longfield, M. J., Mannix, D., Paul, D. F., Stunault, A., Thompson, P., Cooper, M. J., Lucas, C. A. and Stirling, W. G. (2001). *The XMaS beamline at the ESRF : instrumental developments and high resolution diffraction studies*, Journal of Synchrotron Radiation **8**, 1172–1181.

Busing, W. R. and Levy, H. A. (1967). *Angle Calculations for 3- and 4- circle X-ray and Neutron Diffractometers*, Acta Crystallographica **22**, 457–464.

Carra, P., Altarelli, M. and de Bergevin, F. (1989). *Resonant exchange scattering of X-rays in ferromagnetic systems*, Physical Review B **40**(10), 7324–7327.

Castleton, C. W. M. and Altarelli, M. (2000). *Orbital ordering in the manganites: Resonant X-ray scattering predictions at the manganese L_{II} and L_{III} edges*, Physical Review B **62**(2), 1033–1038.

Cava, R. J., van Dover, R. B., Batlogg, B. and Rietman, E. A. (1987). *Bulk superconductivity at 36 K in $La_{1.8}Sr_{0.2}CuO_4$*, Physical Review Letters **58**, 408410.

Chatterji, T., McIntyre, G., Caliebe, W., Suryanarayanan, R., Dhalenne, G. and Revcolevschi, A. (2000). *Reentrant behaviour of the charge and orbital ordering and anti-ferromagnetism in $LaSr_2Mn_2O_7$*, Physical Review B **61**(1), 570–574.

Chen, C. and Cheong, S.-W. (1996). *Commensurate to incommensurate charge ordering and its real space images in $La_{0.5}Ca_{0.5}MnO_3$*, Physical Review Letters **76**(21), 4042–4045.

Cheong, S., Aeppli, G., Mason, T. E., Mook, H., Hayden, S. M., Canfield, P. C., Fisk, Z., Clausen, K. N. and Martinez, J. L. (1991). *Incommensurate magnetic fluctuations in $La_{2-x}Sr_xCuO_4$*, Physical Review Letters **67**(13), 1791–1794.

Cheong, S., Hwang, H. Y., Chen, H. Y., Batlogg, B., Rupp, H. Y. and Carter, S. A. (1994). *Charge-ordered states in $(La,Sr)_2NiO_4$ for hole concentrations $n_h = 1/3$ and 1/2*, Physical Review B **49**(10), 7088–7091.

Cockerton, S., Tanner, B. K. and Derbyshire, G. (1995). *A Novel High Dynamic-Range X-Ray-Detector For Synchrotron- Radiation Studies*, Nucl. Instrum. Methods Phys. Res. Sect. B. **97**(1-4), 561–566.

Crawford, M. K., Harlow, R. L., McCarron, E. M., Farneth, W. E., Axe, J. D., Chou, H. and Huang, Q. (1991). *Lattice Instabilities and the effect of copper-oxygen-sheet distortions on superconductivity in doped La_2CuO_4*, Physical Review B **44**(14), 7749–7752.

Cromer, D. T. and Liberman, D. (1970). *Relativistic Calculation of Anomalous Scattering Factors for X-Rays*, Journal of Chemical Physics **53**(5), 1891–1898.

Cross, J., Newville, M., Rehr, J., Sorensen, L., Bouldin, C., Watson, G., Gouder, T., Lander, G. and Bell, M. (1998). *Inclusion of local structure effects in theoretical x-ray resonant scattering amplitudes using ab initio X-ray-absorption spectra calculations*, Physical Review B **58**(17), 11215–11225.

de Bergevin, F. and Brunel, M. (1981). *Diffraction by Magnetic-Materials .I. General Formulas and Measurements on Ferromagnetic and Ferrimagnetic Compounds.*, Acta Crystallographica **A37**, 314–324.

Dessau, D. S. and Shen, Z.-X. (2000). *Colossal Magnetoresistive Oxides*, Vol. 2, Gordon and Breach Science Publishers.

Dho, J., Kim, W. S., Choi, H. S., Chi, E. O. and Hur, N. H. (2001). *Re-entrant charge-ordering behaviour in the layered manganites $La_{2-2x}Sr_{1+2x}Mn_2O_7$*, Journal of Physics - Condensed Matter **13**, 3655–3660.

Du, C.-H., Ghazi, M. E., Su, Y., Pape, I., Hatton, P. D., Brown, S., Stirling, W. G., Cooper, M. J. and Cheong, S.-W. (2000). *Quenched Disordered 2-Dimensional Charge Stripes in $La_{1.67}Sr_{0.33}NiO_4$*, Physical Review Letters **84**, 3911–3914.

Dudzik, E., Dhesi, S. S., Durr, H. A., Collins, S. P., Roper, M. D., van der Laan, G., Chesnel, K., Belakhovsky, M., Marty, A. and Samson, Y. (2000). *Influence of perpendicular magnetic anisotropy on closure domains studied with X-ray resonant magnetic scattering*, Physical Review B **62**(9), 5779–5785.

Endoh, Y., Hirota, K., Ishihara, S., Okamoto, S., Murakami, Y., Nishizawa, A., Fukuda, T., H., K., Nojiri, H., Kaneko, K. and Maekawa, S. (1999). *Transition between Two Ferromagnetic States Driven by Orbital Ordering in $La_{0.88}Sr_{0.12}MnO_3$*, Physical Review Letters **82**(21), 4328 – 4331.

Fernandez, V., Vettier, C., de Bergevin, F., Giles, C. and Neubeck, W. (1998). *Observation of orbital moment in NiO*, Physical Review B **57**(13), 7870–7876.

Ghazi, M. E. (2002), *High-Resolution X-Ray Scattering Studies of Charge Ordering in Highly Correlated Electron Systems*, Ph.D. thesis, Department of Physics, University of Durham.

Gibbs, D., Harshman, D. R., Isaacs, E. D., McWhan, D. B., Mills, D. and Vettier, C. (1988). *Polarization and Resonance Properties of Magnetic-X-Ray Scattering in Holmium*, Physical Review Letters **61**(10), 1241–1244.

Goodenough, J. (1955). *Theory of the role of covelence in the perovskite-type manganites [La,M(II)]MnO_3*, Physical Review **100**(2), 564–573.

Hannon, J. P., Trammell, G. T., Blume, M. and Gibbs, D. (1988). *X-Ray Resonance Exchange Scattering*, Physical Review Letters **61**(10), 1245–1248. Errata in **62**, 2644(E) (1989).

Hase, T. P. A. (1998), *X-Ray Scattering from Magnetic Metalic Multilayers*, Ph.D. thesis, Department of Physics, University of Durham.

Hase, T. P. A., Pape, I., Tanner, B. K., Durr, H., Dudzik, E., van der Laan, G., Marrows, C. H. and Hickey, B. J. (2000). *Soft-X-ray Resonant Magnetic Diffuse Scattering from Strongly Coupled Cu/Co Multilayers*, Physical Review B **61**, R3792–R3895.

Hazen, R. M., Prewitt, C. T., Angel, R. J., Ross, N. L., Finger, L. W., Hadidiacos, C. G., Veblen, D. R., Heaney, P. J., Hor, P. H., Meng, R. L., Sun, Y. Y., Wang, Y. Q., Xue, Y. Y., Huang, Z. J. Gao, L., Bechtold, J. and Chu, C. W. (1988). *Superconductivity in the high-T_c Bi-Ca-Sr-Cu-O system: Phase identification*, **60**(12), 11741177.

Henke, B. L., Gullikson, E. and J.C., D. (1993). *X-ray interactions: photoabsorption, scattering, transmission, and reflection at E=50-30000 eV, Z=1-92*, Atomic Data and Nuclear Data Tables **54**(2), 181–342.

Hill, J., Kao, C.-C. and McMorrow, D. (1997). *K-edge resonant X-ray magnetic scattering from a transition-metal oxide: NiO*, Physical Review B **55**(14), R8662–R8665.

Hill, J. P. and McMorrow, D. F. (1996). *X-ray Resonant Exchange Scattering: Polarization Dependance and Correlation Functions*, Acta Crystallographica **A52**, 236–244.

Hill, J. P., McMorrow, D. F., Boothroyd, A. T., Stunault, A., Vettier, C., Berman, L. E., von Zimmermann, M. and Wolf, T. (2000). *X-ray-scattering study of copper magnetism in nonsuperconducting $PrBa_2Cu_3O_{6.92}$*, Physical Review B **61**(2), 1251–1255.

Hu, Z. W., Thomas, P. A. and Risk, W. P. (1999). *Studies of periodic ferroelectric domains in $KTiOPO_4$ using high-resolution X-ray scattering and diffraction imaging*, Physical Review B **59**(22), 14259–14264.

Ishihara, S. and Maekawa, S. (1998). *Polarization dependence of anomalous X-ray scattering in orbital-ordered manganites*, Physical Review B **58**(20), 13442–13451.

Jirák, Z., Damay, F., Hervieu, M., Martin, C., Raveau, B., André, G. and Bourée, F. (2000). *Magnetism and charge ordering in $Pr_{0.5}Ca_xSr_{0.5x}MnO_3$ (x = 0.09 and 0.5)*, Physical Review B **61**(2), 1181–1188.

Kajimoto, R., Kakeshita, T., Oohara, Y., Yoshizawa, H., Tomioka, Y. and Tokura, Y. (1998). *Anomalous ferromagnetic spin fluctuations in an antiferromagnetic insulator $Pr_{1-x}Ca_xMnO_3$*, Physical Review B **58**(18), R11837–R11840.

Kajimoto, R., Yoshizawa, H., Kawano, H., Kuwahara, H., Tokura, Y., Ohoyama, K. and Ohashi, M. (1999). *Hole-concentration-induced transformation of the magnetic and orbital structures in $Nd_{1-x}Sr_xMnO_3$*, Physical Review B **60**(13), 9506–9517.

Kimura, H., Matsushita, H., Hirota, K., Endoh, Y., Yamada, K., Shirane, G., Lee, Y. S., Kastner, M. A. and Birgeneau, R. J. (2000). *Incommensurate geometry of the elastic magnetic peaks in superconducting $La_{1.88}Sr_{0.12}CuO_4$*, Physical Review B **61**(21), 14366–14369.

Kimura, T., Kumai, R., Tokura, Y., Li, J. Q. and Matsui, Y. (1998). *Successive structural transitions coupled with magnetotransport properties in $LaSr_2Mn_2O_7$*, Physical Review B **58**, 11081–11084.

Kittel, C. (1996). *Introduction to Solid State Physics*, seventh ed., John Wiley & Sons Ltd., Chichester.

Kivelson, S. A., Fradkin, E. and Emery, V. J. (1998). *Electronic Liquid-Crystal phases of a doped Mott insulator*, Nature **393**, 550–553.

Kubota, M., Yoshizawa, H., Moritomo, Y., Fujioka, H., Hirota, K. and Endoh, Y. (1999). *Interplay of the CE-type charge ordering and the A-type spin ordering in half-doped bilayer manganite* $LaSr_2Mn_2O_7$, Journal of the Physical Society of Japan **68**, 2202–2205.

Kuiper, P., van Elp, J., Sawatzky, G. A., Fujimori, A., Hosoya, S. and de Leeuw, D. M. (1991). *Unoccupied density of states of* $La_{2-x}Sr_xNiO_{4+\delta}$ *studied by polarization-dependent X-ray-absorption spectroscopy and bremsstrahlung isochromat spectroscopy*, Physical Review B **44**(9), 4570–4575.

Lee, S. H. and Cheong, S.-W. (1997). *Melting of Quasi-Two-Dimensional Charge Stripes in* $La_{5/3}Sr_{1/3}NiO_4$, Physical Review Letters **79**(13), 2514–2517.

Lee, S.-H., Cheong, S.-W., Yamada, K. and Majkrzak, C. F. (2001). *Charge and Canted spin order in* $La_{2-x}Sr_xNiO_4$ *(*$x = 0.275$ *and* $\frac{1}{3}$*)*, Physical Review B **63**, 060405(R).

Li, J. Q., Matsui, Y., Kimura, T. and Tokura, Y. (1998). *Structural properties and charge-ordering transition in* $LaSr_2Mn_2O_7$, Physical Review B **57**, R3205–R3208.

Liss, K.-D., Royer, A., Tschentscher, T., Suortti, P. and Williams, A. P. (1998). *On High-Resolution Reciprocal-Space Mapping with a Triple-Crystal Diffractometer for High-Energy X-rays*, Journal of Synchrotron Radiation **5**(2), 82–89.

Longfield, M. J., Stirling, W. G., Lidstrom, E., Mannix, D., H., L. G., Stunault, A., McIntyre, G. J., Mattenberger, K. and Vogt, O. (2001). *U(*$As_{1-x}Se_x$*) solid solutions. I. Resonant X-ray and neutron scattering study of the magnetic phase diagram*, Physical Review B **63**(13), 134401.

Matyi, R. J., Moran, P. D., Hagquist, W. W. D. and Volz, H. M. (2000). *Alignment system for crossed parabolic X-ray mirrors*, Review of Scientific Instruments **71**(6), 2292–2295.

McWhan, D. B., Vettier, C., Isaacs, E. D., Ice, G. E., Siddons, D. P., Hastings, J. B., Peters, C. and Vogt, O. (1990). *Magnetic X-Ray-Scattering Study of Uranium Arsenide*, Physical Review B **42**, 6007–6017.

Mills, A. J. (1996). *Cooperative Jahn-Teller effect and electron-phonon coupling in* $La_{1-x}A_xMnO_3$, Physical Review B **53**(13), 8434–8441.

Mills, A. J. (1998*a*). *Colossal magnetoresistance manganites: a laboratory for electron-phonon physics.*, Philosophical Transactions of the Royal Society of London A **356**, 1473–1480.

Mills, A. J. (1998*b*). *Stripes of a different stripe*, Nature **392**, 438.

Moritomo, Y., Asamitsu, A., Kuwahara, H. and Tokura, Y. (1996). *Giant magnetoresistance of manganese oxides with a layered perovskite structure.*, Nature **380**, 141–144.

Murakami, Y., Hill, J., Gibbs, D., Blume, M., Koyama, I. Tanaka, M., Kawata, H., Arima, T., Tokura, Y., Hirota, K. and Endoh, Y. (1998). *Resonant X-Ray Scattering from Orbital Ordering in* $LaMnO_3$, **81**(3), 582–585.

Nakamura, K., Arima, T., Nakazawa, A., Wakabayashi, Y. and Murakami, Y. (1999). *Polarization-dependent resonant-X-ray diffraction in charge- and orbital-ordering phase of* $Nd_{1/2}Sr_{1/2}MnO_3$, Physical Review B **60**(4), 2425 – 2428.

Neubeck, W., Vettier, C., Lee, K. B. and de Bergevin, F. (1999). *K-edge resonant X-ray magnetic scattering from* CoO, Physical Review B **60**(14), R9912–R9915.

Neumann, H. B., Rutt, U., Schneider, J. R. and Shirane, G. (1995). *Origin Of The Critical Scattering On 2 Length Scales In* $SrTiO_3$ *- A High-Energy Synchrotron-Radiation Diffraction Study*, Physical Review B **52**(6), 3981–3984.

Niemöller, T., von Zimmermann, M., Uhlenbruck, S., Friedt, O., Büchner, B., T., F., Andersen, N., Berthet, P., Pinsard, L., De Léon-Guevara, A., Revcolevschi, A. and Schneider, J. (1999). *The charge ordered phase in* $La_{1-x}Sr_xMnO_3$ *studied by means of high energy X-ray diffraction*, The European Physical Journal B **8**, 5–8.

Prabhakaran, D., Isla, P. and Boothroyd, A. T. (2002). *Growth of large* $La_{2-x}Sr_xNiO_{4+\delta}$ *single crystals by the floating-zone technique*, Journal of Crystal Growth **237**, 815–819.

Radaelli, P., Cox, D., Marezio, M. and Cheong, S.-W. (1997). *Charge, orbital and magnetic ordering in* $La_{0.5}Ca_{0.5}MnO_3$, Physical Review B **55**(5), 3015 – 3023.

Radaelli, P., Cox, D., Marezio, M., Cheong, S.-W., Schiffer, P. and Ramirez, A. (1995). *Simultaneous Structural Magnetic and Electronic Transitions in* $La_{1-x}Ca_xMnO_3$ *with* $x = 0.25$ *and* 0.50, Physical Review Letters **75**(24), 4488–4491.

Renner, C., Aeppli, G., Kim, B.-G., Soh, Y.-A. and Cheong, S.-W. (2002). *Atomic-scale images of charge ordering in a mixed-valence manganite*, Nature **416**, 518–521.

Roper, M. D. (2002), private communication.

Sanchez del Rio, M. and Dejus, R. (2001). *XOP: A Multiplatform Graphical User Interface for Synchrotron Radiation Spectral and Optics Calculations*, SPIE Procedings **3152**, 148–157.

Schuster, M. and Gobel, H. (1995). *Parallel-Beam Coupling Into Channel-Cut Monochromators Using Curved Graded Multilayers*, Journal of Physics D - Applied Physics **28**(4A), A270–A275.

Scopigno, T., Balucani, U., Ruocco, G. and Sette, F. (2001). *Collective dynamics of liquid aluminum probed by inelastic X-ray scattering*, Physical Review E **63**(1), 011210.

Stunault, A., de Bergevin, F., Wermeille, D., Vettier, C., Bruckel, T., Bernhoeft, N., McIntyre, G. J. and Henry, J. Y. (1999). *K-edge resonant X-ray magnetic scattering from $RbMnF_3$*, Physical Review B **60**(14), 10170–10179.

Su, Y., Du, C. H., Hatton, P. D., Collins, S. P. and Cheong, S. W. (1999). *Charge ordering and the related structural phase transition in single-crystal $(Bi_{0.24}Ca_{0.76})MnO_3$*, Physical Review B **59**(18), 11687–11692.

Suortti, P. and Tschentscher, T. (1995). *High energy scattering beamlines at European Synchrotron Radiation Facility*, Review of Scientific Instruments **66**(2), 1798–1801.

Suzuki, T., Goto, T., Chiba, K., Shinoda, T., Fukase, T., Kimura, H., Yamada, K., Ohashi, M. and Yamaguchi, Y. (1998). *Observation of modulated magnetic long-range order in $La_{1.88}Sr_{0.12}CuO_4$*, **57**(6), R3229–R3232.

Tan, Z., Heald, S. M., Cheong, S. W., Cooper, A. S. and Moodenbaugh, A. R. (1993). *Nature of hole doping in Nd_2NiO_4 and La_2NiO_4: Comparison with La_2CuO_4*, Physical Review B **47**(18), 12365–12368.

The TESLA Project (2002), `http://tesla.desy.de/`.

Tranquada, J., Buttrey, D., Sachan, V. and Lorenzo, J. (1994). *Simultaneous ordering of holes and spins in $La_2NiO_{4.125}$*, Physical Review Letters **73**(7), 1003–1006.

Tranquada, J. M. (1995). *Evidence for stripe correlations of spins and holes in copper oxide superconductors*, Nature **375**, 561.

Tranquada, J. M., Axe, J. D., Ichikawa, N., Nakamura, Y., Uchida, S. and Nachumi, B. (1996). *Neutron-scattering study of stripe-phase order of holes and spins in $La_{1.48}Nd_{0.4}Sr_{0.12}CuO_4$*, **41**(10), 7489–7499.

Tranquada, J. M., Wochner, P., Moodenbaugh, A. R. and Buttrey, D. J. (1997). *Field-induced staggered magnetic order in $La_2NiO_{4.133}$*, Physical Review B **55**(10), R6113 – R6116.

von Zimmermann, M., Hill, J., Gibbs, D., Blume, M., Casa, D., Keimer, B., Murakami, Y., Tomioka, Y. and Tokura, Y. (1999). *Interplay between Charge, Orbital, and Magnetic Order in $Pr_{1-x}Ca_xMnO_3$*, Physical Review Letters **82**(23), 4872–4875.

von Zimmermann, M., Nelson, C. S., Hill, J. P., Gibbs, D., Blume, M., Casa, D., Keimer, B., Murakami, Y., Kao, C.-C., Venkataraman, C., Gog, T., Tomioka, Y. and Tokura, Y. (2001). *X-ray resonant scattering studies of orbital and charge ordering in $Pr_{1-x}Ca_xMnO_3$*, Physical Review B **64**, 196133.

von Zimmermann, M., Vigliante, A., Niemöller, T., Ichikawa, N., Frello, T., Madsen, J., Wochner, P., Uchida, S., Andersen, N. H., Tranquada, J. M., Gibbs, D. and Schneider, J. R. (1998). *Hard-X-ray diffraction study of charge stripe order in $La_{1.48}Nd_{0.4}Sr_{0.12}CuO_4$*, Europhysics Letters **41**(6), 629–634.

Wakabayashi, Y., Murakami, Y., Koyama, I., Kimura, T., Tokura, Y., Moritomo, Y., Hirota, K. and Endoh, Y. (2000). *Orbital and charge ordering in $LaSr_2Mn_2O_7$ observed by resonant X-ray scattering*, Journal of the Physical Society of Japan **69**, 2731–2734.

Wakabayashi, Y., Murakami, Y., Moritomo, Y., Ichiro, K., Nakao, H., Kiyama, T., Kimura, T., Tokura, Y. and Wakabayashi, N. (2001). *Orbital and Charge ordering in $La_{1-x}Sr_{1+x}MnO_4$ ($0.4 \leq x \leq 0.5$)*, Journal of the Physical Society of Japan **70**(5), 1194–1197.

Wakimoto, S., Birgeneau, R. J., A., K. M., Lee, Y. S., Erwin, R., Ghering, P. M., Lee, S. H., Fujita, M., Yamada, K., Endoh, Y., Hirota, K. and Shirane, G. (2000). *Direct Observation of a one-dimensional static spin modulation in insulating $La_{1.95}Sr_{0.05}CuO_4$*, Physical Review B **61**(5), 3699–3706.

Wakimoto, S., Birgeneau, R. J., Lee, Y. S. and Shirane, G. (2001). *Hole concentration dependence of the magnetic moment in superconducting and insulating $La_{2-x}Sr_xCuO_4$*, Physical Review B **63**, 172501.

Wilkins, S. B., Spencer, P. D., Hatton, P. D., Tanner, B. K., Lafford, T. A., Spence, J. and Loxley, N. (2002). *Novel Diffractometer Utilising crossed Parabolic Mirrors for the Study of Weak Superlattice Reflections*, Review of Scientific Instruments **73**(7), 2666–2671.

Wilson, J. A. (1998). *The position of the 'one-eighth' anomaly within the high-temperature superconductivity problem: matters concerning stripes and domains. Jahn - Teller effect and negative-U behaviour*, Journal of Physics - Condensed Matter **10**(15), 3387–3410.

Wollan, E. O. and Koehler, W. C. (1955). *Neutron Diffraction Study of the Magnetic Properties of the Series of Perovskite Type Compounds* $[La_{1-x}, Ca_x]MnO_3$, Physical Review **100**(2), 545–563.

Wu, M. K., Ashburn, J. R., Torng, C. J., Hor, P. H., Meng, R. L., Gao, L., Huang, Z. J., Wang, Y. Q. and Chu, C. W. (1987). *Superconductivity at 93 K in a New Mixed-Phase Y-Ba-Cu-O Compound System at Ambient Pressure*, Physical Review Letters **58**(9), 908–910.

Yoshinari, Y., Hammel, P. C. and Cheong, S.-W. (1999). *Magnetism of Stripe-Ordered* $La_{5/3}Sr_{1/3}NiO_4$, Physical Review Letters **82**(17), 3536–3539.

Yoshizawa, H., Kakeshita, T., Kajimoto, R., Tanabe, T., Katsufuji, T. and Tokura, Y. (2000). *Stripe order at low temperatures in* $La_{2-x}Sr_xNiO_4$ *with* $0.289 \leq x \leq 0.5$, Physical Review B **61**(2), R854–R857.

Zheng, G., Xu, C. N., Tomokiyo, Y., Tanaka, E., Yamada, H. and Soejima, Y. (2000). *Observation of Charge Stripes in Cupric Oxide*, Physical Review Letters **85**(24), 5170–5173.